Further development of Severe Accident Management Strategies for a German PWR Konvoi Plant based on the European Severe Accident Code ASTEC

Zur Erlangung des akademischen Grades

Doktor der Ingenieurwissenschaften (Dr.-Ing.)

der Fakultät für Maschinenbau

Karlsruhe Institut für Technologie

genehmigte

Dissertation

von

Ignacio Gómez-García-Toraño

Hauptreferent:	Prof. Dr.-Ing. habil. Robert Stieglitz Karlsruher Institut für Technologie
Korreferent:	Prof. Dr.-Phys. habil. César Queral Universidad Politécnica de Madrid
Tag der mündlichen Prüfung:	25.04.2017

Acknowledgements

First and foremost, I would like to thank to the Institute of Neutron Physics and Reactor Technology of the Karlsruhe Institute of Technology (INR-KIT) and particularly to Robert Stieglitz, who gave me the opportunity to perform my PhD thesis under his supervision. I appreciate very much his technical comments and I am honoured that he shared with me his approach to solve scientific problems. I also owe my deepest gratitude to Víctor-Hugo Sánchez Espinoza for believing in me, for welcoming me warmly in his group of Reactor Physics and Dynamics (RPD), for being always open for technical discussions and, especially, for his support and friendship during this time.

I would like to thank César Queral from Polytechnic University of Madrid (UPM) for accepting to be the co-supervisor of my thesis and offering me continuous support to carry out my PhD research. I would also like to thank Gonzalo Jiménez, who raised in me a particular interest for the topic of severe accidents and encouraged me to take this great career opportunity in KIT.

I am also grateful to the Severe Accident Department at the Institut de Radioprotection et de Sûreté Nucléaire (IRSN) at Cadarache, and especially to Patrick Chatelard, for hosting me during six months and for allowing a close cooperation with the ASTEC developer team. I am especially grateful to Laurent Laborde, Sèbastien Belon and Florian Fichot for their support during that time and ever since then.

I would like to express my warmest gratitude to several people at KIT, whose continuous help in different areas have made possible this work. Firstly, I am grateful to Juri Stuckert for providing me with experimental data from the QUENCH test facility and for his patience to answer the many questions that I had about the phenomenology during this time. Secondly, I am indebted to Javier Jiménez, who helped me so much to improve my computational skills and always had the door open to discuss ways of automatizing tasks and being more efficient at work. Finally, I would like to thank Wolfgang Hering and Christoph Homann for sharing with me their experience in the field of severe accidents and for being always open for technical discussions

I wish to thank Martin Sonnenkalb and Nils Reinke (Gesellschaft für Anlagen und Reaktorsicherheit), Matthias Braun (AREVA) and Michael Buck (University of Stuttgart) for their precious advice as well as for the fruitful discussions, which in turn have helped me to orient my research.

Then, I would like to acknowledge the support from the rest of the members at RPD (Valentino, Uwe, Marcus, Aleksandar, Miriam, Alexander, Joaquín, Alexander, José Ángel, Verónica, Zhuoqi, María José, Jonas and all others), other members of the INR (Wadim and Nerea) and thank the secretaries for helping me to get through tricky administrative issues. I thank them all for creating such an excellent atmosphere at work.

Furthermore, I would like to thank my dearest friends Beatriz, Carlos, Adriana, Kevin, Alberto, Pablo, Edu, Adrián, Luis, Lena, Lila, Alberto and all others for surrounding me during this time. I have been extremely glad to have you by my side.

Por último, me gustaría agradecer de todo corazón a mi hermano Alfonso, a mi madre Isabel, a mi padre Ángel y al resto de mi familia (primos, tíos y abuelos) por ofrecerme una educación exquisita, por estar siempre pendientes de mí y por llenar mi vida de felicidad. Si he conseguido esto, es gracias a vosotros.

Abstract

The Fukushima accidents have shown that a further improvement of Severe Accident Management Guidelines (SAMGs) for the current fleet of Light Water Reactors is still necessary. This requires the generation of a broad database of risk-relevant deterministic analyses using state-of-the-art severe accident software. In this dissertation, the ASTECV2.0 integral severe accident code is used for the verification, optimization and development of selected SAM strategies in a German Konvoi PWR based on the lessons learnt from Fukushima.

For this purpose, first of all the ASTECV2.0 physical models describing the early in-vessel phase are verified using data from the QUENCH-08 experiment, which investigates the quenching of an overheated core with saturated steam. The comparison of the code predictions with the experimental data shows that the code is able to describe the key physical phenomena (e.g. core oxidation, convective and radiative heat transfers) during all experimental phases, leading to a similar oxidation profile and hydrogen generation at the end of the experiment. However, the code underestimates the hydrogen generation during reflooding, which seems to be caused by the systematic underestimation of the radial temperature gradient and of the heat transfer above the active zone of the facility.

The validated ASTECV2.0 version is then used to investigate the efficiency of selected SAM measures in a generic German Konvoi PWR e.g. depressurization and/or water injection into the primary and secondary circuit. The spectrum of selected scenarios includes Medium and Small Break LOCAs (MBLOCA and SBLOCA) and total Station Blackout (SBO), which are risk-relevant scenarios for core damage and containment failure. Based on a systematic and extensive evaluation of the aforementioned severe accident scenarios using ASTECV2.0, a list of promising SAM measures have been identified:

- Secondary bleed and feed must be executed before the Core Exit Temperature (CET) exceeds 400 °C and with at least 15 kg/s to prevent core melting (based on SBO).
- Primary bleed and feed must be initiated at CET= 400 °C or, if not possible, with a maximum delay of 20-30 min in order to delay core melting and vessel failure (based on SBLOCA and SBO).
- Core reflooding must be launched immediately after CET > 650 °C with at least 20 kg/s in order to prevent major core damage (based on MBLOCA, SBLOCA and SBO sequences).
- In case of an external injection into the primary circuit, the deployment order of a high-pressure head (> 50 bar) mobile pump must be issued 1 h after the loss of AC power supply so that reflooding can be initiated near CET 650 °C (based on SBLOCA and SBO sequences).
- Vessel failure cannot be prevented if more than 20 corium tons are present in the lower plenum for more than 20 min regardless of the injection rate (based on MBLOCA, SBLOCA and SBO).

These findings are important for plant operators and shall be verified with the new ASTECV2.1 version, which includes improved 2-D core thermal-hydraulics models. In addition, further efforts are needed to quantify ASTEC uncertainties regarding the modelling of key in-vessel physical phenomena, such as oxidation, corium relocation and stratification in the lower plenum and RPV failure.

The performed investigations on a generic German Konvoi PWR using ASTECV2.0 elucidate the code capabilities to describe the in-vessel phase of severe accident in PWRs and to assess the performance of SAM measures aiming at preventing RPV failure. Furthermore, this dissertation extends the technical basis for the development of optimized SAMGs, contributing to strengthen such type of plant against severe accidents.

Kurzfassung

Der Fukushima-Unfall hat gezeigt, dass weitere Verbesserungen des Handbuchs für Mitigative Notfallschutzmaßnahmen (SAMGs) notwendig sind. Dafür ist es erforderlich, eine umfangreiche Datenbank von Risiko-relevanten Szenarien unter Einsatz deterministischer Analysen basierend auf dem Stand von Wissenschaft und Technik zu generieren. In Rahmen dieser Doktorarbeit wird das Störfallcode ASTEC verifiziert und zur Optimierung und Entwicklung verschiedener Notfallschutzmaßnahmen (SAM) für eine Deutsche Reaktoranlage-Anlage unter Berücksichtigung der aus dem Fukushima-Unfall abgeleiteten Lehren eingesetzt.

Zu diesem Zweck werden die physikalischen Modelle der Frühphase eines schweren Unfalls von ASTECV2.0 anhand vom QUENCH-08 Versuch validiert, wobei einen beheizten Kern mit gesättigtem Wasserdampf geflutet wird. Der Vergleich zwischen den gerechneten und experimentellen Ergebnissen hat zeigt, dass ASTECV2.0 alle wichtigen Phänomene wie z.B. Oxidation, Konvektions-, und Strahlungswärme vom QUENCH-08 Versuch mit guten Genauigkeit beschreiben kann. Daher liegen die berechneten Oxidationsprofile und die freigesetzte Wasserstoffs-Menge nah an den Messdaten. Allerdings wird die Steigerung der Temperaturen während der Flutphase vom ASTEC unterschätzt. Ursachen für diese Unterschätzung sind u.a. die niedrigen, radialen Temperaturgradienten sowie die Wärmeübertragung über den aktiven Teil des Bündels.

Mit dem validierten ASTECV2.0 Code wurde die Wirksamkeit verschiedener SAM-Maßnahmen für unterschiedliche SA-Sequenzen der Konvoi DWR-Anlage wie z.B. primär- und sekundärseitige Druckentlastung und/oder Wassereinspeisung in den Sekundär-, oder Primärkreislauf umfassend untersucht. Zu den ausgewählten SA-Störfallszenarien gehören u.a. den mittleren und kleinen Bruch im Primärkreislauf (MBLOCA und SBLOCA) sowie der Ausfall der Drehstromversorgung (SBO). Unter Berücksichtigung der zahlreichen durchgeführten ASTEC-Analysen der genannten Szenarien haben sich folgende Notfallschutzmaßnahmen als „vielversprechenden und sehr wirksam“ zur Verzögerung oder Verhinderung des Reaktordruckbehälter (RPV)-Versagens herauskristallisiert:

- Sekundärseitige Druckentlastung und Dampferzeugerbespeisung mit mehr als 15 kg/s durchgeführt bevor die Überschreitung der Kernaustrittstemperatur (CET) von 400 °C erreicht wurde um Kernschmelze zu vermeiden (gemäß SBO).
- Primärseitige Druckentlastung durchgeführt beim Erreichen der Kernaustrittstemperatur (CET) von 400 °C oder mit einer maximalen Verspätung von 20-30 min, um Kernschmelze und RPV-Versagen zu verzögern (gemäß SBLOCA und SBO).
- Kernfluten beim Überschreitung der CET> 650 °C mit mehr als 20 kg/s Einspeiserate, um erhebliche Kernschmelze zu vermeiden (gemäß MBLOCA, SBLOCA und SBO).
- Falls eine externe Bespeisung in den Primärkreislauf z.B. mit mobilen Pumpen berücksichtig wird, muss der Einsatz einer Hochdruckmobilpumpe (>50 bar) in der darauf folgenden Stunde nach dem Verlust des ACs erfolgen, damit das Fluten kurz nach dem Erreichen der CET=650 °C erfolgen kann (gemäß SBO).
- Unabhängig vom Einspeiseraten kann RPV Versagen nicht vermieden werden, wenn sich mehr als 20 Tonnen Corium länger als 20 min im unteren Plenum angesammelt hat (gemäß MBLOCA, SBLOCA und SBO).

Die aufgelisteten Notfallmaßnahmen sind von großer Bedeutung für den Betreiber und sollten mit der neusten ASTEC Version 2.1, welche verbesserte Zweiphasenströmungsmodelle für CESAR-Modul zur Beschreibung des Kernverhaltens aufweist, verifiziert werden. Des Weiteren ist es notwendig, eine Quantifizierung der Codeunsicherheiten bezüglich wesentliche physikalischen Phänomene wie z.B. Oxidation, Schmelzeverlagerung und Stratifizierung im unterm Plenum, RPV-Versagen, etc. durchzuführen.

Die durchgeführten Analysen an dem generischen Deutschen Konvoi PWR demonstrieren die Leistungsfähigkeit vom ASTECV2.0 wesentlichen Phänomenen der frühen Kernschmelzphase sowie die Eignung zur Erarbeitung und Optimierung von Notfallschutzmaßnahmen. Abschließend kann herausgestellt werden, dass diese Doktorarbeit wichtige Beiträge zur Erweiterung der technischen Basis für die Entwicklung und Optimierung von SAMGs geleistet hat, welche zur Stärkung der Robustheit der Sicherheitseigenschaften einer PWR-Anlage gegenüber schweren Kernunfällen genutzt werden kann.

.

Table of Contents

ACKNOWLEDGEMENTS ..... *I*

ABSTRACT ..... *III*

KURZFASSUNG ..... *IV*

TABLE OF CONTENTS ..... *VII*

LIST OF ABBREVIATIONS ..... *XI*

1 INTRODUCTION *1*

1.1 Motivation **1**

1.2 Goals of this thesis **3**

1.3 Approach and structure of the thesis **5**

2 IN-VESSEL PROGRESSION OF SEVERE ACCIDENTS IN PWRS *7*

2.1 Early-in vessel phase **7**

2.1.1 Oxidation of core materials 9

2.1.2 Cladding ballooning and burst 11

2.1.3 Dissolution of grid spacers and control rod materials 11

2.1.4 Cladding failure 11

2.1.5 Formation of molten pool and relocation into the Lower Plenum 12

2.2 Late in-vessel phase **13**

2.2.1 Fuel Coolant Interaction and molten pool formation 13

2.2.2 Stratification and behaviour within the Lower Plenum 14

2.2.3 Vessel failure 15

2.3 Core Reflooding **16**

2.4 Impact of In-vessel phase on Ex-vessel phase **18**

2.5 Summary **19**

3 ACCIDENT MANAGEMENT IN PWRS *20*

3.1 Overview **20**

3.1.1 Defence-in-Depth (DiD) 20

3.1.2 Fundamentals about Accident Management 21

3.1.3 Historical development of AM 22

3.2 Transition from preventive AM to SAM **24**

3.2.1 Worldwide 24

3.2.2 Germany 26

3.3 Preventive AM measures in PWRs 27
3.3.1 German Konvoi PWR 27
3.4 Severe Accident Management in PWRs 29
3.4.1 Existing SAMG approaches 29
3.4.2 SAM measures 32
3.4.3 Computational aids 34
3.5 Summary 35
4 THE ASTECV2.0 CODE AND SELECTED PHYSICAL MODELS 36
4.1 Current Status 36
4.2 Structure of the ASTECV2.0 code 37
4.3 The CESAR module 38
4.4 The ICARE module 39
4.4.1 Zircaloy oxidation by steam 40
4.4.2 Cladding failure 41
4.4.3 Relocation of molten material 42
4.4.4 Oxidation of molten material 43
4.4.5 Reflooding for rod-like geometry 44
4.4.6 Models associated to the simplified Lower Plenum 45
4.4.7 Reactor Pressure Vessel failure 48
4.5 Summary 49
5 VALIDATION OF ASTECV2.0 MODELS BASED ON THE QUENCH TEST FACILITY 51
5.1 The QUENCH Test facility 51
5.2 Test Conduct of QUENCH-08 Experiment 53
5.3 ASTEC Model of the QUENCH-08 Experiment 54
5.3.1 Geometry and model assumptions 54
5.3.2 Boundary conditions 55
5.3.3 Physical phenomena 56
5.4 Comparison of ASTEC predictions with QUENCH-08 Experimental data 56
5.5 Comparison with other studies and Discussion 63
5.6 Summary 65
6 GENERIC MODEL OF A GERMAN KONVOI PWR USING ASTECV2.0 67
6.1 Modelling of the PWR Konvoi plant in ASTEC 67
6.1.1 Primary and Secondary circuit 67

6.1.2 Reactor Pressure Vessel (RPV) 68
6.1.3 Containment 70
6.2 Steady State Control Systems 72
6.3 Verification of the ASTEC model using the reference data for stationary conditions 73
6.4 Extensions of the ASTEC integral PWR model for the simulation of SAs 74
6.5 Protection Systems, Safety Systems and SAM actions 75
6.6 Summary 78
7 SIMULATION OF SEVERE ACCIDENTS WITHOUT AM IN A GERMAN KONVOI PWR USING ASTECV2.0 79
7.1 MBLOCA in the cold leg of the pressurizer loop combined with SBO 80
7.1.1 MBLOCA with SBO 1 h after SCRAM 80
7.1.2 MBLOCA sequences with different times of SBO 82
7.1.3 Comparison with other studies and Discussion 83
7.2 SBLOCA in the cold leg of the pressurizer loop combined with SBO 84
7.2.1 SBLOCA with unlimited AC power 84
7.2.2 SBLOCA sequences with different times of SBO 87
7.2.3 Comparison with other studies and Discussion 88
7.3 Station Blackout 89
7.3.1 Comparison with other studies and Discussion 91
7.4 Summary 92
8 SIMULATION OF AM MEASURES IN A GERMAN KONVOI PWR USING ASTECV2.0 93
8.1 MBLOCA in the cold leg of the pressurizer loop combined with SBO 93
8.1.1 Active Core Reflooding 94
8.2 SBLOCA in the cold leg of the pressurizer loop combined with SBO 102
8.2.1 Primary Side Depressurization and Passive Core Reflooding 103
8.2.2 Primary Side Depressurization and Active Core Reflooding 106
8.3 Station Blackout 115
8.3.1 Secondary Side Depressurization (SSD) and Active Injection into the SGs 116
8.3.2 Primary Side Depressurization and Passive Core Reflooding 124
8.3.3 Primary Side Depressurization and Active Core Reflooding 129
8.4 Recommendations concerning SAM for the German PWR Konvoi 135
8.5 Summary 136
9 CONCLUSIONS 137

APPENDIX A OVERVIEW OF THE GERMAN KONVOI PWR AND KEY SAFETY SYSTEMS 141

A.1 Description and general layout 141

A.2 Relevant safety systems 143

APPENDIX B FURTHER RESULTS OF THE ASTECV2.0 VALIDATION ON THE QUENCH-08 EXPERIMENT 145

B.1 Temperature evolutions at several locations during the experiment 145

B.2 Axial temperature and oxide profiles at selected times 150

APPENDIX C ADDITIONAL FEATURES OF THE GENERIC ASTECV2.0 MODEL OF THE GERMAN KONVOI PWR 151

C.1 Pressure control in the Pressurizer 151

C.2 Active systems of the ECCS 154

C.3 External mobile pumps 154

APPENDIX D FURTHER RESULTS OF THE PERFORMED SEQUENCES IN A GERMAN KONVOI PWR USING ASTECV2.0 156

D.1 Medium Break LOCA (440 cm^2) in the cold leg of the pressurizer loop 157

D.2 Small break LOCA (10 cm^2) in the cold leg of the pressurizer loop 164

D.3 Station Blackout 175

BIBLIOGRAPHY 190

LIST OF PUBLICATIONS 200

List of Abbreviations

English Abbreviation	German Abbreviation	Description
AC		Alternating Current
ACCUs		Accumulators
EFWS	LAR	Emergency Feedwater System
AM		Accident Management
PORV		Pilot Operating Relief Valve
BDBAs		Beyond Design Basis Accidents
B&WOG		Babcock and Wilcox Owner Group
CAs		Computational Aids
CDS		Core Damage State
CEOG		Combustion Engineering Owner Group
CET		Core Exit Temperature
CR		Control Room
CSFs		Critical Safety Functions
CVCS	KBA	Chemical and Volume Control System
DBAs		Design Basis Accidents
DC		Direct Current
DCH		Direct Containment Heating
DG		Diesel Generator
DiD		Defence in Depth
EBS	JDH	Extra Borating System
ECCS		Emergency Core Cooling System
EC		European Commission
EOPs		Emergency Operating Procedures
ERO		Emergency Response Organization/Team
FPs		Fission Products
FRS		Fuel Rod Simulator
FW		Feedwater
FWS	LAB	Feedwater System
GRS	GRS	Gesellschaft für Anlagen- und Reaktorsicherheit
HPIS		High Pressure Injection System
IRSN		Institute de Radioprotection et Sureté Nucléaire
KIT		Karlsruhe Institute of Technology
LP		Lower Plenum
LH		Lower Head
LOOP		Loss of Offsite Power

LPIS		Low Pressure Injection System
LWR		Light Water Reactor
MBLOCA		Medium Break LOCA
MCCI		Molten Corium Concrete Interaction
MCL		Main Coolant Line
MCP		Main Coolant Pump
MSL	LBA	Main Steam Line
NEI		Nuclear Energy Institute
OG		Owner Group
PAR		Passive Autocatalytic Recombiners
PBF		Primary Bleed and Feed
PCT		Peak Cladding Temperature
PSA		Probabilistic Safety Analysis
PSD		Primary Side Depressurization
PWR		Pressurized Water Reactor
QF		Quench Front
RCPS		Reactor Control Protection System
RCS		Reactor Coolant System
RMFR		Reflooding Mass Flow Rate
RPV		Reactor Pressure Vessel
SA		Severe Accident
SAM		Severe Accident Management
SAMG		Severe Accident Management Guidelines
SBF		Secondary Bleed and Feed
SBLOCA		Small Break LOCA
SBO		Station Blackout
SG		Steam Generator
SGTR		Steam Generator Tube Rupture
SSD		Secondary Side Depressurization
SRV		Safety Relief Valve
SV		Safety Valve
TBR		Transition Boiling Region
THC		Thermo-Couple
TMI-2		Three Mile Island Unit 2
TSC		Technical Support Center
WOG		Westinghouse Owner Group
Zry		Zircaloy

1 Introduction

1.1 Motivation

In the nuclear power plants (NPPs) operated worldwide, the defence in depth (DiD) concept is applied to protect the public from a harmful release of radioactive material [1]. For that aim, the DiD establishes the necessity of deploying a hierarchy of safety levels with associated provisions to maintain the integrity of the cladding, the vessel and the containment. However, although improbable, these provisions may fail and an abnormal event can turn into a beyond design basis accident (BDBA), also called severe accident.

Severe accidents are characterized by the in-vessel (up to vessel failure) and the ex-vessel (after vessel failure) phases and can be terminated using Accident Management (AM). In particular, AM programs have four goals: prevent core damage, terminate core damage, maintain containment integrity and minimize off-site releases [2]. The AM measures aiming at the first are called preventive and are encompassed in the Emergency Operating Procedures (EOPs), whereas the latter three are called mitigative Severe Accident Management (SAM) measures and belong to the SAM Guidelines (SAMGs).

Significant improvements have been made on the development of AM procedures during the 80s and the 90s, especially after the severe accidents at Three Mile Island Unit 2 – TMI-2 (1979) and Chernobyl (1986). In particular, the Technical Basis Report [3–5], as a compendium of the knowledge of severe accident phenomenology and potential preventive and mitigative measures, has been a cornerstone in this development. However, the severe accidents at Fukushima Daiichi Units 1-2-3 (2011) have shown that further improvements on AM measures are still necessary in order to minimize the consequences of such accidents [6].

In Germany, immediate actions after the Fukushima accidents were taken to review the safety status of all operating NPPs [7]. The conclusions from this investigation reaffirmed the robustness of all German NPPs and identified areas of improvement for the further increase of the safety margins. Based on these outcomes, a German Action plan was drafted for the improvement of AM measures for all NPPs, whose state of implementation has been evaluated every two years since then [8–10]. In particular, the document stated the necessity of including the possibility of internal and external hazards in the SAMGs, the verification and extension of SAM measures during conditions of long term Station Blackout.

In German Konvoi PWRs, severe accidents are initially controlled by EOPs (also called *Notfallhandbuch – NHB*) [11]. The measures contained therein are mostly preventive and aim at restoring the three main critical safety functions (subcriticallity, core coolability and confinement of radioactivity) [12]. If these actions do not succeed before a certain time window, priority shifts to mitigative AM, which is covered by the SAMGs (also called *Handbuch für Mitigative Notfallmaßnahmen – HMN*) [12–14].

Typical preventive and mitigative AM measures in a German Konvoi PWR are the depressurization and water injection into the secondary/primary circuit (secondary/ primary bleed and feed) and the primary circuit (primary bleed and feed) [15]. However, experiments at the CORA and QUENCH facilities have shown that water injection into an overheated core (reflooding) may trigger a sharp hydrogen generation, that could jeopardize the containment integrity at an early stage of the accident [16].

The development of SAMGs requires a deep understanding of the phenomena involved in severe accidents, usually involving neutron physics, thermal-hydraulics, structural mechanics and high temperature chemistry [17]. Significant knowledge about severe accidents in Light Water Reactors (LWRs) has been gained over the last decades after the TMI-2 accident [18] and the Phebus program [19]. However, Fukushima has disclosed that some major issues remain unresolved [20,21]. In addition, the development of SAMGs requires a solid database of risk-relevant deterministic analyses performed with state-of-the-art numerical simulation tools. Consequently, the improvement of severe accident codes is pursued worldwide through dedicated research programs [22,23].

Deterministic severe accident codes are divided in two groups depending on their simulation scope: integral codes (e.g. MELCOR, MAAP and ASTEC) simulate the in-vessel and the ex-vessel phases of a severe accident, whereas mechanistic codes (e.g. ATHLET-CD, SCDAP/RELAP, SAMPSON) solve accurately a specific part of it.

The ASTEC code [24], jointly developed by the Institut de Radioprotection et de Sûreté Nucléaire (IRSN) and the Gesellschaft für Anlagen und Reaktorsicherheit (GRS), is progressively becoming the European reference Severe Accident (SA) integral code. However, it has not been usually used to support the choice of SAM measures for the current fleet of LWRs. For that aim, ASTEC is being improved in the frame of the EU CESAM project [22] in two complementary ways: first, through the validation of the ASTECV2.0 version [25] and its application to all PWR types in Europe; second, through the development of the ASTECV2.1 version [26], characterized by improved physical models, geometrical description of other LWR designs (e.g. BWRs) and numerical stability.

A sketch representing the main events during the in-vessel phase of a hypothetical severe accident, the domain of preventive and mitigative AM measures and the requirements to build EOPs and SAMGs can be found in **Figure 1-1**.

For this doctoral thesis, the ASTECV2.0 (revision 3, patch 0) severe accident code has been selected as the main tool for the verification, optimization and development of the aforementioned SAM measures for a German Konvoi PWR considering the recommendations of the German Action Plan for the implementation of measures after the Fukushima accidents [8–10] and the most risk-relevant sequences for the nuclear plant under consideration [27].

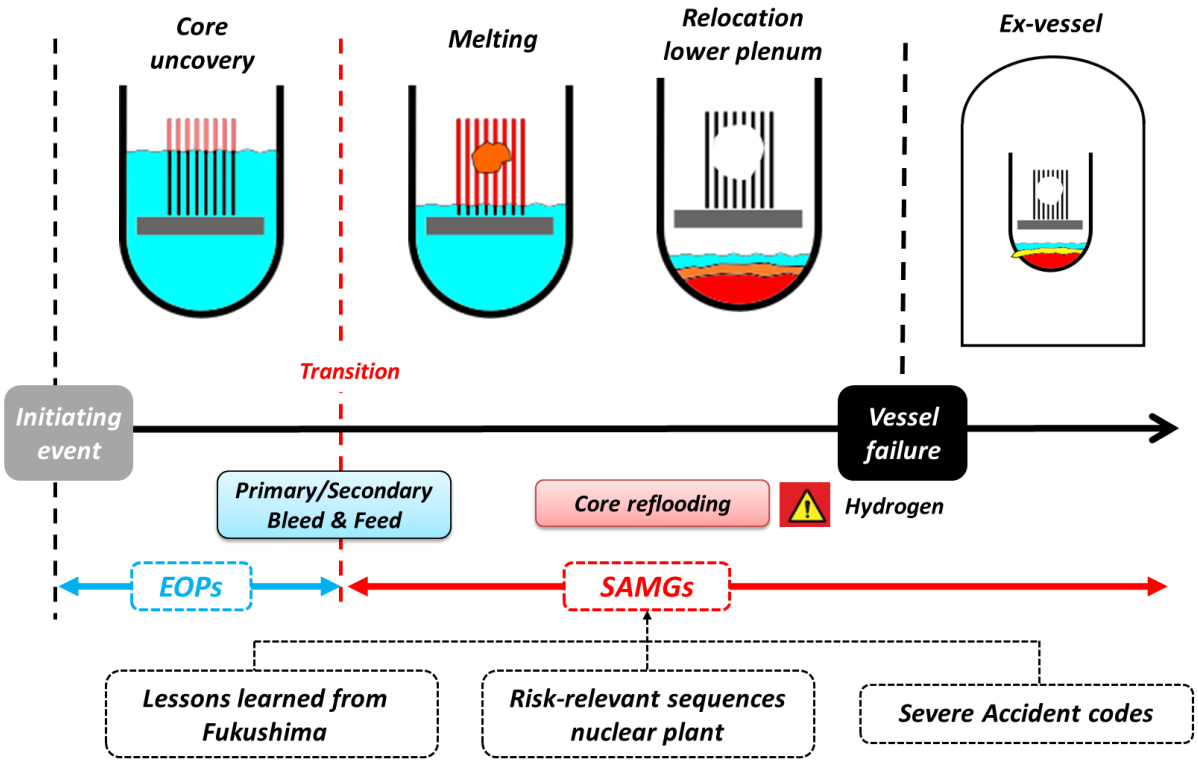

Figure 1-1: Sketch representing the main events during the in-vessel phase of a severe accident, the domain of preventive and mitigative AM measures and the requirements to build EOPs and SAMGs.

1.2 Goals of this thesis

Considering this introductory remarks, the doctoral thesis is focused on the following specific technical goals:

- Develop an ASTECV2.0 model for the QUENCH facility for the validation of the physical models covering the early phase of the severe accident.
- Identify modelling deficiencies of the early in-vessel phase based on the outcomes of this validation (see **Figure 1-2**).
- Develop an ASTECV2.0 model for the German Konvoi PWR for the simulation of the in-vessel phase of selected severe accidents.
- Simulate reference severe accident scenarios (without the intervention of SAM measures) relevant for the risk of core damage and radioactivity release in a German Konvoi PWR using ASTECV2.0.
- Evaluate the performance of in-vessel SAM measures (e.g. secondary bleed and feed, primary side depressurization and core reflooding) on the progression of the reference severe accident scenarios.
- Identify the most appropriate in-vessel SAM measures to delay or prevent core melting and vessel failure.
- Provide recommendations for the improvement of SAM measures in a German Konvoi PWR based on the performed ASTECV2.0 simulations (see **Figure 1-3**).

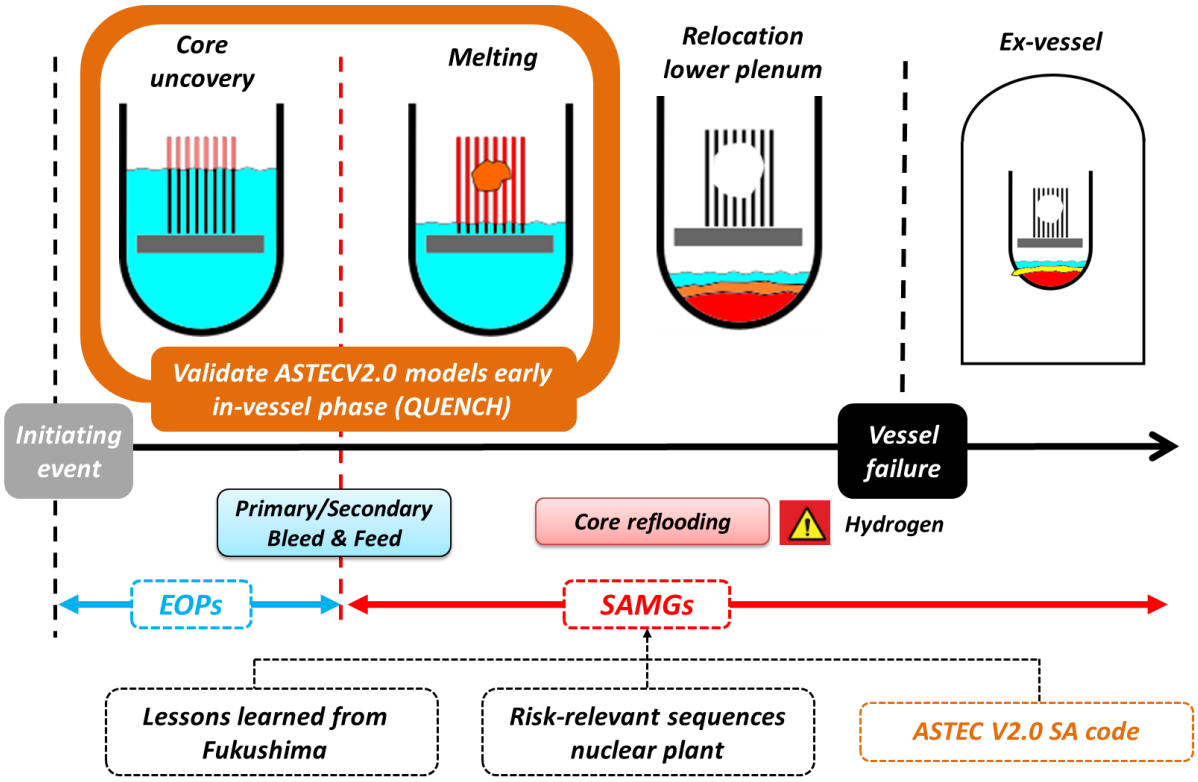

Figure 1-2: First goal of this PhD thesis (validation of ASTECV2.0 models governing the early in-vessel phase of the accident), in perspective to the field of severe accident research in LWRs.

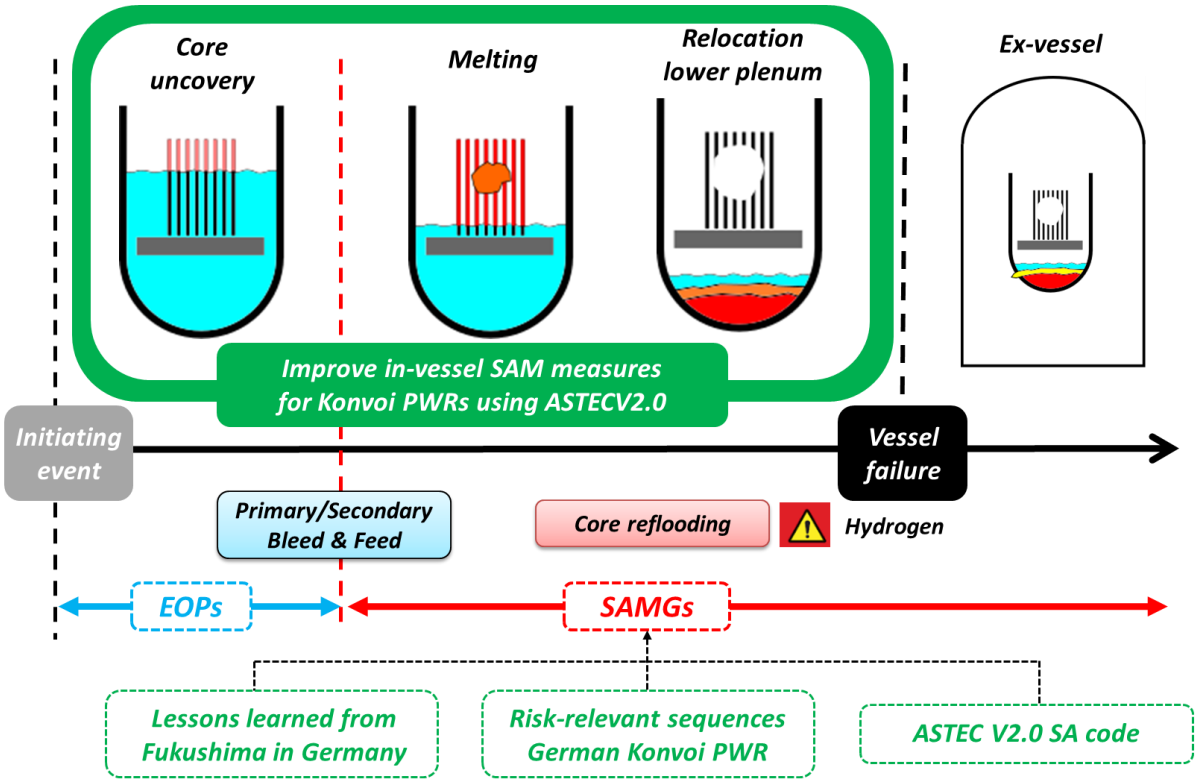

Figure 1-3: Major goal of this PhD thesis (improvement of in-vessel SAM measures for Konvoi PWRs using ASTECV2.0), in perspective to the field of severe accident research in LWRs.

1.3 Approach and structure of the thesis

In order to reach these goals, the doctoral thesis is organized in the following chapters:

First of all, a review of the key physical phenomena occurring during the in-vessel phase of a severe accident in a generic PWR is performed in Chapter **2**. Therein, special attention is paid to the early in-vessel phase of the SA, on which the validation work is focused.

The role of AM and its current status after the Fukushima accidents is described in Chapter **3**. Therein, a review of the current approaches to perform the transition between preventive and mitigative AM, the approaches used to build the SAMGs and the most important preventive and mitigative AM measures are described for several PWR types with a special interest on the German Konvoi PWR.

The approximations made by ASTECV2.0 for the formulation of the key phenomena relevant for the in-vessel phase of the severe accident are described in Chapter **4**. Among others, these are the Zircaloy (Zry) oxidation by steam, corium relocation in the core, corium stratification in the lower plenum, reflooding of slightly degraded cores and vessel failure.

After the explanation of the theoretical aspects for the thesis, the Chapter **5** evaluates ASTECV2.0 capabilities to describe the early in-vessel phase of the severe accident using data from the QUENCH test facility. For that purpose, it has been necessary to improve the ASTECV2.0 model of the QUENCH facility and to adapt it to the particular conditions of the test number 8, which involves the reflooding of a slightly degraded core by steam.

Once the code is validated, the main challenge is the simulation of different SA sequences for a generic German Konvoi PWR using the validated ASTECV2.0 version aiming at the verification, optimization and development of SAM measures. This is performed in different chapters.

The main modelling guidelines of a generic ASTECV2.0 model of the German Konvoi PWR are detailed in Chapter **6**. These include explanations about the modelling of the primary and secondary circuits, reactor core and containment. The key plant parameters obtained by the model in steady state are compared to the reference values of the German Konvoi PWR. Later on, the physical phenomena considered for the simulation of the in-vessel phase of the accident and the main features of the simplified protection, safety systems and AM procedures of the plant model are described.

The generic ASTECV2.0 model is then used in Chapter **7** to simulate the in-vessel progression of severe accident sequences without AM according to the outcomes of the Probabilistic Safety Analysis for the German Konvoi PWR. Subsequently, the efficiency of preventive and mitigative SAM measures (e.g. secondary and primary bleed and feed procedures) on the previous sequences is assessed in Chapter **8**, which concludes with a list of SAM recommendations for such nuclear power plant.

The key findings of the thesis regarding the most appropriate AM measures to delay, mitigate or prevent core melting and vessel failure in a German Konvoi PWR are summarized in Chapter **9**.

In addition, the dissertation includes following Appendixes supporting the main document:

- Appendix **A** describes the main safety systems and their distribution in a German Konvoi PWR.
- Appendix **B** includes further results about the validation of ASTECV2.0 with the QUENCH-08 Experiment.
- Appendix **C** contains additional information about the modelling of relevant control and safety systems in the ASTECV2.0 model of the German Konvoi PWR.
- Appendix **D** includes further results about the ASTECV2.0 simulations of severe accident sequences with and without SAM in a German Konvoi PWR.

2 In-vessel progression of Severe Accidents in PWRs

Severe accidents are initiated by the loss of heat removal from the decay-heated core and are characterized by the gradual loss of core geometry. They can be divided into the in-vessel (from the initiating event to the failure of the vessel) and the ex-vessel phase (from vessel failure to containment failure). At the same time, the first can be broken down into the early in-vessel (from core melting to the break of the in-core molten pool) and the late in-vessel phase (from break of in-core molten pool to vessel failure).

The current chapter gives an overview of the key phenomena involved during the in-vessel phase of hypothetical severe accidents in a German Konvoi PWR (sections **2.1**, **2.2** and **2.3**), whose main features are described in **Appendix A**, and discusses the influence of the in-vessel phase on the later ex-vessel phase (section **2.4**). Since the characterization of diverse SAs occurring in all conceivable accidental sequences is not possible, this chapter is devoted to the description of the key phenomenology occurring in a low pressure sequence, since this is the most likely situation for the actual plant [27]. Further insights on the phenomenology taking place during low and high pressure sequences can be found in [28].

For that purpose, this chapter makes use of the lessons learnt from the TMI-2 accident [18] and of extensive research on LWR in-vessel severe accident phenomenology, the main experimental facilities being encompassed in **Table 2-1**. Therein, the first column entails the name of the experiment and its current status (active/closed), whereas the second one includes a description of its aim.

2.1 Early-in vessel phase

Within this section, a summary of the most relevant phenomena occurring during the early in-vessel phase is given. Further details about the phenomenology can be found in [16,19,29].

After the primary circuit reaches saturation, the water starts to boil off and the core liquid level decreases below the top of the core. Consequently, the heat transfer coefficient between the fuel rod claddings and the surrounding steam declines and the core starts to heat up. At the beginning, the heat-up is low because the natural convection is capable of transferring the decay heat through the entire structures. However, when the Peak Cladding Temperature (PCT) exceeds 1500 K, the influence of the natural circulation starts to become overshadowed by an additional heat source. This heat source is provided by exothermal oxidation reactions of the core materials in steam.

Name	Goal of the Experiment
CORA (1987-1996)	Investigation of phenomena relevant during the early in-vessel phase: Zircaloy (Zry) oxidation by steam; interaction between UO_2 pellets and Zry cladding; interaction among other materials (Inconel, stainless steel, silver-indium-cadmium) [29].
PHEBUS-FP (1993-2004)	Investigation of phenomena governing core degradation during the early and late in-vessel phase, fission product release and transport, containment phenomena and iodine chemistry [30].
QUENCH (1996-)	Investigation of hydrogen generation and bundle degradation derived from the bottom reflooding of slightly degraded cores [16].
PEARL (2013-)	Investigation of bottom and top reflooding of a debris bed at a large scale under representative thermal-hydraulic conditions with sustained heating and variable geometries of the debris bed (e.g. reflooding of degraded cores) [31].
FARO (1991-1999)	Investigation of the debris bed initial conditions and morphology after the corium has slumped and quench into water in a range of conditions typical of in-vessel and ex-vessel situations [32].
RASPLAV-MASCA (1994-2006)	Investigation of the chemical behaviour of molten core materials under severe accident conditions, especially the chemical reactions between corium and other structural materials (e.g. steel) [33].
LIVE (2006-)	Investigation of melt thermal behaviour and melt solidification process in the lower plenum of the vessel under various relocation scenarios [34].
FOREVER (1999-2002)	Investigation of creep deformation and vessel failure mode for prototypical vessel geometries under prototypical thermal and pressure loading conditions and investigation of gap cooling [35].

Table 2-1: Experimental facilities relevant for the understanding of the in-vessel phase of severe accidents in German Konvoi PWRs (**green**: active, **red**: closed).

As a result of this temperature increase, the core materials start melting. The meltdown progression depends on the melting temperature of its constituent materials and on the formation of lower melting temperature alloys, which may appear when core materials come into close contact. Despite the quantification of the melting temperatures of all different core materials is a complex task, the CORA facility [29] and other separate effect tests have identified several temperature regimes for core melting (see **Figure 2-1**): local core damage (temperatures within 1500-1700 K), extended core damage (temperatures within 2100-2300 K) and total core destruction (temperatures within 2900-3100 K).

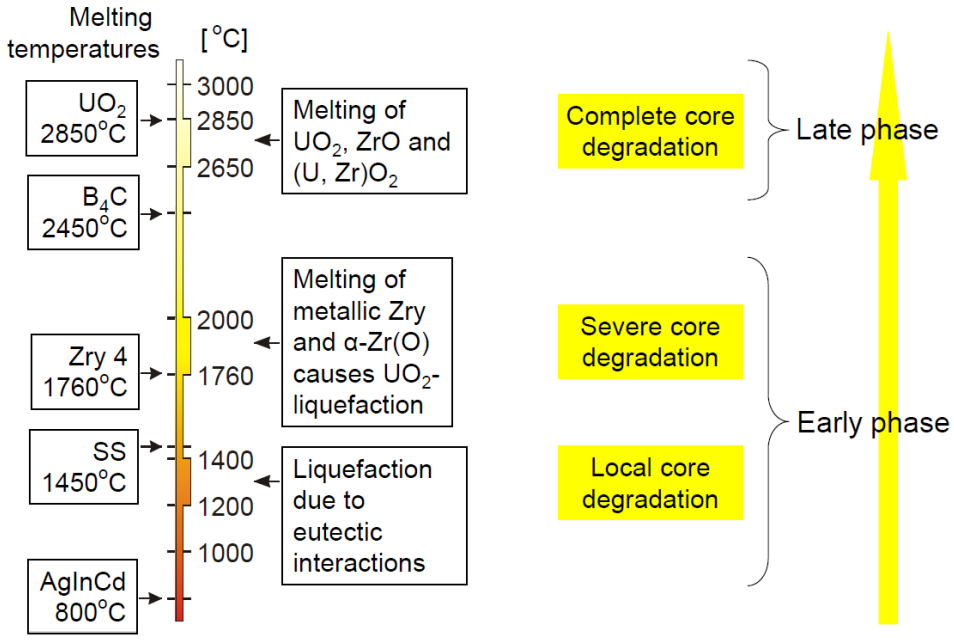

Figure 2-1: Temperature regimes of fuel element damage due to the formation of melts [36] - based on [29].

2.1.1 Oxidation of core materials

The most important oxidation reaction in the core is the one between the steam and the Zircaloy cladding, not only because of its energetic source (-585 kJ/mol), but also due to the large mass of Zry existing in PWR cores [37]. A summary of several Zry alloy compositions can be found in **Table 2-2** (note that the Konvoi uses the M5 type).

Apart from the chemical heat generation, oxidation yields two additional consequences:

- Release of hydrogen, which may jeopardize the containment upon contact with air.
- Deterioration of the cladding mechanical integrity due to phase transformations, which cause the co-existence of the β-Zr (fresh Zry-4), the α-Zr(O) (with up to 35 % at. oxygen) and the ZrO_2 phase (see stratification at the left side of **Figure 2-2**) [38].

Alloy	Sn (%)	Nb (%)	Fe (%)	Cr (%)
Zry-4	1.5	-	0.20	0.10
M5	0.01	1	0.05	0.015
ZIRLO	1	1	0.11	< 0.01
E110	-	1	0.008	0.002

Table 2-2: Composition of different Zry claddings relevant for different types of PWRs (the rest corresponds to Zirconium) [36].

Experimental work has shown that, under certain conditions (unlimited steam supply, temperatures higher than 1200 K and sufficiently thick walls), the oxidation kinetics is controlled by the oxygen diffusion through the cladding [39–41]. In such cases, the oxygen mass gain and the ZrO_2 layer growth are described by parabolic laws, which depend on the temperature according to an Arrhenius law. Therefore, regardless of the accident, once the cladding temperatures exceed 1200 K, the core experiences a temperature escalation. Additionally, this core heat-up is intensified by the microstructural changes in the ZrO_2 layer, which mark the existence three oxidation regimes (see right side of **Figure 2-2**):

- Low temperature oxidation regime within the field of existence of the tetragonal β-ZrO_2 phase (below 1800 K);
- Medium temperature oxidation regime within the transition region of (β+γ)-ZrO_2 (between 1800 K and 1900-2650 K);
- High temperature oxidation regime within the field of existence of the γ-ZrO_2 phase (above the transition region).

The faster kinetics of the medium and high temperature regimes is related to an enhanced diffusivity of oxygen towards the cubic γ phase than towards the tetragonal β one [38–41].

As the cladding becomes strongly oxidized and the amount of hydrogen in the core rises, the penetration of steam into the cladding is hindered and the oxidation rate decreases considerably [42]. This situation is referred to as *steam starvation*, which also causes a reduction of the oxide layer by the underlying metal [16].

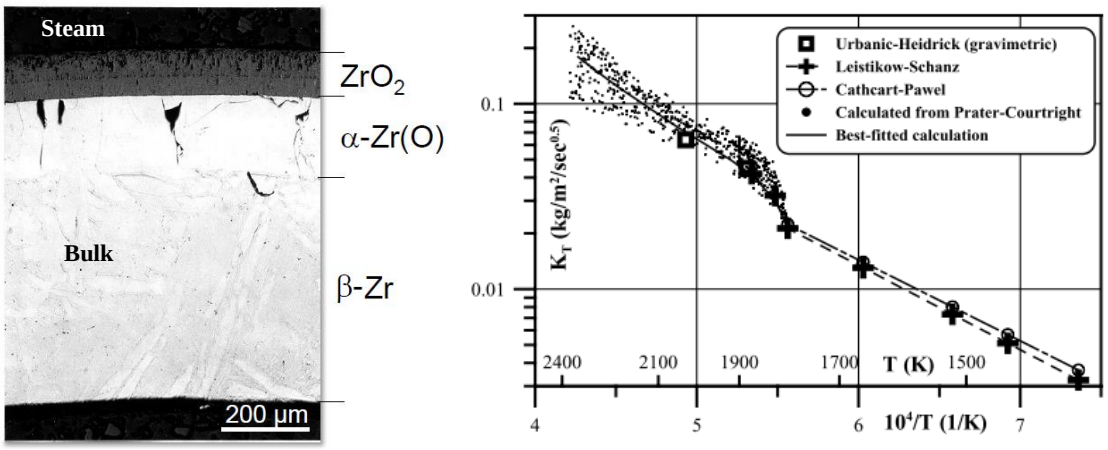

Figure 2-2: Left: Oxide stratification of a Zry-4 cladding in contact with steam [36]. Right: oxygen mass gain as a function of the inverse of the temperature according to existing correlations [43].

2.1.2 Cladding ballooning and burst

The ductility of cladding tubes decreases significantly at temperatures between 1000 K and 1200 K [44]. After the loss of coolant, the rod internal pressure (within 40-90 bars, depending on the fuel burn-up) would be much greater than the system pressure (within 5-20 bars), what leads to ballooning and eventually cladding burst. The main consequence is the release of fission products (FPs) to the Reactor Cooling System (RCS), the modification of the natural convection flow patterns and the oxidation of the inner cladding surface [45].

2.1.3 Dissolution of grid spacers and control rod materials

The first step in the degradation process is the destruction of the grids spacers (Inconel-718) and the meltdown of the control rods (Ag-In-Cd absorber pellet, stainless steel cladding and Zry-4 guiding tube). The degradation of the grid spacers occurs due to the interaction between Inconel-718 and Zry-4. The reaction starts to proceed rapidly above 1523 K (1250 °C) because of the formation of Zr-rich eutectic melt, and destroys the grid spacer shortly after reaching a temperature of 1673 K (1400 °C) [46].

Concerning the absorber rod, the Ag-In-Cd pellet has a melting temperature of 1073 K (800 °C), but it is protected by the steel cladding and by the Zry-4 guiding tube. The initiation of the meltdown is similar to the one of the grid spacers, since the steel starts to significantly interact with the Zry above 1473 K (1200 °C) forming a Zr-rich eutectic melt. Shortly after the destruction of both tubes, the melt reaches the absorber material and dissolves it [47].

In both cases, the melt (Zr-Fe-Ag-In-Cd for absorber rods and Fe-Zr-Ni for grid spacers) moves downwards in form of rivulets and relocates in the lower spacer grids or are dispersed between fuel rods. These melts may penetrate into the cladding tube and dissolve the UO_2 pellets, which can open an early release path for FP towards the RCS [29].

2.1.4 Cladding failure

The dissolution of the Zry-4 cladding occurs over a wide temperature interval (2073-2800 K) depending on the core heat-up rate. Rapid sequences tend to create a thick β-Zr layer and a thin ZrO_2 layer, whereas slow sequences tend to create a thin β-Zr layer and a thick ZrO_2 layer. This affects the cladding failure temperature [48] as summarized here below:

Rapid sequences produce a considerable amount of melt when arriving at temperatures slightly higher than 2073 K due to massive melting of β-Zr. In consequence, the melt generates a high hydrostatic pressure that may not be accommodated by the thin ZrO_2 layer, the oxide shell being thereby dissolved. Cladding failure is shifted to higher temperatures for slow sequences, since the presence of β-Zr phase is residual. Meanwhile, the Zr-U-O melt, which is formed due to the interaction among the molten metallic phase and the surrounding

ZrO_2 and UO_2, is kept in the cladding (*crucible effect*) until reaching mechanical failure (hydrostatic pressure of the melt), chemical dissolution or melting point of the ZrO_2 [16].

To quantify this behaviour, separate-effect and integral experiments were carried out showing complete cladding oxidation for heat-up rates lower than 3 K/s (see **Figure 2-3**). In those cases, cladding failure occurs at a temperature similar to the melting point of the ZrO_2. In contrast, cladding mechanical failure occurs for heat-up rates exceeding 4 K/s (see **Figure 2-4**), the ZrO_2 thickness at oxide shell failure gradually decreasing for increasing heat-up rates (from 450 µm at 4 K/s to100 µm at 8 K/s) and remaining constant above 6 K/s [48].

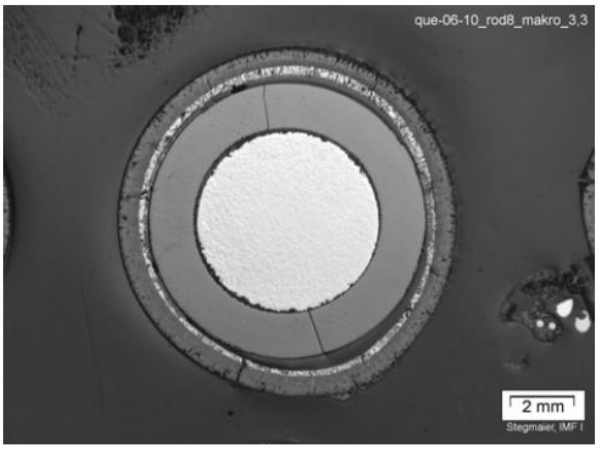

Figure 2-3: Cross section of rod 8 at 950 mm in QUENCH-06 Experiment: cladding intact if heat-up rates below 3 K/s [49].

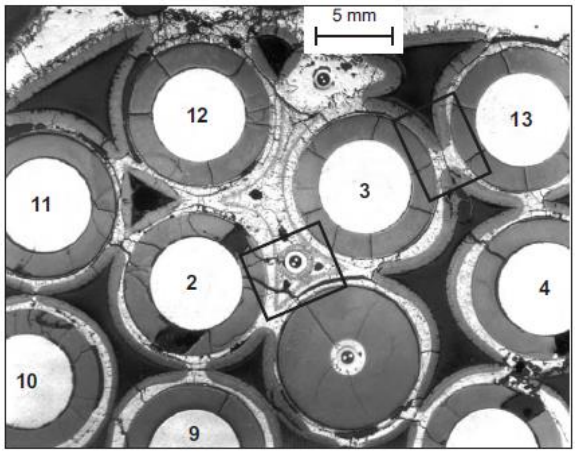

Figure 2-4: Cross section at 750 mm in QUENCH-03 Experiment: failed cladding if heat-up rates above 4 K/s [50].

2.1.5 Formation of molten pool and relocation into the Lower Plenum

After cladding failure, U-Zr-O mixtures are released into the core region and move downwards relocating at colder regions forming blockages. If coolability is not provided, these blockages may re-melt and form a molten pool, which is generally surrounded by a crust. The thickness of the crust varies along the surface of the molten pool and depends on the natural circulation developing inside the molten pool [28]. The higher heat transfer at the upper half of the pool causes the formation of a thinner crust than in the lower half and hence, it is more likely to fail upon contact with other structures.

The molten pool expands radially towards the baffle and axially towards the lower support plate until the failure of the crust. Although there are scarce data to explain this process, the TMI-2 accident indicates that this expansion can occur even if the molten pool is covered with water [18]. This is related to the difficulty of extracting the decay heat generated within the molten pool through the crust. Further research on this topic is intended within the following years [51]. Although this is the most likely scenario, two alternative scenarios may

happen [52]: massive relocation to the lower plenum due to the failure of the lower support plate or the crust bottom failure with subsequent melt jets towards the lower support plate.

In any case, the failure of this crust yields the relocation of corium to the lower plenum (LP) of the Reactor Pressure Vessel (RPV) and marks the beginning of the late in-vessel phase of the SA. At this point, the state of the core is similar to the one experienced at TMI-2 (see **Figure 2-5**), with much of the core molten and 20 corium tons in the lower plenum.

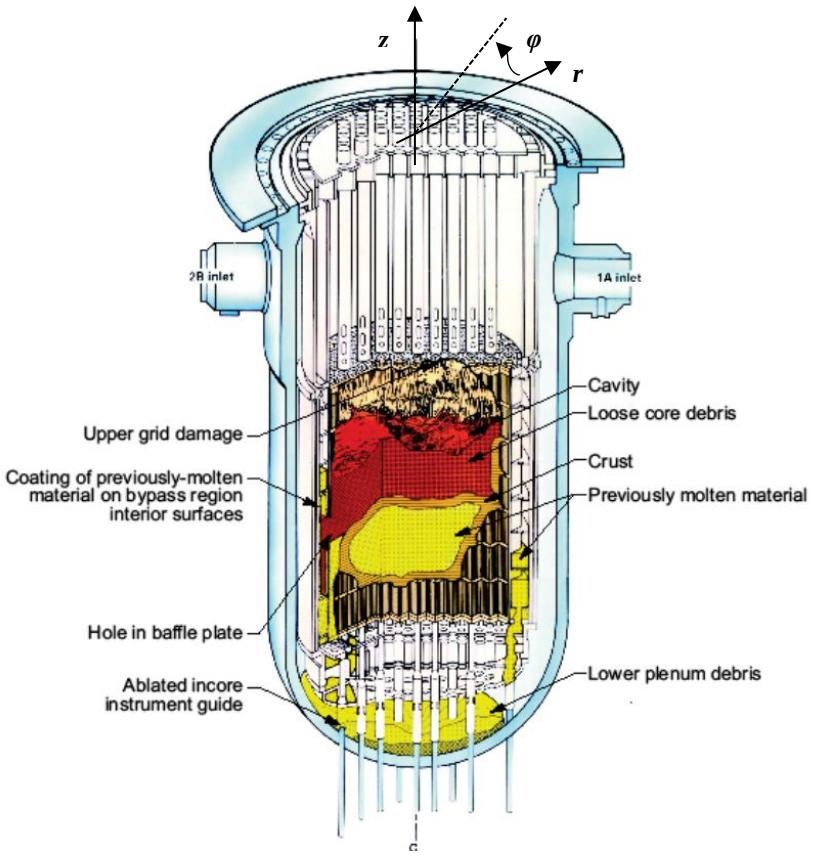

Figure 2-5: Schematic diagram of the reactor core following the TMI-2 accident [53].

2.2 Late in-vessel phase

The relocation of corium into the LP occurs in several steps. Generally, the molten pool propagates radially and partially melts through the baffle upon contact with the upper part of the pool. This way, the melt located above the failed crust is azimuthally distributed along the baffle plates and the flow is split into several jets aiming at the RPV lower head (LH) [54]. The corium located below the failed crust remains in the molten pool until renewed contact with the baffle plate at lower locations, leading to further corium relocation to the LP.

2.2.1 Fuel Coolant Interaction and molten pool formation

The effect of the melt jets on the SA progression depends on the amount of water in the LP: in the unlikely case that the LP is empty, the corium may melt through the lower head wall, especially if it has a metallic rich composition.

In the more likely case that the lower plenum is filled up to the lower core support plate, jets are partially fragmented into loose debris particles [32], which boil off the water inventory. In addition, these particles may remelt in about 2 h if they cannot be cooled down [54]. After the water inventory in the Lower Plenum (LP) has been considerably reduced, further corium entrainment does not lead to further fragmentation, but to the relocation of dense corium layers on top of the already created debris fragments [32].

At that stage, the most common configuration is a metallic layer located on top of an oxidic molten pool. The molten oxidic pool contains liquid corium, solid oxides (ZrO_2 and UO_2), liquid metals (Zr) and absorber materials, and is located on top of the debris fragments. In addition, a crust exists between the oxidic pool and the vessel walls, and between the molten pool and the top metallic layer. However, it may change during the following phases, as explained subsequently.

2.2.2 Stratification and behaviour within the Lower Plenum

The nature of the materials and the temperature conditions are likely to promote chemical reactions among the different materials in the LP, influencing the layer configuration (thickness and composition) and the heat flux distribution along the vessel wall. This is especially important for the metallic layers. Their thickness can focus the heat transfer (received from the lower oxidic layer) on a very small region of the RPV wall, leading to very high heat fluxes (*focusing effect*) at that location [55].

The MASCA Experimental program has shown that, in the local absence of a solid crust between the metallic and oxidic layers, the uranium may migrate from the oxidic to the metallic layer if a sufficient amount of non-oxidized Zirconium is available in the oxidic phase [33]. In that case, the uranium interacts likely with the steel causing a local density increase of the metallic phase. Under certain circumstances this density may become larger than the one of the oxidic phase, and the metallic layer partially relocates below the oxidic pool (*inverse stratification*). In such case, a light metallic layer, separated from a non-miscible oxidic-heavy metallic liquid mixture by a solid crust forms in the LP (see **Figure 2-6**). The presence of the metallic layer at the bottom of the RPV naturally decreases the amount of steel in the top metallic layer and hence, increases the risk of the focusing effect.

The heat transfer in the LP is governed by turbulent natural convection between the oxidic phase and the surfaces, where a solid crust exists. This internal convection is characterized by buoyancy-induced flows arising from the internal decay heat, and it has been shown to be dependent on internal Rayleigh number and the molecular Prandtl number of the mixed fluid

[56,57]. The consequence of the natural convection is that almost 50% of the decay power generated inside the molten pool is transported upwards, while the heat flux along the axial RPV perimeter varies strongly (maximum heat flux at the lateral positions and almost no heat flux at the bottom), as indicated in **Figure 2-7**.

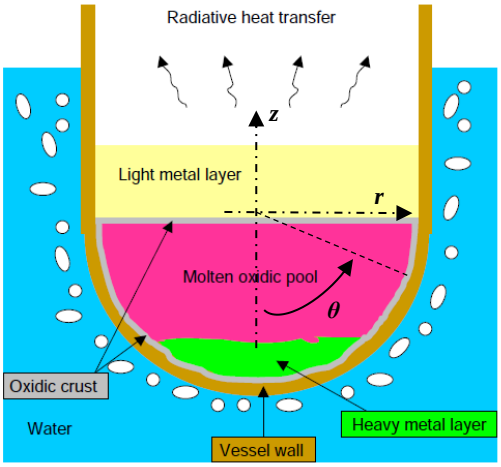

Figure 2-6: Pool configuration in the LH with an inverse stratification [55].

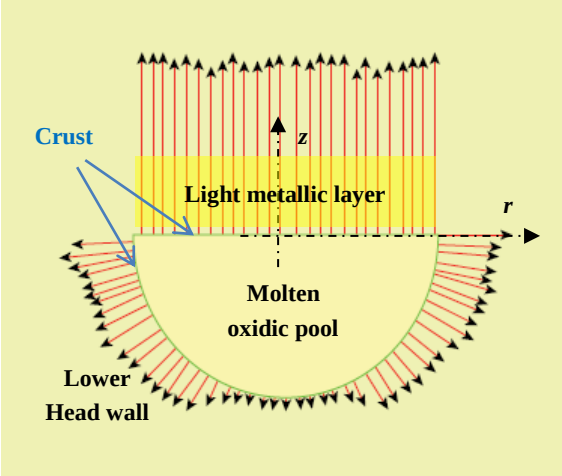

Figure 2-7: Heat flux distribution towards the crust surrounding the molten pool [28].

2.2.3 Vessel failure

At this stage of the accident, the integrity of the LH is challenged by the temperature values (result of the natural convection developed within the oxidic molten pool), the pressure level (result of the pressure in the RCS and the deadweight of the melt pool) and the corrosion degree [28]. The section **2.2.2** already indicated that a high temperature can quickly lead to LH failure in case of a thin metallic layer. However, if this is not the case, vessel failure may occur at other locations and times due to combined mechanical and thermal loads.

The LH is mainly loaded by the RCS pressure and the gravity loads of the relocated corium. The main mechanisms contributing to LH failure are plasticity, which occurs simultaneously with the mechanical load, and creep, which is a time-dependent process caused by the acceleration of wall thickness reduction and the microstructural changes undergone by the wall for high temperatures (> 600 °C) and pressures (> 1 MPa) [58]. Besides, analytical [58] and experimental investigations [35] have identified further conclusions:

- The time of vessel failure depends on the RCS pressure and the maximum temperature from the thermal load, whereas the failure position is not influenced by those.
- The failure location occurs at the highest temperature zones, since they undergo the highest creep strain rates. The crack then travels circumferentially. In addition, this

position depends on the amount of relocated corium in the LP: a completely filled LP is likely to induce RPV failure at the cylindrical part above the weld line, whereas a partially filled LP is likely to fail at an angle $\theta \sim 70°$ (see the definition of θ in **Figure 2-6** and the experimental outcome in **Figure 2-8**).

- The lower center of the LH exhibits a higher strength because of the lower temperatures in this zone, and moves down without significant deformation.

However, the steel ablation at the interface between the corium and the vessel is not only affected by temperatures, but also by the melt composition [59]. In fact, corrosion processes may lead to the formation of eutectic alloys at about 1090 °C (for a corium oxidation degree of 30 %), which are lower than the melting point of steel (1493 °C) and hence, contribute to further steel ablation [60].

2.3 Core Reflooding

One of the most relevant SAM measures in a LWR is the injection of water to cool down the core (*core reflooding*). Despite this measure is usually beneficial, the TMI-2 accident [18] and the QUENCH [16], CORA [29] and LOFT [61] experimental facilities have shown that, under some circumstances, the steam produced may oxidize the remaining Zry-4 claddings. In such cases, water injection leads to a further core destruction and a sharp hydrogen generation that can jeopardize the containment at an early stage of the accident.

Several parameters have been shown to be relevant for the core reflooding success [62,63], the most relevant ones being the Core Damage State (CDS) at reflooding, which describes the history of the transient up to injection time, and the Reflooding Mass Flow Rate (RMFR) injected into the reactor. In principle, the accident can be stabilized with minor core structural damage, if the following two conditions are fulfilled:

- The core geometry is intact or only minor blockages of molten material have been formed (core temperatures up to 2200 K)
- RMFRs above 1 g/s/rod are injected into the RCS. This quantity is similar to all High Pressure and the Low Pressure Injection System (HPIS and LPIS) trains, which respectively provide 1-2 g/s/rod and 2-9 g/s/rod. RMFRs < 1 g/s/rod may arise when systems, originally not thought for core cooling purposes, are activated.

The behaviour of reflooding has been well characterized for intact or slightly degraded geometries [64] and the flow patterns can be divided in three zones (see **Figure 2-9**):

- Nucleate boiling region (upstream the quench front), where the temperature is close to saturation and below the critical heat flux (CHF) temperature (burn-out temperature).

- Transition Boling Region (TBR) (just above the quench front), where there is a non-stable two phase flow at the wall side with intermittent wetting. Within this region, the wall exhibits a large axial temperature gradient.
- Dispersed flow region (above the TBR), where the gas phase is predominant and possibly contains water droplets.

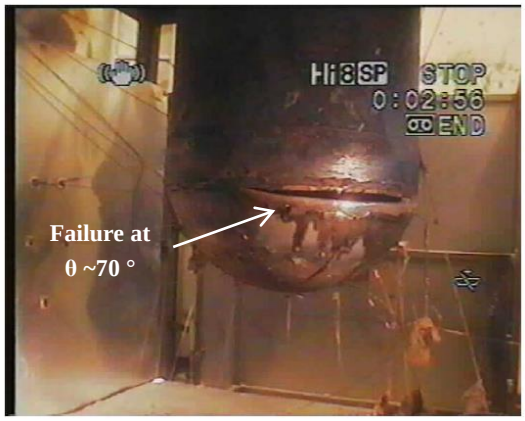

Figure 2-8: Failure site of the vessel in FOREVER-4 Experiment [35].

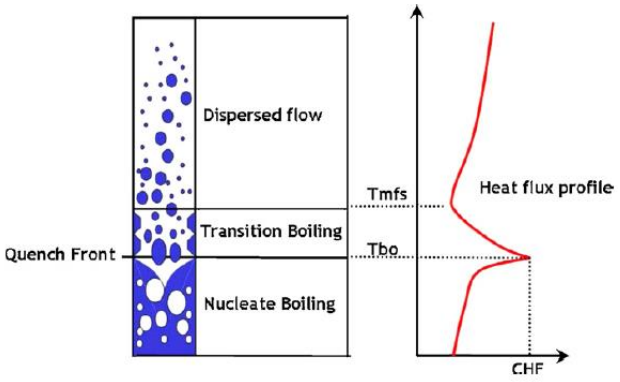

Figure 2-9: Flow regimes during reflooding of a slightly degraded core [65].

However, when the core is severely degraded, reflooding may cause the fragmentation of fuel rods into debris particles, which would relocate on top of the already created blockages forming a debris bed. In such a case, the core coolability depends on additional factors, such as the system pressure, the core configuration and the injection position [63]. Some of them are explained hereafter:

- **Injection position**: a debris bed top reflooding has to fight the counter current flow limitation, in which steam limits the downward water ingression. In contrast, the heat transfer during bottom flooding is affected by the driving pressure of the flow rate. As a matter of fact, the heat removal rates during bottom flooding can be as 8-10 times higher than those obtained by top flooding [66].
- **Debris configuration**: the dry out heat flux and the quenching rates are very low for porosities below 40 % and particle sizes below 2 mm, which reduces even more the efficiency of top flooding [66].

Efforts are underway at the PEARL experimental facility to understand the key variables affecting severely degraded core coolability. To date, the presence of a bypass, the initial temperature and the injection velocity have been shown to play an important role [31,67]. The TMI-2 accident has shown that crust failure might not be prevented even if the molten pool is covered by water [18].

If reflooding is started during the late in-vessel phase, the coolability depends on the same factors as for in-core debris beds, with the particular constraint of top flooding. It has been suggested that the formation of a gap between the crust and the vessel wall admits water, thereby ensuring the integrity of the lower head, but experiments performed at the FOREVER facility have contradicted this statement [35]. Then, it is feasible to assume that molten pool reflooding is not likely to be successful in terms of core coolability [66], leading in turn to RPV failure.

Two strategies are foreseen to solve this problem in upcoming reactors: in-vessel retention by means of external cooling of the vessel like in the AP600 and the AP1000 [56] or ex-vessel retention by means of a core catcher (structure surrounding the LH so that the corium interacts with it after RPV failure) like in the EPR [68].

2.4 Impact of In-vessel phase on Ex-vessel phase

The failure of the RPV-LH marks the end of the in-vessel phase and the beginning of the ex-vessel phase, which now challenges the containment. Phenomena leading to containment failure during the ex-vessel phase can be split with respect to the time scale of their occurrence:

- Phenomena leading to early containment failure: Direct Containment Heating (DCH), which consists of a violent ejection of melt from the RPV if the RCS has not been depressurized; entrainment of large amounts of hydrogen in the containment (due to core reflooding) in a short time potentially leading to detonation; ex-vessel steam explosion, which consists of a strong interaction between the corium and the water in the cavity. However, the last mechanism is excluded in the Konvoi PWRs due to the existence of a dry cavity.
- Phenomena leading to late containment failure: Molten Corium Concrete Interaction (MCCI), occurring for dry cavities (in Konvoi PWRs by design, in other reactors because no water could be injected). This mechanism causes two potential hazards: (1) the generation of gases (some of which are inflammable) that would pressurize the containment, and (2) the melt through of the concrete constituting the basement material, and the potential attack of corium to the ground underneath.

The distinction is relevant, because the amount and nature of FPs varies as a function of time. Core melting may release 60-80% of the volatile FPs (caesium and iodine isotopes), which may form compounds among each other and with the remaining steam. The vapour compounds may form aerosols, which depose in the upper piping of the RCS on their way to the containment. This source term is not immediately available in the containment, but it comes into play be as soon as their decay heat re-vaporizes those.

The late re-vaporization may constitute a hazard to the public in case of an early containment failure. However, if containment failure is delayed 4 h since that instant, the FP concentration can be significantly reduced by a factor of 10^4 [28]. In such a situation, the re-vaporized compounds depose in the containment, and the dominant part of the released FPs would come from the MCCI.

2.5 Summary

This chapter has explained the key phenomena occurring during the in-vessel phase of a hypothetical SA in a generic PWR. During the early in-vessel phase, natural circulation can compensate the decay heat at the beginning, but becomes clearly outweighed by the cladding oxidation for PCTs above 1500 K. The Zry oxidation quickly leads to the melting of core materials, which relocate downwards forming blockages and possibly a molten pool. The failure of the crust surrounding this pool gives rise to the late in-vessel phase, characterized by the entrainment of corium into the LP, corium stratification and RPV failure due to thermo-chemical-mechanical loads. Afterwards, the corium migrates to the containment and the termination of the accident would become increasingly difficult.

It seems therefore essential to:

- Prevent the onset of core melting before the oxidation starts to be significant.
- Stop the SA progression before significant blockages are formed in the core region.
- Retain the corium in the LP if the two previous goals cannot be attained.

This can be done with dedicated provisions in NPPs, as explained in the next chapter.

3 Accident Management in PWRs

The last chapter has described the key phenomena governing the in-vessel progression of a severe accident in a generic PWR. This chapter makes use of that information to acquaint the reader with the most important in-vessel AM measures used in a German Konvoi PWR, whose layout and main safety systems are described in Appendix **A**.

In order to achieve this goal, the chapter is structured in several sections. The section **3.1** provides an overview about the DiD concept, the domains and the worldwide history of AM. The section **3.2** summarizes the approaches to perform the transition between preventive and mitigative AM in several PWR designs. The most important preventive actions are described in section **3.3**. Finally, the section **3.4** describes the approaches to perform SAM in existing PWRs and the most important SAM measures undertaken during the in-vessel phase. Particular attention is paid in each section to the German Konvoi PWR.

3.1 Overview

3.1.1 Defence-in-Depth (DiD)

The DiD concept consists of a hierarchical deployment of different levels, each containing a set of redundant and diverse resources to maintain the integrity of the safety barriers (cladding, RCS and containment) and hence, avoid a harmful release of radioactive material to the public [1]. Should the provisions associated to a given level fail, the provisions of the immediate next higher one would aim at returning the plant to a safe state. Therefore, it is essential that all measures of that next higher level entirely encompass all consequences of the prior level to ensure that no risk path can further progress unidentified. The **Table 3-1** entails the different safety levels and a brief description of the provisions allotted to each.

Levels	Objective	Provisions
L1	Prevent abnormal operation and failures	Adequate site, design, construction, commissioning, operation and maintenance.
L2	Control abnormal operation	Plant control, limiting and protection systems.
L3	Control of design basis accidents (DBA)	Engineered safety features and accident procedures.
L4	**Control of beyond design basis accidents (BDBAs) and severe accidents (SAs)**	**Preventive or mitigative Accident Management measures**
L5	**Mitigation of radiological consequences**	**Off-site Emergency Response**

Table 3-1: Levels of the Defence in Depth according to [1].

3.1.2 Fundamentals about Accident Management

Accident Management (AM) is the provision associated to the fourth safety level of the DiD and has the following objectives depending on the integrity of the safety barriers [2]:

- Prevent accidents from leading to core damage.
- Terminate core damage.
- Maintain containment integrity.
- Minimize on-site and off-site releases and their adverse consequences.

The measures aiming at the first goal are tagged as *preventive* and are included in the EOPs. Although unlikely, these actions may not succeed in controlling the accident and hence, measures have to be appointed to fulfil the latter three objectives. Those measures, tagged as *mitigative*, are included in the SAMGs. A clear distinction between the two domains is depicted in **Figure 3-1.** Both procedures, especially SAMGs vary widely depending on the core loading, safety systems and the plant physical conditions.

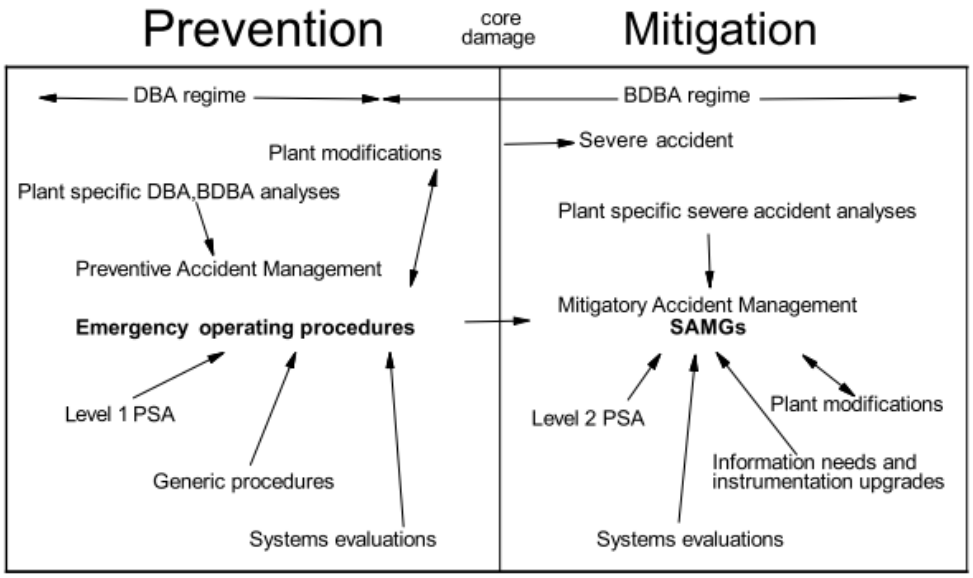

Figure 3-1: Different domains of an Accident Management program (DBA: Design Basis Accidents; BDBA: Beyond Design Basis Accidents) [2].

EOPs are used by the plant crew in the main control room (CR) whenever the plant protection systems are actuated. The procedures contained therein provide a systematic guidance since the beginning of an event, allowing the operator to initiate the appropriate response without having to rely on memorized responses. EOPs are developed in such a way that the execution of an action only depends on the identification of a set of directly measurable plant parameters (often called *symptoms*) [69].

On the other hand, SAMGs are relied upon by the Emergency Response Organization (ERO) at the on-site Technical Support Center (TSC) in the form of guidelines if the restorative actions of the EOPs have failed and if core damage is expected. The situation at this point can be complex, since multiple safety systems may have been lost and the harsh environmental conditions may have caused the failure of the instrumentation. In such case, the diagnosis of the plant would be performed with all available instrumentation or (if not possible) with computational aids.

3.1.3 Historical development of AM

3.1.3.1 Worldwide

After the SA at TMI-2 in 1979 [18], initiatives were undertaken worldwide to enhance AM procedures in NPPs. The initiatives aimed at improving EOPs in order to better diagnose the scenario and preserve the Critical Safety Functions (CSFs) i.e. subcriticallity, core cooling and confinement of radioactivity. These reactions became even more widespread after the SA at Chernobyl in 1986, which accelerated the development of AM procedures.

The response was especially effective in the US, where the nuclear industry developed a technical basis for the determination of potential countermeasures. This task was performed by EPRI and documented in the Technical Basis Report [3–5], from which the Owners' Groups (OGs) of the NPPs and the individual utilities could develop their vendor and plant specific SAMGs. Relevant PWR OGs at that time were the Westinghouse OG (WOG), the Combustion Engineering (CEOG) and the Babcock and Wilcox OGs (B&WOG). Since then and up to 1998, US NPPs have established SAMGs intending to make the maximum use of existing plant capabilities and minor hardware modifications.

As concerns the Western European NPPs, these events had a diverse impact on SAM due to the different vendors, types of NPPs and requirements imposed by each national regulator. Most of the EU countries adopted the WOG SAM approach, except France and Germany, which developed similar ones but without such systematic development. The actions imposed by the regulators mainly focused on the preventive domain through dedicated procedures (e.g. bleed and feed), hardware modifications and back-fitting [70].

In turn, this caused a different degree of SAM implementation in EU member nations, which led the European Commission (EC) to launch the SAM Implementation and Expertise (SAMIME) program to harmonize SAM in European NPPs [70]. From this moment on and up to the SAs accidents in Fukushima, most of the European NPPs implemented or scheduled SAM programs in accordance to the requirements of the national regulatory bodies, generally in compliance with the IAEA [2,71] and the WENRA [72] safety standards. An extended summary of all current SAMG approaches in European NPPs can be found in [73].

Despite this progress, the SAs at Fukushima in 2011 [74] have revealed a number of weaknesses in AM procedures [6]. As a result, enhancements on SAM for LWRs have been suggested worldwide, the response being different in the US and the EU in several ways [75].

In the US, the NRC and the nuclear industry have undertaken separate paths. On one hand, the NRC has required back-fit analyses in order to show that the SAM enhancements provide a cost-effective increase of the plant safety [76]. Simultaneously, the industry has developed flexible strategies to cope with BDBAs (known as FLEX concept) [77] and committed themselves to maintain SAMGs under periodic revision of the NRC. In the EU, however, the regulators have ordered the performance of comprehensive safety reviews to assess the safety of existing NPPs following the methodology of the European Nuclear Safety Regulators Group (ENSREG) [78]. Based on these results, the WENRA AM safety standards have been updated [79] and adopted by the national regulators, which have then required plant specific SAMGs and extensive hardware modifications.

3.1.3.2 Germany

The German response to the events at TMI-2 and Chernobyl was similar than in the rest of Europe. The German RSK ordered the performance of stress tests on existing NPPs and the inclusion of AM measures [80]. However, the key event to SAM development was the publication of the German Risk Study (also called *Deutsche Risikostudie Kernkraftwerke Phase B*) [81], which was the first comprehensive analysis including deterministic and probabilistic results of SAs for a generic Konvoi PWR.

The first requirements on possible SAM measures for German NPPs were issued in 1988 [82], the concept being named *Anlageninterner Notfallschutz*, which was mainly focused on the preventive domain. The document also included a few mitigative measures (e.g. filtered containment venting), which were extended (e.g. hydrogen recombiners) in following updates [83,84]. In turn, this lead to a high degree of SAM implementation in German NPPs [85] and to the development of detailed EOPs (in German *Notfallhandbuch, NHB*). However, the guidance for the mitigative domain was still quite limited.

After Fukushima, the German RSK was again asked to carry out a safety review of existing NPPs. The conclusions drawn from this investigation confirmed the robustness of all German NPPs and stated that existing safety margins could be even increased through the improvement of SAM measures [7]. Subsequent to this review, a German Action Plan was traced for the upcoming years [8], and updated every two years since then [9,10]. The most important requirements regarding AM measures are listed hereafter, the status of implementation of each measure in each German NPP being extensively described in [10].

- **N-1**: Ensure subcriticallity, heat removal and Direct Current (DC) for at least 10 hours by means of all NPP capabilities in case of Station Blackout (SBO).

- **N-2**: AM measures must be provided until Alternating Current (AC) power supply can be established within 10 hours in case of SBOs.
- **N-13**: Improve emergency systems and existing AM measures.
- **N-20**: Review of injection possibilities to ensure core cooling and sub-criticality under the aspects mobile equipment storage, possibilities of injecting water into steam generators.

In addition, the RSK required the implementation of SAMGs (in German *Handbuch für Mitigative Notfallmaßnahmen - HMN*) in the short term. At present, all German NPPs have implemented plant specific SAMGs. The development of those has been established in accordance to the regulations imposed to German NPPs [86], which follow the already mentioned standards of IAEA and WENRA (see section **3.1.3.1**).

Now that the status of AM implementation and the distinction between the two regimes of AM have been explained, it is worthwhile to review the approaches followed by different NPPs to perform the transition from preventive to mitigative AM.

3.2 Transition from preventive AM to SAM

3.2.1 Worldwide

The transition of EOPs to SAMGs is an important step during the accident progression because of the different goals of the strategies and the transfer of responsibilities (see section **3.1.2**). A detailed analysis about the factors influencing the switch can be found in [87]. According to that study, the transition requires a symptom that satisfies, if possible, the following four conditions: easy to measure, unambiguous, representative of the core damage conditions and allowing sufficient time to perform actions.

The Core Exit Temperature (CET) is usually the selected symptom, since it satisfies those conditions. However, transition criteria based on CET vary depending on the philosophy of each OG, as shown in **Figure 3-2**. Therein, some of the approaches used in the US (CEOG, B&WOG and WOG) and Finland (LOVIISA) as well as the French approach for the EPR (OSSA) and for currently operating NPPs (GIAG) are illustrated. Criteria used by other countries can be found in [88]. The figure shows the divergence among the different approaches, which is motivated by the several factors:

- Core condition: core damage is defined in a different way, since there is no physical parameter giving a precise representation of the degree of core degradation. Three states can be distinguished: core uncovered (liquid level below the top of the active core), core deeply uncovered (core superheated) and significant damage in progress (significant release of FPs). For example, CEOG and LOVIISA prefer to switch to SAMGs as soon as the core becomes slightly uncovered, while French NPPs perform the transition when core damage is in progress according to their GIAG.

- Scope of EOPs - SAMGs: the transition has to maximize the available time for core cooling, but also to ensure the retention of FPs in the containment. The usual approach is to use the EOPs up to the point in time when transition criteria are fulfilled. This prevents conflicts with the SAMGs. However, some approaches (CEOG) allow the use of EOPs even after this transition point in order to reduce the stress of operators (existence of hydrogen in RCS not contemplated in any case). Therefore, the switch to SAMGs is initiated earlier.
- Margins to set-points: inaccuracies in instrumentation and delay mechanisms also influence the transition criteria. Although the CET gives the most direct measurement of the PCT, this measure is delayed with respect to the cladding conditions according to several parameters e.g. system pressure [88]. Lower system pressures provide lower steam density and hence, less heat transfer from the core to the fluid, which results in a lower CET for the transition. Whereas some approaches prefer to account for this delay and use a constant CET to perform the switch (LOVIISA, WOG, French GIAG for operating NPP), other approaches prefer to directly account for the system pressure to evaluate the transition (CEOG, French OSSA for EPR).

Although the CET is usually the selected symptom to perform such transition, the thermocouples (THCs), as well as other instrumentation, may be endangered during a severe accident due to effect of temperature, humidity, pressure, radiation or just a simple failure [53,89,90]. In such situations, the plant can take advantage of the equipped back-up instrumentation e.g. vessel water level, containment radiation and hydrogen concentration.

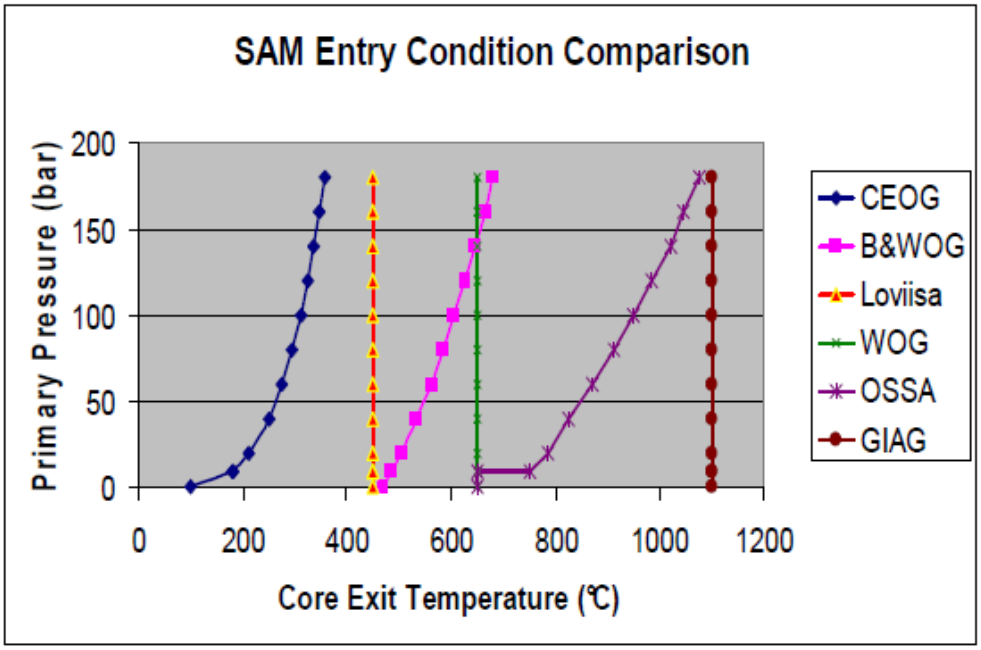

Figure 3-2: Different transition criteria from preventive AM to SAM based on the Core Exit Temperature and the system pressure employed by different vendors and operators [87].

3.2.2 Germany

In Germany, the normal operation and the DBAs are covered by the Operating Manual (in German *Betriebshandbuch - BHB*), which is used by the shift team in the CR. The measures contained therein are preventive and target at maintaining the CSFs. If those become jeopardized, the accident turns into a BDBA, which can be handled by the shift team using the EOPs [11]. If those are neither successful, the ERO orders the transition to mitigative AM.

Mitigative AM measures are contained within SAMGs (HMN) [12], which are divided in two different manuals: *Manual A* contains strategy flow charts, plant status diagnostics and computational aids obtained SA codes, whereas *Manual B* contains the background to deduce the strategies of *Manual A* and is mainly used by AREVA for ERO training. The background material contains information about severe accident phenomenology, plant simulations and detailed discussions about the strategies of *Manual A*.

The transition towards SAM is generally performed by the shift supervisor or the ERO when the CET exceeds 650 °C (and/or dose rate within the containment above 10 Gy/h). From that moment on, the ERO devises a strategy following the *Manual A* of the SAMGs and instructs the plant crew to perform specific actions. At the same time, the plant crew communicates to the ERO the impact of those actions on key plant variables. The assignment of responsibilities to the plant crew and the ERO for the regimes of DBA, BDBA and SA is summarized in **Figure 3-3**, and extensively explained in [12].

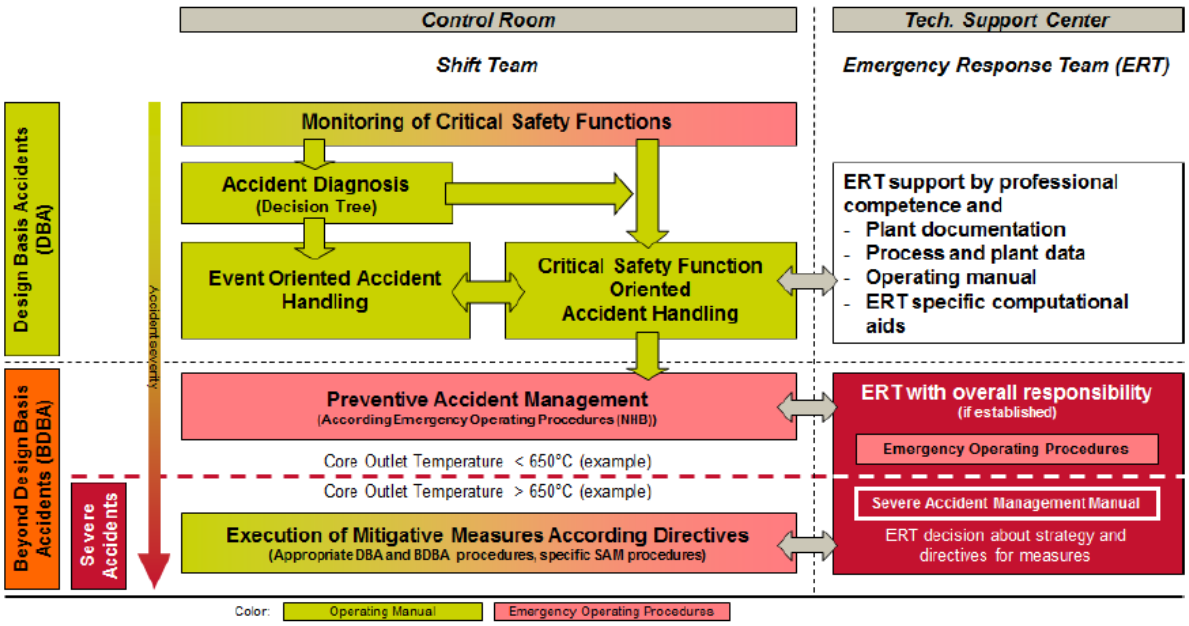

Figure 3-3: Structure of Accident Management in German NPPs [12].

Once the transition approaches from preventive to mitigative AM have been reviewed, the following section moves on to summarize the most important preventive AM measures in existing PWRs, with special attention to the German Konvoi PWR.

3.3 Preventive AM measures in PWRs

While preventive actions can be delayed for several hours without reaching critical plant states during DBAs, the grace time becomes much shortened during BDBAs [15]. As a result, preventive AM measures are usually restricted to a few powerful ones covering a wide spectrum of potential plant states. Existing preventive AM measures of NPPs operated in the EU and the US can be found in [73,91]. The most important ones are listed hereafter:

- Secondary bleed and feed (SBF) i.e. depressurization of the secondary side followed by water injection into the depressurized Steam Generators (SGs).
- Primary bleed and feed (PBF) i.e. depressurization of the primary side followed by water injection into the core.
- Restart the Main Coolant Pumps (MCPs) to transfer the coolant towards the core.
- Retrieval of the main safety systems of the Emergency Core Cooling System (ECCS) either through the reparation of failed components or the restoration of AC power supply (e.g. additional grid connections or mobile diesel generators (DGs)).

3.3.1 German Konvoi PWR

The secondary and primary bleed and feed are the most powerful procedures in a Konvoi PWR [15,85]. Preference is usually given to SBF in order to maintain the water inventory in the RCS and to avoid a release of radioactivity into the containment. However, if it is not successful, PBF is foreseen to enable the ECCS injection into the RCS. The required conditions to start both procedures are depicted in **Figure 3-4**, whereas the relied systems are depicted in **Figure A.1-1**.

3.3.1.1 Secondary bleed and feed (SBF)

SBF aims at restoring the feedwater (FW) to the SGs in case of operational and emergency FW failure. The procedure is prepared when at least one of the two following conditions is fulfilled (represented by the box ***≥ 1*** in **Figure 3-4**):

- Liquid level in all SGs drops below *min2* (below measuring range e.g. SG liquid level 4 m).
- Non-battery supplied AC power has been unavailable for more than 20 min, in case of Station Blackout (i.e. non-battery supplied AC power).

Regarding water injection into the SGs, two resources can be relied upon: the FW tank containing 350 water tons, which injects passively if the pressure falls below 2-3.5 bars, or a

mobile pump extracting water from internal or external resources. The feed from the feedwater tank can be anticipated to 5.7 bars if the pegging steam line of the SGs is opened. The feedwater pipes also contain water (up to a maximum of 300 tons), which can be partially made available (45%) to the SG if its pressure falls below 22 bars [92]. SG depressurization occurs mainly via the main Steam Relief Valve (SRV) to the atmosphere if DC power supply is available.

Although SBF is the preferred preventive AM measure, its successful preparation requires up to 1 h (since the aforementioned criteria are fulfilled) [15]. Hence, a back-up measure is required.

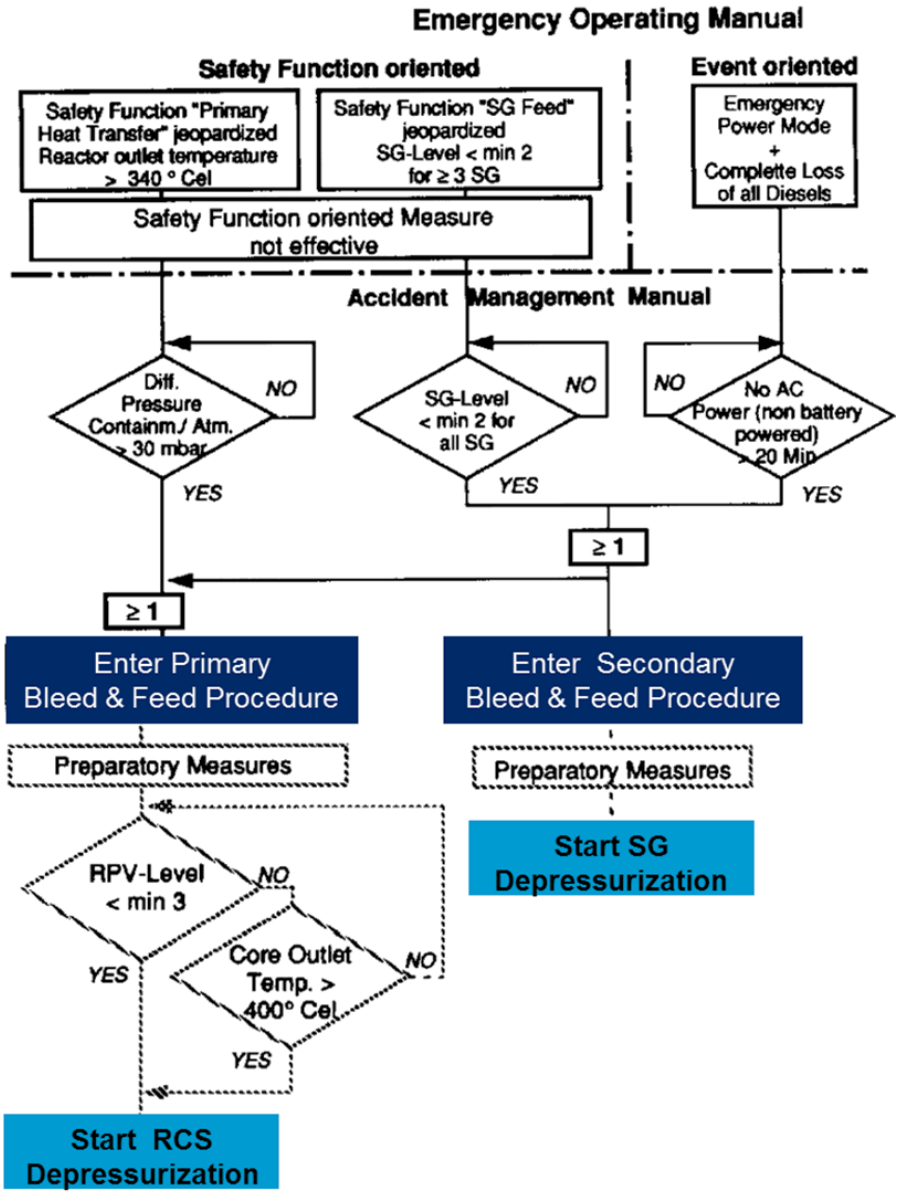

Figure 3-4: Initiation criteria for secondary and primary bleed and feed in German Konvoi PWRs [15].

3.3.1.2 Primary bleed and feed (PBF)

The PBF provides an alternative path for RCS depressurization in case the SBF has not succeeded. The procedure takes 20 min of preparatory actions before the pressurizer valves can be opened from the control room and hence, it is prepared upon the fulfilment of the SBF criteria (see section **3.3.1.1**) or when a containment overpressure of 30 mbar is detected [15]. This translates into a small leak in the primary circuit (of about 100 cm^2 area; 11 cm diameter). PBF is initiated when at least one of the following conditions is fulfilled (represented by the box ***≥ 1*** in **Figure 3-4**):

- Liquid level in the RPV lower than *min3* (15 cm above the top of the active core).
- Core Exit Temperature exceeds 400 °C.

The RCS can be depressurized by means of the Pilot Operated Safety Relief Valve (PORV) and the two Safety Valves (SVs) of the pressurizer, which are actuated from the control room or from the emergency building. This action requires the availability of DC power. Once the pressurizer PORV and the SVs have been opened, water can be injected into the RCS by means of the ECCS (see Appendix **A.2**) or other hardened safety systems, such as the Chemical Volume Control System (CVCS) or the Extra Borating System (EBS) [93].

3.4 Severe Accident Management in PWRs

The previous section has analysed the most important preventive AM measures in several PWR designs. Within this section, the attention is shifted to the mitigative domain and, in particular, to describe the existing SAMG approaches, the implemented SAM measures and the computational aids in generic PWRs. The focus is put on the German Konvoi PWR.

3.4.1 Existing SAMG approaches

3.4.1.1 Worldwide

There are a number of SAMG approaches for PWRs [13,28], the one of the WOG being the most widely used both in the US and many EU countries [70]. Other EU countries follow the CEOG-B&WOG approach e.g. Germany and Switzerland. However, most of NPPs adopt the SAMG structure of each OG. A comparison of these approaches is performed hereafter:

The basic idea of the WOG SAMGs is the existence of two interlinked decision trees that are simultaneously monitored by the ERO. The main tree is the diagnostic flow chart (DFC), which aims at leading the NPP to a stable and controlled state. The actions are decided after evaluating their positive and negative consequences and are only taken if the first outweigh the second. The other decision tree is the Severe Challenge Status Tree (SCST), which directs to take action if a challenge to a FP barrier is observed. The particular feature of the actions recommended by the SCST is that they have to be carried out irrespectively of the negative

consequences, in contrast to those of the DFC. Therefore, although the actions are generally decided by the DFC, priority shifts to the SCST if a FP boundary is challenged.

Whereas the WOG SAMGs require a diagnosis of the scenario to carry out strategies, the CEOG and B&WOG SAMGs require the diagnosis of the plant damage state. This variable is derived with a similar methodology to that of the Technical Basis Report [3–5]. Therein, the plant damage state was a combination of the core damage state (discretized in OX: oxidized fuel but core intact, BD: badly damaged core, EX: core debris ex-vessel) and the containment damaged state (CC: closed and cooled containment, CH: closed but challenged containment, I: impaired containment, B: bypass containment). Furthermore, the SAMGs of the CEOG and B&WOG do not foresee the existence of two interlinked decision trees and decide the actions through the evaluation of the positive and negative consequences.

3.4.1.2 German Konvoi PWR

The SAMGs of German Konvoi PWRs are based on the CEOG concept. Hence, the selection of the SAM strategy depend on the core and containment damage states, which are derived from dedicated flow charts [14]. Differently to the CEOG approach, the core state is discretized in two states (A/B: core damaged but RPV intact, C: molten corium in containment), whereas the containment state is discretized in six (1: integrity ensured, 2: integrity at risk, 3: bypass to secondary side, 4: bypass to annulus, 5: bypass to auxiliary building, 6: large leak in containment). Their combination identifies the plant damage state and determines the strategy that should be followed by the ERO (see **Figure 3-5**). It should be pointed out that the strategy may vary during the SA due to the necessity of updating the plant damage state every 20 min based on the plant instrumentation.

			Containment Vessel State					
			1	2	3	4	5	6
			Integrity ensured	Integrity at risk	Bypass secondary	Bypass annulus	Bypass aux building	Large leak containment
Core Damage State	A/B	Core damage RPV intact	A/B1	A/B2	A/B3	A/B4	A/B5	A/B6
	C	Corium outside RPV, RPV failed	C1	C2	C3	C4	C5	C6

Figure 3-5: Matrix of plant damage states in a German Konvoi PWRs [14].

Each strategy consists of a sequence of prioritized action blocks with SAM measures that are arranged in a decision flow chart. The number and prioritization of the action blocks can be identified by their label number. For instance, the strategy A/B1 (core damaged and vessel

intact together with ensured integrity of the containment) is shown in **Figure 3-6**. In this example, the following three prioritized actions are foreseen:

- Depressurization of the RCS;
- Injection into the RCS (core reflooding);
- Reestablish heat removal via available SG.

Each SAM measure belonging to a strategy has a detailed sheet providing information about the aim of the measure, initiation and termination criteria, required actions and systems, indicators of effectiveness, additional information, link to the operating manual and the EOPs, dedicated computational aids and background information. A sheet with details about RCS depressurization for the particular case of the strategy A/B1 is shown in **Figure 3-7**.

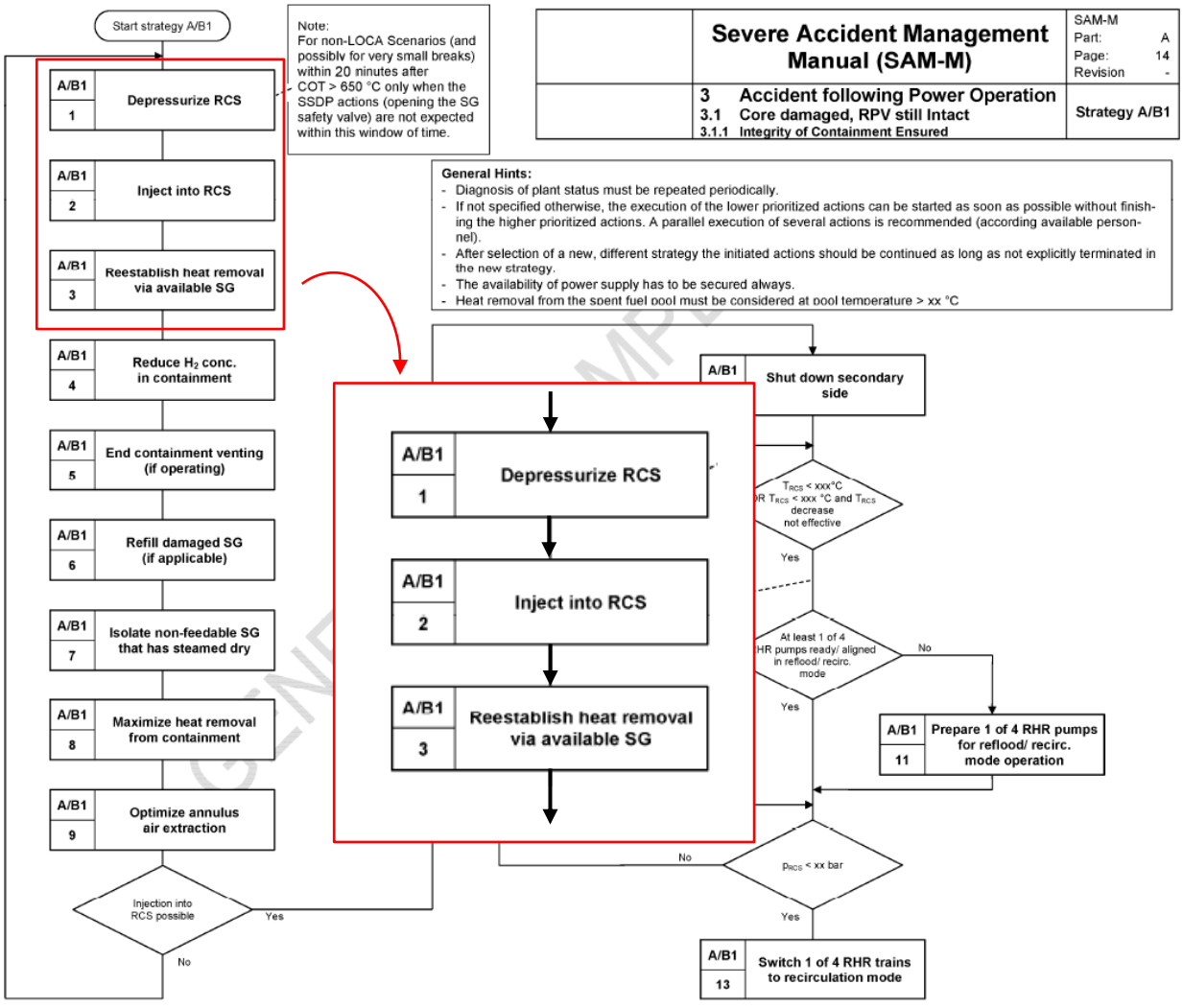

Figure 3-6: SAM strategy flow chart for the plant damage state A/B1 in a German Konvoi PWR [12]. In red, the SAM measures to be analysed within this thesis.

A/B1	Depressurization of RCS
1	

Severe Accident Management Manual (SAM-M)	SAM-M Part: A Page: 15 Revision -
3 Accident following Power Operation 3.1 Core Damaged, RPV still Intact 3.1.1 Integrity of Containment Ensured	

Description and goals	Depressurization of the RCS due to - Achieve an injection to the RCS; - Avoid High Pressure Melt Ejection; - Avoid induced failure of SG-tubes in non-fed steam generators.
Initiation criterion	During non-LOCA scenarios (if applicable, also for very small leakages) within 20 minutes after COT > 650°C only, if the SDE-measures (Opening of the MS relief valves) are expected not within this time frame.
Termination criterion	-
Required systems	- Pressurizer valves AAA (NHB x.x.x) - If applicable pressurizer-PORV (BHB x.x.x)
Effectiveness constraints / plant behavior	Pressure decrease from 167 to 25 bar within 10 - 15 minutes.
Important hints	- After start of injection during the depressurization, a temporary increased oxidation rate of the cladding is possible due to the increased steam production and hence a temperature increase is expected. - The depressurization results in additional mass and energy input to the containment, which is temporary more challenged (pressure increase up to 1 bar within 10 minutes). - With the depressurization the hydrogen, which was stored in the RCS, is ejected into the containment. Therefore, an increased hydrogen concentration is expected in the containment. - With start of the hydrogen generation in the core, the depressurization of the RCS with help of the pressurizer valves is necessary also if the heat removal on the secondary side is available. This is because the hydrogen impairs the heat transfer to the secondary side. Without depressurization the pressure in the RCS would be increased to a value, which warrants a heat removal.
Applicable BHB / NHB	NHB x.x.x (PDE) if applicable BHB x.x.x (Pressure maintenance on primary side)
Available aids	HMN chapter x.x.x

Figure 3-7: Depressurization of RCS for the strategy A/B1 in a German Konvoi PWR [12,14].

3.4.2 SAM measures

3.4.2.1 Generic measures

SAM measures are grouped depending on where they are targeting at: containment, RCS or RPV integrity. A brief summary of the existing SAM measures applied to reach these goals in several PWRs designs [73] is presented hereafter:

- Maintain RCS integrity through the prevention of RPV failure (by means of core reflooding, RCS depressurization, water injection into the SG or external cooling of the RPV), as well as SG Tube Rupture (by means of water injection into the SG and RCS depressurization) and hot leg/pressurizer surge line creep rupture (by means of RCS depressurization).
- Maintain the containment integrity through prevention of phenomena such as DCH (by means of RCS depressurization), pressurization of the containment (by means of containment venting, hydrogen recombination), MCCI (by means of water injection into the reactor cavity).

- Mitigate or terminate FP release through actions in the containment (by means of ventilation, injection with sprays and injection into the cavity), in the steam generator (by means of water injection, SG isolation and dumping steam to the condenser), in the RCS (by means of water injection).

3.4.2.2 German Konvoi PWR

Within this section, the most important in-vessel SAM measures in a German Konvoi PWR are listed (from highest to lowest priority according to the strategy A/B1 of **Figure 3-6**):

- Depressurization of the RCS, also called Primary Side Depressurization (PSD), which is identical to the PBF (see section **3.3.1.2**). This measure targets at preventing vessel failure at high pressures or a bypass to the secondary side through a Steam Generator Tube Rupture (SGTR) [94]. PSD eases the injection from the accumulators (ACCUs) and ECCS active systems, but leads to an increase of pressure and FP concentration in the containment. However, the positive effects outweigh the negative ones [12].
- Water injection into the RCS: this measure targets at recovering the core heat removal, stopping the core degradation and allowing the retention of FPs within the RCS. Despite this action is always recommended, it may bring adverse consequences e.g. sharp hydrogen generation (see section **2.3**) or RCS repressurization (if there are not sufficient venting paths between the RCS and the containment) [12].
- Recovery of water injection into the SGs, which is identical to the feed action of the SBF (see section **3.3.1.1**). This action aims at recovering the heat sink of the RCS, as well as at reducing the risk of a thermally induced SGTR [94]. The same injection systems as the ones exposed for SBF are used. The success of this measure depends on the extent of core degradation, the pressure in the RCS and the amount of hydrogen generation in the RCS. Even though this action is always beneficial, precautions should be taken to not to induce thermal shock of the U-tubes upon injection [5].

For each SAM measure, the ERO has to consider the positive and the negative aspects before issuing the order. It can be noticed that some of the previous measures were already tagged as preventive in section **3.3.1**. The fact that now they are tagged as mitigative is caused by the absence of those before the CET exceeds 650 °C, which is the transition criterion to SAM (see section **3.2.2**).

The German Konvoi PWR also disposes of SAM measures pointing at the prevention of containment failure [12,85]. Two of the most important ones are described hereafter:

- Limitation of the concentration of combustible gases in the containment aiming at avoiding ex-vessel hydrogen deflagration. This is done through the opening of flaps and doors in ceilings and walls of the inner compartment or through passive autocatalytic hydrogen recombiners (PARs).

- Filtered containment venting: this measure aims at minimizing the FP release to the environment through the opening of small leaks. The process is ultimately initiated when the containment pressure increases above the design pressure (although it may be initiated earlier to limit the concentration of combustible gases) to avoid the increase of containment leaks or to reduce the release of FPs via a containment bypass.

3.4.3 Computational aids

Computational Aids (CAs) are a set of tools (e.g. graphs, tables, etc.) displaying relevant parameters that guide the ERO in the execution of SAM measures in the form of grace times, expected FP releases, etc. CAs are a summary of risk-relevant scenarios calculated using SA codes. These aids have been widely implemented in the SAMGs and even in some EOPs of operating NPPs [15,70].

3.4.3.1 German Konvoi PWR

There are a number of CAs in a German Konvoi PWR, that have been derived with MELCOR calculations [12,14]. Of special interest for this work is the CA showing the minimum flow rate necessary to remove the decay and chemical (steam-zirconium oxidation) power as a function of time (see **Figure 3-8**). The following information, extracted from [12], is given for better understanding of the figure:

- The abscissa shows the time elapsed between SCRAM and the detection of CET 650 °C, whereas the ordinate represents the averaged injection rate into the RCS.
- Injection occurs as soon as the CET exceeds 650 °C. Each reflooding simulation has a given time elapsed between SCRAM and CET 650 °C and a given average reflooding mass flow rate.
- The points are interpolated to produce different regions separated by different lines:
    - *Lines*: the green line marks the flow rate to remove the decay heat; the red line shows the reduction of this flow rate if the SG is filled, and the orange line is the dividing line between failure or success of core cooling.
    - *Regions*: the green region indicates that the core is filled sufficiently fast to evacuate the decay and the chemical power; the yellow region shows a potential success of the measure if the SGs involved, and the red region hints the necessity of a higher flow rate to remove, at least, the decay heat.

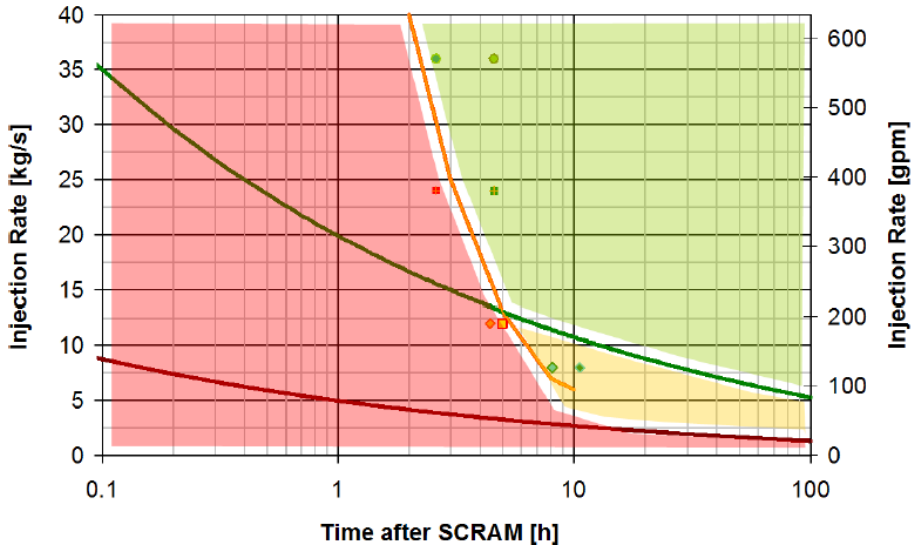

Figure 3-8: Required water mass flow rate into the RCS at CET 650 °C to prevent core damage in a generic Konvoi PWR, according to MELCOR calculations by AREVA [12].

3.5 Summary

This chapter has explained the role of AM within nuclear safety, differentiating between the preventive and the mitigative domains. Preventive procedures aim at maintaining core integrity and are contained within the EOPs, which give a clear guidance to the plant crew on how to prepare and execute each action. On the other hand, mitigative procedures are encompassed in the SAMGs, and prevent, mitigate or delay RPV or containment failure. For that purpose, the ERO follows a strategy composed of different SAM measures, which should be executed by the plant crew when requested.

The development of such strategies relies on a broad database of deterministic analyses performed with SA codes. Moreover, due to harsh plant environmental conditions during a severe accident, the instrumentation may be endangered. In that case, dedicated CAs also obtained with SA codes may be useful when selecting the most appropriate actions. At this point the reader can clearly see the importance of using reliable SA codes on the development of SAMGs.

4 The ASTECV2.0 code and selected physical models

The previous chapter has described the role of AM in NPPs and has highlighted the importance of relying on validated SA software for the development of SAMGs. This chapter acquaints the reader with the basics of the ASTEC code and with the modelling of the key in-vessel phenomena.

The chapter is structured in several sections. Firstly, the status of development of the ASTEC code is detailed in section **4.1**. Then, section **4.2** describes the scope of simulation of each ASTEC module. A more detailed explanation of the modules dealing with the thermal-hydraulics throughout the RCS and with the core degradation phenomena is carried out in sections **4.3** and **4.4**. Furthermore, the section **4.5** explains the approach used in ASTEC to model the most relevant phenomena during core degradation.

4.1 Current Status

The European ASTEC code simulates entire SA sequences in water-cooled nuclear reactors from the initiating event till the release of radioactive elements from the containment [25]. Its application range covers source term determination, Probabilistic Safety Analysis (PSA) level 2 analyses and assessment of SAM efficiency. Initially, ASTEC was a combination of system and containment codes developed at IRSN and GRS. In particular, this first V0 series (1996-2002) aimed at supporting the Phebus FP integral experiments [30]. The simulation scope was extended up to the early in-vessel phase with the release of the V1 version (2004-2009) [95,96]. Since then, ASTEC has improved and gradually become the reference SA code in Europe, benefitting from the activities performed in the frame of the SARNET EU Network of Excellence [97].

This international cooperation enabled the release of the V2.0 versions in 2009, locating the code at the state-of-the-art [25]. That version included substantial model improvements on core degradation and extended the application scope to Gen III reactors e.g. EPR. Currently, within the frame of the EU CESAM project (2013-2017) [22], the V2.0 series are being applied to support the choice of SAM for European NPPs in response to the Fukushima accidents. The implementation of new models based on the EU severe accident R&D priorities [98] and the validation effort from all CESAM partners has yielded the release of the V2.1 series [26], characterized by significant improvements e.g. modelling options for BWRs and CANDU reactors and enhanced treatment of key processes occurring during SAs. However, the V2.1 series are currently not recommended for safety study studies, since the reliability and robustness have not still reached full maturity in all aspects.

4.2 Structure of the ASTECV2.0 code

The structure of ASTECV2.0 is modular, each module describing a particular domain of the reactor or a set of physical phenomena (see **Figure 4-1**). The programming language is mainly FORTRAN (FORTRAN 95 with progressive evolution towards FORTRAN 2003, with some exceptions e.g. CESAR module in C, several ICARE and CPA routines in FORTRAN 77). The ASTEC V2 versions target PCs with Linux (used in current work) and Windows operating systems. Further information about ASTECV2.0 can be found in [25]. A brief description of each ASTEC module is provided hereafter.

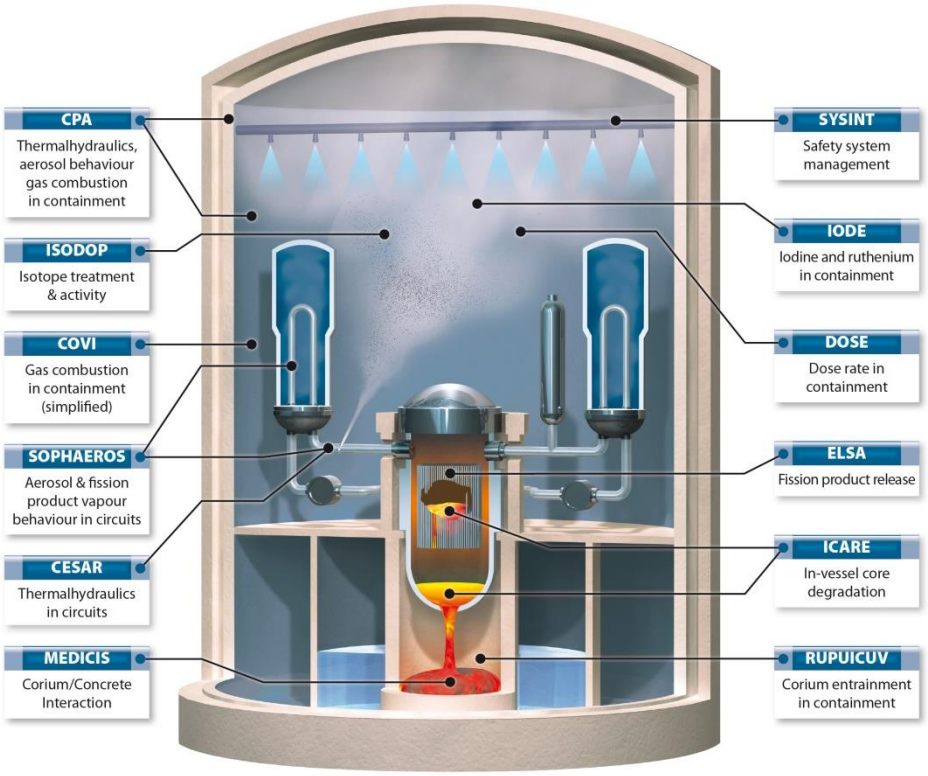

Figure 4-1: Scheme of the different ASTECV2.0 modules and their link to physical plant locations [25].

The **CESAR** module simulates the thermal-hydraulics in the RCS, secondary circuit and in the RPV (with a simplified core modelling) up to the beginning of core degradation i.e. before the start of Zr cladding oxidation by steam. From that point in time, CESAR only computes the thermal-hydraulics in the primary and secondary circuit as well as in the upper plenum and the cold leg collector of the RPV. The thermal-hydraulics in the RPV during the early and late in-vessel phase of the SA is computed by the **ICARE** module. The release of FPs from the fuel rods is determined by the **ELSA** module, whereas **SOPHAEROS** is responsible for the transport of FPs, aerosols and noble gases through the RCS. The module **ISODOP** determines the isotope distribution and hence, the decay heat in the reactor core. **SYSINT** is needed to model active systems like pumps, valves, spray systems etc.

The thermal hydraulic behaviour inside the containment and the aerosol transport and depletion are modelled by the sub-modules THY and AFP of the **CPA** module. Concerning the ex-vessel phenomena, the **RUPUICUV** module calculates the DCH; the **MEDICIS** module calculates the MCCI and the release of gases and fission products originated from it into the containment. The gas combustion is calculated with the FRONT and COVI submodules of CPA. Inside the containment, the module IODE is available for the calculation of the specific behaviour of iodine species and the module DOSE for the calculation of dose rates in the different containment compartments.

For the purposes of the current work, particular attention is paid to the CESAR and ICARE modules.

4.3 The CESAR module

The CESAR module [25], derived from the CATHARE code [99], uses a 5-equation modelling approach to describe one-dimensional two-phase thermal-hydraulics throughout the primary and secondary circuit in ASTECV2.0. This approach introduces a phase slip model relying on interfacial friction in order to model the mechanical non-equilibrium between the liquid and the gas phases. The equations are broken down as follows:

- $2 + n_I$ (with $n_I \leq 5$ and I = N_2, H_2, O_2, He, Ar) mass balance equations: one equation for the gas mixture (vapour and non-condensable gases), one equation for the liquid phase, and n_I equations for the non-condensable gases. The determination of these masses allows the prediction of the void fraction ($\boldsymbol{\alpha}$) and the partial pressures of the vapour and non-condensable ($\boldsymbol{P_V}$ and $\boldsymbol{P_I}$).
- 2 energy balance equations: one equation to calculate the temperature of the gas mixture (vapour and non-condensable gases) $\boldsymbol{T_G}$ and one for the liquid phase $\boldsymbol{T_L}$.
- 1 momentum balance equation calculating the mean velocity of gas and liquid $\boldsymbol{V_M}$.
- 1 algebraic equation calculating the drift velocity between the liquid and the gaseous phase $\boldsymbol{\Delta V = V_G - V_L}$.

The advantage of a 5-equation model over the 6-equation model is a higher computing efficiency derived from the suppression of one momentum balance equation, which is replaced by an algebraic equation. However, the drawback associated to the 5-equation model is that the code cannot handle the mechanical non-equilibrium conditions e.g. Counter Current Flow of water in steam in situations of top flooding. This has to be considered when simulating water injection into the hot legs of the RCS in later chapters.

The resolution of the 1-D thermal-hydraulics allows the calculation of axial velocities. This approach is valid during stationary conditions and during the initial stages of degradation, but it is no longer adequate when significant corium blockages have formed in the core region. For that case, a spatial resolution of 2-D two-phase flow thermal-hydraulics,

which cannot be handled by ASTECV2.0, would be required (see section **2.3**). This has to be considered when simulating reflooding of degraded cores.

CESAR uses a finite volume approach to spatially discretize the geometry using a staggered grid. The discretized geometry consists of three basic elements:

- Volumes (often called control volumes), which are fluid regions connected to any number of junctions;
- Junctions (often called flow paths), which allow fluid transfer between two volumes;
- Walls (often called heat structures), which allow the heat transfer between two fluid volumes.

Within that grid, $\boldsymbol{V_M}$ is calculated at each junction through the momentum balance equation, while the rest of variables ($\boldsymbol{P_V}$, $\boldsymbol{P_I}$, $\boldsymbol{\alpha}$, $\boldsymbol{T_G}$, $\boldsymbol{T_L}$) are calculated at the center of each volume through the mass and energy balance equations. The time integration is performed using a Newton-Raphson method and applying an implicit scheme.

Apart from this, CESAR introduces a specific type of volume to define large two phase flow domains (e.g. pressurizer), called swollen level volume. In contrast to the previous homogenous volumes, swollen level volumes can calculate the temperature and the pressure in each sub-volume through a clear-cut distinction between the values above and below the water level. Besides, CESAR allows the modelling of other specific components such as hydro-accumulators, pumps, valves, breaks, pressurizer sprays and heater systems.

The following relevant physical phenomena are modelled in CESAR: the critical break flow rate, forced convection to liquid, nucleate boiling, critical heat flux, transition boiling, film boiling, forced convection to vapour and radiative heat transfer. Further information about the CESAR physical constitutive laws can be found in [100].

4.4 The ICARE module

The ICARE module [25,101] describes the core degradation phenomena. In order to solve the thermal-hydraulics, ICARE also uses 5+N equations to describe a one-dimensional two phase flow. Therefore, the difficulties concerning cross flows and top flooding are the same ones as in CESAR (see section **4.3**). ICARE takes over the thermal-hydraulics in the RPV when certain criteria are fulfilled (e.g. void fraction in the upper plenum higher than 0.925, steam temperature at the top of the core above 300 °C). Relevant models of ICARE are described hereafter for a better understanding of the upcoming chapters.

4.4.1 Zircaloy oxidation by steam

In order to reproduce the stratified cladding configuration shown in **Figure 2-2**, ASTEC does not solve the diffusion equation, but considers that the cladding can be made of up to three layers (β-Zr, α-ZrO and ZrO_2). Besides, the model makes the following assumptions:

- The β-Zr layer is oxygen free.
- The α-ZrO phase is composed of 20 % mole of oxygen and 80 % mole of Zirconium (i.e. $Zr_{0.80}O_{0.20}$ or $ZrO_{0.25}$).
- The ZrO_2 has a stoichiometric configuration.

Based on experimental results, ASTEC models the oxidation kinetics through parabolic laws under the following conditions: unlimited steam supply (no steam starvation), no breakaway effect between 900-1200 K and sufficiently thick cladding thickness [16]. The parabolic law governing this behaviour is shown in **Eq. 4-1**, where ***X*** represents the oxygen mass gain or the zirconia (ZrO_2) layer growth in the cladding:

$$\frac{dX^2}{dx} = K \,. \qquad \textbf{Eq. 4-1}$$

The kinetics constant ***K*** depends on the temperature according to an Arrhenius law (see **Eq. 4-2**), where ***T*** is the temperature of the considered cladding component, ***A*** the pre-exponential factor, ***B*** the activation energy for oxidation and ***R*** the perfect gas constant.

$$K = A * e^{-\frac{B}{RT}} \,. \qquad \textbf{Eq. 4-2}$$

As highlighted in section **2.1.1**, the kinetic constant experiences changes due to ZrO_2 phase transformation with the temperature, producing a very exothermic reaction above 1900 K. In ASTEC, this is modelled by setting different values of ***A*** and ***B*** according to three temperature regimes: below 1800 K, within 1800-1900 K and above 1900 K. The values used in this study are taken from the Best-Fit correlation [43], which is a regression of many experimental points on Zry-4 oxidation by steam performed at different temperatures.

In order to calculate the disappearance of the α-ZrO phase and of the β-Zr phase, ASTEC makes use of **Eq. 4-3** and **Eq. 4-4** respectively, where x is 0.25. If the temperature of the cladding component is higher than the melting temperature of the β-Zr phase (~ 2000 K) and/or the α-ZrO phase (2250 K), one or the two phases become molten. In that case, the oxidation of those mixtures continues to be calculated with the Best-fit correlation, and not to the specific model for molten material oxidation (see section **4.4.4**).

$$ZrO_x + (2 - x)O \rightarrow ZrO_2 \,, \qquad \textbf{Eq. 4-3}$$

$$Zr + xO \rightarrow ZrO_x \,. \qquad \textbf{Eq. 4-4}$$

The effect of steam starvation on the oxidation kinetics is modelled through specific corrections on the mass balance equations. Likewise, the effect of finite cladding thickness is taken into account through the correction of the kinetic constant. Further details about these approaches can be found in [102]. The Best-fit correlation has been validated with several separate effect tests and integral experiments, as described in [103].

4.4.2 Cladding failure

The failure of the outer ZrO_2 layer of the fuel rod cladding is managed by the loss of integrity criteria, which changes the physical state of a cladding component if certain conditions are satisfied. The following physical states are defined in ASTEC:

- Compact : Component keeps the mechanical integrity.
- Perforated : Component is no longer compact but the loss of integrity not very serious. Release of FPs to the neighbouring channel is allowed.
- Cracked : Same consequences as for perforated, but with the additional feature of a possible cladding internal oxidation.
- Dislocated : Component has lost its mechanical integrity and is susceptible to move radially and then axially along the core.

In order for a cladding component to become dislocated, several criteria can be defined. Generally, two are used (as soon as one is fulfilled, the component becomes dislocated): temperature above 2300 K and ZrO_2 thickness below 250 µm [48] or temperature above 2500 K, the last accounting for the formation of eutectic alloys. The consequence of cladding dislocation is the mass transfer from the cladding to a specific structure representing the corium in the core, referred to as MAGMA.

The loss of integrity criteria can also be applied to handle the cracking or melting of other structures such as the grid spacers and the control rods. For that aim, the user can rely on parameters such as the thickness and the heat-up of the component or the time, etc. Criteria to trigger such events have been elaborated by means of extensive experimental investigations (see section **2.1.4**).

4.4.3 Relocation of molten material

In order to describe the relocation of corium outside cylindrical tubes (1-D) along different MAGMA cells, ASTEC makes use of a specific hydrodynamic model, described in [104]. The model can also calculate the 2-D relocation across particle debris beds. However, since core fragmentation is not considered, it only focuses on cylindrical geometries. In order to derive the equations, some hypotheses are made e.g. melt is incompressible, the movement of the gas has a negligible effect on the liquid motion, the inertial effects are neglected. Using these assumptions, balance equations for mass, momentum and energy are written for each MAGMA cell.

The mass conservation for the falling corium is given by **Eq. 4-5**, where $\boldsymbol{\rho_l}$ is the liquid density, $\boldsymbol{\varepsilon_l}$ is the liquid volumetric fraction within the mesh, $\boldsymbol{\vec{u}_l}$ the velocity field of the liquid phase and $\boldsymbol{\dot{m}_l}$ the melt generation rate.

$$\rho_l \frac{\partial \varepsilon_l}{\partial t} + \rho_l \nabla . \vec{u}_l = \dot{m}_l \, . \qquad \textbf{Eq. 4-5}$$

The momentum conservation equation for the liquid phase is given by **Eq. 4-6**, using a generalized Darcy approach, where μ_l represents the viscosity of the liquid; $\boldsymbol{K^z}$ and $\boldsymbol{K^z_{rl}}$ the absolute and the relative axial permeability, which are dependent on the rod diameter and the porosity (defined as the volume fraction of non-solid material within the mesh). Additionally, $\boldsymbol{K^z_{rl}}$ depends on the liquid saturation (defined as the volumetric fraction of the melt that is occupied by liquid) and the residual saturation. The latter is defined as the threshold below which the liquid cannot move ($u_{l,z}$ = 0), and depends on surface tension effects.

$$\rho_l \frac{\partial u_{l,z}}{\partial t} = -\frac{\partial P_l}{\partial z} - \rho_l g - \frac{\mu_l}{K^z K^z_{rl}} u_{l,z} \, . \qquad \textbf{Eq. 4-6}$$

Therein, $\boldsymbol{g}$ denotes the gravity vector and $\boldsymbol{z}$ the vertical coordinate. The most important term of **Eq. 4-6** is the last one, due to the predominance of the viscous forces among others. On the right hand side, the first term represents the axial pressure gradient due to pressure losses and capillary pressure (dependent on the surface tension), the second term is the hydrostatic pressure gradient, whereas the last corresponds to the volumetric forces (viscous friction).

Finally, the energy conservation equation for the liquid phase is given by **Eq. 4-7**, where $\boldsymbol{h_{gl}(z)}$ is the convective heat transfer coefficients; $\boldsymbol{A_{gl}}$ the interface area between the liquid/gas; $\boldsymbol{T_l/T_g}$ are temperatures of the liquid and gaseous phases; $\boldsymbol{q_l}$ represents the internal heat source within the liquid phase; $\boldsymbol{k_l^{eff}}$ represents the effective conductivity of the liquid phase.

$$\frac{\partial(\varepsilon s\,\rho_l H_l)}{\partial t}+\frac{\partial(u_l\rho_l H_l)}{\partial z}=\frac{\partial}{\partial z}\left(k_l^{eff}\frac{\partial T_l}{\partial z}\right)+h_{gl}(z)A_{gl}\left(T_g-T_l\right)+\varepsilon_l\rho_l q_l\,. \qquad \textbf{Eq. 4-7}$$

Concerning **Eq. 4-7**, the first term on the right side represents the axial heat transfer towards the actual mesh, the second the convective heat transfer between the fluid and the liquid corium and the last the internal heat source within the liquid phase.

For slightly degraded cores, the relocation model is able to predict the relocation along the fuel rods [96,105]. For more degraded configurations the model has not been completely validated, due to the scarce experimental database (see section **2.1.5**).

4.4.4 Oxidation of molten material

The model for molten material oxidation is applied to U-Zr-O mixtures surrounding fuel rods. The mixture consists of two zones: an external solid zone in contact with the outer fluid (crust - ***c***) and a liquid zone (melt - ***m***). The molten material surrounds the fuel rod (fuel - ***f***). With this distribution, two interfaces can be differentiated: crust-melt (***cm***) and fuel-melt (***fm***). A schematic representation of the geometry is shown in **Figure 4-2**.

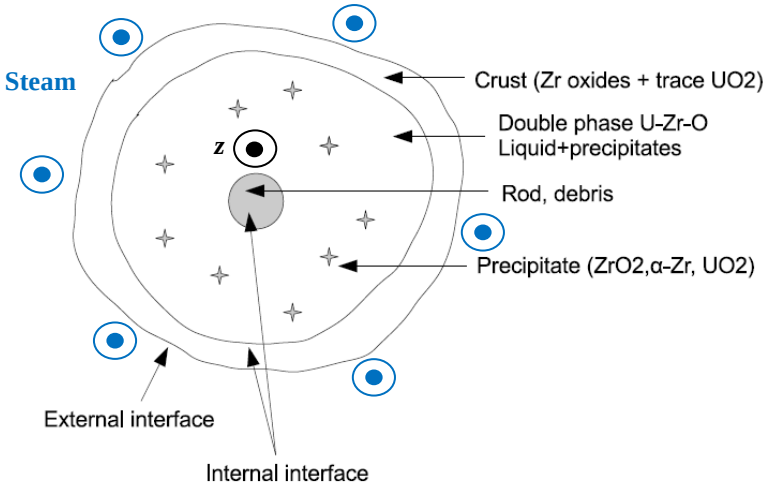

Figure 4-2: Modelling of melt oxidation [106].

For the formulation of the problem, the following mass fluxes are considered:

- $\boldsymbol{F_{c\to cm}}$: Diffusive flux from the crust to the interface crust/melt.
- $\boldsymbol{F_{f\to fm}}$: Diffusive flux from the fuel to the interface fuel/melt.
- $\boldsymbol{F_{cm\to m}}$: Convective flux from the interface crust/melt to the melt.
- $\boldsymbol{F_{fm\to m}}$: Convective flux from the interface fuel/melt to the melt.
- $\boldsymbol{F_{dcm}}$: Movement of the interface crust/melt towards the melt.

- $\boldsymbol{F_{dfm}}$: Movement of the interface fuel/melt towards the melt.
- $\boldsymbol{F_{ext\rightarrow c/m}}$: External flux towards the crust or melt (if crust has disappeared).

With those fluxes, mass balance equations can be written for each species $\boldsymbol{i = Zr, U, O}$ in the crust (**Eq. 4-8**), the fuel (**Eq. 4-9**) and the melt (**Eq. 4-10**). Continuity equations are also placed at each interface to equalize the mass fluxes through the solid/melt interface seen by the solid to those through the solid/melt interface seen by the fluid.

$$\frac{dm_c^i}{dt} = F_{ext\rightarrow c} - F_{c\rightarrow cm} - F_{dcm}\,, \qquad \textbf{Eq. 4-8}$$

$$\frac{dm_f^i}{dt} = -F_{f\rightarrow fm} - F_{dfm}\,, \qquad \textbf{Eq. 4-9}$$

$$\frac{dm_m^i}{dt} = F_{ext\rightarrow m} + F_{cm\rightarrow m} + F_{fm\rightarrow m} + F_{dcm} + F_{dfm}\,. \qquad \textbf{Eq. 4-10}$$

Further information about the additional hypotheses made to calculate these mass fluxes and details about the validation of this model can be found in [106].

4.4.5 Reflooding for rod-like geometry

In order to accurately calculate the quench front (QF) position and the wall temperature gradient along the TBR, DBA codes use a very refined mesh (0.1 mm). However, the associated long CPU time is beyond the capabilities of SA codes. With the aim of solving this problem, ASTEC makes use of a simplified model, which deals with bottom to top reflooding, and considers that the core geometry is sufficiently intact so that it can be treated by a 1-D approach. Further details about the model can be found in [65]. The different regions and the distribution of the heat flux along for water flowing along the rods can be qualitatively taken from **Figure 2-9**.

The model considers that the temperature profile is flat upstream the quench front due to the large temperature difference across the TBR, and well above downstream the TBR due to the low efficiency of heat exchange. The approximated temperature profile along the TBR corresponds to a step, where the lower bound is the temperature of the mesh located below the quench front ($T^- = T_w(IQF - 1)$), and the upper bound is the temperature of the mesh located just above it ($T^+ = Z_+(IQF + 1)$). The quench front location Z_{QF} is determined as the first mesh from the bottom, whose wall temperature exceeds the burn-out temperature (T_{BO}) (which depends on the CHF and the saturation temperature), according to **Eq. 4-11**.

$$T(Z_{QF}) = \frac{Z_{QF}}{Z_+(IQF) - Z_-(IQF)} T^- + \left(1 - \frac{Z_{QF}}{Z_+(IQF) - Z_-(IQF)}\right) T^+ > T_{BO} \,. \qquad \textbf{Eq. 4-11}$$

As far as the heat flux along the TBR is concerned, the model approximates it similarly to a Nukiyama curve. The heat flux is maximum and equal to the CHF at the quench front location, and decreases exponentially with the height according to **Eq. 4-12**. Within that equation, L_1 represents the exponential length, which is a function of the Capillary number, defined according to **Eq. 4-13**. For the regimes of nucleate boiling and dispersed flow, the heat transfer depends on the heat transfer coefficient according to several correlations [65]. The distinction of the flow regimes in each mesh is based on the wall temperature except for the TBR, which takes place in the mesh, where the quench front has been detected and possibly above (according to L_1).

$$\phi_{TB}(Z) = CHF\, e^{-\frac{Z_{QF}-Z}{L_1}} \,, \qquad \textbf{Eq. 4-12}$$

$$Ca = \frac{\mu_L v_L}{\sigma_L} \,. \qquad \textbf{Eq. 4-13}$$

In order to calculate T_{BO} and ϕ_{TB}, the CHF is needed. The CHF depends on several parameters, such as the system pressure, the sub-cooling, the flow rate and the wall geometry. Within ASTEC, the CHF is calculated by means of the CATHARE correlation [107], and modified depending on the void fraction and the liquid velocity of the quench front. In particular, the CHF tends to zero when the void fraction tends to 1 and decreases with increasing liquid velocities.

The model has been validated against PERICLES (design basis conditions) [65] and selected QUENCH experiments (slightly degraded cores) [105,108–110]. For situations where significant core blockages have been formed, the model is not applicable due to the lack of ASTECV2.0 capabilities to represent the quench front progression in degraded cores and the limitation to 1-D (see section **4.3**). This limitation will be partly overcome with the new V2.1 series [26], which includes a new 2-D treatment of the thermal-hydraulics in CESAR and a new reflooding model for degraded cores [111].

4.4.6 Models associated to the simplified Lower Plenum

In an intact configuration, ASTEC models the LP with the LH vessel wall, the internal structures and the fluid. The fluid region is modelled according to a 0-D approach and hence, it consists of one sole component. In contrast, the internals can be axially divided and the LH wall can be axially and radially discretized. For degraded configurations ASTEC follows a simplified approach to distribute the corium and the debris in different layers, as shown in **Figure 4-3**. Within this figure, several components can be identified:

- Debris bed at the bottom of the LH, formed as a consequence of the corium fragmentation upon contact with water.
- Dense corium layers (up to three, although only two are represented in the picture), corresponding to the non-fragmented material: the oxidic at the bottom (in pink) and the light metallic on top (in yellow). The potential heavy metallic layer, which is not shown in the picture, has not been considered in this work. Each layer is perfectly horizontal and homogenous in terms of composition and temperature.
- Debris bed at the top of the corium layers, generated as a result of the corium fragmentation after the corium dense layers have been formed.
- Water and gas among the upper debris bed (and above it), in contact with the upper dense corium layer.

It should be noted that debris particles are not modelled in current work here and hence, the decay heat is purely produced in the oxidic phase.

The entry of corium into the LP is modelled through a numerical filter on the mass transfer from the core to the LP. For this aim, ASTEC introduces a "slump cell" (see **Figure 4-4**), which stores the corium exiting the core region and distributes it to the upper corium layer according to different criteria (time constant, maximum mass flow rate). Within this work, the mass flow rate $\boldsymbol{Q_s}$ is given by **Eq. 4-14**, where $\boldsymbol{\tau}$ is the time constant (10 s by default) and $\boldsymbol{m_s^0}$ is the mass of corium in the slump cell at the beginning of the time step.

$$Q_s = \frac{m_s^0}{\tau + \Delta t}. \qquad \textbf{Eq. 4-14}$$

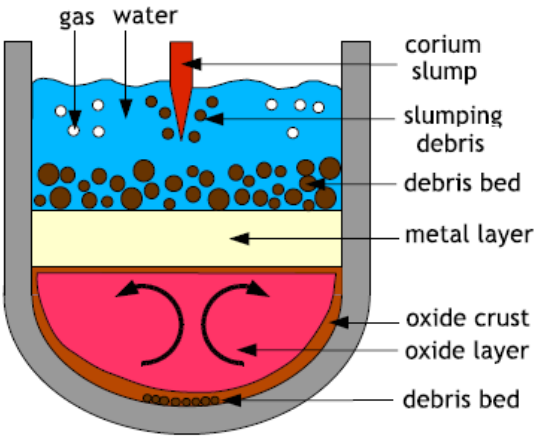

Figure 4-3: Modelling of the lower plenum in ASTEC [102].

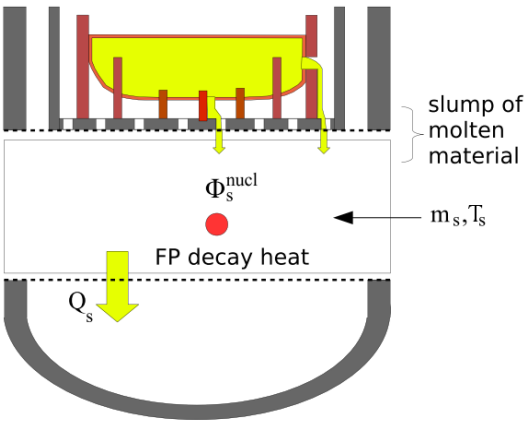

Figure 4-4: Modelling of the slump cell in ASTEC [102].

Regarding the heat transfer in the simplified lower plenum, several mechanisms are considered in the metallic and oxidic layers. Correlations for the different heat transfer modes in those layer, as well as for other components, can be found in [102].

- Oxidic layer: internal heat generation (boundary condition on time), convection towards the vessel wall and the internals, and convection towards the metallic layer.
- Light metallic layer: convection towards the vessel wall and the internals and convection towards the oxidic layer. Concerning the upward heat transfer, two mechanisms are possible: if water is present, convective heat transfer between the water and the metallic layer is considered. Otherwise, radiative heat transfer between the metallic layer and the reactor structures is calculated.

In order to model the stratification of corium into the LP, ASTEC can use a simple or a detailed model. Within this work, the simple stratification model has been used, and the existence of up to two layers (metallic and oxidic) is permitted. Information on the detailed thermochemical phase separation model can be found in [112]. The idea of the simplified model is to transfer mass between layers by comparing the density of the layer to the one of the layer located just above and below, and to the density of the oxidic and metallic phases within that layer.

The oxide and metal densities within each corium layer are computed according to **Eq. 4-15** and **Eq. 4-16** respectively, where $\boldsymbol{N_{oxide}}$ and $\boldsymbol{N_{metal}}$ are the number of oxide and metal species; $\boldsymbol{m^0_{i,k}}$ is the mass of species $\boldsymbol{k}$ before phase separation transport and $\boldsymbol{\rho_{i,k}}$ is the density of species $\boldsymbol{k}$ within the corium layer $\boldsymbol{i}$:

$$\rho_i^{ox} = \frac{\sum_{k=1}^{N_{oxide}} m_{i,k}^0}{\sum_{k=1}^{N_{oxide}} \frac{m_{i,k}^0}{\rho_{i,k}}}, \qquad \textbf{Eq. 4-15}$$

$$\rho_i^{met} = \frac{\sum_{k=1}^{N_{metal}} m_{i,k}^0}{\sum_{k=1}^{N_{metal}} \frac{m_{i,k}^0}{\rho_{i,k}}}. \qquad \textbf{Eq. 4-16}$$

With the knowledge of these densities, it is then possible to calculate the transfer of species according to one of the four following possibilities:

- If the layer $\boldsymbol{i}$ is the uppermost one and its oxide density is greater than the average density of the corium below ($\rho_i^{ox} > \rho_{i-1}$), then each oxide species $\boldsymbol{k}$ moves down.
- If the layer $\boldsymbol{i}$ is the lowest one and its oxide density is lower than the average density of the corium above ($\rho_i^{ox} < \rho_{i+1}$), then each oxide species $\boldsymbol{k}$ moves up.
- If the metal density of the layer $\boldsymbol{i}$ is greater than its oxide density ($\rho_i^{met} > \rho_i^{ox}$):

  - If the layer ***i*** is the lowest one, then each oxide species ***k*** moves up.
  - Else, each metal species ***k*** moves down.
- If the oxide density of the layer ***i*** is greater/equal to its metal density ($\rho_i^{ox} \geq \rho_i^{met}$):
  - If the layer ***i*** is the uppermost one, then each oxide species ***k*** moves down.
  - Else, each metal species ***k*** moves up.

The mass flow rate of each species ***k*** entering or exiting the corium layer ***i*** ($\boldsymbol{Q_{ci,k}^{sep}}$) is defined according to **Eq. 4-17**, where $\boldsymbol{\tau}$ is the time constant (10 s by default).

$$Q_{ci,k}^{sep} = \frac{m_{ci,k}^{0}}{\tau + \Delta t} \qquad \textbf{Eq. 4-17}$$

The models describing the heat transfer in the LP have been validated against the BALI, the RASPLAV and the LIVE experiments in [113,114], whereas those describing the stratification have been validated against the MASCA experiments in [114].

4.4.7 Reactor Pressure Vessel failure

A mechanistic calculation of the deformation is out of scope of SA codes. Hence, it is necessary to develop simplified models to calculate the deformation and the failure of the LH retaining enough details to capture the most important phenomena. For this aim, ASTEC disposes of three mechanical models (Combescure, Oeuf and Lohey) to evaluate the challenges from thermal, mechanical and weight loads. Within this work, the Combescure model has been used [115]. Details about the rest of models and about other approaches followed to analyse such loads can be found in [116]. Within the Combescure model, failure can occur due to two contributions: plastic or creep rupture.

Considering that $\boldsymbol{F_k}$ is the force applied against the LH wall at the axial level ***k***, that ***(k,j)*** is an elementary mesh of the lower head vessel wall ***v*** (see **Figure 4-5**) and that $\boldsymbol{N_{rad}}$ is the number of radial elements at a constant height, the applied stress can be defined according to **Eq. 4-18**. It can be seen that the stress increases with the decrease of the wall thickness. On the other hand, the ultimate stress of the wall at one axial level is represented by $\boldsymbol{\sigma_{ult,k}}$, which decreases with increasing wall temperature and depends on parameters related to the wall material. Plastic failure of the LH occurs when the applied stress at an axial level exceeds the ultimate stress, either due to an increase of the applied stress (for wall thickness reduction) or a decrease of the ultimate stress (for increasing temperatures).

$$\sigma_{vk} = \frac{F_k}{\sum_{k=1}^{N_{rad}} S_{kj}^{upp} cos(\theta_{kj}^{upp})}. \qquad \textbf{Eq. 4-18}$$

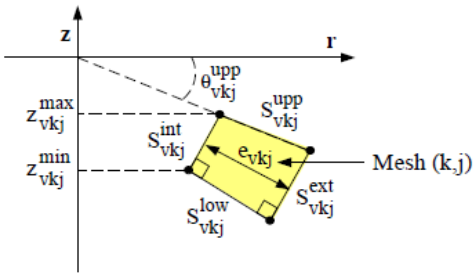

Figure 4-5: Elementary mesh *(k,j)* of the vessel lower head (denoted as *v*) [102].

Plasticity of the RPV competes with creep in the sense that the first represents the speed for which σ_k tends to $\sigma_{ult,k}$, whereas the second one the speed for which the material is deformed beyond its rupture strain (ε_r). The total deformation rate at a given level ($\dot{\varepsilon}_k^t$) is mainly caused by creep, which increases with increasing temperature gradient through the wall thickness and depends on other parameters related to the wall material. Instead of comparing at each time step the LH deformation, ASTEC calculates a rupture time at each level according to **Eq. 4-19**, and compares it with the current time. RPV failure due to creep occurs if the rupture time exceeds the current simulation time. Creep deformation can only be activated when the average temperature at a given axial level exceeds 800 K.

$$t_r = \frac{\varepsilon_r}{\dot{\varepsilon}_k^t}. \qquad \textbf{Eq. 4-19}$$

The models describing RPV failure have been validated against several OLHF experiments in [114].

4.5 Summary

This chapter has provided an overview about the status of the ASTEC code, its main application scope and the aim of each module, paying special attention to the CESAR and the ICARE modules. Furthermore, the chapter has acquainted the reader with the approach followed by ICARE to describe the key in-vessel SA phenomena e.g. Zry oxidation, cladding failure, relocation and oxidation of U-Zr-O mixtures, reflooding of slightly degraded cores, slumping of molten material, heat transfer and stratification in the LP and RPV failure.

The main shortcomings associated to ASTECV2.0 for the analysis of the in-vessel phase of SAs are the inadequacy of the 1-D approach to describe the multi-dimensional thermal-hydraulics and the lack of validity of the reflooding model for degraded core configurations. These problems will be partly solved by the future V2.1 series.

In turn, the phenomena associated with a real core meltdown are complex and cannot be described with the required precision, since all models are making use of numerous

approximations and simplifications. In this context, integral experiments involving the most important physical and chemical phenomena appear as an optimal calibration source for the validation of integral severe accident codes.

5 Validation of ASTECV2.0 models based on the QUENCH test facility

The previous chapter has described the ASTECV2.0 approach to describe the main physical phenomena occurring during the in-vessel phase and their validation status. This chapter aims at extending the ASTECV2.0 validation matrix concerning the early in-vessel phase of a SA based on selected data from the QUENCH facility.

The chapter starts with a brief description of the QUENCH facility in section **5.1**. Then, the QUENCH-08 test conduct is detailed in section **5.2**. The section **5.3** explains the main modelling guidelines to build the ASTECV2.0 model of the QUENCH-08 facility. The detailed comparison between the experimental data and the code predictions is provided in section **5.4**, and the outcomes of this analysis are discussed in section **5.5**.

5.1 The QUENCH Test facility

The QUENCH program at the Karlsruhe Institute of Technology (KIT) was initiated in 1996 as the successor of the CORA program [29], which investigated material interactions under SA conditions and, to a lower extent, the phenomena involved during core reflooding [117]. For such tests, it was shown that core reflooding triggered a bundle temperature escalation and sharp hydrogen generation rates. However, the mechanisms contributing to such behaviour were not clear at that time. Therefore, the QUENCH program was launched to provide a quantitative determination of the hydrogen source term during reflooding [118].

Up to present, 17 tests representing SA conditions have been performed [19]. Generally, reflooding of slightly degraded cores during low pressure scenarios has been investigated. The influence of the following parameters on the hydrogen generation have been studied: degree of cladding pre-oxidation, temperature at the onset of reflooding, steam starvation, air ingress, water (steam) mass flow rate, effect of absorber material (e.g. boron carbide, silver-indium-cadmium), effect of cladding material (e.g. E110, M5, ZIRLO). A general overview of all performed and upcoming experiments can be found in [16] and [119] respectively.

The main component of the QUENCH facility is the test bundle. Superheated steam from a steam generator with argon as a carrier gas enters the bundle at the bottom and move upwards along the bundle (left side **Figure 5-1**). The argon, the steam not consumed, and the generated hydrogen (due to Zry oxidation) exit the bundle at the top. The reflooding medium (water or saturated steam) enters the test section through a separate line at the bottom of the bundle.

The test bundle consists of twenty one fuel rod simulators (FRSs), each of which has an approximate length of 2.5 m. Out of these FRSs, twenty are electrically heated over a length of 1024 mm through a 6 mm diameter tungsten rod, in contrast to the unheated one placed at the center of the test section (right side **Figure 5-1**). Each heated FRS is composed of a tungsten center rod, surrounded by ZrO_2 annular pellets and a Zry-4 cladding. The tungsten rods are in contact with molybdenum and copper electrodes at the top and bottom, both electrodes being connected to the DC power supply and coated with a ZrO_2 fiber. The unheated FRS is composed of ZrO_2 pellets and Zry-4 cladding along its entire length. All FRSs are fixed in their positions by five grid spacers (the lowest made of Inconel, the rest of Zry). Four corner rods are installed to ensure similar thermal hydraulic conditions across the test section and to obtain a uniform temperature distribution. The corner rod B can be removed at any time to measure the oxide scale at selected elevations before reflooding.

The FRSs and the corner rods are surrounded by a shroud, which is surrounded by a tubular cooling jacket. The gap between the shroud and the cooling jacket is filled with a porous ZrO_2 fiber insulation along the heated length of the bundle, and with stagnant argon gas above the heated length (1024-1300 mm). The cooling jacket is argon-cooled along the heated length of the bundle, and water-cooled above the heated length of the bundle. Further details about the geometry of the QUENCH facility can be found in [118] and [120].

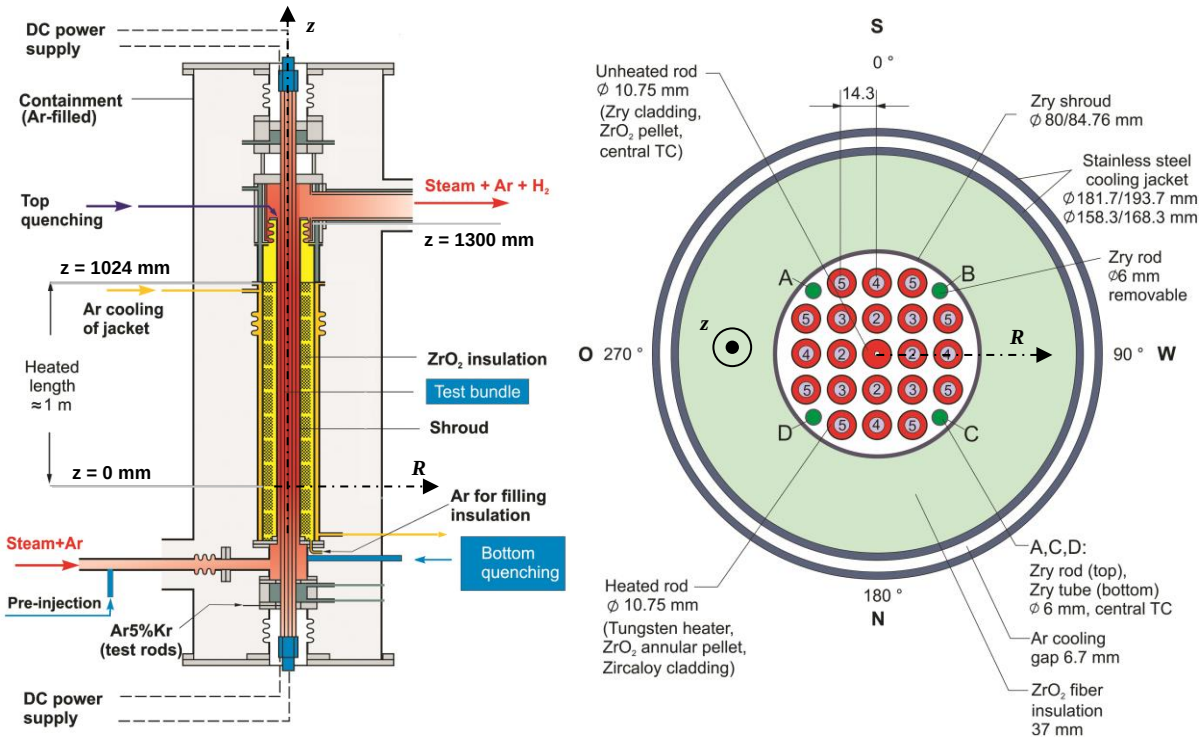

Figure 5-1: Left: Schematic view of the QUENCH facility;
Right: Horizontal cut of the QUENCH-08 bundle [120].

5.2 Test Conduct of QUENCH-08 Experiment

The test QUENCH-08 [120] was performed as a reference test for the QUENCH experiments Nr. 07 and 09, which investigated the impact of boron carbide on the hydrogen generation. In contrast to the tests 07 and 09, the QUENCH-08 did not contain boron carbide in the test section. The test Nr 08 has been selected for code validation, since it has not been previously included in the ASTEC validation matrix. In all cases i.e. for tests Nr. 07, 08 and 09, bottom reflooding was performed by means of 15 g/s of saturated steam (0.60 g/s/rod in QUENCH, considering that there are 21 FRSs and 4 corner rods). This situation may occur if a low mass flow rate is injected into the core, and would represent the dispersed flow region located above the TBR (see **Figure 2-9**).

The test conduction is illustrated in **Figure 5-2** and explained here below according to the different experimental phases:

- In the stabilization phase, the bundle is heated up from room temperature to 873 K by means of a stepwise increase of the electrical power to 4 kW in presence of argon (3 g/s) and steam flow (3 g/s). Steam and argon flow rates remain constant from this moment on until the reflooding phase.
- The first heat-up phase consists of a gradual increase of the electrical power from 4 kW to 13.1 kW, leading to a PCT escalation till 1700 K at a rate of 0.3-0.6 (K/s). For t > 2277 s, the electrical power is regulated so that the total input of electrical and oxidation power is kept constant.
- During the pre-oxidation phase (2277 – 3240 s), the temperatures oscillate within 1700-1750 K and a maximum oxide layer of 274 µm was built on the outer surface of the claddings. The corner rod B was extracted at the end of the pre-oxidation phase to measure the oxide layer profile.
- In the second heat-up phase (3240 – 3776 s) the temperature increased from 1740 K up to 2200 K with a power rate of 6 W/s.
- The reflooding phase was initiated when the shroud temperature reached 2073 K at 950 mm (3776 s) with the injection of 15 g/s of saturated steam, where the term effective subtracts the surface of the shroud from the total wetted surface. The test was terminated by switching off the superheated steam injection and reducing the electrical power to 4 kW and then to zero.

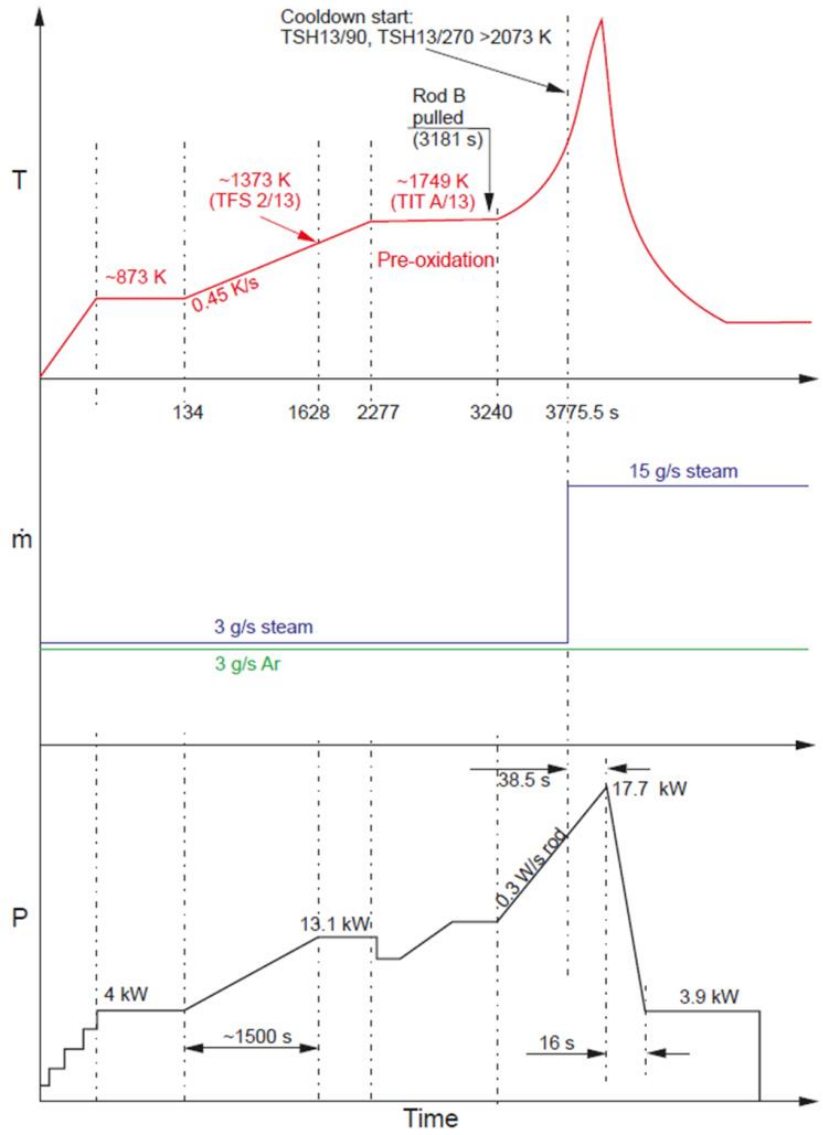

Figure 5-2: Evolution of selected parameters of the QUENCH-08 test (shroud temperature at 950 mm, inlet mass flow rate and electrical power) [120].

5.3 ASTEC Model of the QUENCH-08 Experiment

5.3.1 Geometry and model assumptions

The model of the test section consists of an unheated FRS (whose cladding is identified by CLAD1), 8 electrically heated FRSs constituting the inner ring (whose cladding is identified by CLAD2) and 12 electrically heated FRSs forming the outer ring (whose cladding is identified by CLAD3). Additionally, there are 5 corner rods (ZRROD), 5 grid spacers, the shroud (BZIR), the fiber insulation along the active zone (heated with tungsten heaters), the argon gap along the unheated length and the inner tube of the annular cooling jacket (C. JACK).

The FRSs and the corner rods are embedded into one radial channel (CHAN). All elements are represented in **Figure 5-3** (left) and follow the experimental values [120]. The model considers azimuthal symmetry at all times. Concerning the axial discretization, the bundle is divided into equidistant staggered slices of 55 mm height. This discretization and the distribution of materials throughout the core are shown at the right side of **Figure 5-3**. Therein, the O_2Zr corresponds to the ZrO_2 and ZOFR corresponds to the specific ZrO_2 alloy composing the fiber insulation.

In addition, the following assumptions have been made:

- The tungsten heater is in contact with the fuel pellets to avoid the consideration of radiation from heater with unknown surface properties (e.g. roughness).
- The four corner rods are present during the whole transient, although in the experiment the corner rod B was extracted after the pre-oxidation phase, since it is not possible to remove physical elements from ICARE during the calculation.
- The electrical resistance between the electrode of each heated rod and the external cables attached to it i.e. resistance in the sliding contacts, is assumed to be 7 mΩ/rod [121]. However, this parameter is subjected to high uncertainties [122,123].
- Conductive heat exchange has been defined between the shroud and the cooling jacket through the argon gap (1024-1300 mm), since the direct radiative exchange between the shroud and the cooling jacket cannot be directly calculated by ASTEC. As a result, the gap is considered to be a solid argon cell, whose thermal resistance is updated at each time step to take into account the radiative and convective exchange between shroud and cooling jacket. This methodology is valid as long as the temperature gradient between the shroud and the cooling jacket remains small, since the average temperature of the argon cell is properly calculated. However, this methodology diverts from the real behaviour depending on the deviation between the temperature of the shroud and the cooling jacket.

5.3.2 Boundary conditions

Several time-dependent boundary conditions have been introduced according to the experimental measurements [120]: electrical power generated in the inner and outer ring e.g. currents (measurement channels E501 and E502) and voltages (E503 and E504); pressure and temperature of the inlet fluid (P511 and TFS2/1F respectively); mass of inlet fluid (FM401 for the argon, F205 for the steam); temperature at the external surface of the cooling jacket along its height (TCI X/level), where X represents the elevation of the thermocouple. As far as the condition for reflooding is concerned, the experimental criterion was the detection of at least 2077 K in two shroud thermocouples at 950 mm. Since the shroud temperature prediction is difficult in ASTECV2.0 due to the absence of cross flows and the modelling of one channel, it has been decided to start reflooding at the experimental time (i.e. 3776 s).

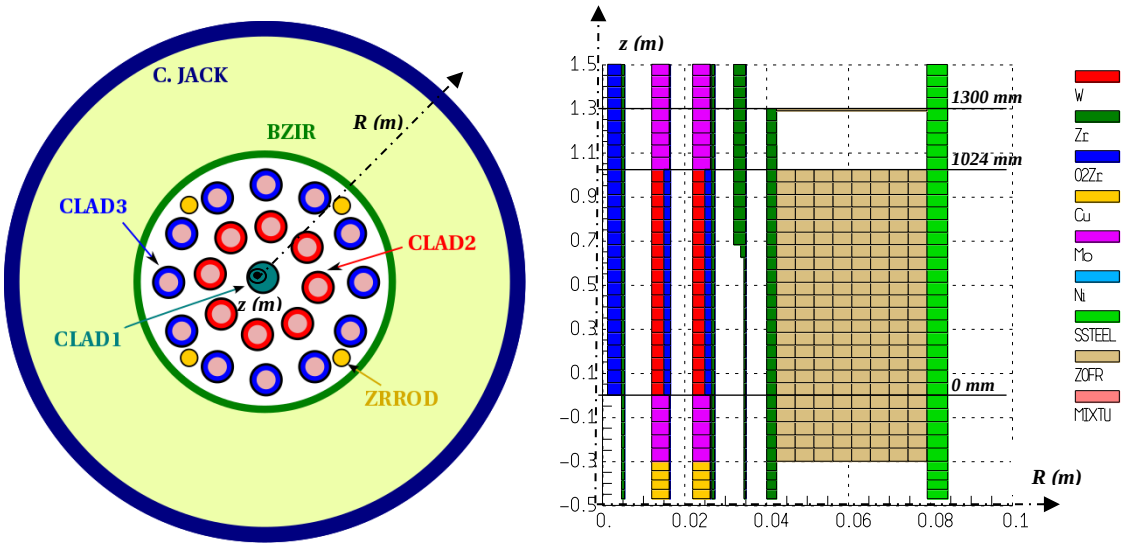

Figure 5-3: Radial view of the QUENCH-08 model in ASTECV2.0 (left); Translation of the QUENCH-08 model into the ASTECV2.0 computational together with the distribution of materials throughout the core (right).

5.3.3 Physical phenomena

The following physical phenomena relevant for the early in-vessel phase have been considered:

- Heat transfers:
  - Conduction within each element and between the different elements in contact.
  - Convection between each element facing the channel (i.e. fuel rods, corner rods, grids and shroud).
  - Radiation among FRS claddings, corner rods and the shroud.
- Chemical interactions:
  - Oxidation of both Zry-4 by steam according to the Best-fit correlation. The shroud and corner rods can also oxidize.
  - Steam entrainment into the fiber or the argon gap after shroud failure has not been modelled.
- Mechanical processes:
  - Cladding, corner rod and shroud component failure if its temperature is greater than 2300 K and their ZrO_2 thickness is lower than 250 µm).
  - Relocation of molten material along the rods and molten material oxidation.

5.4 Comparison of ASTEC predictions with QUENCH-08 Experimental data

Several graphs have been used to compare ASTEC predictions and the experimental values: the temperature evolution of the different elements composing the bundle at the elevations 550 mm, 950 mm and 1250 mm are shown in **Figure 5-4** to **Figure 5-6**; the

temperature and oxide profiles at the end of the pre-oxidation phase and at the end of the second heat-up phase are shown from **Figure 5-7** to **Figure 5-8**. Further temperature evolutions and axial profiles are shown in **Appendix B**.

Within those temperature graphs, red corresponds to CLAD2, blue to CLAD3, green to the SHR and orange to CHAN. The solid lines correspond to ASTEC values, while the dashed lines correspond to the experimental data. The names of the experimental temperatures have been changed by the name of the ASTEC element followed by their orientation (north (N), south (S), east (E) and west (W)) according to **Figure 5-1** (right). For example, *Exp_CLAD2_W* refers to the thermocouple attached to CLAD2 at the west orientation of the bundle). Temperature lines with abrupt reduction to zero represent THC failure.

It can be observed that ASTEC is able to properly describe the first heat-up phase, mainly governed by the tungsten conduction, the convection to the outer channel and the radiation among rods. During this phase, the bundle oxidation is negligible (see **Figure B.2-1**) due to the low temperatures. Despite the good agreement, some discrepancies are observed:

- The shroud temperature experiences a sharp change of slope at about 900 K in contrast to the experiment. This is caused by the exceedance of the oxidation threshold (set by the user in 900 K). Later on, the ZrO_2 layer builds up and hence, the radiative absorptivity coefficient increases. Consequently, the shroud heat-up rate increases and that of the claddings decreases.
- The radial temperature gradient is lower than the experimental one. It seems that this deviation arises the modelling of one single fluid channel. As a result, only one fluid temperature is radially calculated, in contrast to the test conditions (fluid colder/hotter at the outer/inner part of the bundle). Hence, less heat can be transported from the shroud, which translates into a flatter radial temperature profile. This behaviour is maintained along the experiment at all elevations.

ASTEC can properly describe the pre-oxidation phase. Similarly to the first heat-up phase, it seems that the lack of radial discretization is leading to a higher shroud temperature and lower temperature gradient at the end of the pre-oxidation phase (left side of **Figure 5-7**). Concerning the temperature deviation, the shroud temperature overestimation is more significant along the upper unheated zone (1024-1300 mm) than along the active zone of the bundle. This greater deviation can be explained by the difficulty to reproduce the heat transfer from the shroud to the cooling jacket through the argon gap with ASTEC. As commented in section **5.3.1**, the heat transfer in this region is approximated by heat conduction through the use of an effective thermal conductivity. The model can reproduce this exchange for low shroud temperatures, but underestimates the heat transfer when the radiative heat transport contributes significantly to the energy balance.

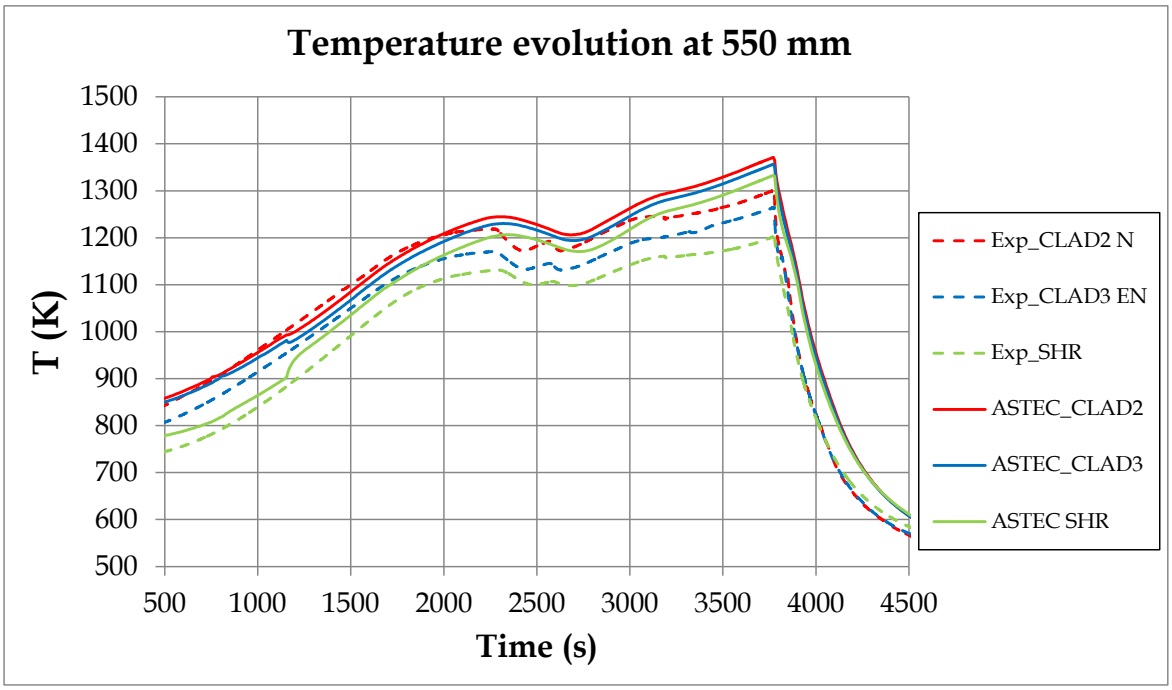

Figure 5-4: Comparison of the temporal evolution of predicted (solid lines) and experimental (dashed lines) temperatures at an axial height of z = **550** mm at several radial positions (colour legend).

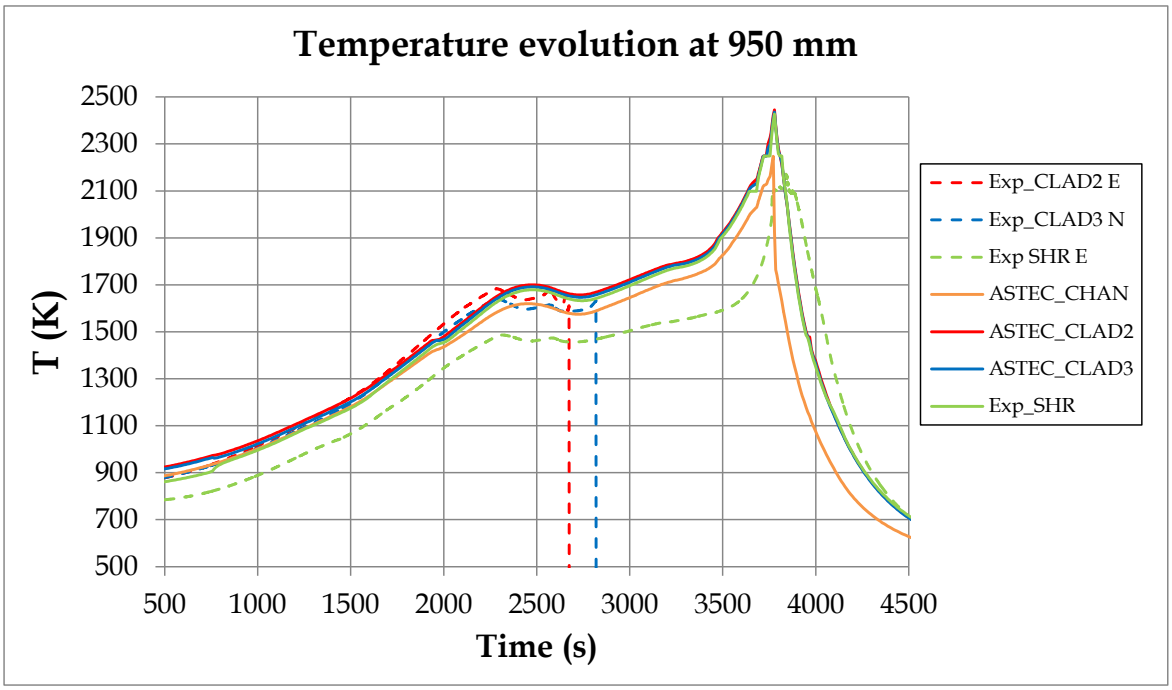

Figure 5-5: Comparison of the temporal evolution of predicted (solid lines) and experimental (dashed lines) temperatures at an axial height of z = **950** mm at several radial positions (colour legend).

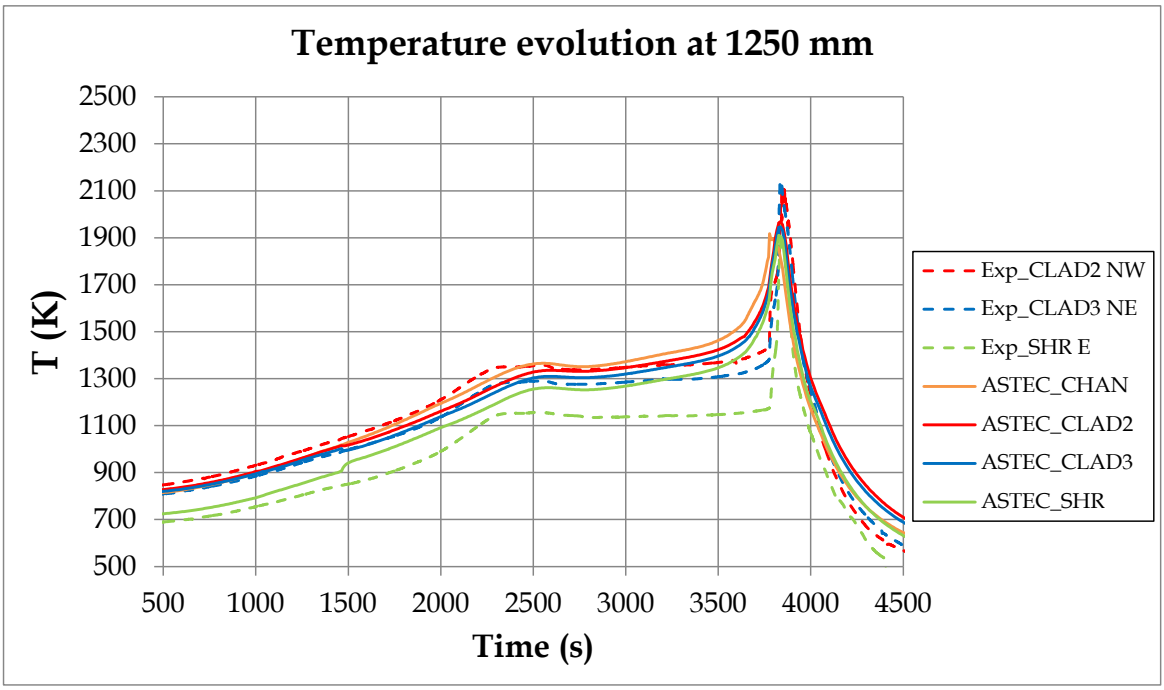

Figure 5-6: Comparison of the temporal evolution of predicted (solid lines) and experimental (dashed lines) temperatures at an axial height of z = **1250** mm at several radial positions (colour legend).

Since the temperature of the cooling jacket (boundary condition) fixes the shroud temperature and the predicted radial temperature gradient is very small because of the aforementioned effects, the FRSs experience their maximum temperatures at around 1050 mm, in contrast to the experiment (at about 950 mm). This temperature deviation leads to a deviation on the oxide thickness along the corner rod B at the end of the pre-oxidation phase, which is contained in **Table 5-1**. Therein, experimental values are shown for two measurement principles: metallography and eddy current. The eddy current method gives a higher value due to the influence of the underneath α-Zr (O) layer. The oxidation behaviour and the temperature history are coherent: the oxidation is overestimated within a height of z =1024-1100 mm and greatly underestimated for z within a height of 800-950 mm. Consequently, the oxidation peak is shifted upwards and is lower compared to the experiment.

After the oxide scale has been built, the second heat-up phase starts. From this moment on, most of the THCs measuring the temperatures in the FRSs fail and hence, only shroud temperatures can be used for comparison. Like in the previous phases, ASTEC is able to describe the temporal evolution of the experimental data at all heights (see **Figure 5-4** to **Figure 5-6**). However, it deviates due to the aforementioned discrepancies. In particular, the poor convection from the shroud to the fluid drives the FRSs temperatures above 1800 K, which corresponds to the entrance in the medium oxidation regime (see section **4.4.1**). In contrast, the experiment shows a slower axial temperature rise along the bundle, which is mainly motivated by the higher power transferred radially from the shroud to the surrounding

steam. This early temperature escalation is propagating downstream, as illustrated in the axial temperature profile at reflooding onset (see right side of **Figure 5-7**).

Bundle elevation z (mm)	**Experimental oxide layer thickness (µm)**		**Predicted oxide layer thickness by ASTEC (µm)**
	Metallography	Eddy-current	
550	11	5	**11.61**
650	32	22	**34.87**
750	74	66	**64.58**
800	103	106	**89.32**
850	145	172	**114.06**
870	164	203	**127.10**
950	274	351	**193.57**
1020	153	167	**188.12**
1050	115	114	**169.2125**
1100	75	63	**138.23**

Table 5-1: Oxide layer thickness along corner rod B as a function of the axial height z at the end of the pre-oxidation phase: ASTEC vs. Experiment [120] (red/blue – over/underestimation, green – within the experimental range of measurement).

The aforementioned discrepancies propagate to the reflooding phase, during which ASTEC predictions deviate from experimental data. In order to evaluate reflooding success, oxidation profiles along CLAD2 are drawn at the beginning of the quenching phase and 400 s later (see **Figure 5-8**). A zoom on the temperature evolution at z =950, 1050, 1150 and 1250 mm during quenching is also depicted from **Figure B.1-5** to **Figure B.1-8**.

Results show that reflooding has different effects at different elevations of the bundle: the cladding components located below 700 mm are immediately cooled down (see **Figure 5-4**) since the PCTs are below 1500 K, whereas those located above 1024 mm undergo a temperature increase (see **Figure 5-6**) due to the oxidation of the hot α-ZrO and the inner molten material. This is reflected in the ZrO_2 layer build-up within 1024-1300 mm (see right side of **Figure 5-8**). By comparing the experimental data with the predicted values, the following deviations are observed:

- The temperature escalation occurs at the upper unheated zone (above 1024 mm) because of the discrepancies shown during the previous phases. In the experiment, a temperature escalation occurs above 950 mm.
- The predicted temperature escalation is weaker than the experimental, since the cladding is more oxidized than in the experiment at reflooding onset. As a result, a further oxidation is hindered, which limits the temperature escalation.

- The cooldown rate approaches the experimental one below 950 mm. However, it increasingly deviates within the upper unheated zone, due to the low convective power extracted from the shroud.

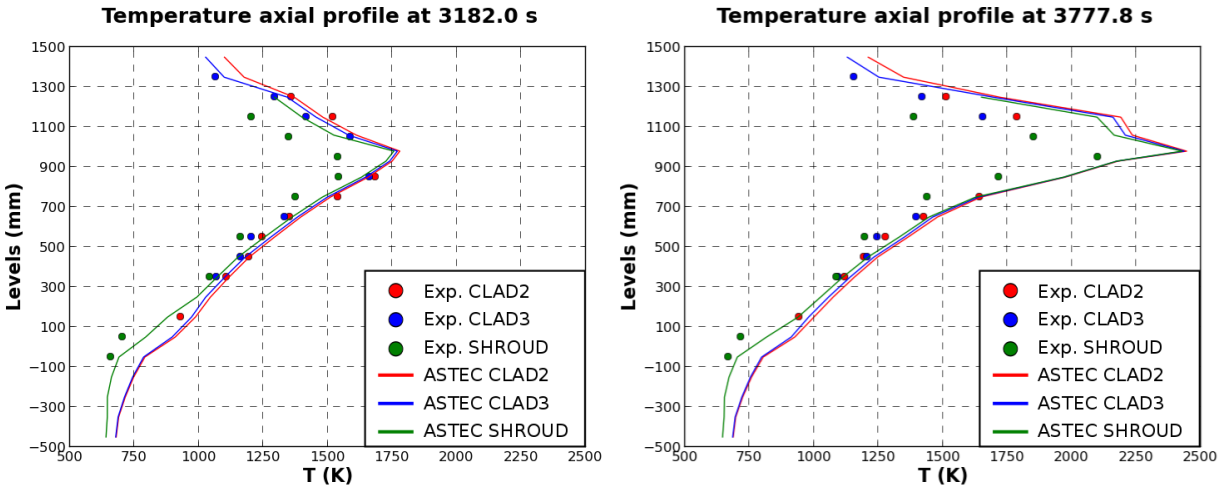

Figure 5-7: Comparison of the predicted (solid lines) and the experimental (data points) axial temperature profiles at several radial positions (colour) at the end of the pre-oxidation phase (left) and at reflooding onset (right).

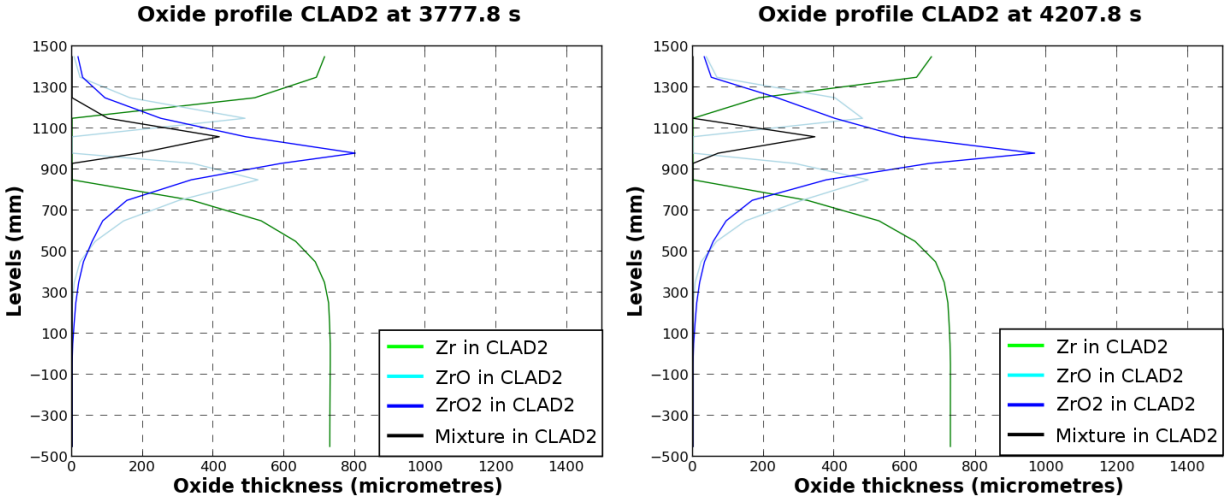

Figure 5-8: Predicted oxidation profile at reflooding onset (left) and 400 s afterwards (right) on CLAD2 (representative cladding of the inner ring).

The effect of quenching on the oxide layer along CLAD2 at the end of the experiment can be observed in **Figure 5-9**. Therein, the minimum, average and maximum oxide thickness measured with metallography have been included. The graph reveals an asymmetrical ZrO_2 thickness within the upper unheated zone and a minor oxidation degree below 750 mm. Although the predicted profile is within the experimental measurement at the hottest bundle zone (with the exception at 950 mm), several differences are observed.

- The oxidation gradient within 800-1000 mm is underestimated;
- The oxidation peak is underestimated;
- No cladding failure is calculated, whereas the experiment predicted local shroud and cladding dissolution within 900-1100 mm.

All things considered, ASTEC underestimates in the mean the oxidation layer thickness during reflooding, but the predictions are still in the spread of the experimental observations. By now, it is not clear if the deviations can be attributed to the model simplifications.

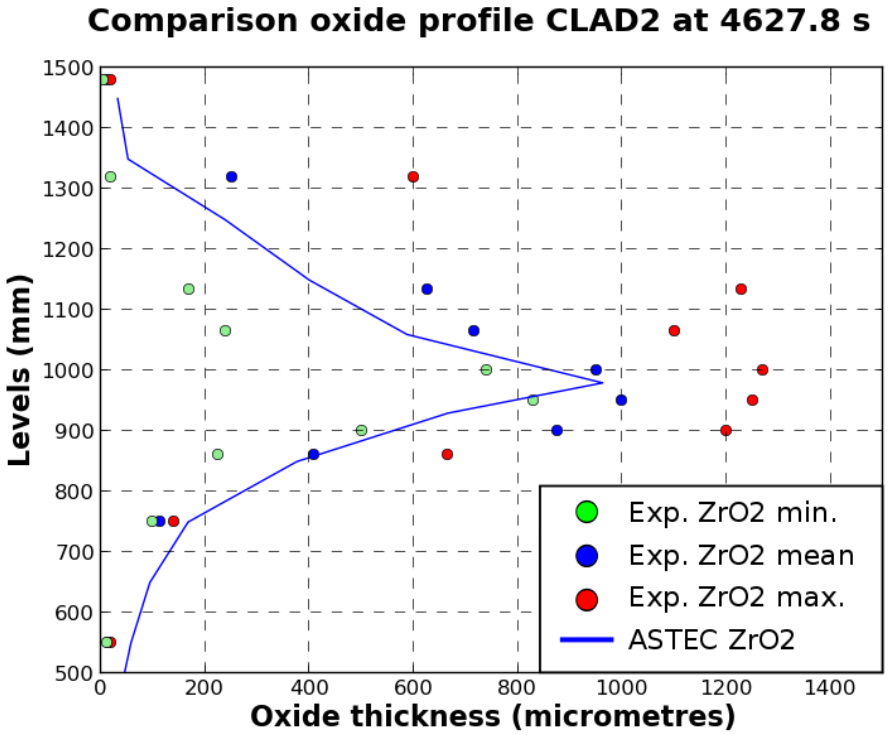

Figure 5-9: Comparison of the predicted (blue solid line) and the experimental (red (maximum), green (minimum) and blue (mean) points) oxidation layer (ZrO_2) thickness at the end of the experiment.

The global temperature and oxidation history of the bundle has an influence on the total hydrogen generation (rate), which is illustrated in **Figure 5-10**. The left ordinate represents the evolution of the total mass of hydrogen, whereas the right represents the hydrogen generation rate. A zoom for the quenching phase is shown in **Figure B.1-9**. The experimental data correspond to those obtained by the mass spectrometer. The quantities of hydrogen generated before and after reflooding are compared in **Table 5-2**. Post-test investigations of the experimental configuration have shown that the correction of the hydrogen due to the oxidation of molybdenum and tungsten [124] and due shroud external oxidation [120] are negligible.

Predictions are in accordance to the experimental values up to the beginning of the second heat-up phase (3350 s). From this point in time, ASTEC deviates from the experimental data due to the earlier entrance in the high temperature oxidation regime. Then, the hydrogen generation at reflooding time is overestimated (57.10 g ASTEC vs 46.80 g Experiment). However, after reflooding onset, the experiment registers a significant hydrogen generation compared to ASTEC (11.66 g ASTEC vs 36.80 g Experiment) due to the further oxidation at the upper part of the facility, which is hot and contains a higher extent of fresh Zry-4. In terms of hydrogen generation rate, the graph shows that both the number of peaks and their magnitude are significantly underestimated. Additionally, it shows that this rate decreases immediately after the occurrence of reflooding, differently to the experimental data.

Total H2 production (g)		**Before quenching (g)**		**After quenching (g)**	
Experiment	ASTEC	Experiment	ASTEC	Experiment	ASTEC
83.60	68.80	46.80	57.10	36.80	11.66

Table 5-2: Total hydrogen generation: ASTEC vs. Experimental data.

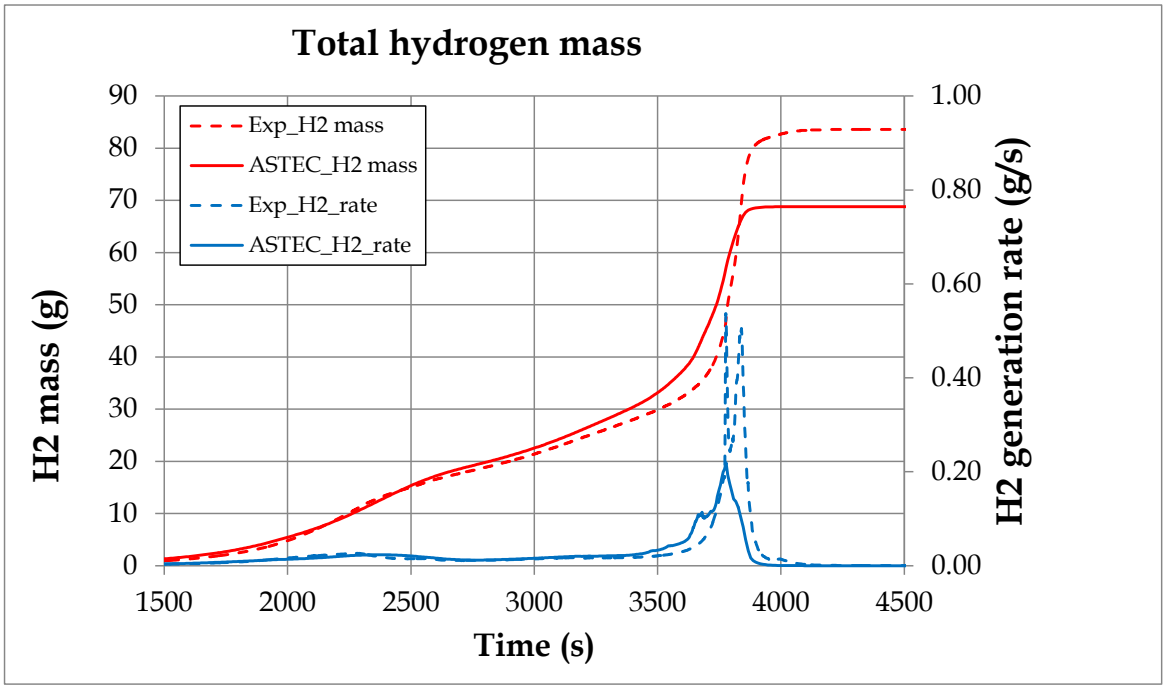

Figure 5-10: Comparison of the temporal evolution of the predicted (solid lines) and experimental (dashed lines) hydrogen generation mass (red)/flow rate (blue).

5.5 Comparison with other studies and Discussion

The calculations presented have shown the ASTECV2.0 capabilities to simulate the QUENCH-08 Experiment, although the temperature escalation during reflooding is not fully captured. The deviations occurring during the reflooding phase are originating from

deviations of the prior calculated phases (first heat-up phase and pre-oxidation phase). The first source of deviation seems to be the too small radial temperature gradient predicted in the model; the second, the inadequate reproduction of the heat transfer through the argon gap by the code.

As concerns the first factor, previous post-test calculations of other QUENCH tests using ICARE-CATHARE [105,108] have underestimated the radial temperature gradient between the inner and the outer FRSs. Therein, shroud temperatures are not shown, but it is possible that they had similar deviations to the ones described in this work. The common feature in both studies is the use of one channel to represent the fluid, which may be leading to a lower power extraction from the shroud. In contrast, calculations modelling the existence of two channels (one containing all FRSs and a bypass), such as the one performed for QUENCH-08 using ATHLET-CD [121], are able to depict the experimentally measured radial temperature gradient.

As for the modelling of the argon gap, its importance on the predicted hydrogen generation depends whether the hot region is located within the upper unheated zone or within the active height of the bundle. Within the QUENCH-08, the upper unheated region undergoes an intense oxidation and hence, plays an important role. The modelling of the argon gap remains a source of uncertainty in the QUENCH calculations. It also seems to be responsible for the heat transfer underestimation within the upper unheated zone in other studies [110,125].

This suggests that both factors are the reason for an earlier temperature escalation during the second heat-up phase in several of the aforementioned studies on the QUENCH-08 [120,121,125]. Therefore, a higher oxidation degree and hydrogen generation is predicted at reflooding onset in comparison to the experiment. This behaviour is congruent with the one presented in this work. However, those studies still predict a significant temperature escalation during reflooding, which is not observed in the present simulations.

In order to reduce the effect of these parameters on the results, further studies have been performed using ASTECV2.1 [126], these yielding the following results:

- The radial temperature gradient and the shroud temperature are better reproduced when the bundle is radially discretized in at least two channels. As a result, the temperatures of the FRSs are less underestimated at reflooding time than ASTECV2.0 predictions. This is reflected in the lower hydrogen generation before reflooding onset (see **Figure 5-11**). The inclusion of third channel next to the shroud (bypass) even allows a better reproduction of the radial temperature gradient [126]. However, the unpleasant effect is the addition of a new uncertainty to the model: the internal bypass radius.

- The influence of the argon gap has been diminished by setting a temperature boundary condition along the shroud within 1100-1300 mm. Results show a better prediction of the temperature evolution at $z > 900$ mm during reflooding. In turn, this is translated in a better agreement of the ASTECV2.1 hydrogen evolution with the experimental data compared to the results obtained with ASTECV2.0 (see **Figure 5-11**).
- The axial discretization and the outer electrical resistance (5 % around the value 7 mΩ/rod) play a fundamental role in the temporal evolution of the temperature and the oxidation prior to reflooding. Hence, they affect significantly the overall hydrogen generation rate and mass.

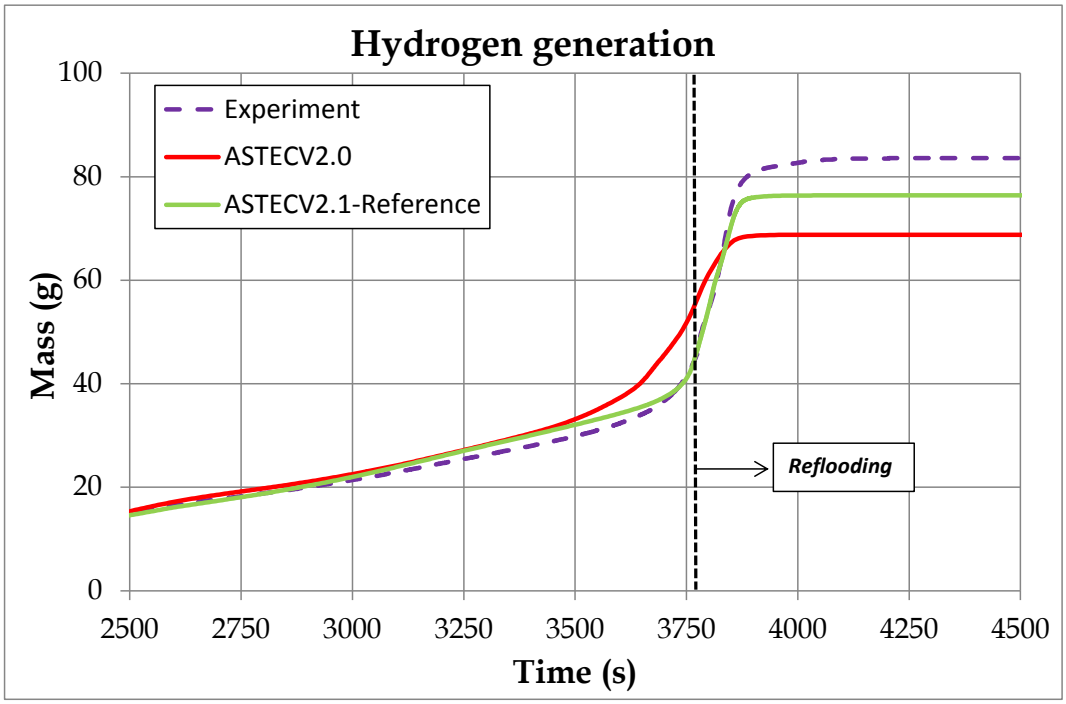

Figure 5-11: Comparison of the temporal evolution of the predicted (solid lines) and experimental (dashed lines) hydrogen generation mass. The red line corresponds to ASTECV2.0 predictions; the blue line corresponds to ASTECV2.1 predictions with two radial channels and improved modelling of the heat transfer in the argon gap at the upper unheated zone of the facility.

5.6 Summary

This chapter has demonstrated the capability of the ASTECV2.0 physical models to describe the early in-vessel phase of a SA by means of data from the QUENCH-08 experiment. For that aim, a brief description of the QUENCH facility and its ASTECV2.0 model has been given. Then, the comparison of the code predictions and the experimental data showed that the code is able to capture the key phenomena occurring in QUENCH-08. However, discrepancies have been identified, such as the underestimation of the radial temperature gradient and the overestimation of shroud temperature in the first heat-up phase.

The most important contributors to these deviations seem to be the lack of a bypass channel along the bundle as well as the underestimation of the heat transfer through the argon gap within the upper unheated part. These deviations accumulate up to to the reflooding phase, affecting the prediction of the hydrogen generation.

In the meantime, the new version ASTECV2.1 was delivered by the code developers and the test has been reanalysed using the latest modelling features. The results of ASTECV2.1 have shown a higher radial temperature gradient if a bypass channel is considered. Additionally, a more intense escalation during reflooding is observed. Hence, a better agreement of the temperature, oxidation behaviour and the hydrogen generation has been achieved between experimental data and numerical predictions.

The validation of ASTEC with data from QUENCH and other experimental facilities is essential to verify that the code is able to predict the key phenomena occurring during a SA. However, the main aim of SA codes is not to simulate pre and post-test analyses for experimental facilities, but to produce a database for the development of SAMGs. For that aim, it is first necessary to build a suitable model of the NPP under consideration.

6 Generic model of a German Konvoi PWR using ASTECV2.0

In order to extend the technical basis for the verification and development of SAM measures for a German Konvoi PWR, a model for this plant [127–129] is required at first. Details about the Konvoi PWR can also be found in **Appendix A**. This work makes use of an improved ASTECV2.0 (revision 3, patch 0) model for a German Konvoi, which is based on a generic ASTECV2.0 (revision 2, patch 0) model used by GRS in previous studies [130,131]. The improved features concern the modelling of additional safety systems and the inclusion of the existing AM procedures in a German Konvoi PWR.

The chapter starts with section **6.1**, which describes the ASTEC modelling of the vessel, the primary and secondary circuit, and continues with section **6.2**, which defines the most important control systems needed by ASTEC to reach steady state plant conditions. Then, the main steady state parameters predicted by ASTEC are compared to the operational values of the German Konvoi PWR in section **6.3**. The chapter moves then to section **6.4**, which lists the most important in-vessel physical phenomena considered in the present work. Finally, section **6.5** explains the modelling of the most important protection and safety systems, as well as the modelling of AM procedures.

6.1 Modelling of the PWR Konvoi plant in ASTEC

6.1.1 Primary and Secondary circuit

The four loop Konvoi PWR is represented by two loops, in which the loop B is connected to the pressurizer and the loop A represents the other three loops. A simplified sketch of the primary and secondary side (together with the main safety systems) is depicted in **Figure 6-1**. The discretization of the loop A is analogue to the one of loop B, except for the pressurizer and the surge line.

The primary coolant leaving the core enters the upper plenum, and from there it flows mainly through the hot legs and the upper head of the RPV. From the hot leg, the coolant flows towards the SG inlet hot box. The hot leg of loop B is connected to the pressurizer through the surge line (discretized in three volumes). The pressurizer is equipped with a Pilot Operated Relief Valve (PORV), which opens when the system pressure increases above 166 bars, and two Safety Valves (SV1 and SV2), which open for system pressures above 170 and 176 bars (see dedicated section in **Appendix C**). From the SG inlet boxes, the water rises along the SG U-tubes, divided in 15 axial cells, and descends to the outlet cold box. Then, the coolant enters the cold leg (discretized in three volumes: inlet, pump suction and outlet). The Main Coolant Pumps (MCP-A/B) are located between the pump suction and the

cold leg outlet. Finally, the primary coolant is recirculated by the MCPs to the cold leg collector (which is common for both loops), reaching this way the RPV downcomer.

Concerning the secondary circuit, 513 kg/s of feedwater at 218 °C are injected into the SG downcomer head. Then, the water descends along the downcomer (discretized in three volumes: head, middle and bottom) and enters the riser region, which has been divided in eight axial cells. The humid steam passes through the separators of the corresponding SG and the dry steam reaches the SG dome. Then, the steam passes to the Main Steam Line (MSL), where a pressure boundary condition of 63.50 bars is fixed. Each steam line disposes of one Safety Valve (SV SG-A/B) opening for secondary pressures higher than 85.80 bars. The two MSLs merge in the steam collector.

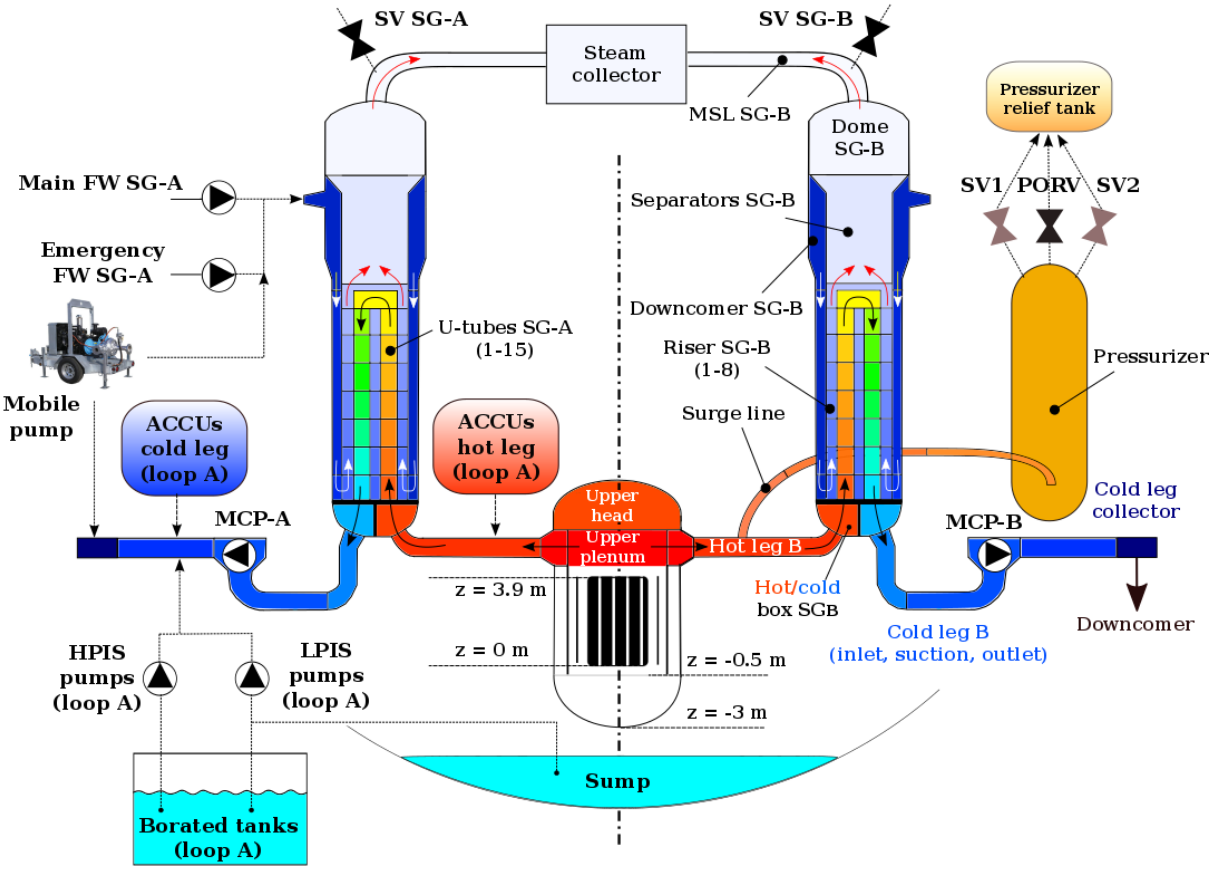

Figure 6-1: Sketch of the Primary and Secondary circuit modelling for a generic German Konvoi PWR by ASTECV2.0.

6.1.2 Reactor Pressure Vessel (RPV)

The core (fluid) region is represented by six cylindrical rings called thermal-hydraulic channels (**Figure 6-2**). Two additional channels represent the downcomer and the bypass region. In each core channel, representative fuel rods, control rods, grid spacers and plates are modelled. These are weighted according to the number of fuel assemblies in each channel.

The fuel rods consist of UO_2 pellets and Zry-4 cladding, and the control rods of SIC (Silver-Indium-Cadmium) absorber pellets, stainless steel cladding and Zry-4 guiding tube. The total mass of UO_2 and Zry-4 in the core is about 150 tons. The baffle separates the sixth channel from the bypass, and the barrel separates the bypass from the downcomer. The vessel wall and its insulation surround the downcomer. The downcomer is connected at the top to the cold leg collector and each core channel is connected at the top with the upper plenum (see **Figure 6-1**).

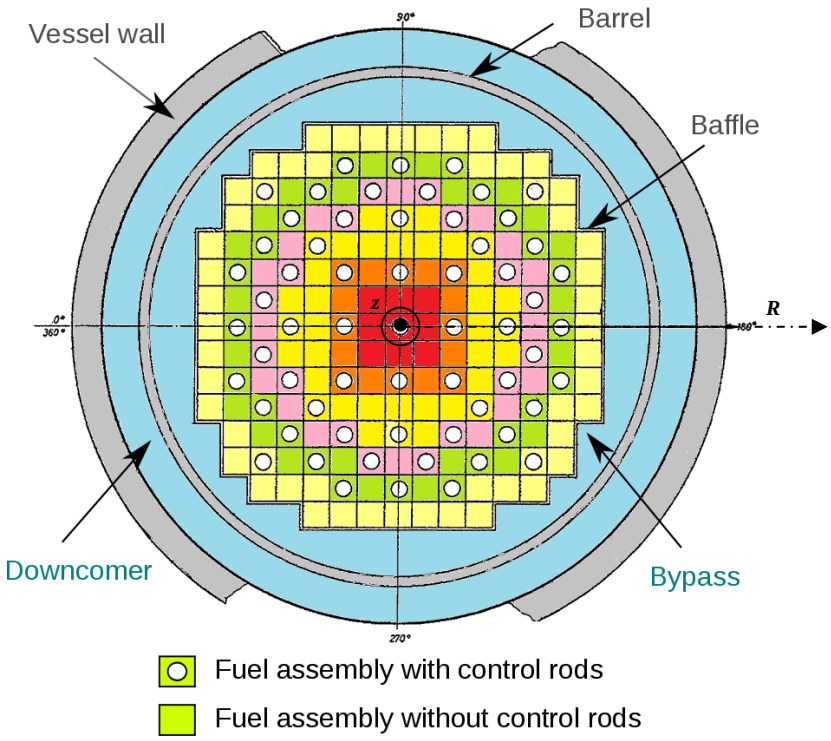

Figure 6-2: Sketch of the reactor core modelling of a generic German Konvoi PWR by ASTECV2.0 (radial view).

Concerning the axial discretization, the elements belonging to the active core zone (from 0.00 m to 3.90 m) - e.g. fuel rods, control rods, barrel - are vertically divided in slices of 300 mm i.e. 13 axial regions. Two additional nodes are placed at the bottom of the lower core support plate (-0.50 m) and at the top of the core region (4.34 m). The fluid region in the lower head cannot be radially or axially discretized and therefore, it is only represented by one cell. However, the solid domains corresponding to the wall are radially discretized in three regions and axially discretized in eight regions. The minimum elevation of the RPV lower head is - 3 m and the maximum is -0.50 m. All vessel components have an azimuthal symmetry.

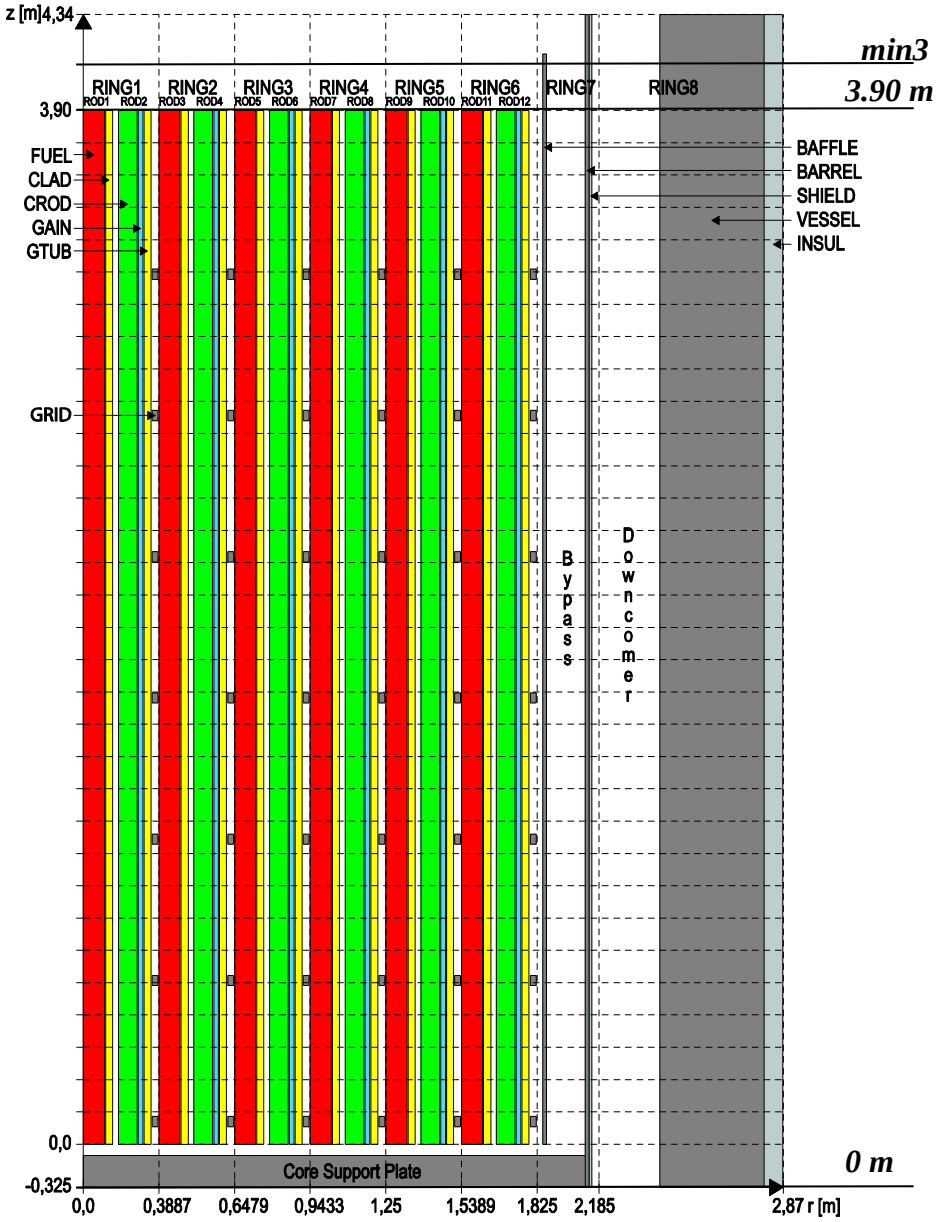

Figure 6-3: Sketch of the reactor core modelling of a generic German Konvoi PWR by ASTECV2.0 (axial view) [132].

6.1.3 Containment

The modelling of the containment is done with the CPA module, which allows the definition of control volumes to represent the compartments and to connect these volumes with junctions. The discretization of the containment and the reactor building annulus is depicted in **Figure 6-4** [130]. Alike the RCS, the containment model makes use of two symmetric halves 'A' and 'B'. The loop with pressurizer and one third of the triple loop A are assigned to part 'B' of the containment, whereas the two remaining loops are assigned to part 'A'. Heat losses from the RCS to the containment are considered by means of dedicated connections between the each loop and the respective containment half.

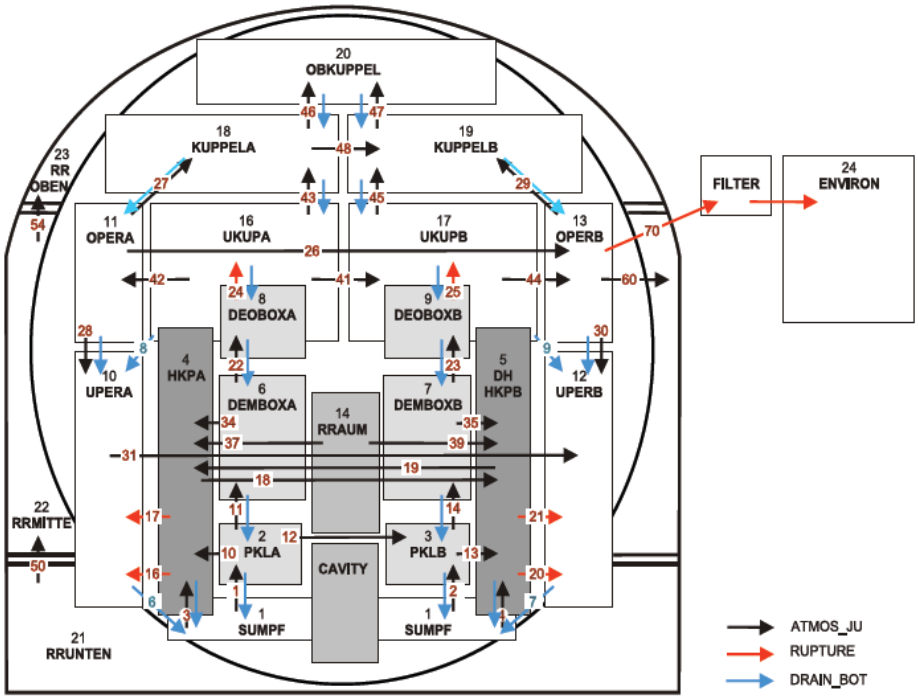

Figure 6-4: Sketch of the assignment of compartments, flow paths and connections of a generic German Konvoi PWR by the ASTECV2.0 [130] (numbers represent the number associated to the compartment, atmospheric junction, rupture junction or drainage respectively).

The PWR containment is divided into 23 zones, 11 of which are equipment rooms (marked in grey). The equipment rooms are separated from the rest of containment zones by means of rupture disks (marked in red). The following equipment rooms are considered in the model: the cavity of the reactor (CAVITY); the regions near the cold legs of the RCS (PKLA/B); the region near the hot legs, and in the case of loop B the pressurizer and surge lines (DH-HKPB, HKPA); the regions close to the middle (DEMBOXA/B) and the upper part of the SGs (DEOBOXA/B). The perimeter region, which is situated between the mobile equipment and the containment steel wall, has been discretized in two axial zones (lower is UPERA/B, and upper is OPERA/B), alike the dome (lower is UKUPA/B, middle is KUPPELA/B and upper is OBKUPPEL) and the annulus (lower is RRUNTEN, middle is RRMITTE and upper is RROBEN). The sump region (SUMPF), filled with water, has been also modelled. Finally, the environment is modelled by a large zone named ENVIRON.

Several types of flow connections are defined in the containment: atmospheric junctions (marked with black arrows) allowing the exchange of gases between two zones; rupture disks (marked with red arrows) allowing the same exchange once a user-defined pressure difference is exceeded and finally, drainages (marked with blue arrows) allowing downward flow through opening at the bottom of a zone driven by gravity. A design leakage is considered from OPERB into RRMITTE.

6.2 Steady State Control Systems

Several control systems have been defined to achieve a converged steady state solution with ASTEC. Each of those, except the ones affecting the heating and the sprays in the pressurizer, contains an expected value of a given variable i.e. value that should be obtained at the end of the simulation (e.g. mass flow rate along each loop of the RCS equal to 4700 kg/s), and the parameter that is adjusted to reach such a value (e.g. torque of the MCPs). All regulations except the sprays and the heaters are switched off as soon as the steady state is reached.

- Heating power in the pressurizer depending on the system pressure (pressure in the pressurizer volume). Additionally, spray mass flow rate in the pressurizer, which comes from the cold leg, and also depends on the system pressure. More information about these controls can be found in a dedicated section of **Appendix C**.
- Mass flow rate in the RCS: a mass flow rate of 4700 kg/s is expected in each loop according to the literature. For this purpose, a regulation modifies the torque given by the MCPs depending on the deviation of the flow rate from the expected value.
- Liquid level in the pressurizer: a liquid level of 7.85 m is expected according to the literature. For that aim, a function modifies the flow rate entering the pressurizer depending on the deviation of its liquid level with respect to this value.
- Steam mass flow rate at the outlet of the SGs: a steam mass flow rate equal to the FW mass flow rate is expected in stationary conditions. For that aim, a regulation modifies the FW mass flow rate depending on the deviation with the steam mass flow rate at the outlet of the SG. One regulation of this kind has been modelled for each SG.
- Liquid level in the SGs: a liquid level of 12.20 m is expected according to the literature. Therefore, a regulation modifies the mass flow rate provided by a fictive pump depending on the deviation of the liquid level with respect to this level. One regulation of this kind has been modelled for each SG.
- Pressure losses along the core channels: a pressure loss of 2.40 bars is expected in stationary condition. Therefore, a regulation modifies the pressure loss coefficients at the channel inlet and outlet depending on the deviation of the pressure loss with respect to this pressure value.
- Redistribution of flow between core and bypass: 3 % of the mass flow rate flowing through the core is expected to go through the bypass. Therefore, a control function modifies the pressure loss coefficient at the inlet and outlet of the bypass depending on the deviation of the bypass mass flow rate with respect to the expected value.

6.3 Verification of the ASTEC model using the reference data for stationary conditions

In order to demonstrate that the described model is representing the key plant systems and predicting the stationary plant parameters, ASTECV2.0 results are compared to the reference values in the available literature [128]. The code predictions, the reference values and the relative error between both are compared in **Table 6-1**. The relative error of the pressure at the turbine admission, the FW temperature and the nominal power is zero, because these parameters have been used as boundary conditions.

The calculated pressure in the RCS is almost identical to the reference value due to the consistent prediction of the pressurizer liquid level. The mass flow rate circulating along the RCS is also identical to the reference one thanks to the control systems introduced (see section **6.2**). However, it is not translated in a similar pressure loss through the core, which is underestimated. A possible reason for this behaviour may be that the mass flow rate is adjusted with the pump torque (see section **6.2**) and not with the core pressure loss.

The congruence in the mass flow rate along the RCS is reflected in a similar but slightly higher heat transfer rate between the RCS and the secondary side. This slight overestimation leads to a lower temperature at the vessel inlet. Additionally, the correct prediction of the flow rate through core and the bypass leads to an agreement in the core heat-up. Consequently, the slight overestimation of the temperature at the vessel inlet is directly translated to the one at the vessel outlet. Finally, the steam mass flow rate generated in the secondary side and its outlet temperature are in accordance to the reference values, and their slight overestimation is caused by the slightly higher heat transfer rate coming from the secondary side.

All relative errors corresponding to the key operational parameters are lower than 5 %. The greatest error is the pressure loss through the reactor core (4.13 %). Further analysis is needed to evaluate why the deviation on the pressure loss is much different to the other parameters. Despite this, the results obtained by ASTECV2.0 demonstrate that the code is capable of reproducing the key operational plant parameters.

Name of parameter	Unit	Literature	ASTECV2.0	Rel. Error (%)
Pressure in RCS	bar	157.00	157.11	0.07
Liquid level in pressurizer	m	7.85	7.86	0.18
Temperature at vessel inlet	°C	291.30	290.38	-0.31
Temperature at vessel outlet	°C	326.10	325.19	-0.28
Core heat-up	°C	34.80	34.81	0.01
Pressure loss through RPV	bar	2.40	2.305	-4.13
Thermal power reactor	MWth	3765.00	3765.00	0.00
Mass flow rate along RCS	kg/s	18800.00	18800.10	0.00
Mass flow rate RCS loop A/B	kg/s	4700.00	4700.01	0.00
Mass flow rate along bypass	kg/s	564.00	564.00	0.00
Heat transfer in SGs	MWth	3782.00	3786.23	0.11
Heat transfer in each SGA/B	MWth	945.50	946.64	0.12
Steam mass flow rate	kg/s	2052.00	2053.23	0.06
Steam mass flow rate SGA/B	kg/s	513.00	513.36	0.07
Pressure turbine admission SGA/B	bar	63.50	63.50	0.00
Feedwater temperature SGA/B	°C	218.00	218.00	0.00
Outlet steam temperature SGA/B	°C	279.25	279.59	0.12

Table 6-1: Key plant parameters of the Konvoi PWR in steady state: ASTECV2.0 vs Literature [128].

6.4 Extensions of the ASTEC integral PWR model for the simulation of SAs

For the study of SA scenarios, physical models describing the key phenomena of SAs need to be activated. Since this work focuses on the investigation of in-vessel scenarios, all ASTEC modules dealing with ex-vessel severe accident phenomena (RUPUICUV, MEDICIS and the COVI and FRONT modules of CPA) have not been used. The decay of the FP inventory is considered through a power boundary condition (see below). Consequently, all ASTEC modules dealing with FP release (ELSA), transport and deposition either in the RCS (SOPHAEROS) or in the containment (CPA-AFP) are not activated.

Hereafter, the key in-vessel physical phenomena considered in the present work are listed:

- Heat transfer: axial and radial conduction, convective exchange with fluid. The radiative heat exchange among intact and through damaged core structures is calculated according to [104]. The decay heat generated in the fuel rods has been introduced as a boundary condition in time, according to previous calculations of GRS, and distributed throughout the core according to axial and radial peaking factors.

- Chemical interactions: oxidation of Zry-4 by steam according to the best fit correlation [103], oxidation of stainless steel by steam, dissolution of UO_2 and ZrO_2 by molten Zry, cladding dissolution by molten material when the cladding temperature is greater than 2300 K and the ZrO_2 thickness lower than 250 μm [48], interactions among Zr-Ag-Fe-In (guiding tubes and steel claddings for control rods, grid spacers and claddings), oxidation of the relocating molten mixture (U-O-Zr) according to [133].
- Movement of materials: relocation of molten material according to [104] and its eventual slump from the core region into the lower plenum. Corium stratification is modelled in the lower plenum, the segregation being handled by a simplified separation model, which assumes that oxidic and metallic species can move to adjacent layers depending on their density with respect to the layer where they are embedded in, as well as on the density of the adjacent corium layers [114].
- Mechanical behaviour: ballooning and burst of the cladding leading to FP release. The failure of the Reactor Pressure Vessel occurs when the average temperature, stress or molten material of the vessel wall components at a given height exceed threshold values, or due to plastic or creep failure according to the Combescure model [116].

6.5 Protection Systems, Safety Systems and SAM actions

Safety systems must be also included in the model for the investigation of accidental scenarios. All automatic actions undertaken by the Reactor Control Protection System (RCPS) following a transient sequence are listed hereafter.

- SCRAM (reactor shutdown) is triggered by the RCPS when the pressure in the RCS is lower than 132 bars, or when the overpressure of the containment exceeds 30 mbar.
- Following SCRAM, the turbine stop valves are closed blocking the steam flow to the turbine and the FW pumps are shut down so that no FW is injected into the SGs. Furthermore, if those two conditions are fulfilled simultaneously, the reactor is cooled down at a rate of 100 K/h through the cooldown of the secondary side.
- The ECCS is activated when two of the following three conditions are fulfilled: overpressure in the containment above 30 mbar, pressure in the pressurizer below 110 bars or liquid level in the pressurizer below 2.30 m.
- Following the ECCS criterion, the MCPs are coasted down and the pressure regulation in the pressurizer is switched off (heaters and sprays do no longer operate).

Once the automatisms of the model have been described, this section moves on to explain the main modelling features of selected safety systems. More details can be found in the dedicated **Appendix C**.

Water injection into the SGs is assumed to occur only by means of active systems i.e. the Emergency Feedwater System (EFWS). The EFWS consists of four trains, each of them

injecting up to 35 kg/s into the downcomer head of the SGs (see **Figure 6-1**). The EFWS is activated when the liquid level of one SG falls below 4.50 m (relative to the bottom of the riser region), and injects water up to covering of the SG U-tubes of the primary side. Passive injection coming from the FW piping system and the FW tank (see section **3.3.1.1**) has not been considered following a conservative approach.

The EBS consists of four trains that take water from specific borated tanks with a capacity of 18 m^3 and inject it with a constant mass flow rate of 2 kg/(s train) in the cold legs of the RCS. The system is activated as soon as the pressurizer water level falls below 2.30 m (relative to the bottom of the pressurizer).

The ECCS consists of passive (ACCUs) and active (LPIS and HPIS) safety systems. The ACCUs discharge up to 30 tons of borated water at an initial pressure 25 bars into the hot and cold legs of the RCS. Each train of the HPIS injects up to a maximum of 75 kg/s into the RCS below 110 bars, whereas each of the LPIS injects up to 150 kg/s below 12 bars. Each train of the HPIS and the LPIS takes water from a different borated water tank with a capacity of 480 m^3. Trains injecting in the same loop take water from the same borated tank. Details about the mass flow curves of the HPIS and LPIS pumps as a function of the RCS pressure can be found in **Appendix C.** Moreover, the following assumptions have been made:

- Injection via the HPIS and the LPIS occurs in the cold leg collector of the RPV (see **Figure 6-1**). Despite the HPIS and the LPIS also inject borated water into the hot legs of the RCS in the real plant, this assumption is taken due to the ASTECV2.0 limitations regarding top reflooding (see sections **4.3** and **4.4.4**).
- Active safety systems injecting in loop B are assumed to be unavailable.
- The aspiration of the LPIS is changed from the borated tanks to the containment sump if the water inventory of the borated tanks is lower than 5 m^3 and the pressure conditions in the reactor allow the use of the LPIS. The HPIS cannot be used in sump recirculation mode.

The Chemical Volume Control System (CVCS) has not been modelled in the present work, but it may inject up to 12 kg/(s train) up at a very high pressure head.

An external water injection into the cold leg collector or into the downcomer head of the SGs has been also included as an alternative injection in the primary and secondary circuit (see **Figure 6-1**). This injection is possible by means of different mobile pumps, which are powered by an own diesel generator (DG). The name of the mobile pumps used in this work, their type (low pressure, medium pressure, and high pressure), the nominal mass flow rate, the pressure head and the injection location is enclosed in **Table 6-2**. Further information about these systems is available in [134,135]. A dedicated section of the **Appendix C** explains the

process followed to introduce these characteristic curves in ASTEC. Core recriticallity is neglected despite the injection of unborated water.

Equipment name	Pressure Type	Flow rate (kg/s)	Head (bar)	Location
HH80 [136]	Low	30	10	RCS, Steam Generator B (SGB)
HH125 [137]	Low	45	10	RCS
AE16G [138]	Low	100	6	RCS
AE18G [138]	Low	130	7	RCS
M403l [139]	Medium	4	20	SGB
M651lpr [139]	Medium	10	20	RCS, SGB
M100l [139]	Medium	15	20	SGB
XH100 [140]	Medium	60-80	18	RCS
M651h [139]	High	22	50	RCS
M100h [139]	High	40	45	RCS

Table 6-2: Mobile Equipment relied upon for an external injection in the Primary and Secondary circuit (final "l/h" in the name of the equipment indicates if the system is of low/high pressure).

Up to this point, the key (safety) systems included in plant model have been described, some of them injecting diverse mass flow rates in the reactor and being powered by diverse power supply types. Therefore, it is convenient to summarize this information in **Table 6-3** for a better understanding of the subsequent chapters. The table represents main features and the power supply required for each safety system. As indicated therein, most of the safety systems are unavailable during an AC supply loss (Station Blackout).

Finally, it is convenient to describe the hypothesis assumed when modelling two of the most important AM measures used in the current work:

- SBF is modelled by opening the Safety Valve of the corresponding SG (SV SG-A/B) when the liquid level in all SGs falls below 4 m (relative to the bottom of the riser region), or when the AC power supply is lost for more than 20 min (see section **3.3.1.1**). The passive injection from the FW tank and from the FW pipes is not considered.
- PBF is modelled by opening the valves PORV, SV1 and SV2 at CET=400 °C. This criterion is slightly different to the one stated in section **3.3.1.2** in the sense that it omits the additional condition of liquid level lower than *min3* (15 cm above active core height). This represents a scenario where the measurement of the liquid level is unavailable.

Name	Requires AC	Requires DC	Main features
Main FW	Yes	No	
MCPs	Yes	No	
EFWS	Yes	No	Up to 35 kg/s, high pressure head
LPIS	Yes	No	Up to 150 kg/s/train; Head:12 bars
HPIS	Yes	No	Up to 75 kg/s/train; Head 110 bars
EBS	Yes	No	Up to 8 kg/s, high pressure head
CVCS	Yes	No	Up to 12 kg/s/train, high pressure head
ACCUs	No	No	30000 kg at 25 bars
PORV PRZ	No	Yes	Area: 20.00 cm^2
SV1/2 PRZ	No	Yes	Area: 38.50 cm^2
SVA/B SGs	No	Yes	Area: 660.0 cm^2

Table 6-3: Main features and type of power supply required by each safety system implemented in the generic ASTECV2.0 model of the German Konvoi PWR.

6.6 Summary

This chapter has described the generic ASTECV2.0 model of the German Konvoi PWR, and verified the predictions on key plant operational parameters at steady state by comparing them to the reference plant values. In the model, CESAR is used to build the RCS and secondary circuit, while ICARE is used to build the RPV geometry. In addition, CPA represents the geometry of the containment. Several control functions have been introduced to obtain a converged prediction of the steady state parameters. In this context, the key in-vessel SA phenomena considered in the ASTEC plant model have been exposed. Finally, the general features of selected safety systems considered in the model aiming at preventing, mitigating or delaying the severe accident have been described.

At this stage the generic ASTECV2.0 model of the German Konvoi PWR is ready for the analysis of the in-vessel phase of selected severe accident scenarios.

7 Simulation of Severe Accidents without AM in a German Konvoi PWR using ASTECV2.0

In order to verify, improve and develop SAM strategies, it is first necessary to understand the progression of accidental sequences without AM. The selection of sequences is based on the outcomes of the PSA of the German Konvoi PWR. This way, improvements on SAM can be directly translated into a reduction of the risk of core damage (PSA-1) and the risk of a radiological release to the public (PSA-2).

PSA studies performed on the Neckarwestheim Konvoi PWR (GKN-2) have shown that the risk of core damage is dominated by Small Break LOCAs (SBLOCA) in the Main Coolant Line (MCL) (52 %), the pressurizer leak via a stuck-open safety valve (15 %), the Loss of Offsite Power (LOOP) (10 %) and SGTR (9 %). On the other hand, the risk of FP release is dominated by uncovered SGTR (rupture located above water level in the SG) and sequences leading to RPV failure at high pressures (Loss of Feedwater (LOFW) and LOOP) [27]. These statements have been confirmed in a recent re-evaluation [141].

Taking into account these previous investigations, the current chapter studies the following sequences in a German Konvoi PWR using ASTECV2.0:

- Medium Break LOCA (MBLOCA) of 440 cm^2 in the cold leg of the pressurizer loop, which is not risk-significant for plant, but is simulated to test ASTEC capabilities.
- SBLOCA of 10 cm^2 at the same location, relevant for the PSA-1.
- SBO (entailing LOOP and LOFW), relevant for the PSA-2.

The block of automatic actions described in section **6.5** applies for all sequences analysed in this chapter, except if the hypotheses of the sequence exclude the intervention of a system. For each sequence it is considered that the plant undergoes SBO (LOOP together with the loss of Diesel Generators (DGs)) at a given stage of the accident, in consonance with the lessons learnt from Fukushima [8,9]. From that moment on, all active systems are considered unavailable, and only systems powered by DC can be used (see **Table 6-3**). The following additional hypotheses have been made:

- No AM measures are applied during the transient.
- No failure of the surge line due to high temperatures is considered.
- The MCPs are sealed and hence, there is no leakage from the RCS.
- No thermally induced SGTR is modelled.

For each scenario, the ASTECV2.0 prediction of the in-vessel phase is analysed and compared to the results obtained by other institutions with other SA codes. The evolution of the plant parameters for each SA scenario can be found in **Appendix D**.

7.1 MBLOCA in the cold leg of the pressurizer loop combined with SBO

The reference sequences analysed in this section postulate a MBLOCA (440 cm^2) in the cold leg outlet of the pressurizer loop at 0.00 h (see **Figure 6-1**). Besides, the loss of AC power is assumed at a certain time after SCRAM. The sequences are identified with (*MBLOCA-) ACXh*, where *X* is the time when the AC power is lost since SCRAM (in hours). All sequences consider the failure of the automatic 100 K/h reactor cooldown procedure and the intervention of 3 out of 4 LPIS trains. The intervention of the HPIS has not been considered due to the large break size.

7.1.1 MBLOCA with SBO 1 h after SCRAM

The sequence assumes that SBO occurs 1 h after SCRAM. The sequence is identified with (*MBLOCA-) AC1h*. The evolution of pressures in selected control volumes, mass flow rates injected by selected safety systems or exiting the break and relevant heat transfer rates in the reactor is depicted in **Figure 7-1** as a function of the time after SCRAM. Additional plant parameters are illustrated in **Figure D.1-1** and **Figure D.1-2**. The coloured vertical lines mark occurrence times of major events in the simulation. The summary of events occurring in the simulation relative to the break opening is shown in **Table D.1-1**. The simulation yields the following temporal evolution:

Just after the break, the primary circuit starts to depressurize and reaches saturation conditions. From this moment on, the water inventory starts to evaporate throughout the RCS, the pressure being constant and equal to the one of the secondary circuit during a short period of time (up to about 0.08 h). After RCS has been much voided, the steam is quickly released through the break and hence, there is a sharp decrease of the pressure in the RCS.

The ACCUs and the LPIS, which injects water coming from the borated tanks and from the sump as long as AC power is available, are able to fill the cold legs of the reactor core. These injections even manage to decrease the void fraction in the hot legs before the loss of AC power (0.90 h and 0.95 h). The peak in the void fraction of the hot legs at about 0.95 h occurs during the switch to the sump recirculation mode, since the global mass flow rate injected by the LPIS is lower than the maximum that it could give i.e. 150 kg/s.

After SBO, the regions close to the hot legs reach again saturation, this causing a decline of the core liquid level. The heat transfer from the core to the steam is reduced due to the poor heat transfer coefficient. As a result, the core heats up and the CET (gas temperature in the upper plenum) rises above 650 °C. In turn, this causes cladding heat-up acceleration due to the exponentially increase of the oxidation rate by temperature. For the core regions where PCTs are greater than 2500 K, the outer ZrO_2 layer reaches its melting point and the molten material, composed of U-Zr-O, is released into the channel.

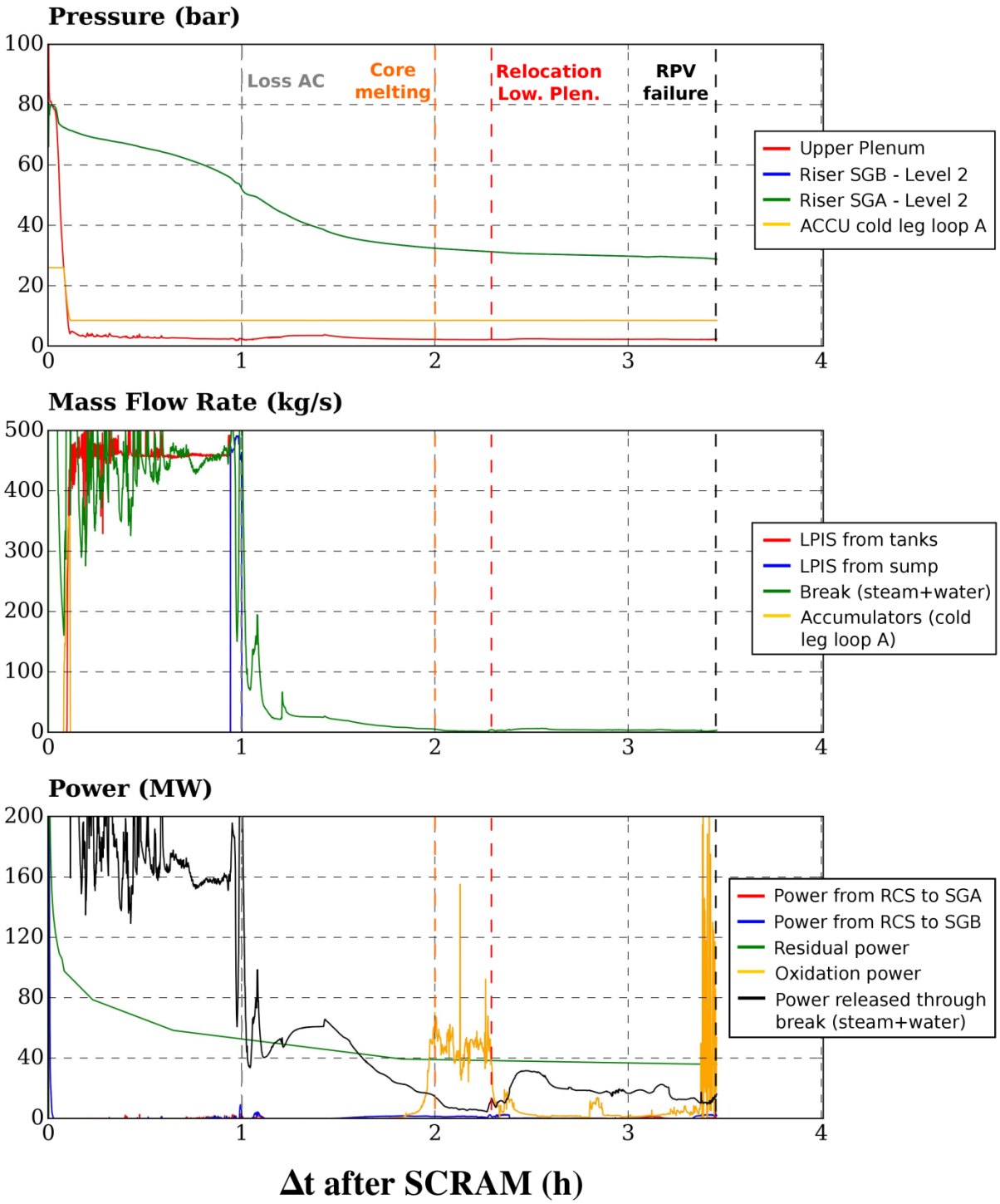

Figure 7-1: Evolution of pressures (in selected control volumes), mass flow rates (given by relevant safety systems or exiting through the break) and relevant heat transfer rates during *MBLOCA-AC1h* as a function of Δt after SCRAM. Major events of the simulation are represented by dashed vertical lines.

The initial hot spots spread out within the core and generate more molten material, which relocates downwards and potentially falls into the LP. The first slump into the LP occurs at 2.27 h. A first massive slump (about 20 corium tons) is computed at 2.38 h. The material relocated into the slump cell mainly consists of UO_2 (from the fuel rods), ZrO_2 (from claddings and guide tubes) and steel. The molten steel is distributed to the metallic layer, and is segregated into its constituent elements (Fe, Cr and Ni), whereas UO_2 and ZrO_2 are distributed to the oxidic layer. The metallic layer initially shows an increase of UO_2 and ZrO_2. However, these elements are rapidly transported to the oxidic layer due to the higher density of the oxide phase than the metallic one within the metallic layer.

Despite a significant quantity of the material is distributed from the slump cells to the different layers, a small amount of UO_2 and Fe remain in the core region. These are smoothly delivered to the oxidic and metallic layer up to 3.30 h, when a second major relocation occurs. Before that, the RPV wall components in contact with the metallic corium layer start to heat up, because of decay heat transferred to it by the lower oxidic layer.

The second corium slump (15 tons) occurs at about 3.30 h and consists of α-Zr (O) (claddings and guide tubes), FeO (oxidized baffle and internals), ZrO_2 and UO_2. Alike the previous slump, the materials are first allocated in the metallic layer (at the top), and then to the oxidic layer (at the bottom) depending on their densities. Although the α-Zr(O) is a slightly oxidized element, its density is lower than the one of the metallic species within the metallic layer, and hence, it remains within the oxidic one.

In the absence of SAM actions, the hot spot of the RPV wall keeps heating-up, leading to a decrease of the ultimate stress and causing a plastic failure of the RPV at about 3.50 h.

7.1.2 MBLOCA sequences with different times of SBO

Additional sequences with other SBO times (from 0 to 4 h) have been simulated with the same hypotheses as in section **7.1.1**. The sequence *AC0h* considers that SBO occurs before the LPIS manages to inject into the RCS, whereas the *AC1h* assumes that the LPIS works up to some seconds after the borated water tanks are emptied. The occurrence times of main events are in **Figure 7-2** as a function of the relative time since the loss of AC power.

Simulation results show that there is a time window of about 1 h to avoid core melting if the LPIS manages to inject the inventory of the borated tanks (i.e. if SBO occurs later than 1 h after SCRAM). Besides, the later the plant enters in SBO, the broader the relative time span to prevent corium relocation into the LP and a subsequent RPV failure. This is related to the decrease of the residual power for late AC power losses. Regarding the relocation to the lower plenum, a lower decay heat causes a lower heat-up and hence, a higher oxidation degree of

the bundle is permitted. As a result, the corium has a higher oxidic fraction and the melt progresses slower to the LP compared to the cases with early AC losses. As concerns RPV failure, the lower decay power generated in the oxidic layer is translated into lower heat transfer to the metallic layer and hence, a longer time interval for the RPV wall to heat-up and fail.

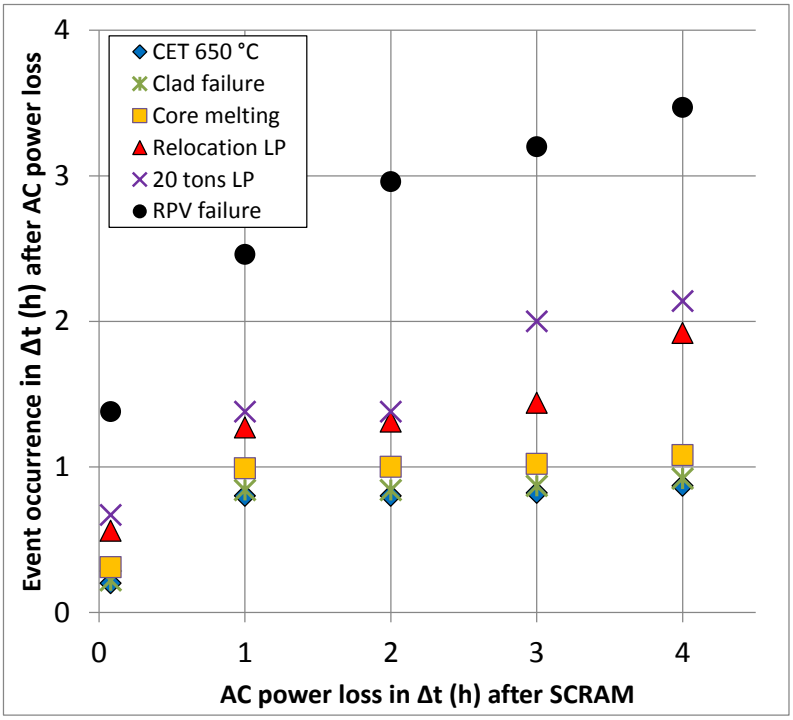

Figure 7-2: Occurrence time of main events for selected MBLOCA sequences (relative to the loss of AC power) as a function of the AC power loss (relative to SCRAM).

7.1.3 Comparison with other studies and Discussion

As the simulations indicate, MBLOCA sequences can be controlled as long as the LPIS injects coolant into the RCS. Otherwise, core cooling becomes compromised and ends up in RPV failure. Additionally, the SBO time strongly influences the SA progression, especially the time to RPV failure (e.g. time elapsed since SBO and RPV failure is 1.50 h for SBO at 0 h after SCRAM, and 2 h for SBO at 4 h after SCRAM). In order to extract the maximum time to prevent a RPV failure after AC loss, it would is necessary to perform further MBLOCA calculations with later SBOs, and to analyse for which time RPV failure would remain invariable.

It is especially interesting at this point to verify if ASTEC predictions for the selected MBLOCA sequences are similar to those obtained with other SA codes. The main difficulty to attain this goal is the scarcity of literature on MBLOCAs. Besides, previous simulations on this scenario have usually postulated the break in the hot leg of the pressurizer or the surge line [142]. The only reference is the ATHLET-CD V3.0 preliminary analysis on a Large

Break LOCA (LBLOCA) in the cold leg of the pressurizer loop [143]. The ASTEC sequence selected for comparison is *(MBLOCA-) AC0h*, due to its similarity to the aforementioned study. The differences between both sequences are the break size and the decay heat. The occurrence times of main events for both sequences is compared in **Table 7-1**.

Event	ASTEC (s)	ATHLET-CD (s)
SCRAM	4	0
Accumulator discharge	280-414	71-200
Begin of core melting	1433	1693
Corium slump into the LP	2306	3194
RPV failure	5255	-

Table 7-1: Comparison between ASTECV2.0 and ATHLET-CDV3.0 [143] on the scenario *(MBLOCA-) AC0h*.

It can be observed that ATHLET-CD calculates a rapid depressurization of the RCS compared to ASTEC. This occurs due to the short thermo-dynamical coupling between the primary and the secondary circuits after the break (200 s). Afterwards, the RCS pressure decreases sharply and the ACCUs inject water during the same time span as in the ATHLET-CD simulation. Both codes predict a similar order of magnitude in time for the onset of core melting. Likewise, corium relocation occurs earlier in ASTEC. Deviations are likely originating from the different decay heat assumptions. Although the calculation with ATHLET-CD offered a value for RPV failure, the used version could not handle adequately the behaviour in the LP and hence, it has been ruled out. However, the time to RPV failure predicted by ASTEC is of the same order of magnitude than other Medium and Large Break LOCA simulations in the hot leg of the pressurizer simulated with MELCOR [142].

7.2 SBLOCA in the cold leg of the pressurizer loop combined with SBO

The reference sequences analysed in this section postulate a SBLOCA (10 cm^2) in the cold leg of the pressurizer loop at 0.00 h. Alike section **7.1**, the break occurs at the cold leg outlet region of the pressurizer loop. It is assumed that all active systems except the LPIS are available and that the 100 K/h reactor cooldown fails. Only 3 of 4 HPIS trains are assumed to be available (the other is supposed to be under maintenance). The analysis is divided in two parts: SBLOCA with unlimited AC power availability (section **7.2.1**) and admission of different SBO times after SCRAM (section **7.2.2**).

7.2.1 SBLOCA with unlimited AC power

This SBLOCA sequence assumes the availability of AC during the whole transient, and is identified with (*SBLOCA-) Ref*. The evolution of pressures in selected control volumes, mass

flow rates injected by selected safety systems or exiting the break and relevant heat transfer rates in the reactor is depicted in **Figure 7-3** as a function of the time after SCRAM. Additional plant parameters are illustrated in **Figure D.2-1**. The coloured vertical lines mark occurrence times of major events in the simulation. The summary of events occurring in the simulation relative to the break opening is shown in **Table D.2-1**. The simulation yields the following temporal evolution:

After the break opening, the containment pressure rapidly increases to 30 mbar, leading to SCRAM. Afterwards, the RCPS initiates a turbine trip, which triggers the stop of FW injection into the SGs and the closure of steam admission to the turbine. Meanwhile, the pressurizer reaches saturation conditions and its liquid level decreases below 2.30 m, which causes the activation of the EBS. Thereby, the RCPS (1) coasts-down the MCPs, (2) stops the pressure regulation in the pressurizer and (3) activates the ECCS active systems (HPIS).

The performance of the HPIS is limited during the first minutes (50-70 kg/s), since the pressure in the RCS is still high (100 bars), and does not manage to compensate the loss of inventory through the break. Then, the pressure continues down to 75 bars. From that point in time, the HPIS is able to compensate the loss of water inventory through the break (110 kg/s) and hence, the pressure of the RCS is constant. Meanwhile, the pressure in the secondary circuit decreases due to steam condensation caused by the forced circulation of subcooled water through the primary side of the U-tubes. Hence, the depletion of water inventory in the secondary side of the SGs is reduced.

The thermal equilibrium of the RCS is maintained as long as the HPIS injects water into the circuit. However, when the borated tanks are empty at ca. 4 h, the RCS starts losing inventory through the break and the pressure falls below 25 bars. At this pressure, the ACCUs start injecting cold water into the RCS yielding a core cooldown. However, when these have been emptied, the decay power cannot be removed through the SGs and the break. Consequently, the RCS pressure builds up at about 4.50 h.

During this pressure increase, the volumes near the core outlet (upper plenum and hot legs) reach saturation. Moreover, the temperatures start to increase, hindering steam condensation in the U-tubes. The lower flow rate through the loop A than through the loop B leads to an earlier dry-out of the SGA primary side. When the dry-out occurs (at about 6.50 h in SGA and 7.50 h in SGB) the void fraction at the entrance of the cold leg jumps to 0.25. The reason for this is an insufficient heat removal. The void fraction in these volumes remains constant because the steam, which is flowing from the core to the break, blocks the water flow from those volumes to the break.

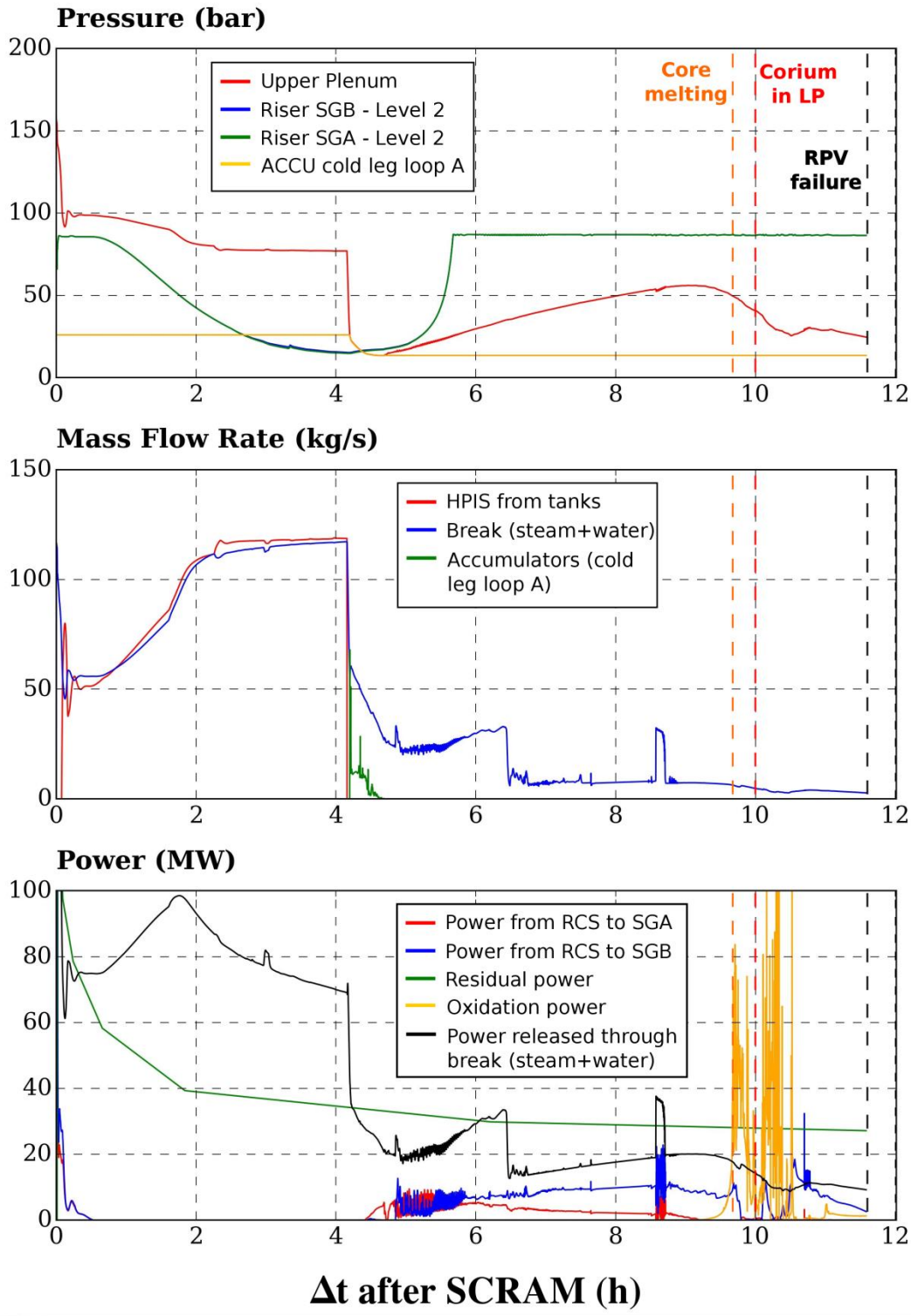

Figure 7-3: Evolution of pressures (in selected control volumes), mass flow rates (given by relevant safety systems or exiting through the break) and relevant heat transfer rates during *Ref-SBLOCA* as a function of Δt after SCRAM. Major events of the simulation are represented by dashed vertical lines.

Afterwards, the coolant in the cold leg volumes reaches saturation, resulting in a sharp void fraction increase at 8.50 h. The increased steam production leads to enhanced circulation

through loops A and B, which eases the condensation in the U-tubes (see void fraction decrease in the cold legs up to 9.50 h). Later on, a large amount of steam is evacuated through the break and the circulation through loops A and B is vanished. This again leads to a void fraction increase in the cold legs. As soon as the condensation in the SGs is stopped at about 8.20 h, the core liquid level starts to decrease causing a core uncovery.

As a result, the core temperature increases, first due to the decay heat and then, after about 9.50 h, due to the reaction enthalpy caused by the exothermic Zry oxidation with steam. In the absence of AM, the SA continues its progression, with the release of U-Zr-O mixtures into the core shortly after CET exceeds 650 °C, their relocation into the LP (the first at 10 h and containing a few tons; the second 30 min later and containing 20 tons) and a subsequent RPV failure at 11.50 h.

7.2.2 SBLOCA sequences with different times of SBO

Based on the SBLOCA sequence with unlimited AC power availability, the aim now is to investigate the behaviour of the reactor if a SBO occurs. The loss of AC power is assumed to occur at 1 h and 6 h after the SCRAM. The sequences are identified with *(SBLOCA-) AC1h* and *AC6h*. The computed evolution of the system pressure, the core and the liquid level in the Steam Generator B for *AC1h* and *AC6h* are shown in **Figure 7-4** together with the reference sequence with unlimited AC power. The evolution of key plant parameters for the sequence *AC1h* is illustrated in **Figure D.2-2** and **Figure D.2-3**, whereas the summary of events can be found in **Table D.2-2**.

For *AC1h*, the EFWS does not manage to inject water into the SGs, since the set point is not reached (see section **6.5**). As a result, the SGs cannot cool down the RCS, which is maintained at high pressures until the reactor is fully voided. For this case and for all cases undergoing SBO before the onset of the EFWS (at about 2.51 h), the core degradation progresses fast and ends with RPV failure at high pressure (50 bars).

The accident progression is slowed down if SBO occurs after one of the SGs has been filled e.g. *AC6h*. In this case, as soon as the EFWS injection is stopped, the heat transfer from the primary to the secondary circuit is deteriorated, which leads to less condensation in the RCS and hence, a higher increase of pressure than the reference case. However, steam condensation manages to significantly delay the entrance in core degradation. The cooling effect of the secondary side also allows limiting the RCS pressure peaks occurred after reaching saturation in the hot and cold legs.

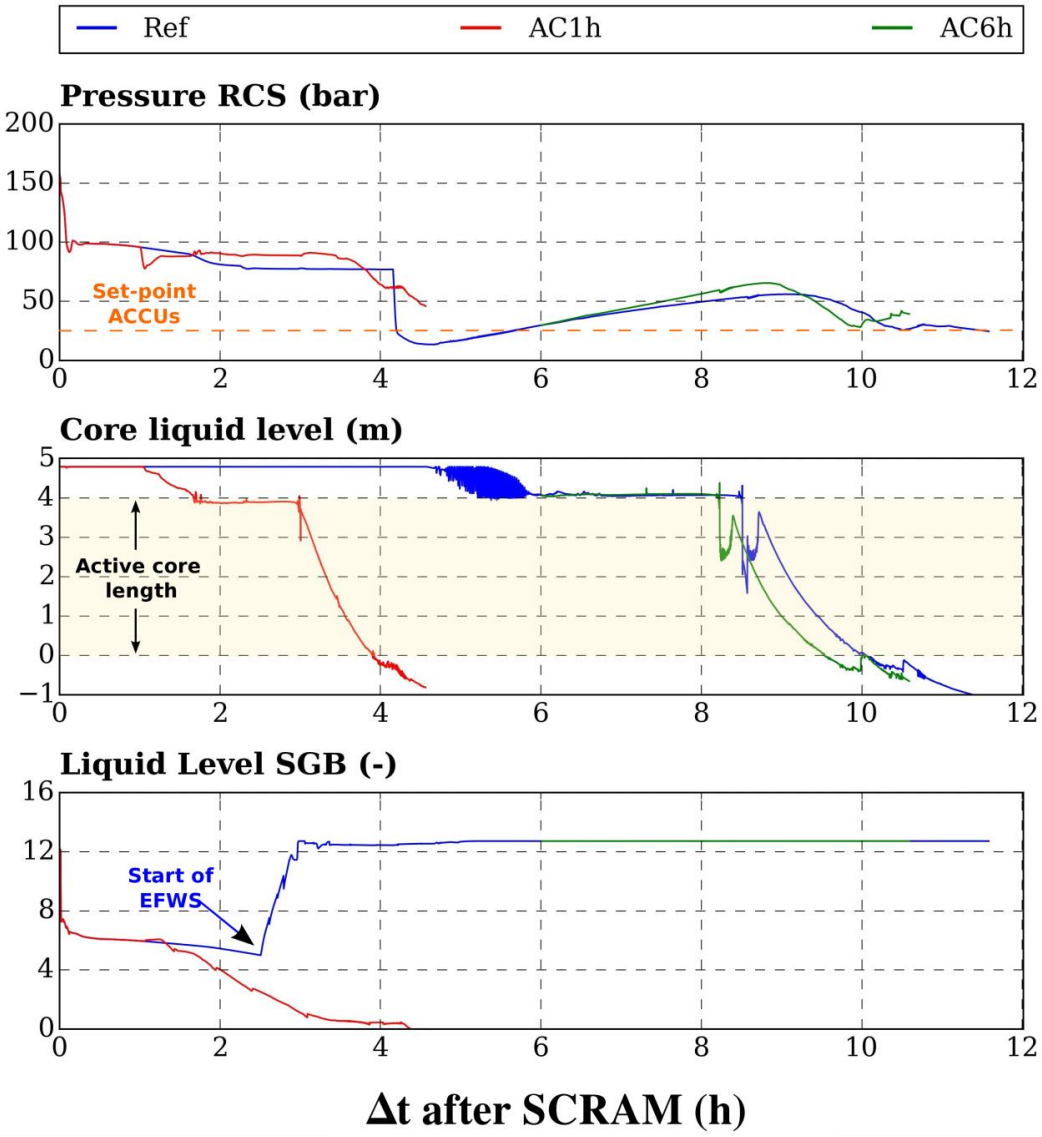

Figure 7-4: Evolution of the RCS pressure, the core and the SGB liquid level (relative to the bottom of the active core and to the bottom of the riser region in SGB respectively) during SBLOCA sequences without (*Ref*) and with SBO (*AC1h* and *AC6h*) as a function of the Δt after SCRAM.

7.2.3 Comparison with other studies and Discussion

Results have shown that, in the absence of AM, SBLOCAs lead to core degradation after the unavailability of the HPIS. If the plant is additionally struck by an SBO, the time when this happens has been shown to be relevant for the SA progression, as described in section **7.1**. However, in this case the influence of the SBO time is more significant, since it has an impact on the liquid level in the secondary side and hence, on the global energy balance in the reactor.

In the following, a comparison is made between ASTEC predictions and the results obtained by MELCOR 1.8.4 [144]. The ASTEC sequence selected for the comparison is

(*SBLOCA-) Ref*. The sequences are identical in the sense that they consider a leak of 10 cm^2 in the cold leg outlet of the pressurizer loop and the failure of the 100 K/h cooldown. In ASTEC simulations the intervention of the EFWS and the availability of 3 out of 4 HPIS trains are considered, while in the MELCOR simulations they are not. Despite these divergences, a qualitative comparison can be made. The occurrence times of the main events predicted by those codes can be found in **Table D.2-3**.

The comparison shows that ASTEC and MELCOR predict a similar transient evolution. The operation of the HPIS is shorter in ASTEC, because one HPIS train is assumed unavailable. Later on, the ACCUs inject into the RCS over the same time window. Despite the ACCUs are depleted earlier in ASTEC, core degradation starts later. This is caused by the cooling effect of the SGs on the RCS, in contrast to the MELCOR calculation. As a result, ASTEC predicts steam condensation over a broader time and shifts forward the entrance in core degradation. Once this happens, the relative accident progression is similar, the main difference being the time between relocation and RPV failure. Overall, it can be stated that both predictions are consistent.

7.3 Station Blackout

In contrast to sections **7.1** and **7.2**, this section discusses the behaviour of the reactor in the absence of a break in the RCS. In this case, the sequence considers a SBO (LOOP together with the failure of DGs) at the beginning of the transient (0.0 h). The evolution of pressures in selected control volumes, mass flow rates exiting different valves and relevant heat transfer rates in the reactor is depicted in **Figure 7-5** as a function of the time after SCRAM. The evolution of additional plant parameters is illustrated in **Figure D.3-1** and **Figure D.3-2**. The coloured vertical lines mark occurrence times of major events in the simulation. The summary of events occurring in the simulation relative to the loss of AC power supply is shown in **Table D.3-1**. The behaviour of the reactor is explained as follows:

The first consequence of the SBO is SCRAM, the stop of FW into the SGs and the unavailability of the MCPs. After SCRAM, the RCPS issues a signal for turbine trip. This event does not lead to RCS depressurization because the systems that perform the automatic 100 K/h cooldown through the SGs are assumed unavailable after SBO (see section **6.5**). Since no FW is provided, the SGs inventory is progressively depleted, leading to a deteriorated heat transfer through the SGs. In turn, this leads to SG pressure increase up to the set-point of the Safety Valves of SGA/B and RCS pressure increase up to the set-point of the PORV.

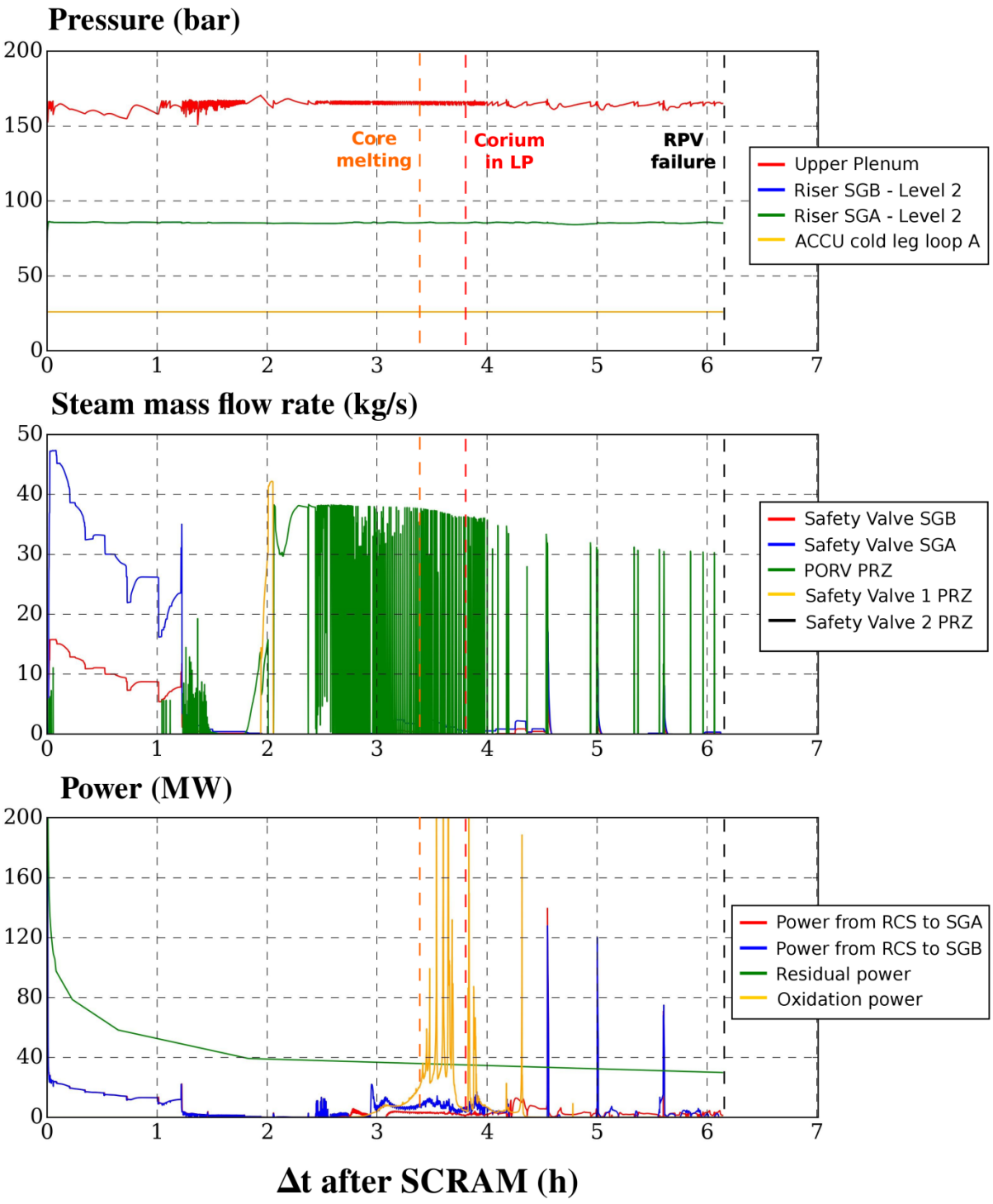

Figure 7-5: Evolution of pressures (in selected control volumes), steam mass flow rates through selected valves and relevant heat transfer rates during the sequence *Ref-SBO* as a function of the Δt after SCRAM. Major events of the simulation are represented by dashed vertical lines.

This continues up to the dry-out of the SGs (at about 1.20 h). From this moment on, the heat sink (secondary side) is lost, and the RCS experiences a rapid temperature increase. As a result, the pressurizer liquid level becomes filled with liquid at 1.40 h and the RCS pressure is

released through the PORV. However, this valve does not have enough capacity to bring the overall RCS pressure down and maintains it around its opening set-point. Under such conditions, the temperatures continue increasing until the liquid reaches saturation (first at the pressurizer and hot legs at about 1.80 h, then at the cold legs at about 2.00 h). This provokes a slight decrease of the pressurizer liquid level, but not of the overall RCS pressure, since the liquid level is still high (above 8 m).

The core starts to become uncovered when the hot legs reach saturation. At the beginning, natural circulation within the RPV delays the core heat-up. However, when the core head becomes uncovered, the heat transfer from the fuel rods to the coolant declines. As a result, temperatures start to increase rapidly due to the released oxidation enthalpy, which introduces a higher power input (peaks of 200 MW) than the residual power (about 40 MW). Although the PORV and SV1 contribute to RCS pressure relief, the presence of overheated steam compensates the first and hence, the pressure in the RCS remains at a high level during the transient.

In the absence of AM, the high pressure sequence continues its progression, leading to core heat-up, melting (3.40 h), corium relocation to the LP (3.84 h) and finally to a RPV failure (6.14 h).

7.3.1 Comparison with other studies and Discussion

The performed simulations have shown that, if FW is not provided into the SGs during an SBO scenario, the cooling effect of the secondary side is lost and hence, the RCS coolant starts to heats-up and eventually reaches saturation. In such case, RPV failure occurs at high pressures.

In order to confirm the correctness of ASTECV2.0 predictions, the results are compared to the ones obtained with MELCOR 1.8.4 [144] and ATHLET-CD V3.0 [145]. Calculations mainly differ in the modelling of the late in-vessel phase as well as on the decay heat. The occurrence times of main events corresponding to each work can be found in **Table D.3-2**.

The code-to-code comparison shows a qualitatively similar transient evolution. Slight deviations of about 40 min exist in the prediction of the SGs dry-out, which depends on the heat transfer between the RCS and the secondary circuit, and hence, on the RCS heat-up. Therefore, it is likely that these differences stem from the different decay heat. The comparison shows that, the earlier the dry-out occurs, the earlier the core melts and the pressurizer becomes voided. After core melt occurs, the results differ possibly due to the different relocation models. This has an impact on the amount of corium relocated to the LP (2 tons in ASTEC vs more than 100 tons in ATHLET) and on RPV failure. Overall, it can be concluded that all codes predict similar trends except for the late in-vessel phase.

7.4 Summary

In this chapter, ASTECV2.0 analyses on risk-relevant sequences (e.g. MBLOCA, SBLOCA and SBO) in a generic Konvoi PWR have been performed. For the sequences involving a break in the RCS, a Station Blackout has been assumed at a certain time after the accident initiation. For the total SBO without breaks in the RCS, the sequence has postulated the loss of AC power supply at the beginning of the transient.

ASTECV2.0 predictions have been verified by a satisfactory comparison with the work performed by other institutions using other SA codes e.g. ATHLET-CD and MELCOR. The results can be summarized in the following points:

- MBLOCA sequences quickly lead to core uncovery after the loss of the LPIS. If SBO occurs in the following hour after SCRAM, RPV failure happens shortly afterwards. Otherwise, the grace time can be increased up to 1 h after the occurrence of SBO.
- SBLOCA sequences exhibit a slower accident progression than MBLOCAs. However, they are particularly dangerous, because they may cause a RPV failure at high pressures, especially if the plant enters in SBO before the intervention of the Emergency Feedwater System.
- SBO sequences without breaks in the RCS lead to a quick dry-out of the SGs and to a rapid RCS heat-up, which is maintained at high pressures up to RPV failure. However, in contrast to MBLOCA sequences, there is a broader grace time for the performance of SAM.

Summarizing, it can be concluded that proper AM measures are extremely important to prevent, mitigate or delay the SA progression. For that aim, several questions must be answered. For example: What actions should be followed? When should these actions be launched? Is there an optimum time window to execute them?

8 Simulation of AM measures in a German Konvoi PWR using ASTECV2.0

The previous chapter has analysed the evolution of different severe accident scenarios in a German Konvoi PWR using ASTECV2.0. The performed simulations did not consider any preventive or mitigative AM. Within this chapter, the aim is to study the efficiency of selected AM measures existing in a Konvoi PWR (see Chapter **3**) and to investigate if these can be improved, considering the lessons learnt in Germany after the Fukushima accidents [9,10].

First, an analysis of core reflooding for MBLOCA sequences is performed in section **8.1**. Then, a study of primary side depressurization and core reflooding for SBLOCA sequences is carried out in section **8.2**. A similar approach is adopted for the SBO sequences discussed in section **8.3**, where the efficiency of secondary bleed and feed is also investigated. Finally, section **8.4** finishes with recommendations on selected SAM measures for the German Konvoi PWR based on the performed simulations.

All the calculations assume a Station Blackout at a discrete stage of the accident. This means that the injection from active systems of the ECCS cannot be performed, which makes necessary one of the following injection alternative:

- Dispose of emergency Diesel Generators that restore key safety systems.
- Provide an external injection into the RCS or the SGs.

Herein, the second approach has been followed. However, the first approach is answered based on the analyses on the external injection.

8.1 MBLOCA in the cold leg of the pressurizer loop combined with SBO

The MBLOCA sequences analysed in section **7.1** have led to a rapid depressurization of the RCS and hence, an additional depressurization of the RCS is not necessary. In this context, the injection of water into the reactor becomes the prime SAM strategy to mitigate the SA, according to **Figure 3-6**. Therefore, this section studies active core reflooding with the following roadmap:

A detailed analysis on core reflooding is firstly performed in section **8.1.1.1** considering that a SBO occurs 1 h after SCRAM. Therein, the influence of the injection time (performed at CET 650 °C or different time intervals beyond) and the type of mobile pump on the success of core reflooding is studied. Then, the section **8.1.1.2** adopts the same approach to evaluate the impact of a later loss of AC power supply (e.g. 4 h after SCRAM) on core reflooding success. A flow chart representing the calculations performed within this section can be found in **Figure 8-1**.

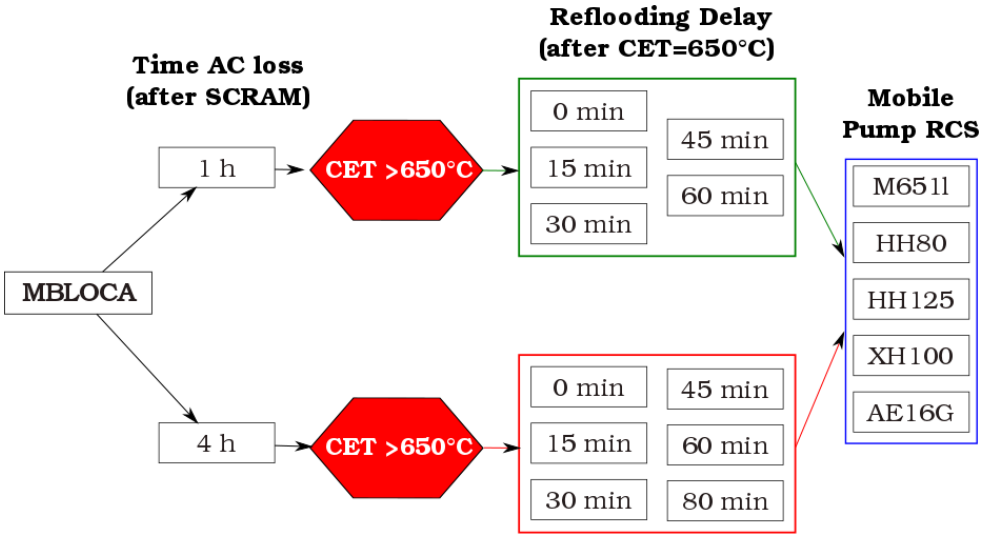

Figure 8-1: Flow chart of performed MBLOCA calculations (1st level: time of AC power loss (since SCRAM); 2nd level: delay in core reflooding (since the detection of CET=650 °C); 3rd level: mobile pump used for core reflooding).

8.1.1 Active Core Reflooding

The sequences *AC1h* and *AC4h* have been subjected to core reflooding. For both, injection occurs as soon as the CET exceeds 650 °C or with 15, 30, 45 and 60 min delay. The considered mobile pumps are M651l, HH80, HH125, XH100 and AE16G (see features in **Table 6-2**). Calculations are terminated when one of the following conditions is fulfilled:

- Core liquid level higher than *min3*, which corresponds to the lower edge of the hot leg [15]. In this work, *min3* is assumed to be at an elevation of 15 cm above core head.
- Final time of the simulation is reached (i.e. 10 h since reflooding onset).
- RPV failure.

The impact of reflooding on *AC1h* progression is firstly analysed in section **8.1.1.1**, while the additional impact of a later loss of AC power (i.e. *AC4h*) is investigated in section **8.1.1.2**.

8.1.1.1 Loss of AC power 1 h after SCRAM

In order to study the influence of the mobile equipment and the injection time, three studies are carried out: reflooding with different mobile pumps (fixed injection time); at different injection times (fixed mobile pump); and at different injection times with different mobile pumps.

➢ *Influence of Reflooding Mass Flow Rate (RMFR)*

This section assumes that core reflooding is realized by means of different pumps when the CET reaches 650 °C. The influence of the mobile equipment on the liquid water level and the corium mass in core (corium mass in the lower plenum is not included) is shown in

Figure 8-2 as a function of the time since CET 650 °C was reached. The reference case without any active core reflooding *(MBLOCA-) AC1h* has also been included. Additional variables such as the mass flow rate injected by each mobile system and the corium mass in the LP are shown in **Figure D.1-3**. Simulations are terminated when one of the criteria exposed at the beginning of section **8.1.1** is satisfied e.g. core liquid level, time of simulation or RPV failure. The simulations yield the following computational results:

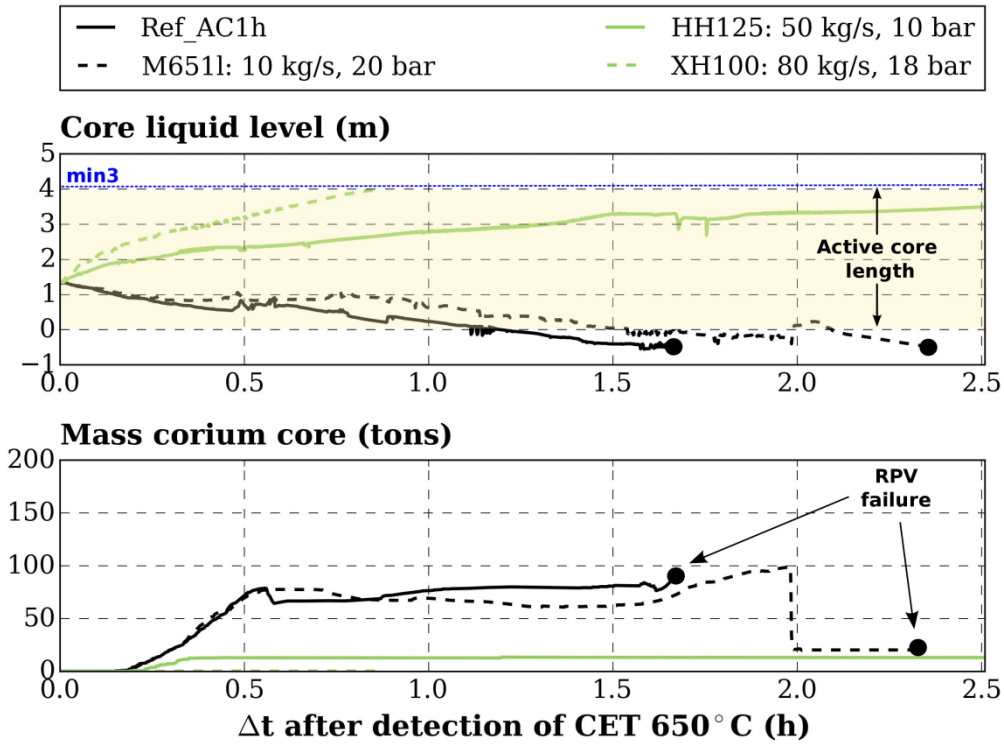

Figure 8-2: Influence of mobile equipment during a 0-min delayed (after detection of CET=650 °C) core reflooding on the evolution of the core liquid level and the corium mass in the core in comparison to the sequence *MBLOCA-AC1h* (MBLOCA with SBO **1 h** after SCRAM and without reflooding). Black points mark RPV failure occurrences.

The mobile pump *XH100*, which provides a mass flow rate of about 60 kg/s according to **Figure D.1-3**, is able to quickly refill the RPV and cool down the core before a significant oxidation starts. Therefore, the release of U-Zr-O mixtures into the core is prevented. On the other hand, the pump *M651l*, which injects a mass flow rate of 10 kg/s, is not capable of stopping core voiding and leads to sudden water evaporation. Hence, the hydrogen generation rate remains high over an extended time window (see **Figure D.1-3**) compared to the rest of the cases. The behaviour is similar to the reference sequence without reflooding. However, differently to the reference case, the corium mass in the core falls from 100 tons to 25 tons, which means that 75 corium tons are relocated from the core to the LP (see **Figure D.1-3**). This may be related to the higher extent of oxidation of this case compared to the reference one. Finally, the pump *HH125*, which injects an intermediate flow rate, is able to stop the accident progression but it cannot avoid corium relocation into the core region (10-40 tons).

The higher the mass flow rate, the higher the velocity of the quench front is. Also, the core is subjected to minor oxidation. Consequently, it can be concluded the mass of corium released to the core region decreases with increasing mass flow rate.

- *Influence of water injection time*

Considering now a water injection occurring with different delays after the detection of a CET 650 °C by means of the pump AE16G (nominal flow rate of 100 kg/s, pressure head 6 bar). The influence of a delayed core reflooding on selected variables is shown in **Figure 8-3** as a function of the time after reaching CET 650 °C, together with the reference case without reflooding (*MBLOCA-AC1h*). The impact on the evolution of other variables such as the relocation of corium into the LP can be taken from **Figure D.1-4**. Simulations are terminated when one of the criteria exposed at the beginning of section **8.1.1** is satisfied. The calculations yield the following results:

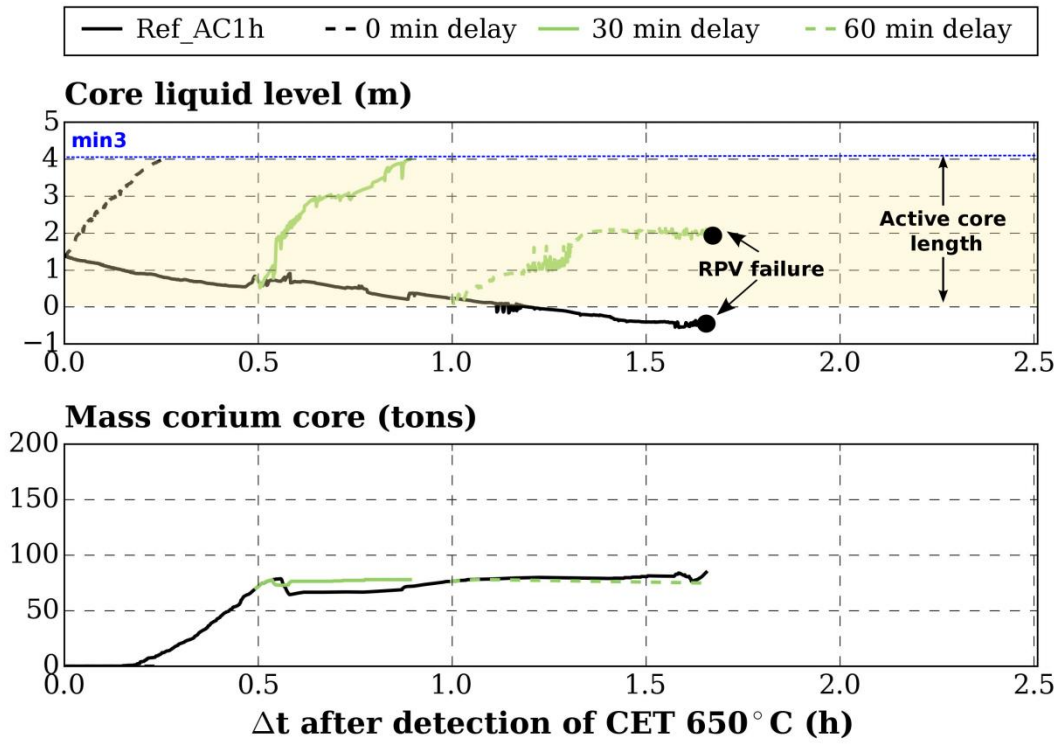

Figure 8-3: Influence of a delayed (after detection of CET 650 °C) core reflooding by means of the mobile pump AE16Glp on the core liquid level and the corium mass in the core in comparison to the sequence *MBLOCA-AC1h* (MBLOCA with SBO at **1 h** after SCRAM and without core reflooding). Black points indicate RPV failure occurrences.

If core reflooding is immediately launched at CET=650 °C, the accident is terminated without any core degradation, since the quench front reaches in 15 min the bundle head and hence, the height *min3*. If, however, the mobile pump is deployed with a 30 min delay, a large molten pool containing about 80 corium tons is present in the core region. In such conditions, ASTEC predicts the retention of corium in the core and in the LP, but this seems to occur

more due to the external simulation criteria (core liquid level exceeds *min3*) than to the real behaviour in the reactor (see section **2.2.2**). Besides, the predictions of ASTECV2.0 are questionable due to the lack of capabilities to describe degraded core reflooding (see section **4.4.4**).

Injections performed with a delay beyond 1 h cannot prevent a RPV failure regardless the RMFR. In those cases, at least 20 corium tons are in contact with the RPV wall for at least 20 min (see **Figure D.1-4**). Therefore, the metallic layer cannot be rapidly cooled down and the temperature increase of the wall in contact with the metallic layer cannot be stopped. Eventually, the ultimate stress (which decreases with increasing temperature) falls below the applied stress, leading in turn to a RPV failure.

Then, it can be concluded that, in order to prevent significant corium relocation into the core, it is necessary to initiate core reflooding immediately after the detection of CET 650 °C.

- *Influence of RMFR and water injection time on selected FOMs*

So far, the individual influence of mobile equipment and injection time on the severe accident progression has been studied. The goal now is to investigate the combined influence of both variables on selected Figures of Merit (FOMs): the final Core Damage State (CDS) after reflooding (**Figure 8-4**-a), the final mass of corium relocated within the core (**Figure 8-4**-b), the final mass of corium in the LP (**Figure 8-4**-c) and the relative time to RPV failure since SBO (**Figure 8-4**-d). The influence on the mass of water injected during reflooding and the refilling time at the end of the simulation can be found in **Figure D.1-5**. Additional information of the diagrams is provided hereafter for a better understanding:

- The abscissa represents the injection time relative to the detection of CET 650 °C. The ordinate represents the average RMFR provided by the mobile system from the start of injection up to the end of the simulation. Therefore, the ordinate depends on the RCS pressure evolution during reflooding.
- The black dashed vertical lines are the previous damage curves [146], which represent the most relevant transition times in the sequence without reflooding (*MBLOCA-AC1h*). These lines allow identifying the initial state of the core when reflooding is initiated. A description of the events is attached next to each vertical line for the two upper subplots.
- Each point refers to one simulation with a defined injection time and mobile system. Each point has two attributes: colour (according to the FOM e.g. Final Core Damage State, etc.) and geometrical form.
    - The geometrical form represents the mobile equipment used in the calculation. The different systems can be found at upper part of **Figure 8-4**.
    - The colour defines the interval where the output variable of the simulation (final CDS, corium mass in LP, etc.) belongs to. Intervals are different for each output variable, and can be found at the right side of each subplot.

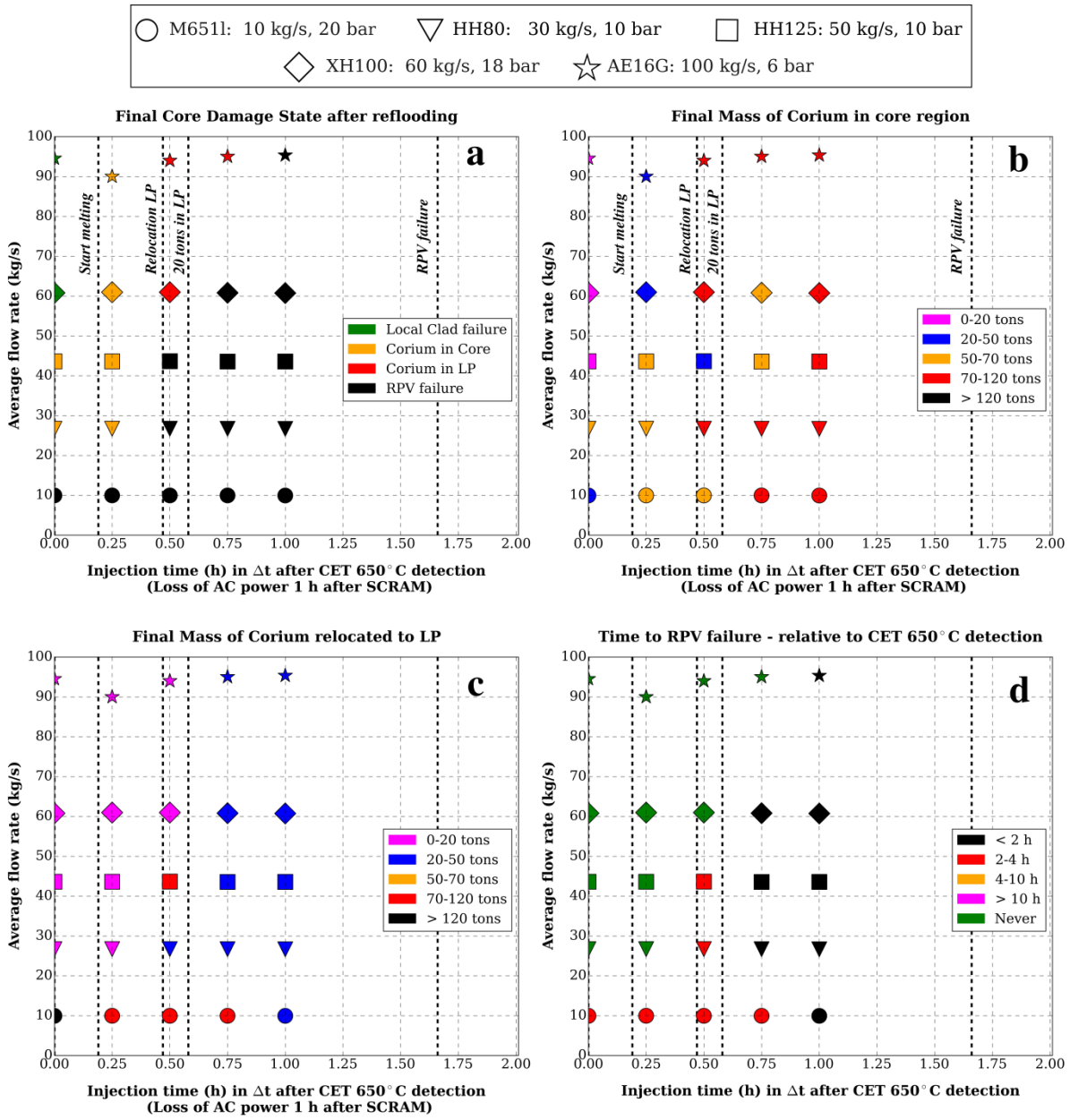

Figure 8-4: Final (a) Core Damage State, (b) Mass of corium in Core, (c) Mass of corium in the LP and (d) time to RPV failure as a function of RMFR and the injection time (relative to the detection of CET=650°C). Black dashed vertical lines represent occurrence times of major events in *MBLOCA-AC1h* (MBLOCA with SBO at **1 h** after SCRAM and without core reflooding).

Summing up, the initial CDS (at reflooding) is given by the last vertical line previous to the injection time, whereas the final CDS after reflooding is given by the colour of the point. For example, let us consider a 15-min delayed (since CET 650 °C) injection – this corresponds to 0.25 h - with HH125 in **Figure 8-4**-a. At reflooding onset, the corium has already started melting (indicated by the last vertical line before that instant). At the end of reflooding, ASTEC predicts corium retention in the core (indicated by the orange colour of the point). Besides, at the end of reflooding there are 50-70 corium tons in the core region (**Figure 8-4**-b), 0-20 corium tons in the LP (**Figure 8-4**-c) and no RPV failure (**Figure 8-4**-d).

The calculations yield the following computational results:

- Injections performed at CET 650 °C are able to quickly refill the core with localized cladding failures at RMFRs higher than 60 kg/s (see AE16G and XH100 in **Figure 8-4**-a). In those cases, the quench front is able to reach the bundle head in less than 1 h, which demands the provision of about 100-200 water tons (see **Figure D.1-5**-f-h). If this is not possible, the core can be refilled without major damage (less than 20 corium tons in the core) if at least 40 kg/s of water are supplied.
- Injections started up to 15 min after detecting CET 650 °C cannot prevent core melting, but still have the chance to retain the corium in the core if RMFRs of more than 30 kg/s are supplied (**Figure 8-4**-a). In those cases, ASTEC predicts the existence of more than 20 corium tons in the core after reflooding (**Figure 8-4**-b). However, the scope of validity of this prediction is limited, as discussed in section **4.4.4**.
- All mobile systems are able to supply an average RMFR close to the nominal one, since the large break avoids a RCS repressurization during injection. This can be done by comparing the nominal flows shown in the legends with the point ordinates. However, the pump AE16G seems slightly more susceptible to repressurization if the injection is started after the onset of core melting. In that case, the pump efficiency decreases slightly from about 100 % to 90 % (90 kg/s out of a nominal of 100 kg/s).
- RMFRs below 10 kg/s (e.g. M651l) cannot avoid the ongoing loss of inventory (see the liquid level evolution in **Figure 8-2**). They even lead to a higher extent of corium relocation to the lower plenum. In such cases, RPV failure can be neither prevented nor delayed.

8.1.1.2 Influence of SBO time

Next, the additional effect of a later loss of AC power (e.g. 4 h after SCRAM) on core reflooding success is studied. The combined effect of the RMFR and the injection time on the final Core Damage State and the final mass of corium in the core are depicted in **Figure 8-5**. Further results can be found in **Figure D.1-6**. In those figures, the vertical lines correspond to the occurrence times of major events of *MBLOCA-AC4h*.

At first glance, some similarities with an early SBO can be identified, which are:

- Minimum RMFRs above 60 kg/s (e.g. AE16G and XH100) have to be supplied as soon as the CET exceeds 650 °C in order to prevent core melting.
- RMFRs lower than 10 kg/s cannot prevent the failure of the RPV. The only exception occurred for a 15-min delayed reflooding with M651l, where the simulation did not finish due to numerical problems.
- Injections performed 15 min after CET 650 °C cannot avoid core melting.
- The pumps provide an excellent performance due to the absence of RCS repressurization.

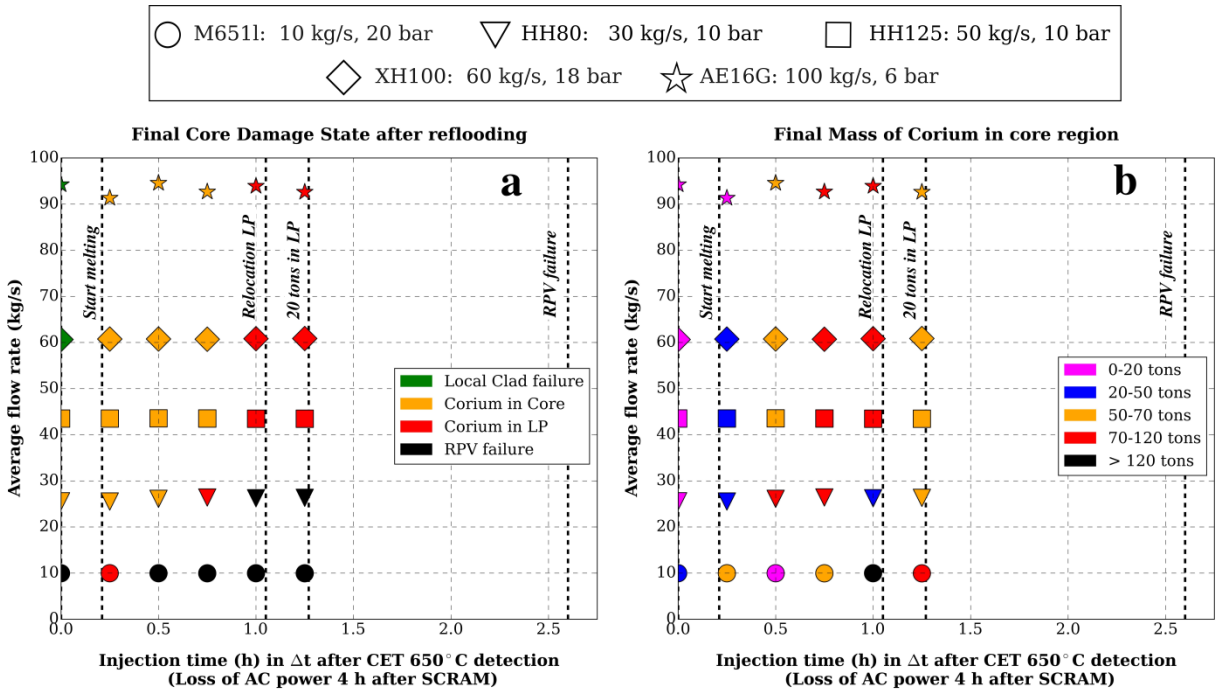

Figure 8-5: Final (a) Core Damage State and (b) Mass of Corium in Core as a function of RMFR and the injection time (relative to the detection of CET=650°C). Black dashed vertical lines represent occurrence times of major events in *AC4h* (MBLOCA with SBO at **4 h** after SCRAM and without reflooding).

However, differences can be noted regarding corium retention in the core region:

- The minimum RMFR to stop the SA without major damage for a late SBO is 25 kg/s at CET 650 °C. This amount is lower than the 40 kg/s required in case of an early SBO. The reason for it is the decrease of the decay heat from 39 MW (1 h after SCRAM) to 33 MW (4 h after SCRAM).
- Water injections started with a 15 min delay after detecting CET 650 °C cause the release of 20-50 corium tons into the core, which is lower than the 50-70 tons predicted for an early SBO. From that point in time, injection ends with the retention of more than 50 corium tons in the core for both cases. However, the validity of this finding is also limited, as described in the previous section.

Simulations aiming at identifying the maximum admissible time to prevent RPV failure could not be performed for *AC4h* due to time constraints. However, one can deduce (based on the results of later sections in **8.2.2** and **8.3.3**) that a RPV cannot be prevented if 20 corium tons are present in the lower plenum for at least 1 h regardless of the supplied RMFR.

8.1.1.3 Comparison with other studies and Discussion

The reflooding simulations presented in section **8.1.1** have predicted the existence of a minimum RMFR of about 25-40 kg/s to mitigate the accident without a major damage, the value depending on the time elapsed from SCRAM up to the loss of AC power supply. In

order to confirm the consistency of ASTEC predictions, the results are compared to studies performed by AREVA using MELCOR [12]. Therein, the minimum RMFR required to stop degradation was calculated as a function of SCRAM for several sequences, considering that the injection always occurred immediately after the detection of CET 650 °C. The influence of the secondary side (filled or empty) on the minimum RMFR was also investigated. In order to perform the comparison, the following ASTEC scenarios are considered:

- *AC1h* with active core reflooding at CET = 650 °C (~ 1.70 h after SCRAM).
- *AC4h* with active core reflooding at CET = 650 °C (~ 4.70 h after SCRAM).

The state of the secondary circuit is neglected, since AREVA predicts an influence of the secondary side for "times elapsed between SCRAM and CET 650 °C" of more than 5 hours.

Results of the comparison are shown in **Table 8-1**. For the representation of MELCOR results, only one row has been defined, because AREVA presents the results with continuous damage domains but with a minor amount of point data. On the other hand, ASTEC values are presented in two rows: the first contains the minimum RMFR necessary to prevent major core damage considering point data, while the second contains ASTEC interpolated values. The results show a satisfactory agreement between ASTEC and MELCOR predictions, the minimum RMFR being slightly overestimated for a later loss of AC power supply.

	SCRAM-CET650°C: 1.70 h		SCRAM-CET650°C: 4.70 h	
	ASTEC	MELCOR	ASTEC	MELCOR
Minimum RMFR	40 kg/s	40 kg/s	25 kg/s	15 kg/s
Minimum RMFR (ASTEC interpolation)	35 kg/s		18 kg/s	

Table 8-1: Comparison ASTEC-MELCOR [12] on the minimum RMFRs to mitigate the SA without major core damage. ASTEC values correspond to selected MBLOCA sequences.

Based on these results, SAM improvements regarding the most suitable mobile pumps to prevent degradation and their deployment time can be suggested. Nevertheless, since MBLOCAs do not play a significant role for PSA-1 or PSA-2 analyses [27], it is not likely that such measures result in a decrease of core damage or containment failure risk. This task is shifted to the sections **8.2** and **8.3** of this chapter.

In the absence of an external injection, the other path to provide coolability to the reactor is the recovery of AC power supply through additional grid connections or mobile DGs. Considering that this is performed within a threshold of 15 min after the detection of a CET 650 °C, the efficiency of the different safety systems related to core cooling (see **Table 6-3**) are predictable. The retrieval of one HPIS or LPIS train refills the core without major

damage, whereas the EBS cannot prevent nor delay a RPV failure. Finally, the retrieval of two CVCS trains prevents major core damage for a late SBO, but not for an early one.

8.2 SBLOCA in the cold leg of the pressurizer loop combined with SBO

The SBLOCA sequences analysed in section **7.2** have led to medium-high pressures in the RCS until RPV failure. In that context, the first SAM measure is the depressurization of the RCS by means of a PSD (see **Figure 3-6**). SSD is not an option, since PSA studies for the Konvoi PWR have shown the lack of time to prepare such procedure in SBLOCAs [15,27]. Once the RCS is depressurized, the most imperative SAM measure is core reflooding. Within this section, the following roadmap has been followed:

Firstly, the impact of a delayed PSD on the SA progression is investigated both for a late and early SBO in section **8.2.1**. The delay is relative to the fulfilment of the PBF criteria i.e. detection of a CET=400 °C. Afterwards, the section **8.2.2** investigates the impact of core reflooding considering that PSD occurs at CET=400°C by means of all pressurizer valves. Therein, a combined analysis of the reflooding delay (relative to PSD onset i.e. CET 400 °C), the used mobile pump and the SBO time is investigated. A flow chart summarizing all performed SBLOCA calculations is shown in **Figure 8-6**.

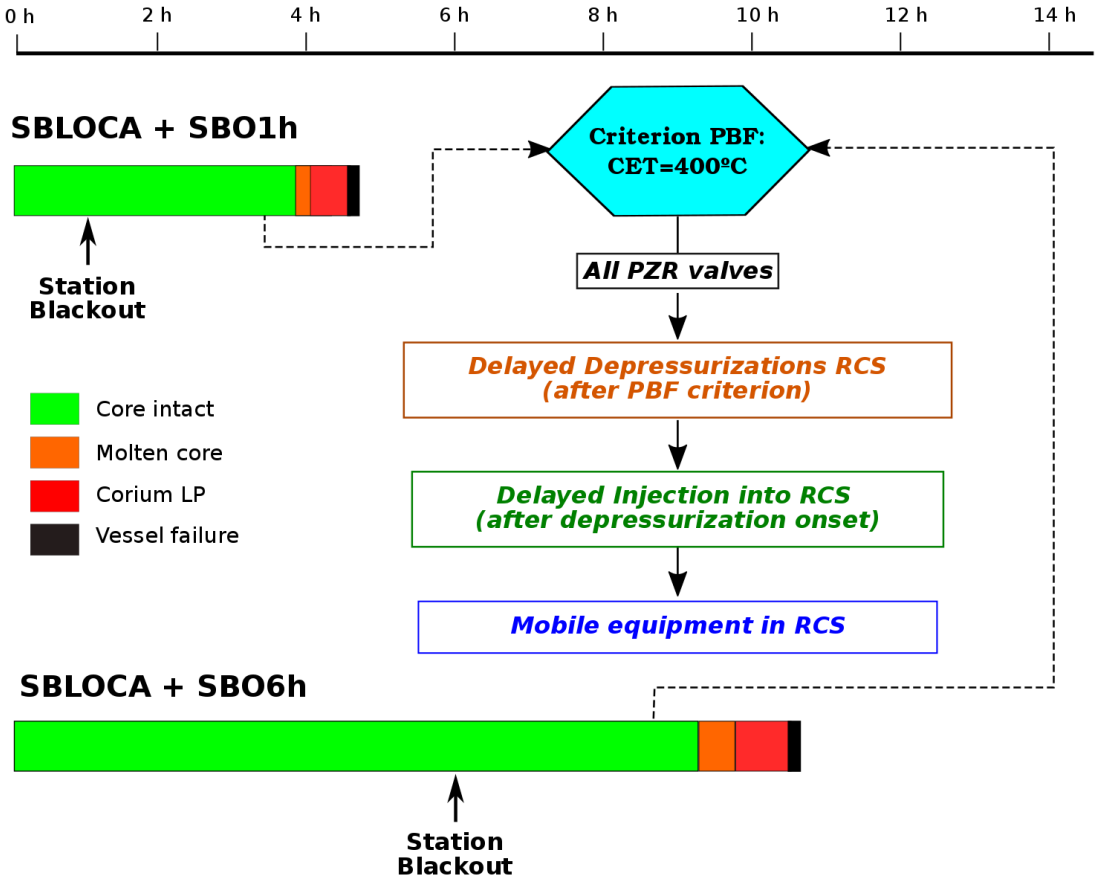

Figure 8-6: Flow chart of performed SBLOCA calculations (1st level: time of AC power loss; 2nd level: delay in PSD initiation after CET 400 °C detection; 3rd level: delay in core reflooding after PSD initiation, initiated at CET 400 °C; 4th level: mobile pump used for core reflooding).

8.2.1 Primary Side Depressurization and Passive Core Reflooding

PSD is the most imperative SAM measure during SBLOCA sequences in a German Konvoi PWR (see **Figure 3-6**). Within this section, the sequences *AC1h* and *AC6h* are subjected to a 0-80 min delayed PSD with respect to the detection of CET=400 °C (see section **6.5**). These delays may happen due to the harsh environmental conditions experienced by the plant crew.

Firstly, the influence of different PSD initiations on the progression of *AC6h* is analysed in section **8.2.1.1**, while the additional impact of the SBO time is investigated in section **8.2.1.2**.

8.2.1.1 Loss of AC power at 6 h

Within this section, the impact of a delayed PSD on the sequence *AC6h* is investigated. For that aim, the grace times gained due to PSD (with respect to the sequence *AC6h*) are represented in **Figure 8-7**-b as a function of the PSD delay (relative to the detection of CET 400 °C). The graph contains several black dashed vertical lines, which are the previous damage curves of the sequence without PSD i.e. *AC6h*. The meaning of these is similar to the one introduced in section **8.1.1.1**.

For example, let us consider that a 40-min delayed PSD is carried out aiming at delaying the progression of *AC6h*. At the moment of PSD initiation, the core has already started melting (indicated by the last vertical line). In addition, the action would anticipate the corium relocation to the LP (- 0.20 h), delay a 20-ton-corium relocation to the LP (+ 3 h) and delay RPV failure (+ 3.7 h) with respect to *AC6h*.

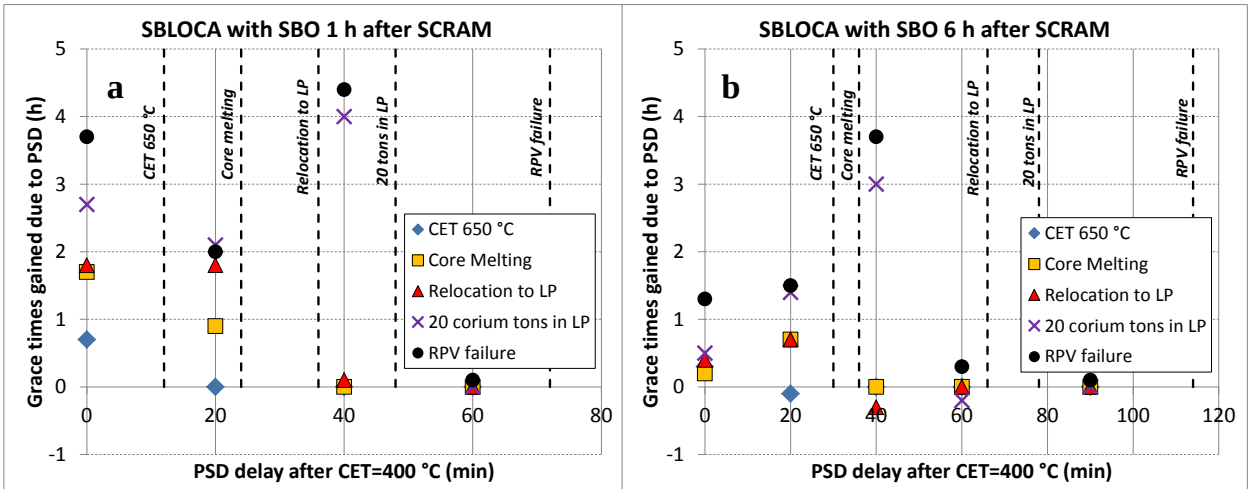

Figure 8-7: Grace times gained due to PSD in comparison to the sequences (a) *SBLOCA-AC1h* and (b) *SBLOCA-AC6h* (SBLOCA with SBO **1 h / 6 h** after SCRAM without PSD) as a function of the delay after the detection of CET=400 °C. Black dashed vertical lines mark occurrence times of major events in the sequences (a) *AC1h* and (b) *AC6h*.

Additionally, the **Figure 8-8** illustrates the influence of a delayed PSD on the RCS pressure and the temperature of the metallic layer in the LP as a function of the time after the detection of CET 400 °C. Therein, red crosses mark PSD initiation (for the sequences with PSD) and black points mark the occurrence of RPV failure. The influence on the core liquid level, the corium mass in the lower plenum can be taken from **Figure D.2-5**.

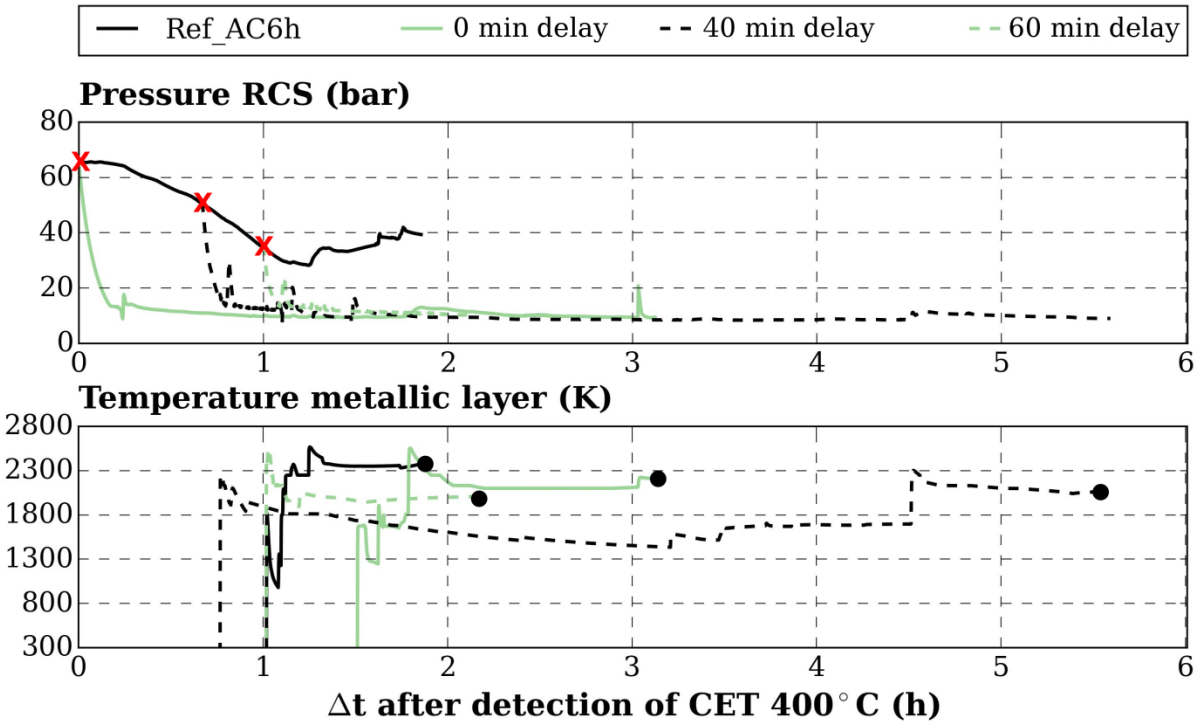

Figure 8-8: Influence of a delayed (after the detection of CET 400 °C) PSD on the evolution of the RCS pressure and the temperature of the metallic layer in the lower plenum in comparison to the sequence *SBLOCA-AC6h* (SBLOCA with SBO at **6 h** after SCRAM without PSD). Red crosses mark PSD initiation; black points mark RPV failure occurrences.

Results show that PSD does not delay significantly core melting nor the corium relocation to the lower plenum, but it extends at least 1.30 h the time to RPV failure if performed within the first 40 min after detecting CET 400 °C (see **Figure 8-7**-b). In fact, a 40-min delayed PSD provides the longest grace times to prevent the relocation of 20 corium tons to the lower plenum (+ 3 h) and RPV failure (+ 3.7 h).

This behaviour occurs because the ACCUs manage to cool down the metallic layer in the lower plenum (see second plot in **Figure 8-8**). As a result, the heat transfer from the metallic layer to the vessel wall (node 3, see dimensions in section **6.1.2**) decreases and the wall heats up slowly. The cooldown continues until the ACCUs become empty and 70 additional corium tons relocate to the LP (see **Figure D.2-5**), which leads to the heat up of the metallic layer until vessel failure. It must be present that the validity of the last finding is limited, since the reality shows that the corium may still relocate to the LP even if the molten pool is surrounded by water (see section **2.1.5**).

8.2.1.2 Influence of SBO time

The attention is now focused on the effect of SBO time on PSD performance. For that aim, another set of calculations with different PSD delays has been simulated based on *AC1h*. The grace times gained due to PSD are illustrated in **Figure 8-7**-a, which, in comparison to **Figure 8-7**-b, yields the following results:

- The grace times to avoid core melting, relocation to LP and RPV failure are extended if a PSD is initiated immediately after CET 400 °C. Moreover, the grace times are more significant in $AC1h_{PSDCET400}$ (1.7 h, 1.8 h and 3.7 h) than in $AC6h_{PSDCET400}$ (0.2 h, 0.4 h and 1.30 h). This is motivated by the higher mass flow rate injected by the ACCUs in the first case (reflected in a higher core liquid level in **Figure 8-9**), which is related to their higher discharge pressure upon PSD initiation (25 bars vs 12 bars). In turn, this happens because the ACCUs were involved at previous stages of the scenario in *AC6h*, differently to *AC1h* (see section **7.2.1**). Grace times are also extended for PSDs with 20 min delay, but less significantly than for the sequences without delay.
- The maximum PSD delay admissible to significantly shift the time of RPV failure is 40 min after the detection of CET 400 °C. In fact, although relocation to the lower plenum has already occurred in this case, the PSD manages to delay RPV failure by 4.4 h ($AC1h_{PSD40min}$ vs *AC1h*) and by 3.7 h ($AC1h_{PSD40min}$ vs *AC6h*). The reasons for this effect and statements about the validity of such result have been discussed in section **8.1.1.1**.
- A 60-min delayed PSD after the CET 400 °C detection does not influence the time to RPV failure, because more than 20 corium tons have been already heating up the RPV lower wall for at least 20 min. However, it allows avoiding a RPV failure at high pressures, as already shown in the previous section.

Summing up, the performance of PSD at CET=400 °C allows an extension of the grace time to prevent core melting and RPV failure. The delays are higher for *AC1h* than for *AC6h* due to the higher inventory of the ACCUs. However, the global grace time to prevent RPV failure is still higher in $AC6h_{PSDCET400}$ (5.90h + 6.00h = 11.90h vs. 10.60h of *AC6h*) than in $AC1h_{PSDCET400}$ (7.25h + 1.00h = 8.25 h vs 4.60h of *AC1h*).

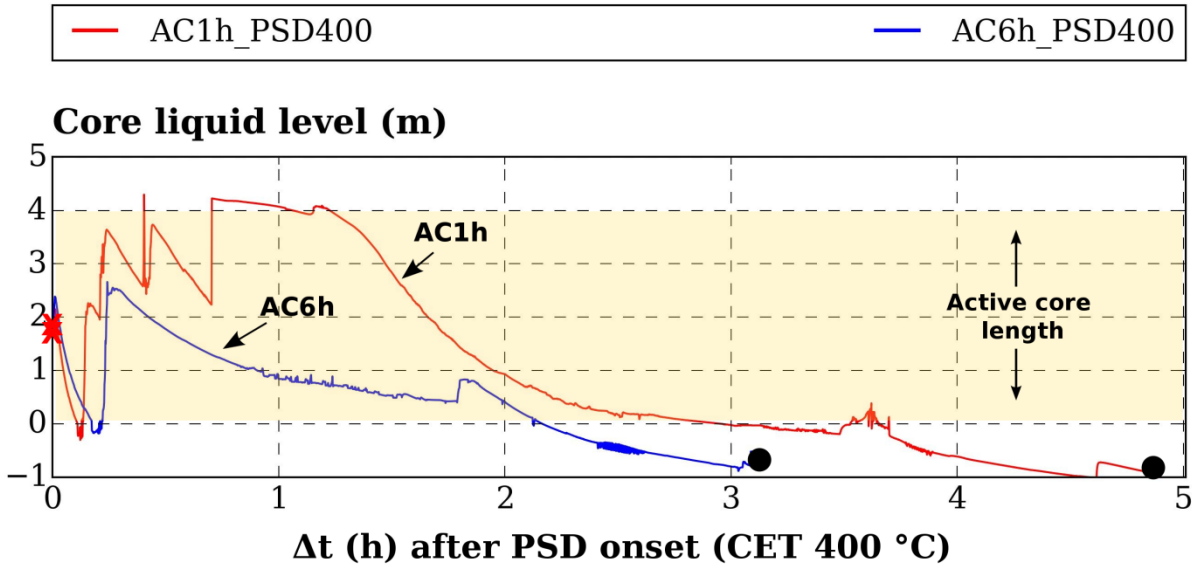

Figure 8-9: Evolution of the core liquid level during the sequences *SBLOCA-AC1h*$_{PSDCET400}$ and *SBLOCA-AC6h*$_{PSDCET400}$ (SBLOCA with SBO **1/6 h** after SCRAM, PSD at CET 400 °C). Red crosses mark PSD initiation; black points mark RPV failure occurrences.

8.2.1.3 Comparison with other studies and Discussion

Unfortunately, it has not been possible to compare ASTEC predictions on *AC1h*$_{PSDCET400}$ and *AC6h*$_{PSDCET400}$ with other SA codes. SBLOCA sequences analysed with MELCOR 1.8.4 in [144] involve PSD at CET 400 °C, but the break is located in the hot leg of the pressurizer loop, in contrast to this study i.e. cold leg. This implies the release of a steam-water mixture through the break, differently to the condensed water of this work. Therefore, it is reasonable that the current work predicts a shorter time to core melting (9.55 h ASTEC vs. 22 h MELCOR).

Turning now to the investigations on PSD, the section **8.2.1** has shown the existence of a time window by which a PSD significantly delays core melting, relocation to the LP and/or RPV failure. In particular, the operator needs to **initiate PSD at the stipulated time** (i.e. CET 400 °C) **or, if not possible, during the following 20 min**. This value is in agreement with that of the SAMGs for very small breaks (see **Figure 3-7** and **Figure 3-8**) [12,14]. In addition, the section **8.2.1** has predicted the longest grace time to prevent RPV failure for 40-min-delayed PSDs. However, it is difficult to extrapolate such finding to the reality, since a trained plant crew will likely not wait 40 min to initiate PSD, but rather launch it immediately to prevent RPV failure at high pressures.

8.2.2 Primary Side Depressurization and Active Core Reflooding

Once the RCS has been depressurized through a PSD, the subsequent SAM measure is the injection of water into the RCS (see **Figure 3-6**). Within this section, the sequences *AC1h*$_{PSDCET400}$ and *AC6h*$_{PSDCET400}$ (which assume a successful PSD at CET 400 °C) have been

subjected to core reflooding. For both sequences, injection occurs at different times after PSD initiation. This delay shall represent realistic time scales for successful pump activation. The considered mobile pumps are M651h, M100h, XH100, HH125 and AE18G (see features in **Table 6-2**). These sequences are marked as green and red boxes in **Figure 8-6**. The criteria to finish the simulations are identical to the ones shown at the beginning of section **8.1.1** (i.e. core liquid level, time elapsed since reflooding onset, RPV failure).

A detailed analysis on reflooding is firstly performed for the sequence $AC6h_{PSDCET400}$. Afterwards, the influence of an early loss of AC power supply ($AC1h_{PSDCET400}$) is compared to a late one in terms of core reflooding success.

8.2.2.1 Loss of AC power at 6 h

Following the same procedure as in MBLOCA, the study is divided in three parts: individual influence of mobile equipment (fixed pump), individual influence of reflooding time (fixed injection time) and combined influence of reflooding time and mobile equipment.

- *Influence of mobile equipment*

At first, the influence of different mobile equipment on the core liquid level and the corium mass in the core during a 40-min-delayed reflooding (relative to PSD initiation i.e. CET 400 °C) is studied. The evolution of such variables is depicted in **Figure 8-10** as a function of the time after PSD initiation, together with the case without active core reflooding ($AC6h_{PSDCET400}$). The RCS pressure, the flow rate injected by the equipment and the corium mass relocated to the LP can be found in **Figure D.2-6**. The red line marks reflooding initiation (for the cases involving reflooding), whereas black points at the end of certain curves mark the occurrence of RPV failure. The criteria to finish the simulations are identical to the ones shown at the beginning of section **8.1.1**.

Results show that *AE18G* cannot to supply water, because the RCS cannot be depressurized below the pump pressure head (see **Figure D.2-6**). Hence, core uncovery evolves similarly to $AC6h_{PSDCET400}$. The timing of the sequence is slightly different due to the additional venting paths opened in the RCS. A slight pump pressure head increase (*HH125*) results in a higher efficiency, but still low, because the RCS pressure is slightly higher than the pressure head of the equipment (see **Figure D.2-6**). A higher amount of corium in the core was expected, since the core is half covered during several hours after reflooding. However, only a few corium tons are released during this time. The influence of repressurization is overcome with increasing pressure heads (*M651h*) that, together with a high flow rate, allow a quick refill of the RPV avoiding any major core damage.

Therefore, it can be concluded that high pressure equipment (pressure heads above 50 bars) have an excellent performance in the sense that they are not affected by a RCS repressurization.

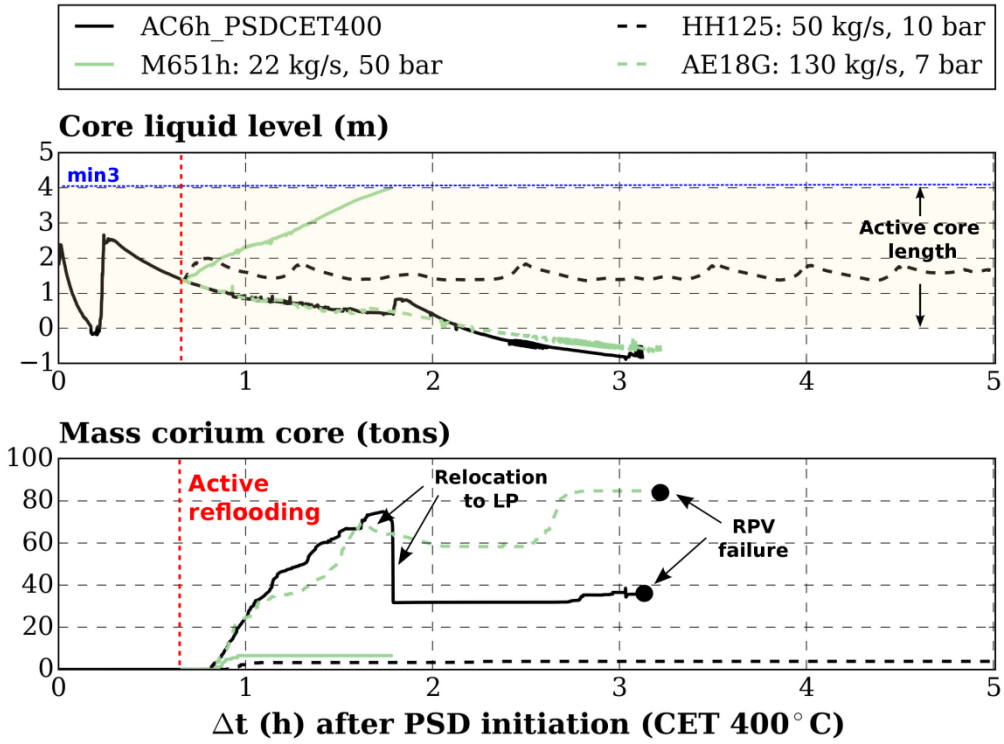

Figure 8-10: Influence of mobile equipment during a 40-min delayed (after PSD initiation) reflooding on the core liquid level and the corium mass in the core in comparison to the sequence *AC6h*$_{PSDCET400}$ (SBLOCA with SBO **6 h** after SCRAM, with **PSD at CET 400 °C** and without core reflooding). The red line marks the reflooding initiation; black points mark RPV failure occurrences.

➢ *Influence of water injection time*

Turning now to the water injection time, several delays (with respect to PSD initiation i.e. CET 400 °C) on the deployment of the pump M651h (see features in **Table 6-2**) have been simulated. The influence of this delay on the core liquid level and the corium mass in the core is shown in **Figure 8-11** as a function of the time after PSD initiation. The graph also includes the sequence without active core reflooding (*AC6h*$_{PSDCET400}$). Additional variables can be found in **Figure D.2-7**. In both graphs, red crosses indicate reflooding initiation (for the cases involving reflooding) whereas black points at the end of certain curves indicate RPV failure. The criteria to finish the simulations are identical to the ones shown at the beginning of section **8.1.1**. The calculations yield the following results:

- Reflooding with a delay of less than 40 min produces a temperature excursion (see PCT in **Figure D.2-7**), which leads to the release of several corium tons into the core region. However, the high velocity of the quench front allows terminating the accident without major core damage (i.e. less than 10 corium tons released to the core).
- Reflooding with a delay of more than 3 h cannot prevent nor delay the failure of the RPV. This happens because at least 40 corium tons relocate from the core region to the lower plenum at about 1.80 h (see decline of the corium mass in core in **Figure 8-11**) and heat-up the RPV wall for almost 1 h, leading ultimately to RPV failure.

In between, intermediate behaviours can be seen. For example, a 2-h delayed reflooding already meets 30 corium tons in the core and 50 corium tons in the lower plenum (**Figure D.2-7**). In that case, core reflooding does not cause further degradation, but a cool down of the bundle (see PCTs in **Figure D.2-7**). In addition, the generated pressure peaks (**Figure D.2-7**) do not affect the performance of the mobile pump, which has a pressure head (50 bars) well above them. However, these may affect the efficiency of low and medium pressure pumps.

Therefore, it can be concluded that core reflooding has to be initiated as early as possible in order to terminate the accident without any major damage. If that is not possible, reflooding encounters a severely degraded core, and may not prevent nor avoid RPV failure.

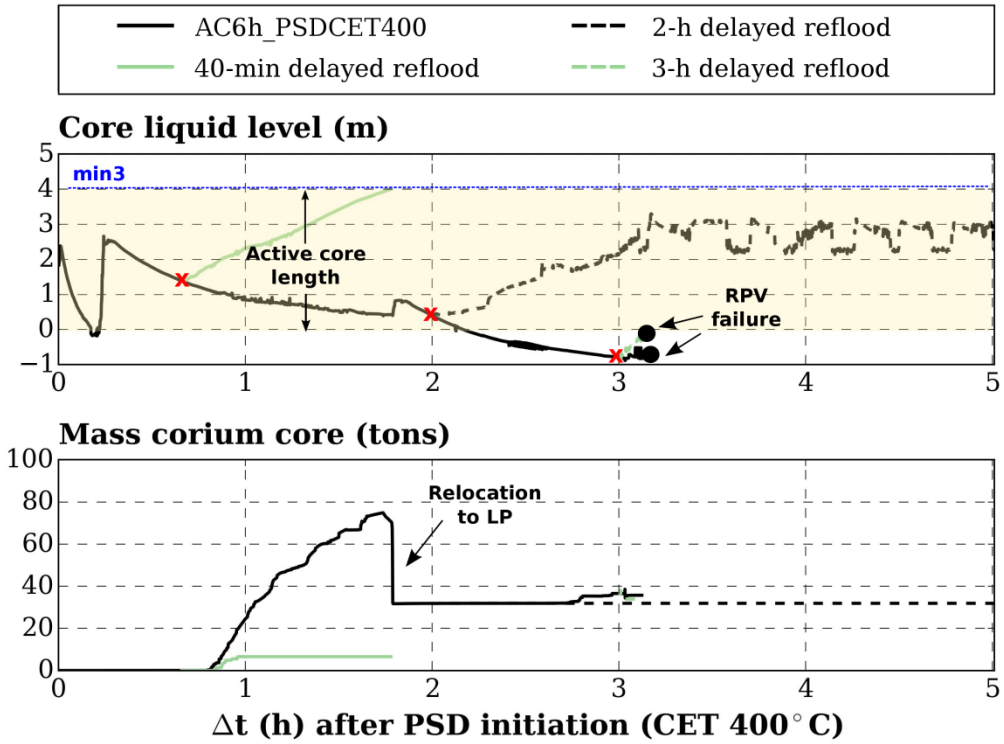

Figure 8-11: Influence of a delayed (after PSD initiation) core reflooding by means of the equipment M651h on the core liquid level and the corium mass in the core in comparison to $AC6h_{PSDCET400}$ (SBLOCA with SBO **6 h** after SCRAM, with **PSD at CET 400 °C** and without core reflooding). Red crosses mark the initiation of core reflooding; black points mark RPV failure occurrences.

➢ *Impact of mobile system and water injection time on selected FOMs*

Having studied the individual impact of the injection time and the mobile equipment on the progression of $AC6h_{PSDCET400}$, this section addresses the influence of both on the final CDS (**Figure 8-12**-a), mass of corium in the core (**Figure 8-12**-b), mass of corium in the LP (**Figure 8-12**-c) and relative time to RPV failure since PSD initiation (**Figure 8-12**-d). Further FOMs such as the final hydrogen generation, mass of water needed, RCS pressure and refilling time are shown in **Figure D.2-8**.

The graphs can be read using the same methodology as the one detailed for MBLOCAs in section **8.1.1.1**, but they differ in two aspects: first, the abscissa represents the delay in core reflooding with respect to PSD initiation; second, the vertical lines represent the occurrence times of major events (relative to PSD onset) in the sequence without any active core reflooding i.e. $AC6h_{PSDCET400}$.

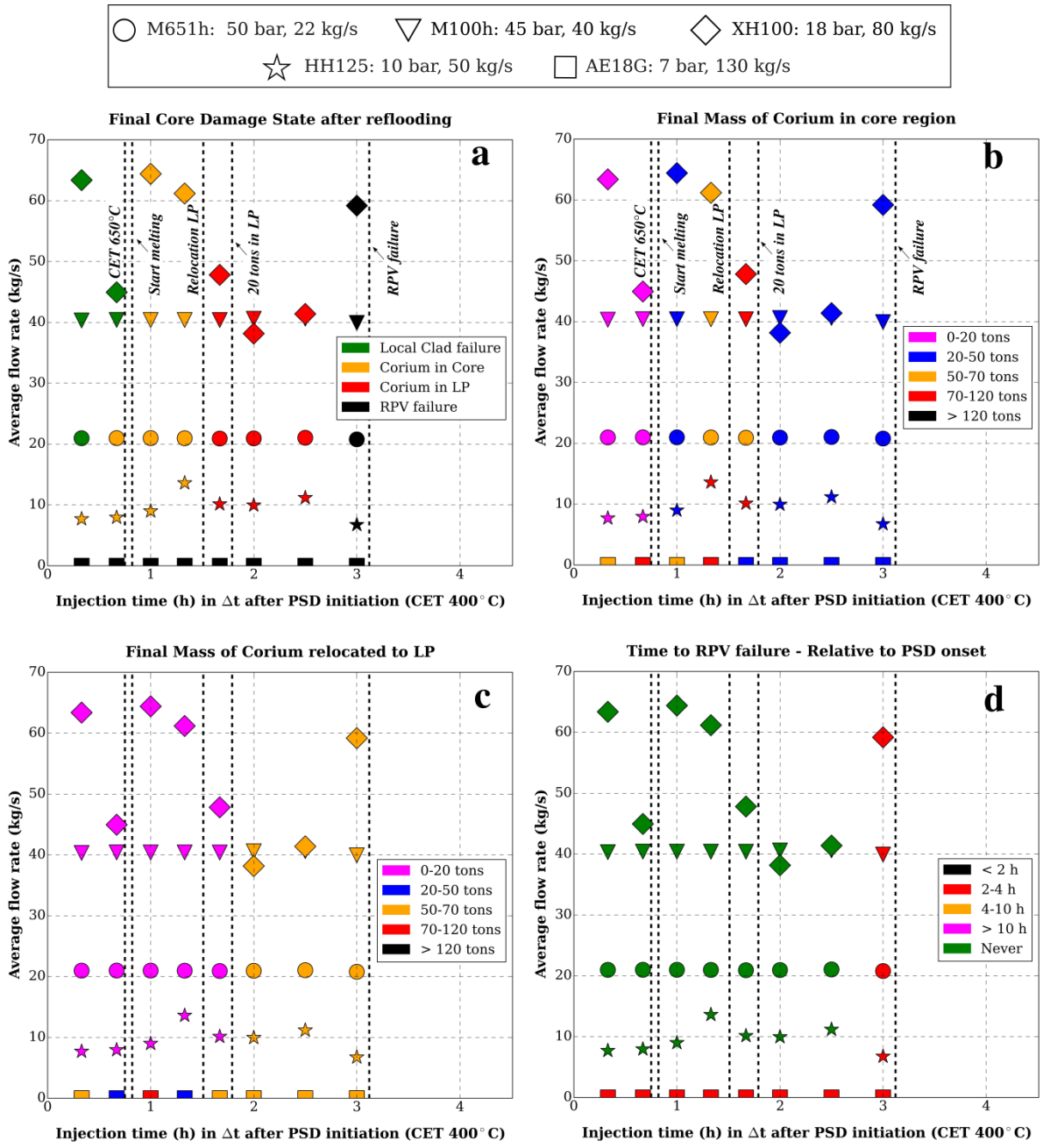

Figure 8-12: Final (a) CDS, (b) Mass of corium in Core, (c) Mass of corium in the LP and (d) Time to RPV failure as a function of the average RMFR and the injection time (relative to PSD initiation). Black dashed vertical lines represent occurrence times of major events in $AC6h_{PSDCET400}$ (SBLOCA with SBO at **6 h** after SCRAM with **PSD at CET 400 °C** and without core reflooding).

If we restrict the analysis to the injection time and the RMFR, the following statements can be formulated:

- Injections performed before detecting CET 650 °C (maximum delays of ~ 40 min) manage to refill the core in about 30 min – 1 h with localized burst of some claddings if RMFRs are higher than 40 kg/s. This demands 1 water ton (**Figure D.2-8**-f). If this is not possible, the corium release to the core region could still be limited to 20 corium tons if RMFRs are higher than 7.75 kg/s (**Figure 8-12**-a-b). However, in the last case, the refilling times exceed 1-2 h or even never reach the active core head.
- Injections performed 1 h after the relocation of 20 corium tons into the LP (purple vertical line in any graph) can neither prevent nor delay a failure of the RPV. This is determined by the fact that 40 corium tons (second plot **Figure D.2-7**) have heated up the top metallic layer (and hence, the RPV wall in contact with it) that water injection cannot rapidly cool down this layer.

Concerning injection rates exceeding 10 kg/s, it can be observed that (1) the retention of 20-70 corium tons in the core region is predicted for delays between 1 h and 1 h 20 min; (2) the retention of 50-70 corium tons in the LP and 20-50 corium tons in the core region is predicted for delays within 2 h- 2 h 30 min. However, it has to be highlighted that the last two conclusions are questionable due to ASTEC intrinsic limitations concerning degraded core reflooding (see sections **4.3** and **4.4.4**) and the external simulation criteria.

Up to this point, the combined influence of injection time and average RMFR injected into the RCS has been explained. However, the feedback of the system pressure on mobile system performance remains to be discussed. It is worthwhile to recall that this dependency influences the ordinate of each point in **Figure 8-12**. The following statements can be formulated with respect to this dependency:

- The efficiency of low pressure pumps (AE18G and HH125) is very low even having initiated PSD at CET 400 °C because any water injection in the RCS yields a repressurization (first plot **Figure D.2-6**) regardless of the injection time. Therefore, the RCS pressure rises above the pressure head of the equipment and the water supply is stopped. For example, the pump AE18G delivers a RMFR close to zero although its nominal RMFR is 130 kg/s (0 % efficiency). Similarly, the pump HH125 delivers 8 kg/s although it can potentially deliver 45 kg/s (20 % efficiency).
- High pressure pumps (M651h and M100h) are highly efficient at any injection time even if the RCS becomes repressurized, because the created pressure peaks (first subplot of **Figure D.2-7**) are well below their pressure head (45 and 50 bars).
- Medium pressure equipment such as the XH100 provide, as anticipated, an intermediate performance. Although the RMFR injected by the pumps is lower than the nominal, the repressurization does not prevent the equipment from supplying a considerable RMFR (50-75 % efficiency).

In contrast to the high and low pressure pumps, the injection time plays an important role for the medium pressure pumps, especially when the core starts to heat-up (between 0.50 h and 1.00 h) and when a considerable amount of corium is released into the core (between 1.50 h and 2.00 h). This happens because there is a high steam production that causes enhanced core oxidation and global temperature increase, which affects the pump performance. Once a considerable quantity of corium has relocated into the LP, the RMFR provided by such system becomes higher, since the quench front progresses in the core region in the absence of active material.

8.2.2.2 Influence of SBO time

The previous section has identified a domain in which core melting can be prevented or mitigated considering that a PSD is launched at CET 400 °C and that an SBO occurs at 6 h after SCRAM. Within this section, the additional influence of an early SBO on the success of core reflooding is investigated. Therefore, a parametric study on the reflooding time and the mobile equipment is performed for the sequence *AC1h*$_{PSDCET400}$. The influence of those parameters on the final CDS and the corium mass in the core is depicted in **Figure 8-13**. The influence of the SBO time can be derived by comparing these graphs with the ones in **Figure 8-12**. Additional FOMs such as the mass of corium in the LP and the time to RPV failure are shown in **Figure D.2-4**. Here, the injection is restricted to times beyond 1.20 h after PSD initiation, because the core is covered up to this time (see **Figure 8-9**).

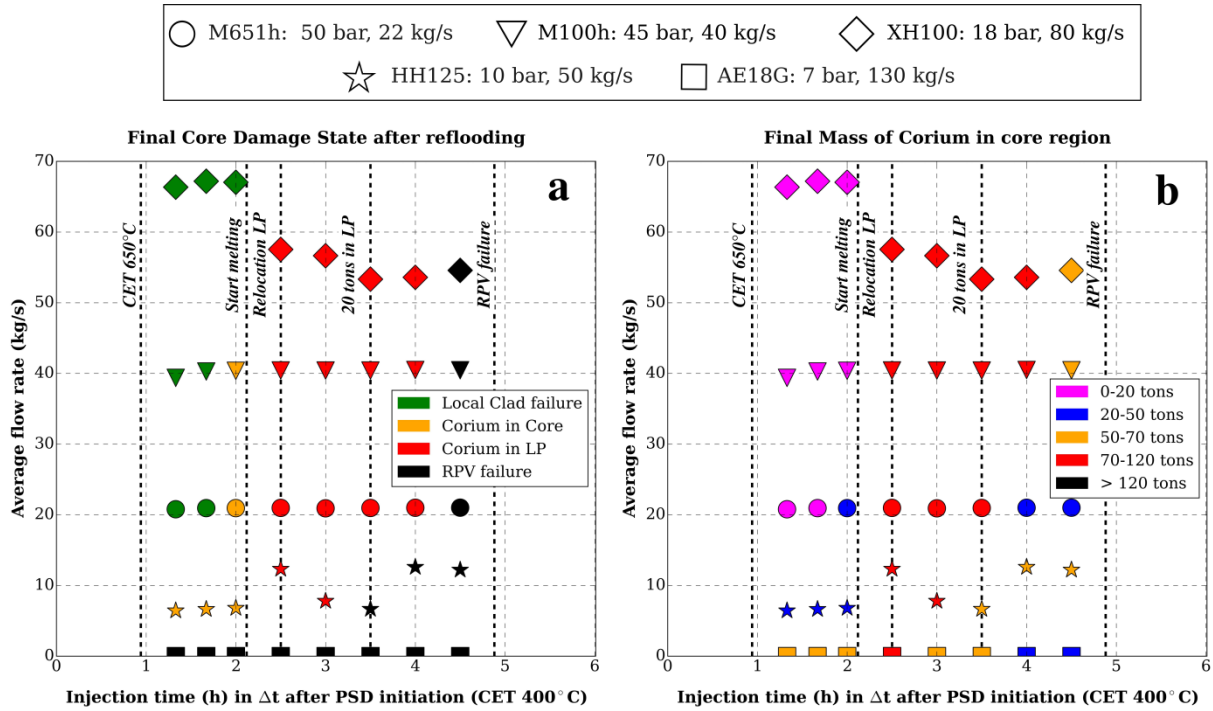

Figure 8-13: Final (a) Core Damage State, (b) Mass of corium in Core as a function of the average RMFR and the injection time (relative to PSD initiation). Black dashed vertical lines represent occurrence times of major events in the sequence *AC1h*$_{PSDCET400}$ (SBLOCA with SBO at **1 h** after SCRAM with **PSD at CET 400 °C** and without core reflooding).

Hereafter, results are compared to those obtained in section **8.2.1.1**:

- Once the PSD is initiated, the grace time to prevent core melting is higher in $AC1h_{PSDCET400}$ than in $AC6h_{PSDCET400}$ (2 h vs 20 min). This occurs because the ACCUs inject enough water into the RCS to completely cover the core in $AC1h_{PSDCET400}$. Nevertheless, in $AC6h_{PSDCET400}$, they are not capable of pushing the core liquid level above 2 m (half of the active length of the core) (see **Figure 8-9**).
- The minimum RMFR to mitigate an accident without a major damage is higher in $AC1h_{PSDCET400}$ than in $AC6h_{PSDCET400}$ (20 kg/s vs.7.75 kg/s), because the decay power is higher at CET=650 °C (32 MW vs 28.50MW). To put the times in an absolute scale, a CET 650 °C is detected at 1.00 h (since PSD initiation) + 2.50 h (between loss AC and PSD) + 1.00 h (between SCRAM and loss of AC) ~ 5 h since SCRAM in $AC1h_{PSDCET400}$, in contrast to 8.80 h in $AC6h_{PSDCET400}$. The cooling effect of the secondary side additionally contributes to the reduction of the minimum RMFR in the case of $AC6h_{PSDCET400}$. However, it seems to be very limited, since non-condensable gases start to be produced above CET 650 °C.
- Similarly to $AC6h_{PSDCET400}$, RMFRs below 5 kg/s performed at any time can neither prevent nor delay the failure of the RPV, because they cannot compensate the loss of the water inventory. Likewise, injections carried out 1 h after the relocation of 20 corium tons in the LP do not influence RPV failure regardless of the RMFR injected. Corium retention from that moment on is predicted more due to the external simulation criteria (termination 10 h after reflooding onset) than to the actual reactor conditions, which limits the validity of such finding.
- The performance of the mobile equipment is comparable to that explained for late losses of AC power (see section **8.2.1.1**) in the sense that low pressure (AE18G and HH125) and high pressure (M100h and M651h) equipment have a poor/excellent performance respectively, and medium pressure equipment has an intermediate one. However, differently to the previous chapter, the medium pressure equipment has a better performance at any time (60-80 % nominal flow rate) than in $AC6h_{PSDCET400}$.

8.2.2.3 Comparison with other studies and Discussion

The section **8.2.2** has predicted the existence of a minimum RMFR of about 7.75 – 20 kg/s to mitigate the accident without major damage (less than 20 corium tons in core) if injection is performed near CET 650 °C. These values are in accordance to the 300 gpm (~ 20 kg/s) recommended in [134] for American PWRs and to the values obtained by AREVA using MELCOR for the German Konvoi PWR [12], as discussed hereafter.

The comparison ASTEC-MELCOR is carried out in a similar way as in section **8.1.1.3**. However, there are several differences: first, the minimum RMFRs do not only depend on the time elapsed between SCRAM and CET 650 °C, but also on the state of the secondary side;

second, none of the performed ASTEC simulations started reflooding at CET 650 °C, but at a slightly different instant. Hence, two sequences have been selected for comparison:

- *AC1h$_{PSDCET400}$*, which involves a 40-min-delayed reflooding after PSD initiation. Within this simulation, reflooding is carried out shortly after detecting CET 650 °C, which occurs ~ 5.00 h after SCRAM, and the SGs are completely empty.
- *AC6h$_{PSDCET400}$*, which involves a 60-min-delayed reflooding after PSD initiation. Within this simulation, reflooding is carried out shortly before detecting CET 650 °C, which occurs ~ 8.80 h after SCRAM, and the SGs are filled above the U-tubes.

The third difference is that minimum RMFRs predicted by MELCOR are taken from different curves (see **Figure 3-8**): the first value (at 5 h since SCRAM) is taken considering that the SG is empty, while the second one (at 8.80 h since SCRAM) is taken assuming that the SG is filled above the U-tubes. The comparison is shown in **Table 8-2**.

	SCRAM-CET650°C: 5.00 h SG Empty		SCRAM-CET650°C: 8.80 h SG filled	
	ASTEC	MELCOR	ASTEC	MELCOR
RMFR minor damage	20.00 kg/s	12.50 kg/s	7.75 kg/s	5.80 kg/s
RMFR minor damage (ASTEC interpolation)	13.50 kg/s		4.50 kg/s	

Table 8-2: Comparison ASTEC-MELCOR [12] on the minimum RMFRs to mitigate the SA without major core damage. ASTEC values correspond to selected SBLOCAs.

Similarly to the investigations on MBLOCA sequences, ASTEC and MELCOR show that the minimum RMFR to prevent significant degradation decreases for longer times elapsed between SCRAM and CET 650 °C. Additionally, the minimum RMFR is reduced from 11 kg/s to 5.80 kg/s in MELCOR if the secondary side of the SGs is filled at the moment of reflooding [12]. Unluckily, this information cannot be known with the performed SBLOCA sequences in ASTEC, since none of them started injection at 8.80 h with an empty SG. It is worth noting that these values are congruent with the ones discussed in section **8.1.1.3**.

In addition, if mobile systems are used to provide this minimum RMFR, further implications regarding their deployment can be drawn.

The analysed SBLOCA sequences have shown the existence of the following time windows after the loss of AC power supply, if PSD occurs at CET 400 °C (values according to **Table D.2-2** and **Figure 8-7**):

- About 2 h up to CET 400 °C i.e. initiation of primary bleed and passive feed.
- About 3 h up to the detection of CET 650 °C i.e. close to core melting.

- About 4 h up to the relocation of corium to the LP.
- About 5 h up to RPV failure.

Practical exercises in an American three-loop Westinghouse PWR have estimated that the time window between the mobile pump deployment order and the injection into the RCS is about 2 h [147]. Extrapolating a similar measure for the Konvoi PWR, this means that the deployment order of a **high pressure pump** should be issued with a maximum delay of **1 h after the entrance in SBO** so that the pump can inject before the CET exceeds 650 °C. However, it must be present that, once the PSD is initiated, the radionuclide activity increases in the containment, which complicates the pump connection into the RCS.

In the absence of an external injection, the other path to provide core coolability would be the restoration of AC power by means of an additional grid connection or emergency DGs. Considering that the operators succeeded in restoring the AC before the CET exceeds 650 °C, it would be possible to derive the potential efficiency of the retrieved core cooling systems (see **Table 6-3**). In this case, however, the influence of a potential RCS repressurization has to be considered, in contrast to the analysis of section **8.1.1.3**.

The retrieval of one HPIS train or two CVCS trains would immediately cool down the bundle, since their efficiency is not affected by the RCS repressurization. The recovery of one train of the LPIS would have a low performance (as the rest of low pressure equipment analysed in this work), but it would be higher than the 20 % obtained with the pump HH125 due to the higher pressure head (see **Figure C.2-1**). Considering an efficiency of 20 % for one train of the LPIS, this means 30 kg/s per train. Therefore, the recovery of one train of the LPIS should also cool down the core. The recovery of the EBS may mitigate the accident without major damage if the SG has been filled, but cannot avoid RPV failure in case of an empty SG according to **Table 8-2**.

8.3 Station Blackout

The SBO sequence analysed in section **7.3** has led to high pressures in the RCS until RPV failure. Therefore, similarly to SBLOCA sequences, the prime action is to depressurize the reactor. In this case, however, the depressurization is primarily done through a secondary bleed and feed (SBF) as a preventive AM measure (see section **3.3.1.1**). If this action is not successful, the depressurization can be done through a PSD as a preventive AM measure (see section **3.3.1.2**) or, if the CET exceeds than 650 °C, as a SAM measure (see section **3.4.2**). Once the RCS is depressurized, the most imperative measure is core reflooding (see **Figure 3-6**). Within this section, the following roadmap has been followed:

Firstly, the impact of a delayed SBF in the Steam Generator B on the accident progression is investigated in section **8.3.1**. Therein, a combined analysis of the SSD delay and injection flow rate into the SGB is performed in order to quantify the maximum delay for the performance of SBF. Then, the section **8.3.2** investigates the impact of a delayed PSD and the

number of valves used for that purpose. Finally, the section **8.3.3** considers that PSD occurs at CET=400 °C by means of all pressurizer valves and investigates the combined effect of reflooding delay and the used mobile pump on the severe accident progression. A flow chart summarizing all performed SBO calculations is represented in **Figure 8-14**.

Since the behaviour of the reference sequence during the late in-vessel phase has been shown to differ from the available literature (see section **7.3.1**), the study of PSD and SSD is restricted to the early in-vessel phase of the severe accident.

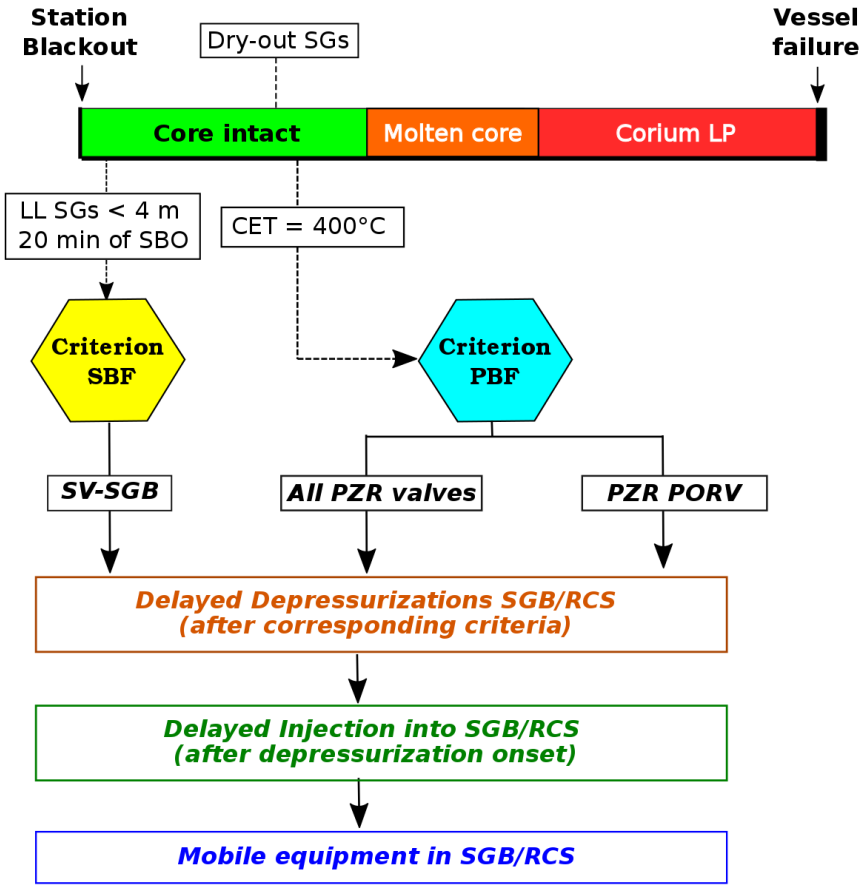

Figure 8-14: Flow chart of the performed SBO calculations (1st level: delay in PSD initiation/ SSD initiation; 2nd level: delay in core reflooding/SGB injection; 3rd level: mobile pump used for core reflooding/injection into SGB).

8.3.1 Secondary Side Depressurization (SSD) and Active Injection into the SGs

The criteria to model the SBF have been already introduced in section **6.5** (i.e. liquid level in all SGs is lower than 4 m or 20 min without AC power). Within this section, the sequence *Ref-SBO* is subjected to a delayed SSD ranging from 0-120 min. The depressurization is performed in Steam Generator B following its isolation from the other SGs. Injection is modelled with a 10-min delay after SSD initiation by means of several mobile pumps. Further injection delays could have been simulated, but the outcomes would have been unrealistic due to the risk of thermally induced SGTR [94]. The section is divided in three parts: study of

SBF at different times (fixed mobile pump); with different mobile systems (fixed injection time); and at different times with different mobile systems.

The criteria to finish the simulations are identical to the ones introduced at the beginning of section **8.1.1**: core liquid level higher than *min3* (15 cm above core head), final time of the simulation is reached (i.e. 10 h since injection onset) and RPV failure.

- *Influence of SBF time*

First, the study focuses on the effect of a delayed SBF of SGB (with respect to the fulfilment of SBF criteria – see section **6.5**) on the accident progression. The SBF consists of a depressurization of the SGB followed by a 10-min delayed water injection using the pump HH80 (see **Table 6-2**). The impact of such measure on the RCS pressure and the hydrogen mass flow rate circulating through the SGB U-tubes is shown in **Figure 8-15**. The sequence without any AM measure (*Ref-SBO*) has also been included. The start of hydrogen generation in *Ref-SBO* is indicated by an orange vertical line; red crosses and blue triangles mark the initiation of bleed and feed; black points mark RPV failure occurrences. Additional variables can be found in **Figure D.3-3**. Results are analysed according to the conditions of the RCS at the moment of SBF initiation. It is worth to point out that the *Ref-SBO* leads to a total dry-out of the SGs (and hence voiding in RCS) at about 1.20 h after SCRAM i.e. 0.87 h after transgression of SBF criteria.

For an overheated but not voided reactor (30 min-delayed SBF) or for a slightly voided reactor (1 h 30 min-delayed SBF) i.e. core slightly uncovered with hot legs in saturation, the RCS can be cooled down and core degradation can be prevented. This is reflected in the inexistent hydrogen generation and a core liquid level above 4 m during the whole transient (see **Figure D.3-3**). In case of a 1 h 30 min-delayed SBF, the cooldown of the RCS is particularly fast due to the lower thermal inertia of the steam circulating through the U-tubes compared to water. This rapid tendency is in contrast to the one with 30-min delay, where a broader time window is needed to cool down the RCS. The limit for this behaviour is the total dry-out of the SGs i.e. 0.87 h after transgression of SBF criteria.

For a strongly voided reactor with a large amount of non-condensable gases (3 h-delayed SBF), RPV failure cannot be prevented, but can be delayed 2 h with respect to *Ref-SBO*. In this case, SBF also leads to an initial cooldown. Nonetheless, differently to the previous cases, this is not translated in a significant increase of the core liquid level due to the presence of the non-condensable gases (see **Figure 8-15**). Therefore, the core continues overheating and the RCS pressure increases up to the end of the transient.

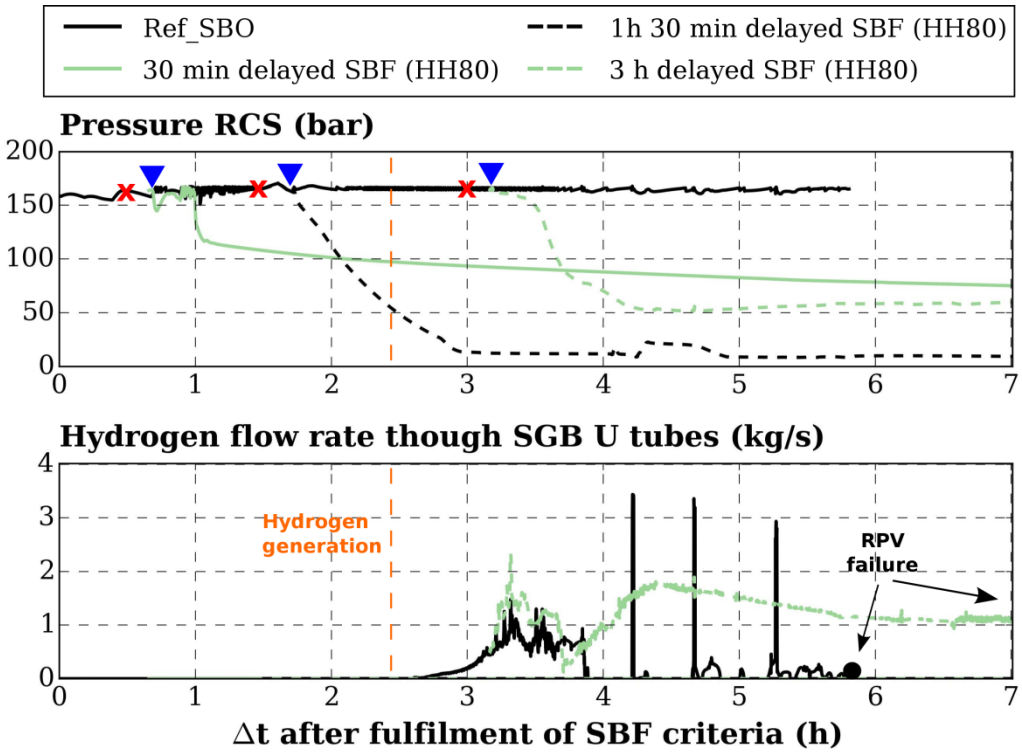

Figure 8-15: Influence of a delayed SBF (after transgression of SBF criteria) of SGB by means of HH80 on the RCS pressure and the hydrogen flow rate through the SGB U-tubes compared to *Ref-SBO* (SBO at **0 h** without AM measures). The orange vertical line marks hydrogen generation onset in *Ref-SBO*; crosses/triangles mark bleed/feed initiation black dots mark RPV failure occurrences.

The same analysis has been performed using the equipment M651l, which provides a mass flow rate of about 10 kg/s into the SGB, in order to extract additional insights. The evolution of the pressure and the core liquid level is depicted in **Figure 8-16** as a function of time after the SBF criteria were fulfilled, together with the reference sequence *Ref-SBO*. Further information can be found in **Figure D.3-4**.

Results show that SBF by means of M651l is effective to prevent core degradation if is performed before the release of hydrogen from the core (see increasing liquid level in **Figure D.3-4**). However, in contrast to HH80, the injection is not able to cool down the RCS, which remains at high pressure regardless of the SBF initiation time. This means that the SGB is condensing the steam, which enters into the core through the downcomer, whereas the water in contact with the upper part of the core is evaporating and accumulating in the upper part of the RCS.

Based on these two cases, it can be concluded that, if the pumps M651l and HH80 are used to perform the feed of SGB, the SBF should be initiated with a maximum delay of 1 h 30 min after the fulfilment of the SBF criteria.

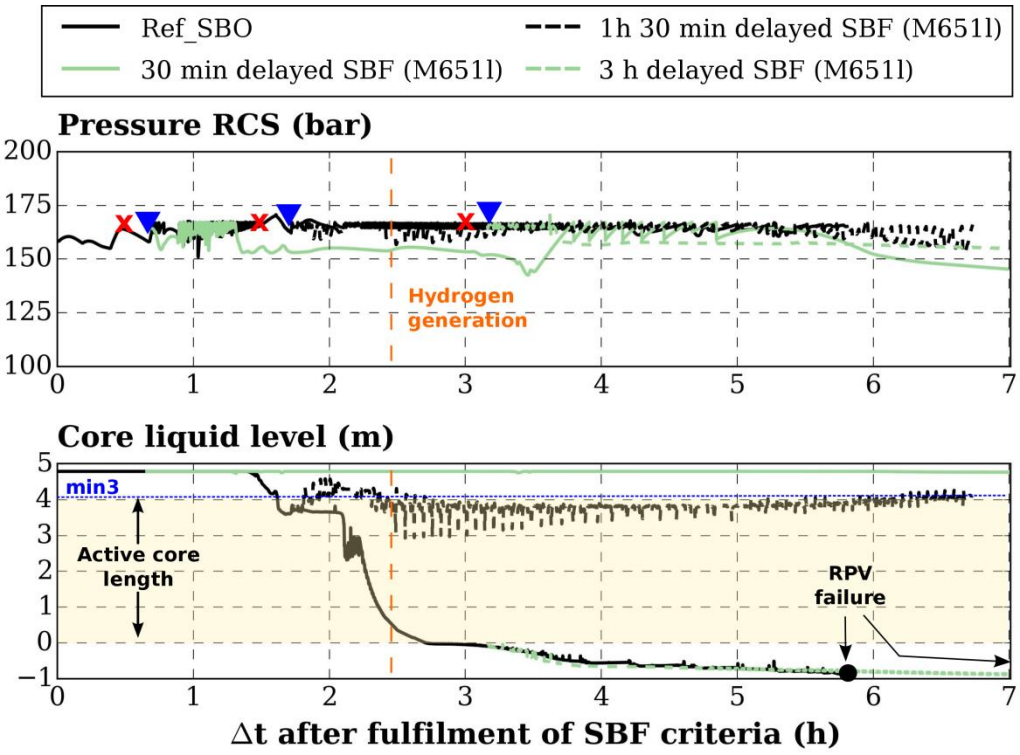

Figure 8-16: Influence of a delayed SBF (after transgression of SBF criteria) of SGB by means of the pump M651h on the RCS pressure and the core liquid level in comparison to *Ref-SBO* (SBO at **0 h** without AM measures). The orange vertical line marks the onset of hydrogen generation in *Ref-SBO*; crosses/triangles mark bleed/feed initiation; black dots mark RPV failure occurrences.

- *Influence of mobile equipment*

The analysis now focuses on the influence of different mobile systems (see features in **Table 6-2**) on the accident progression. The SBF consists of a 1.50 h-delayed bleed after the fulfilment of SBF criteria (see section **6.5**) and a 10-min delayed feed after bleed initiation. The impact of such measure on key plant variables is shown in **Figure 8-17**, together with the reference sequence *Ref-SBO*. The orange vertical line marks the onset of hydrogen generation in the sequence without SBF (*Ref-SBO*); the red and blue lines mark the initiation of bleed and feed respectively; black points mark RPV failure occurrence. Additional can be taken from **Figure D.3-5.** Results are analysed according to the mass flow rate injected by the equipment into the SGB.

Mass flow rates of more than 15 kg/s into the SGB (e.g. pump *HH80*), are able to cool down the reactor and prevent core melting. Furthermore, this causes a significant steam condensation in the U-tubes, which yields a rise in the core liquid level.

On the contrary, flow rates below 5 kg/s (e.g. pump *M403l*) are only able to condense a minor quantity of steam in the U-tubes, this being not sufficient to yield an increase of the water level above the top of the core. Since the steam cannot be condensed, the pressure in the

reactor remains high until the end of the transient. This behaviour is similar to the one of the reference sequence, but the simulation could not reach the end due to numerical problems.

Flow rates in a range from 5-15 kg/s (e.g. pump *M651*) manage to prevent core melting, but not to cool down the RCS, which remains at high pressure levels. This behaviour exhibits a mixture of the two previous cases. On one hand, since there are no no-condensable gases flowing through the RCS, water injection leads to steam condensation in the U-tubes. In turn, this leads to a gradual increase of the core liquid level. On the other hand, since the cooling capacity of the SGB is very small, the generated steam remains in the primary loop at high temperatures providing a high pressure level.

Therefore, it can be concluded that, if SBF is performed with 1 h 30 min delay with respect to the SBF criteria, an injection rate of 10 kg/s is needed in SGB in order to prevent core melting. However, a higher injection rate is necessary to depressurize the RCS.

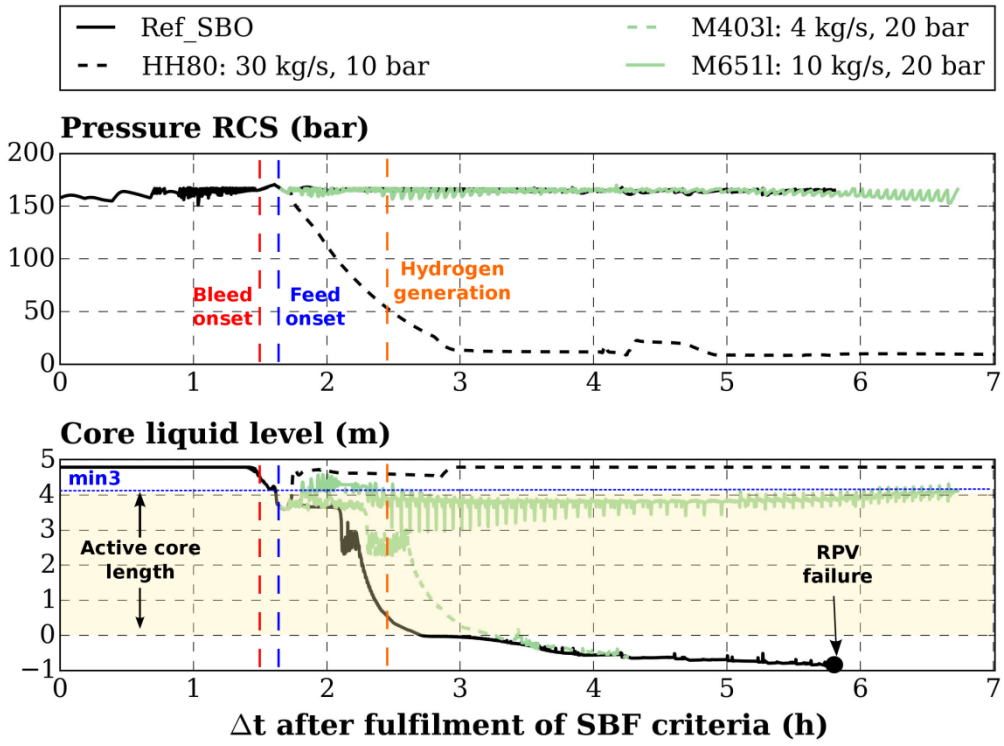

Figure 8-17: Influence of mobile equipment during a 1.50 h-delayed SBF (after transgression of SBF criteria) of SGB on the RCS pressure and the core liquid level compared to *Ref-SBO* (SBO at **0 h** without AM measures). The orange vertical line marks the onset of hydrogen generation in *Ref-SBO*; red/blue lines mark the initiation of bleed/feed; black points mark RPV failure occurrences.

➢ *Influence of SBF time and Mobile Equipment on selected FOMs*

Repeating the analysis for different injection times and various mobile systems, it is possible to identify the optimal time domain and equipment type to perform SBF in SGB. The selected FOMs are: the final Core Damage State (**Figure 8-18**-a), the corium mass in the core (**Figure 8-18**-b), the RCS pressure (**Figure 8-18**-c) and the time to RPV failure (relative to

SBF initiation) (**Figure 8-18**-d). Additional values can be found in **Figure D.3-6**. The graphs can be read using the methodology of section **8.1.1.1**. However, two aspects differ: first, core intact is used as a final CDS instead of local cladding failure; second, the vertical lines represent the occurrence times of major events in *Ref-SBO* (SBO at 0 h after SCRAM without AM measures).

Results show that mobile pumps providing less than 5 kg/s of water into the SGB (e.g. M403) cannot prevent or delay a RPV failure irrespective of the SBF initiation time. Concerning the efficiency of mobile equipment, systems with a pressure head above 20 bars are not affected by the repressurization of the SGBs upon injection and hence, inject a constant mass flow rate. On the other hand, systems with a head below 10 bars have a varying performance depending on the temperature of the U-tubes upon injection.

As concerns the pump equipment injecting more than 10 kg/s of water into the SGB, the following results are obtained:

- SBF manages to prevent core degradation if it is performed before CET>400 °C. From that point in time, the heat transfer between RCS and secondary side is worsened by the presence of hydrogen in the U-tubes of SGB (see **Figure 8-15**), which hinders steam condensation in the SGs.
- The cooldown behaviour depends on the cooling capacity of the secondary side, which in turn depends on the mass flow rate injected in SGB. For example, M100l is able to reduce RCS pressures below 50 bars, in contrast to M651l (see **Figure 8-18**-c). This is caused by a higher steam condensation and thereby a greater sub-cooling degree. Additionally, the cooldown rate depends on how much the RCS is voided at SBF initiation: the presence of water (SBF before 0.87 h) leads to a slow cooldown rate originating from the high thermal inertia of water, whereas the presence of steam allows a faster depressurization.
- SBF can still be beneficial if it is performed as soon as CET exceeds 650 °C, since it mitigates the SA. In such cases, steam condensation and the intervention of ACCUs allow for the accumulation of only 20 corium tons in the core. The higher the mass flow rate injected, the earlier the reactor core is covered by water (see effect of HH80 in **Figure 8-17**).
- For later times, SBF cannot mitigate the SA, because the increasing concentration of hydrogen hinders the steam condensation in the U-tubes of the SGB. Therefore, the core remains uncovered and the steam continues overheating. This translates into an increase of pressure in the RCS (see effect of 3-h delayed SBF in **Figure 8-15**).

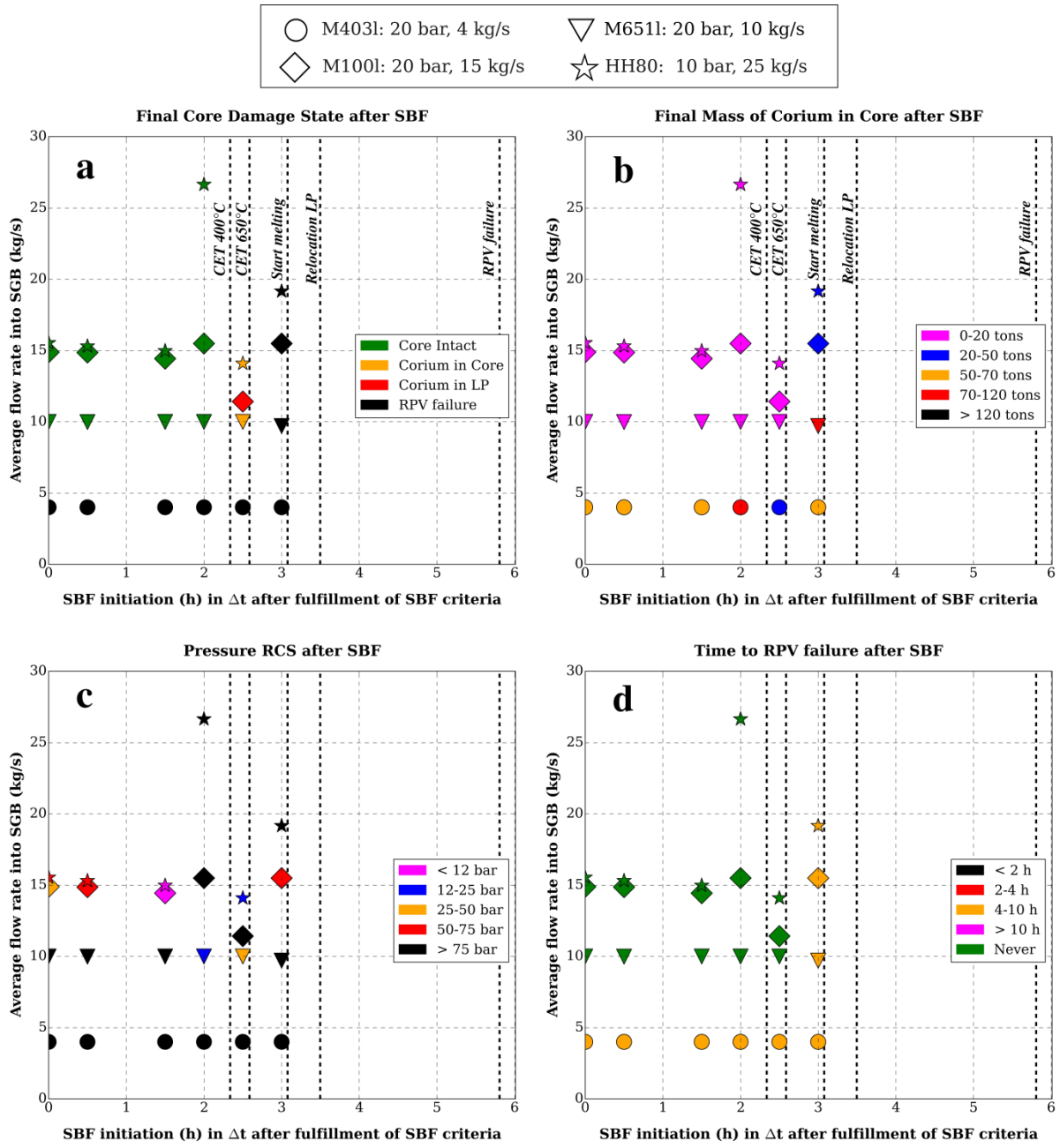

Figure 8-18: Final (a) Core Damage State, (b) Mass of corium in core, (c) Pressure in the RCS and (d) Time to RPV failure (relative to SBF initiation) as a function of the average injection rate into the SGB and the SBF initiation relative to the fulfilment of SBF criteria. Black dashed vertical lines represent occurrence times of major events in *Ref-SBO* (SBO at **0 h** without AM measures).

8.3.1.1 Comparison with other studies and Discussion

A sketch illustrating the most relevant findings of section **8.3.1** regarding SBF of SGB can be found in **Figure 8-19**. Therein, the occurrence times of the reference scenario and of the six most representative sequences involving SBF are represented.

The performed calculations performed show that the RCS can be depressurized without core melting if SBF is performed before CET exceeds 400 °C and if a **minimum mass flow**

rate of 15 kg/s is injected into the depressurized SG. This value is similar to the 200 gpm (about 12.50 kg/s) suggested in [134]. Beyond that time, the hydrogen generated in the core hinders a RCS cooldown regardless of the injection rate. Therefore, these results suggest that the **priority should be shifted from SSD to PSD when a CET>400 °C**. This is in agreement with the current AM procedures in the German Konvoi PWR [15]. Despite SBF is no longer effective in terms of RCS depressurization beyond that time, this does not mean that the action should not be performed. In fact, the action is still beneficial, because it reduces the risk of a thermally induced SGTR [94].

Taking into account that SBF conditions are detected at 0.33 h and that CET=400 °C at 2.66 h after the loss of AC power supply, there is a time window of **2 h for the performance of SBF if all conditions for that procedure are satisfied**. This is in line with the 1.60 h predicted by SCDAP/RELAP for a German Konvoi PWR [15]. The time window seems to be sufficient to connect a **low-medium pressure pump (e.g. 10-20 bars)** into the SG, providing that the plant crew has issued the order of deployment as soon as the SBF criteria are met. It should be pointed out that this time is conservative and can be even more extended if passive injections into the SG are considered (see section **6.5**).

This work considers an instantaneous bleed and feed of the secondary side, since the SSD is always followed by a 10-min delayed water injection into the SGs. For further injection delays, thermally induced SGTR may occur. However, if passive feeding was considered, the U-tubes would be covered over a longer time, and the study of a delayed injection since SSD initiation could be performed similarly to the study of PSD in SBLOCAs (see section **8.2.2**).

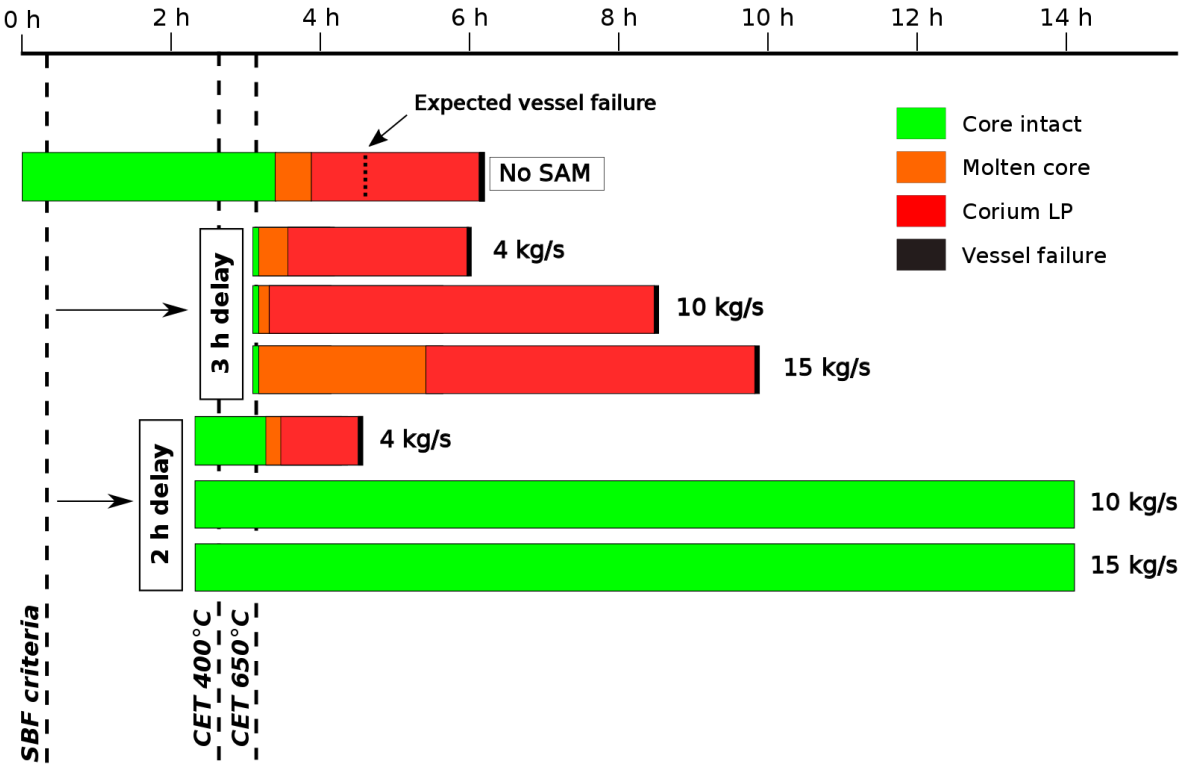

Figure 8-19: Sketch summarizing the effect of Secondary Bleed and Feed in SGB during an SBO.

8.3.2 Primary Side Depressurization and Passive Core Reflooding

If the secondary side actions do not turn to be successful, the AM procedures of the Konvoi PWR foresee a PSD by means of all pressurizer valves as a preventive or mitigative AM measure (see **Figure 3-4** and **Figure 3-6**). The measure is tagged as preventive or mitigative depending on when the action is initiated (i.e. before or after CET 650 °C).

The study on PSD is divided in two parts: in section **8.3.2.1**, it is assumed that PSD by means of all pressurizer valves is initiated with a delay ranging from 0 min to 2 h after the detection of CET 400 °C (see section **6.5**). The section **8.3.2.2** assumes that PSD is initiated at CET=400 °C by means of the PORV or all pressurizer valves in order to quantify the impact of the number of opened pressurizer valves on PSD performance.

8.3.2.1 Influence of PSD initiation

Here, the influence of a delayed PSD (after the detection of a CET 400 °C) by means of all pressurizer valves is investigated. For that aim, the grace times gained due to PSD (with respect to the sequence *Ref-SBO*) are represented in **Figure 8-20** as a function of the PSD delay (relative to the detection of a CET 400 °C). The graph can be read following the same indications as section **8.2.1**. However, they differ in two aspects: first, the black dashed vertical lines represent the occurrence times of major events in *Ref-SBO* (SBO at 0 h after SCRAM without AM measures); second, the relocation of 20 corium tons in the LP has been omitted, since *Ref-SBO* predicted RPV failure with less than such amount (see section **7.3.1**).

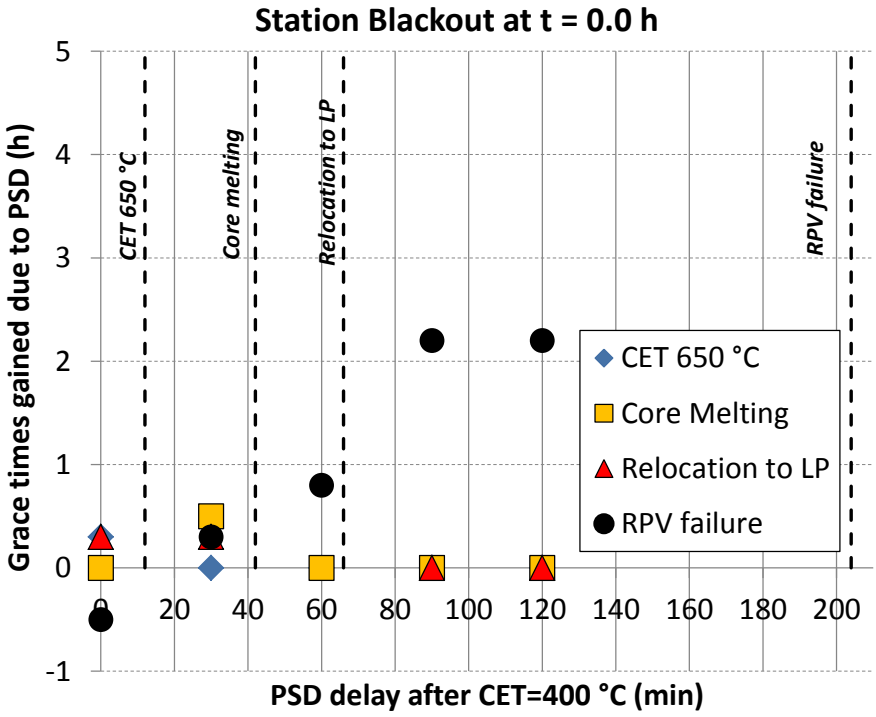

Figure 8-20: Grace times gained due to PSD in comparison to the sequence *Ref-SBO* (SBO at **0 h** without AM measures) as a function of the PSD delay after the detection of CET=400 °C. Black dashed vertical lines mark occurrence times of major events in *Ref-SBO*.

The previous graph is supported by **Figure 8-21**, which illustrates the impact of a PSD delay on relevant plant variables as a function of the time after the detection of CET 400 °C. Therein, red crosses mark PSD initiation (for the sequences involving PSD), whereas black points mark RPV failure occurrence. Additional variables, such as the hydrogen and steam mass in the RCS and the corium masses in the core and LP can be found in **Figure D.3-7**.

Results from **Figure 8-21** show that the RCS is slightly repressurized in case of a 1 h-delayed PSD compared to a 30-min delayed PSD. This happens because a 1-h delayed PSD leads to the reflooding (due to injection of the ACCUs) of a partially degraded core (see corium mass in core in **Figure D.3-7**) in contrast to a 30-min delayed PSD. Therefore, in the first case, the generated steam repressurizes the RCS and delays the following injection from the ACCUs. In turn, this is translated into a slightly longer extension (few minutes) of the depressurization process.

The effect of PSD on the temperatures can be deduced from the core net power. Depressurizations with up to 1 h delay lead to an enhanced power extraction from the core, which contributes to cool down the bundle before the ACCUs start the injection (see power extraction from core and PCT in **Figure 8-21**). After the ACCUs are empty, vaporization continues and the PCT increases up to 2500 K, causing first a cladding failure, then core melting and relocation to the lower plenum ultimately ending up in a RPV failure.

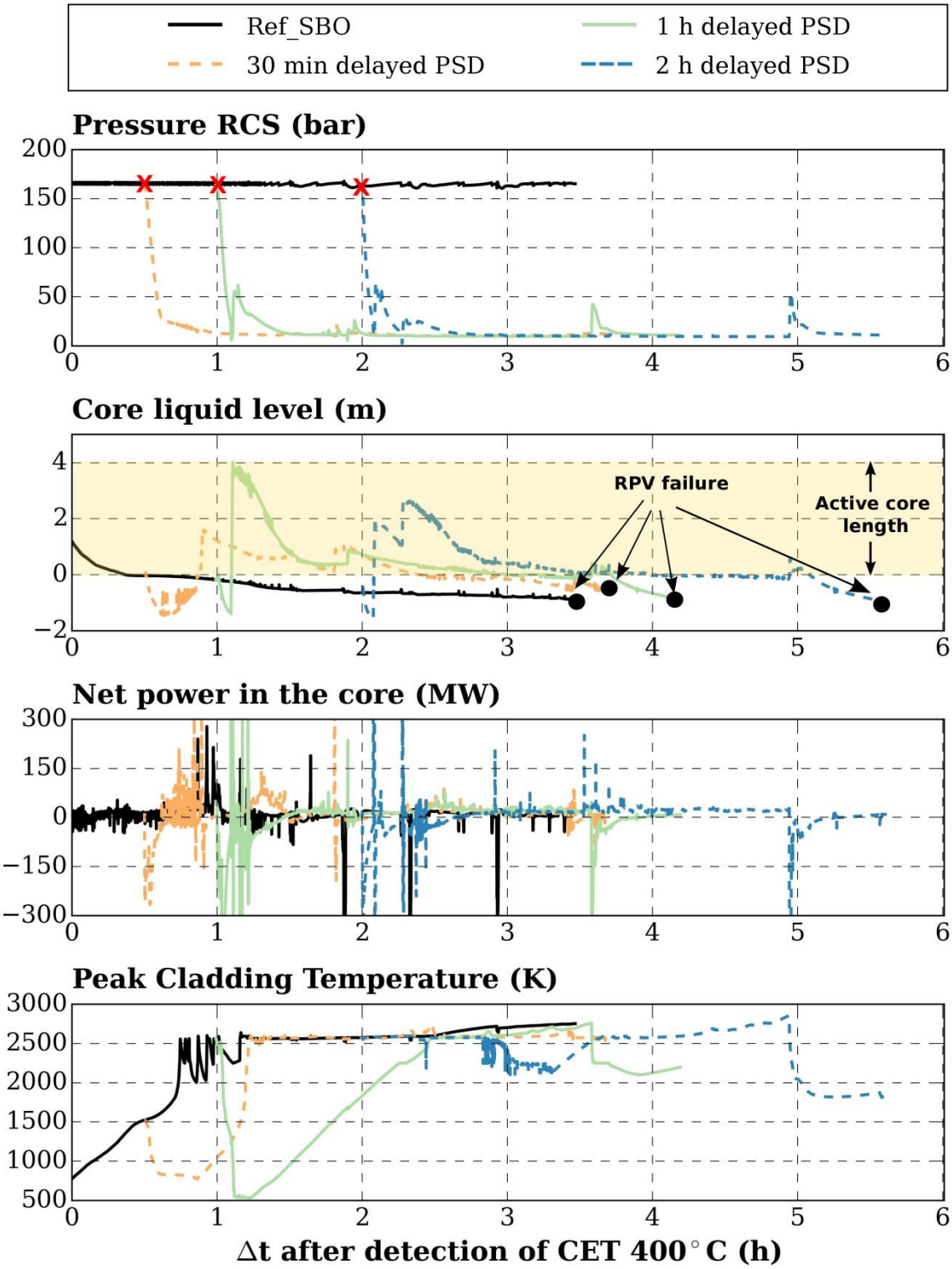

Figure 8-21: Influence of a delayed (after the detection of CET=400 °C) PSD with all pressurizer valves on the evolution of a first set of variables in comparison to the sequence *Ref-SBO* (SBO at **0 h** without AM measures). Red crosses mark PSD initiation (for the cases involving PSD); black points mark RPV failure occurrences.

Discrepancies arise for longer delays (2 h delayed PSD): despite the PCTs are above 2000 K (see **Figure 8-21**), the injection from the accumulators does not lead to any temperature escalation or further corium release into the core region (see **Figure D.3-7**), which remains constant until the end of the simulation. Reasons behind this discrepancy may be related to the unusual behaviour of *Ref-SBO* during the late in-vessel phase (within 2-6 h after the loss of AC power), as discussed in section **7.3.1**.

Overall, the global benefit of PSD is the prevention of RPV failure at high pressures. However, according to **Figure 8-20**, it does not yield a considerable extension of the grace time to onset of core melting, corium relocation to the LP or RPV failure. In fact, it may even anticipate some of these events (e.g. RPV failure occurs 0.5 h earlier than reference case for PSD at CET 400 °C). The longest grace time to prevent RPV failure is predicted for a 90-min-delayed PSD or later. However, as discussed later in section **8.2.1**, the validity of this result is disputable due to the lack of ASTECV2.0 capabilities to simulate degraded core reflooding.

8.3.2.2 Influence of the number of valves used for PSD

Now, it is assumed that PSD is initiated by the operator at CET 400 °C and the aim is to study the impact of depressurizing the RCS by means of one (PORV) or all (PORV, SV1 and SV2) pressurizer valves. The influence of the number of valves on the evolution of key plant variables is shown in **Figure 8-22** as a function of the time after the detection of CET 400 °C. The evolution of additional variables can be taken from **Figure D.3-8**. Similarly to previous graphs, red crosses mark PSD initiation, whereas black points mark RPV failure occurrence.

The computational results show that RCS depressurization takes about 20 min and occurs without RCS repressurization if all pressurizer valves are used for such purpose. On the other hand, a PSD at CET 400 °C by the only means of the pressurizer PORV requires at least 1 h to drive the pressure below the set-point of the ACCUs (i.e. 25 bars), which repressurize the RCS upon reflooding due to the high temperature levels in the core region (see PCTs in **Figure 8-22**). The repressurization becomes stronger in case of a 1 h-delayed PSD (see the sharp pressure increase up to 180 bars in **Figure 8-22**) due to the generation of more than 2 steam tons upon reflooding (see **Figure D.3-8**).

The calculations also show that the core heat-up is delayed if PSD is performed with the PORV instead of all pressurizer valves (see PCTs in **Figure 8-22**). This happens because of the higher mass flow rate of steam going through the core in the first case, which allows a higher power extraction from the core until the RCS gets repressurized.

All things considered, despite the PSD by means of the pressurizer PORV slightly delays core melting, the use of all pressurizer valves always exhibits more benefits in the sense of providing more coolant to the RCS (and hence delaying a RPV failure) and especially avoiding a RPV failure at medium-high pressures.

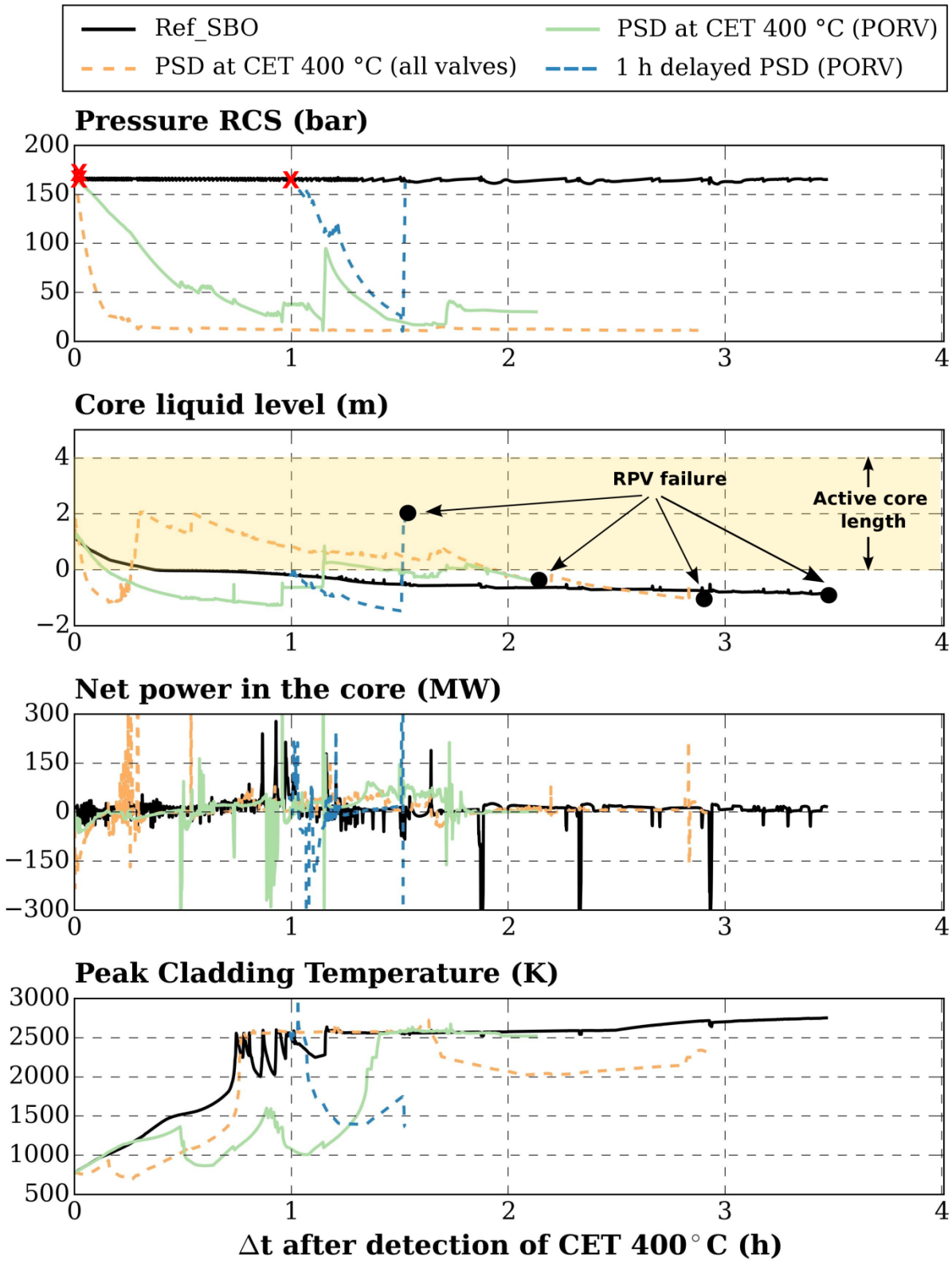

Figure 8-22: Influence of delayed PSD by means of the pressurizer PORV on the evolution of a first set of variables in comparison to *Ref-SBO* (SBO at **0 h** without AM measures) and to the case where PSD is initiated at CET 400 °C by means of all pressurizer valves. Red crosses mark PSD initiation (for the cases involving PSD); black points mark RPV failure occurrences.

8.3.2.3 Comparison with other studies and Discussion

The calculations presented in section **8.3.2** suggest that the most appropriate time to initiate PSD in terms of delaying RPV failure is 1-2 h delay after detecting CET 400 °C. This finding is a direct consequence of the unusual behaviour (mild degradation) of the reference sequence without AM during the late phase (see section **7.3**) and hence, its validity is limited. Therefore, it seems more reasonable to discuss the findings based on early PSDs (with 0-1 h delay), which also present a similar behaviour to the one predicted by ATHLET-CD [145].

Restricting the domain to such time window, the calculations have shown that PSD should be executed by means of **all pressurizer valves** in order to reduce the RCS pressure, even if the time to RPV failure is decreased with respect to the case without SAM measures. As far as the time is concerned, calculations have predicted that the optimum time to initiate PSD is 30-60 min after detecting CET 400 °C due to the increase of void in the RCS. However, it is difficult to imagine that the plant crew will wait some minutes under such stressful conditions. Summarizing all aspects, the calculations suggest that **PSD should be performed by means of opening all pressurizer valves once CET>400 °C** or, if not possible, during the following 30 min.

8.3.3 Primary Side Depressurization and Active Core Reflooding

Once the RCS is depressurized through a PSD, the following SAM measure is the injection of water into the RCS (see **Figure 3-6**). Within this section, the sequence *Ref-SBO*$_{PSDCET400C}$ (with PSD at CET 400 °C) is subjected to core reflooding. The injection occurs with different delays after PSD initiation by means of different mobile systems. The criteria to finish the simulations are alike sections **8.1.1** and **8.2.2** (i.e. core liquid level, time elapsed after reflooding onset and RPV failure). For this aim, the section is divided in three parts: study of core reflooding (1) at different injection times (fixed pump), (2) with different mobile pumps (fixed injection time) and (3) at different injection times and with different mobile pumps.

- *Influence of injection time*

Firstly, the attention is focused on the injection time. The influence of a delayed reflooding on selected variables is shown in **Figure 8-23** as a function of the time after PSD initiation (at CET 400 °C). The graph also includes the evolution of the sequence without active core reflooding (*Ref-SBO*$_{PSDCET400C}$). Additional variables such as the RCS pressure, the hydrogen generation rate and the mass of steam in the RCS are shown from **Figure D.3-9** to **Figure D.3-10**. The behaviour is analysed according to the Core Damage State at injection time:

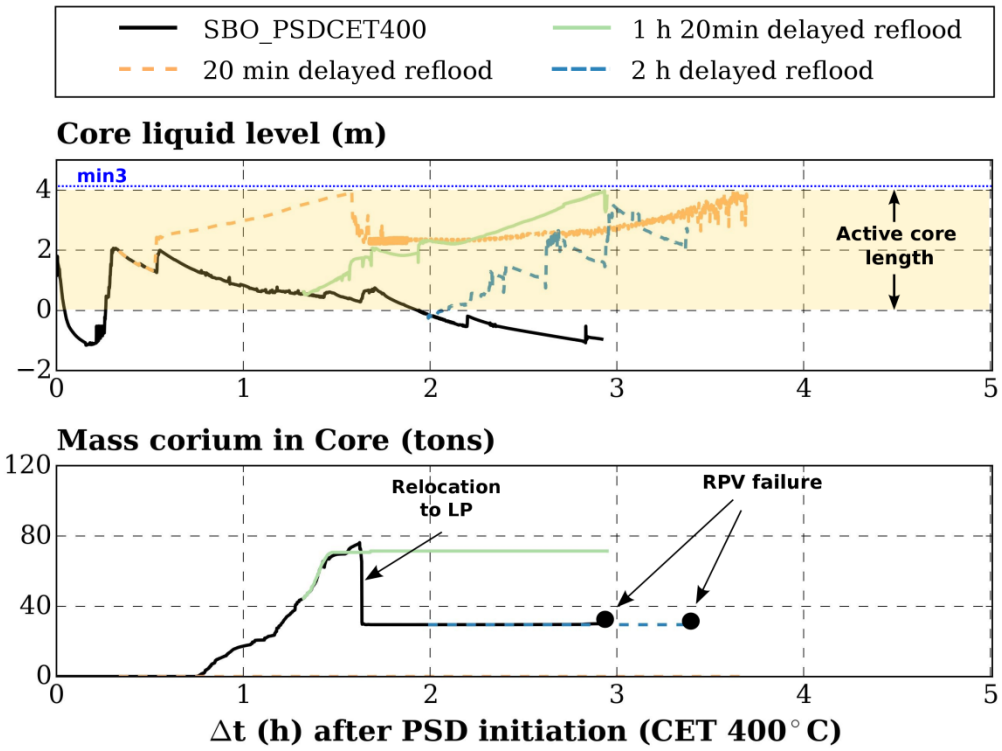

Figure 8-23: Influence of a delayed reflooding (after PSD initiation i.e. CET 400 °C) by means of M651h on the evolution of the core liquid level and the corium mass in the core in comparison to $SBO_{PSDCET400}$ (SBO at **0 h**, with **PSD at CET 400 °C** and without core reflooding). Black points mark RPV failure occurrences.

Reflooding of an intact core (e.g. 20 min-delayed reflooding) leads to an increase of the core liquid level, the recovery of the sub-cooling and an immediate core cooldown (see PCTs in **Figure D.3-9**). However, as soon as the RCS pressure decreases, water evaporates and saturated steam is generated. Correspondingly, the core liquid level decreases suddenly (at 1.5 and 1.9 h respectively). From this point in time, the quench front progression is slowed down, but the low core temperatures prevent further oxidation and core degradation.

Reflooding of a degraded core i.e. 20-60 corium tons in core, which is the case of a 1 h 20-min delayed reflooding, causes massive steam generation and hydrogen generation (see **Figure D.3-9**). As a result, the RCS is repressurized. For longer delays (e.g. 2-h delayed reflooding) reflooding causes pressure fluctuations and thereby oscillations on the temperature and the core liquid level. Despite the rise of the core liquid level, reflooding cannot stop the temperature increase of the metallic layer. Therefore, a RPV failure cannot be prevented.

- *Influence of mobile equipment*

This analysis focuses on the influence of different mobile pumps (see **Table 6-2**) on the core liquid level and the corium mass in the core for a 40-min delayed injection (relative to PSD initiation). The evolution of such variables is shown in **Figure 8-24** as a function of the

time after PSD onset (at CET 400 °C). The evolution of the sequence without active core reflooding (*Ref-SBO$_{PSDCET400C}$*) has also been included. The evolution of additional variables can be taken from **Figure D.3-11** and **Figure D.3-12**. The behaviour is analysed according to the type of mobile equipment used in the analysis:

The low pressure pump *AE18lp* supplies a null RMFR (although it could potentially inject 120 kg/s), because the RCS is instantaneously repressurizing upon injection from the ACCUs. Therefore, the overall efficiency of this pump is close to 0 %. On the other hand, the high pressure equipment *M651h* supplies its nominal mass flow rate, because it is capable of overcoming the actual RCS pressure peaks at any time. Therefore, the efficiency of this pump is close to 100 %. A similar behaviour is observed for the pump *XH100*, whose efficiency is more affected by the RCS repressurization due to the lower pressure head than *M651h* (efficiency of 80 %). Therefore, the obtained results comply with the conclusions drawn from SBLOCA sequences (see section **8.2.2**).

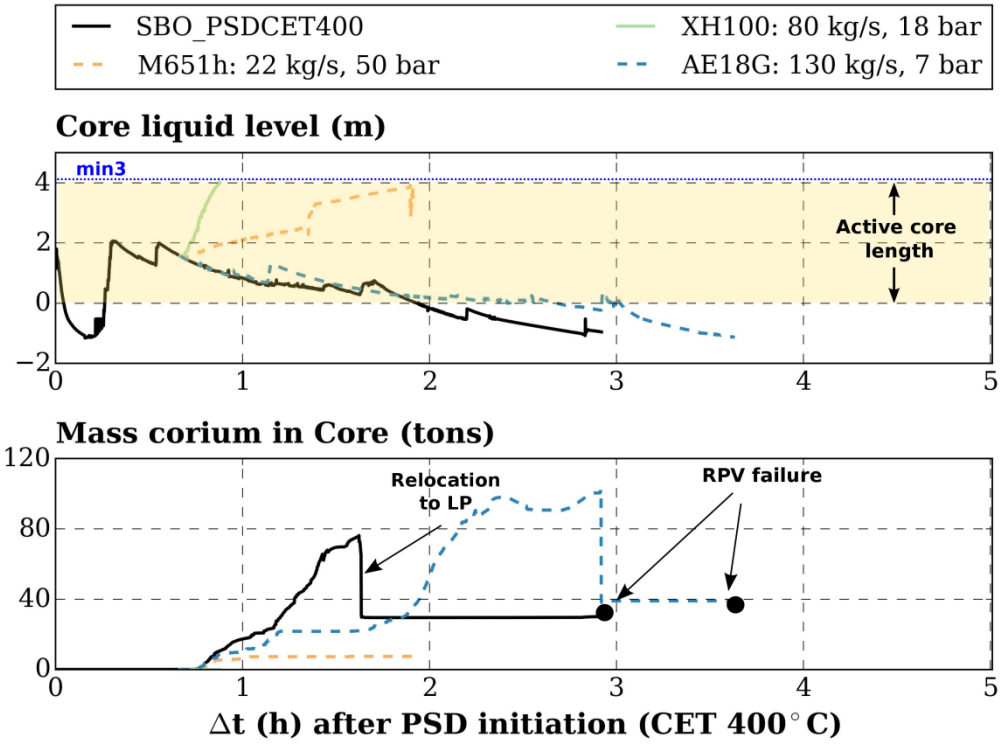

Figure 8-24: Influence of mobile equipment for a 40-min delayed reflooding (after PSD initiation) on the evolution of the core liquid level and the corium mass in the core compared to *SBO$_{PSDCET400}$* (SBO at **0 h**, with **PSD at CET 400 °C** and without core reflooding). Black points mark RPV failure occurrences.

➢ *Influence of injection time and Mobile Equipment on selected FOMs*

Repeating the analysis for further injection times and mobile systems, it is possible to identify the optimal region to execute core reflooding. The selected FOMs are the final CDS (**Figure 8-25**-a), mass of corium in the core (**Figure 8-25**-b) and in the LP (**Figure 8-25**-c)

and the time to RPV failure after PSD initiation (**Figure 8-25**-d). Further FOMs such as the hydrogen generation, the mass of water needed and the RCS pressure at the end of the simulation as well as the refilling time can be found in **Figure D.3-13**.

The graphs can be read using the methodology described in section **8.2.2.1**. Here, the vertical lines represent the previous damage curves of the reference sequence with PSD at CET 400 °C and without core reflooding (*Ref-SBO*$_{PSDCET400C}$). Based on these diagrams, the following observations are made:

- Injections initiated shortly after CET>650 °C manage to refill the core in less than 30 min with localized burst of some claddings if RMFRs are higher 40 kg/s (**Figure 8-25**-a, **Figure D.3-13**-h). This requires the availability of less than 1 water ton (**Figure D.3-13**-f). RMFRs higher than 20 kg/s may terminate the accident without major damage if the injection is launched in the following 30 min after the detection of a CET=650°C. However, in that case, refilling times increase are longer than 2 h and 3-5 water tons are required.
- Injections initiated 1 h after the relocation of 20 corium tons into the LP cannot prevent or delay RPV failure. Although corium retention is predicted for RMFRs above 40 kg/s, this occurs more due to external simulation criteria (level above *min3*) than to the conditions in the RCS. In particular, the presence of 60 corium tons during 30 min in the LP should lead ultimately to RPV failure (see **Figure 8-23**).
- In between, corium retention is predicted either in the core or in the LP. However, as mentioned in MBLOCA and SBLOCA studies, the validity of this finding is limited due the lack of ASTECV2.0 capabilities to simulate degraded core reflooding.
- The high and (to a lower extent) the medium pressure pumps, have an excellent performance. This is in contrast to the low pressure pumps, which are essentially affected by the RCS repressurization. For the particular case of the medium pressure pump, the efficiency depends on the Core Damage State upon injection (injection time). This behaviour is congruent with the findings of section **8.2.2** (i.e. SBLOCA sequences).

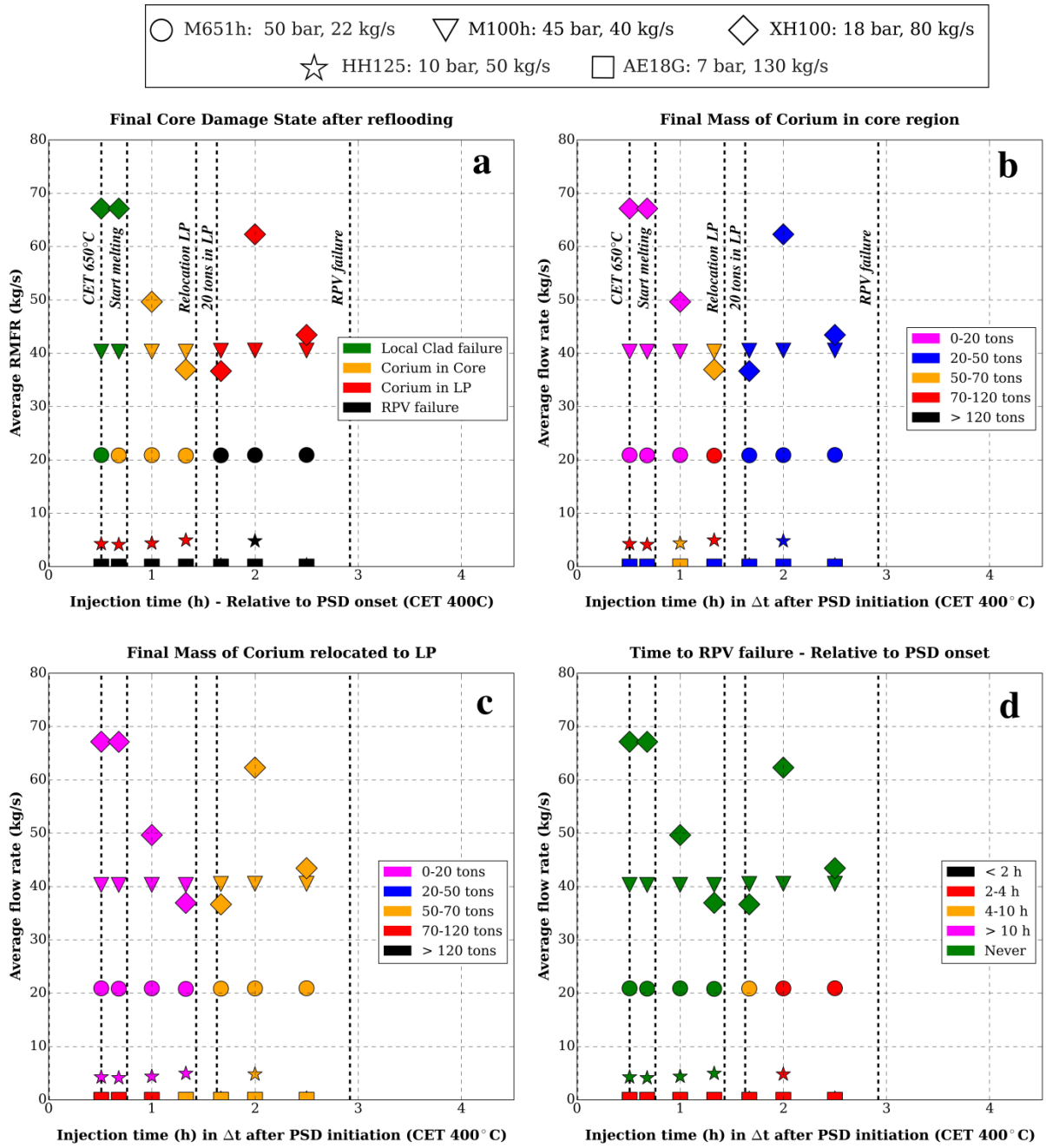

Figure 8-25: Final (a) Core Damage State, (b) Mass of corium in Core, (c) Mass of corium in the LP and (d) Time to RPV failure as a function of the average RMFR and the injection time (relative to PSD initiation). Black dashed vertical lines represent occurrence times of major events in the sequence *Ref-SBO$_{PSDCET400C}$* (SBO at **0 h** after SCRAM, with **PSD at CET 400 °C** and without core reflooding).

8.3.3.1 Comparison with other studies and Discussion

Similarly to the study of SBF, the **Figure 8-26** illustrates the most relevant findings concerning PSD and core reflooding. Therein, the occurrence times of the reference scenario without AM measures, of the scenario with PSD at CET=400 °C and of four scenarios involving reflooding after the aforementioned PSD are depicted. Further implications from the obtained results are explained here below.

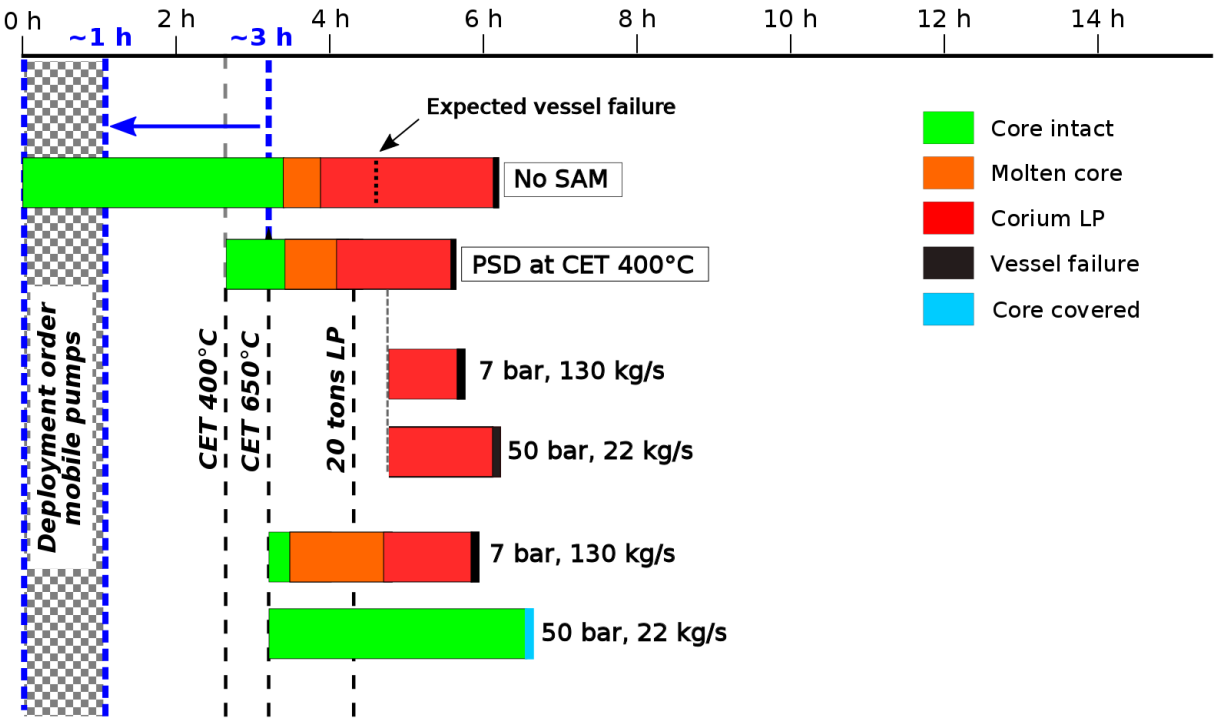

Figure 8-26: Sketch summarizing the effect of PSD and core reflooding during an SBO.

The performed calculations in section **8.3.3** predict the existence of a minimum RMFR of 20 kg/s to mitigate the SA without major damage if an injection is performed shortly after the detection of a CET=650 °C. This value is similar to the 300 gpm (~ 20 kg/s) recommended for American PWRs in [134] and to the 22 kg/s predicted by AREVA using MELCOR for the German Konvoi PWR (see **Table 8-3**) [12]. Here, only one sequence with reflooding at CET 650 °C has been simulated and hence, only one minimum RMFR at CET 650 °C is compared.

	SCRAM - CET650°C: 3.10 h	
	ASTEC	MELCOR
RMFR minor damage	20 kg/s	22 kg/s
RMFR minor damage (ASTEC interpolation)	12.5 kg/s	

Table 8-3: Comparison ASTEC-MELCOR [12] on the minimum RMFRs to mitigate the SA without major core damage. ASTEC values correspond to a total SBO sequence with PSD at CET 400 °C.

If mobile systems are used to provide this minimum RMFR, further implications regarding their deployment can be drawn. The analysis is identical to the one adopted for SBLOCA sequences in section **8.2.2.3**. Looking at the occurrence times of $SBO_{PSDCET400C}$, it can be seen that there is a time window of about 3 h (since the loss of AC power supply) up to the detection of CET 650 °C. Considering that the deployment of a mobile pump into the RCS takes at least 2 h for an American three-loop Westinghouse PWR [147] and extrapolating a

similar measure for the Konvoi, this means that the deployment order should be issued with a maximum delay of **1 h after the entrance in SBO** so that injection can be launched before CET>650 °C (see **Figure 8-26**). This time is identical to that obtained in section **8.2.2.3**. Furthermore, the mobile pump should provide a high enough pressure head (at least 18 bars) in order to overcome the pressure build-up caused in the RCS by evaporation.

In the absence of an external injection, the restoration of AC power supply is another viable path to maintain core integrity. If the action occurs shortly after detecting CET 650 °C, the potential of the retrieved core cooling systems (see **Table 6-3**) can be estimated. For example, the retrieval of one HPIS train or two CVCS trains in the cold leg can cool down the core without any RCS repressurization. As for the LPIS, the performance is slightly higher than the efficiency of HH125 (i.e. 10 %) and should provide about 15 kg/s. Consequently, it is not clear if the recovery of only one LPIS train is sufficient to mitigate a further progression of the accident. The same applies for the Extra Borating System, which serves an even lower RMFRs.

8.4 Recommendations concerning SAM for the German PWR Konvoi

Based on the investigations performed, general conclusions concerning SAM measures for German Konvoi PWRs can be drawn. The importance of each conclusion is naturally balanced by the contribution of each sequence to the total core damage and the containment failure risk for this plant.

Core reflooding is the prime SAM measure for low pressure sequences, such as medium or large breaks in the primary circuit. For those cases, the RCS is quickly depressurized and an additional depressurization is not necessary. For high pressure sequences, however, the most imperative measure is the depressurization of the RCS either through a secondary bleed and feed (SBF) or a primary bleed and feed (PBF).

The depressurization of the RCS through a SBF should be executed if the shift team believes that enough time (about 1 h) is available for such action, the maximum delay for its execution being the detection of CET 400 °C. Additionally, calculations on SBO exhibit a grace time of 2 h to initiate this action after meeting the criteria for SBF. The feed should be ensured with 15 kg/s of water injection into the depressurized SG. The pump used for such aim can have low-medium pressure heads (10-20 bars) if it supplies the aforementioned flow rate.

For times beyond CET 400 °C, the top priority are the primary bleed and feed measures, which should be executed within the first 20 min after such detection by means of opening all pressurizer valves in order to delay the severe accident progression.

After RCS depressurization via a PSD, the subsequent essential measure is core reflooding. The injection has to occur in the following 30 min after detecting CET 650 °C with a minimum mass flow rate higher than 20 kg/s in order to mitigate the SA without a core

major damage. The exact value depends on the transient speed, and has been derived considering that the AC power is available at least 1 h after SCRAM. The safety systems used for that purpose have to provide at minimum a medium-high pressure head (> 20 bars) to overcome RCS repressurization by steam generation. However, for medium breaks in the RCS, a low pressure injection pump (within 6-10 bars) also has a good performance.

In case of SBO, the injection of water into the RCS has to be performed either through the restoration of safety systems or alternatively through an external injection shortly after detecting CET = 650 °C. If the second approach is adopted, the mobile pump deployment order has to be issued within the one hour after the entrance in SBO, so that the equipment injects before the aforementioned CET is reached. Otherwise, diesel generators must be triggered to retrieve, at least, one HPIS train or two CVCS trains. The retrieval of one LPIS train can also terminate the accident, but its efficiency depends on the degree of the RCS repressurization.

8.5 Summary

In this chapter, the efficiency of in-vessel SAM measures for risk-relevant sequences in a German Konvoi PWR has been investigated using ASTECV2.0. The efficiency has been assessed in terms of the capacity of each measure to prevent, mitigate or delay core melting, corium relocation to the lower plenum and RPV failure, with respect to the sequences (without SAM) described in chapter **7**.

The success of each SAM measure has been shown to depend on the sequence and hence, on the initiating event and the combination of failures of selected safety systems. For instance, simulated MBLOCAs require an injection of water to avoid core melting, since the reactor is depressurized through the break. However, SBLOCAs and short term SBOs demand a depressurization of the RCS through the primary or the secondary side before core reflooding is initiated.

The performed calculations have aimed at answering some of the suggested improvements on SAM for German NPPs in the light of the conclusions drawn from the Fukushima accident. In particular, the time windows for the performance of primary and secondary bleed and feed, the characterization of the mobile equipment injecting into the primary or the secondary side and the time when the AC power supply needs to be restored (by additional grids or DGs) are extensively investigated with the current ASTECV2.0 modelling capabilities.

9 Conclusions

Severe accidents in nuclear power plants are a major concern because of the hazardous consequences that they can inflict in terms of land contamination, cancer fatalities and their related economic costs and, even more, the trust of the society to handle technically complex facilities in critical situations. In order to prevent such accidents, the Defence in Depth concept of a nuclear reactor deploys several safety levels with dedicated provisions to stop their progression.

However, although improbable as in any technical system, provisions may fail and an abnormal event can develop into an accident beyond the design basis or, more specifically, into a severe accident. In such situation, the plant crew must initiate Accident Management procedures (e.g. EOPs and SAMGs) either to prevent or to stop the accident progression and/or to minimize the radiological consequences.

The main focus of this thesis is to re-investigate selected severe accident sequences for a German Konvoi PWR using the EU reference code ASTEC and to identify potential improvements on SAM procedures and their temporal initiation chronology in the view of the lessons learnt from the Fukushima accident.

For this purpose, at first all ASTECV2.0 physical models describing the early in-vessel phase of a severe accident are extensively validated using experimental data from the QUENCH test facility. The main outcomes of the validation work are:

- The models governing the early in-vessel phase of the severe accident can reproduce the major physical features observed in the QUENCH-08 experiment.
- The deviations between code predictions and experimental data mainly concern the low temperature gradient among the cladding of the inner ring, outer ring and shroud and the overestimation of the shroud temperature at the upper unheated zone. The reason for these deviations is likely the lack of radial discretization in the QUENCH model and an insufficient modelling of the heat transfer through the argon gap within the upper unheated zone of the facility.
- These deviations lead to an earlier temperature escalation compared to the experiment during the second heat-up phase and hence, to a higher oxidation degree of the bundle at reflooding time. Therefore, the hydrogen generation during reflooding (12 g ASTEC vs 37 g Experiment) and during all the experiment (69 g ASTEC vs 84 g Experiment) is underestimated by the code and hence, it is not conservative.
- New modelling features, such as the improvement of the heat transfer through the argon gap and the inclusion of two and up to three channels for the fluid, are introduced in the ASTECV2.1 model of the QUENCH-08 in order to overcome these

deficiencies. They result in a better prediction of the global hydrogen generation during reflooding (30 g ASTEC vs 37 g Experiment) and during all the experiment (76 g ASTEC vs 84 g Experiment). However, still the hydrogen generation is underestimated.

The central part of the investigations is devoted to the analysis of a generic German Konvoi PWR during the in-vessel phase of a severe accident and to derive optimized SAM measures. To achieve this goal, risk-relevant sequences in a German Konvoi PWR with and without AM have been simulated. Based on these simulations, the following conclusions are drawn:

- The ASTECV2.0 model of the German Konvoi PWR has been improved through the inclusion of new physical models for the late in-vessel phase and through the modelling of new protection and safety systems and AM procedures. The key plant parameters have been verified in stationary conditions with the prototypical values for the German Konvoi PWR.
- Three different types of sequences are simulated. They entail the Medium and Small Break LOCA in the cold leg of the pressurizer loop (with the total loss of AC at a given stage of the accident) and the total Station Blackout. The last two are significant contributors to the risk of core damage and containment failure. The evolution of all sequences predicted by ASTEC correspond to those predicted by MELCOR 1.8.4 and ATHLET-CD 3.0 by other institutions, especially during the early in-vessel phase of the severe accident.
- The priority of each SAM measure essentially depends on the accident type and the combination of system failures. The simulations show that high pressure sequences (involving the loss of heat sink or a small break in the RCS) require a depressurization of the RCS through a Secondary or Primary Bleed and Feed as a prime SAM measure in order to ease water injection and avoid SGTR. In case of low pressure sequences (involving a medium or large break in the MCL or a small break together with the RCS depressurization), the most important SAM measure is core reflooding.
- The maximum delay for the execution of a SBF in order to prevent core melting is the detection of a CET 400 °C, according to SBO calculations. Beyond that time, the core undergoes oxidation and the generated hydrogen hinders steam condensation. Consequently, the RCS cannot be cooled down and remains at high pressures up to RPV failure. This gives a 2 h time margin to perform this action since the criteria for SBF are satisfied. Additionally, for SBFs performed before CET 400 °C, a minimum mass flow rate of 15 kg/s has to be injected into the SG in order to effectively depressurize the RCS. This value is in agreement with the one recommended by the Nuclear Energy Institute (NEI).

- Priority has to be shifted from SBF to a PBF when the CET exceeds 400 °C according to SBO calculations, which is in agreement with the preventive AM procedures of a Konvoi PWR. Besides, PSD has to be performed in the following 20-30 min after such detection by means of all pressurizer valves, according to the SBLOCA and SBO calculations. This time window is in agreement with the SAMGs of the German Konvoi PWR.
- Considering that the PSD is performed at CET 400 °C, core reflooding must be launched shortly after the detection of CET=650 °C and with a minimum flow rate of about 20 kg/s in order to mitigate the accident without major damage (< 20 corium tons released to the core region) according to SBLOCA (with AC power availability at least 1 h after SCRAM) and SBO calculations. This value depends on the time elapsed since SCRAM and the water inventory in the SGs. The values correspond to those mentioned by the NEI and obtained by AREVA. This work scopes also the simulation domain to injections performed after CET=650 °C detection and characterizes the final state of the reactor, which is unique for a German Konvoi PWR.
- In case of an external injection into the RCS, the deployment order for the mobile pump has to be issued with a maximum delay of 1 h after the loss of AC power so that injection can be started near CET 650 °C, according to SBLOCA and SBO calculations. Additionally, the pump should have a high pressure head to avoid a reduced efficiency caused by the RCS repressurization and should supply at least 20 kg/s of water (according to the previous point). If the restoration of the AC power is preferred through the deployment of mobile diesel generators, the efforts should be directed towards the retrieval of at least one HPIS train or two CVCS trains. If this is not possible, the retrieval of the LPIS could terminate the accident, but the success depends on the degree of repressurization upon injection, which is sequence-dependent.

In addition, conclusions on SAM performance during degraded core conditions in a German Konvoi PWR are listed as follows:

- Vessel failure can be considerably delayed in case of a 40-min delayed PSD (according to SBLOCA and SBO calculations). This happens because the simulations predict a less than 20 corium tons in the lower plenum at the time of PSD and hence, a long lasting corium retention at that location.
- Vessel failure cannot be prevented if at least 20 corium tons are present in the lower plenum for at least 20-30 min regardless of the supplied water flow rate (according to MBLOCA, SBLOCA and SBO calculations). In this configuration, the water cannot cool down the wall in contact with the top metallic layer, which has been heated up excessively by the oxidic layer below it.

Future simulation work aiming at confirming the findings on degraded core conditions is planned with ASTECV2.1 [26], which includes a 2-D treatment of the thermal-hydraulics and a new reflooding model for degraded cores. An improved ASTEC model of the Konvoi PWR, the consideration of additional risk relevant sequences (e.g. SGTR), the stepwise introduction of more mechanistic models describing key in-vessel phenomena (e.g. jet fragmentation, material segregation in lower plenum and RPV failure), the extension of the simulation scope to the ex-vessel phase (e.g. MCCI and hydrogen in containment) and the coupling of code with uncertainty tools (e.g. URANIE) will also be appointed.

The investigations performed with ASTECV2.0 on a generic German Konvoi PWR elucidate that the code capabilities are well suited for a sound description of PWR relevant in-vessel phenomena and for the assessment of SAM measures aiming at preventing RPV failure. Furthermore, they extend the technical basis for the development of optimized SAMGs, contributing this way to reduce the risk of core melt accidents (such as the ones experienced at Fukushima and Three Mile Island), thereby increasing existing safety margins of NPPs.

Appendix A Overview of the German Konvoi PWR and key safety systems

This Appendix describes the general layout of the German Konvoi PWR and its main safety systems. This allows a better understanding of the PWR in-vessel progression and the AM procedures in such plant (chapters **2** and **3**) and certainly, of the ASTECV2.0 investigations on the German Konvoi PWR (chapters **6, 7** and **8**). The Appendix is structured in two sections: first, the general functional scheme of a German Konvoi PWR and its main components is explained in section **A.1**. Then, the key safety systems and their position within the plant are described in section **A.2**. Further information about the design of the primary and the secondary circuits, RPV, the containment and the control and safety systems can be found in [27,127–129].

A.1 Description and general layout

The German Konvoi plant (e.g. GKN-2, KKI-2 and KKE) is a four-loop PWR supplying up to 1300 MW of electrical power. The functional scheme of the Konvoi is represented in **Figure A.1-1** and described as follows:

The heat produced in the reactor core by nuclear fission is transferred to the primary circuit and from there to the water of the secondary side through the SGs. The MCPs deliver the coolant through the RCS. The water in the SG is partly evaporated by the heat transferred from the primary side. The generated steam is dried with the separators and delivered to the Main Steam Line, propelling the turbine and the generator. The remaining steam is transformed into water in the condenser thanks to the flow of cold water through the tertiary circuit, which is cooled down by means of cooling towers. The condensed water is transported into the FW tank and from there to the SGs via the FW pumps.

The RCS is composed of the RPV, the hot and cold legs of coolant loops, the primary side of the SGs (i.e. U-tubes and the inlet and outlet boxes), the MCPs and the pressurizer, which controls the system pressure. The power distribution and the heat generation in the reactor core can be controlled and shut down by the insertion of neutron absorbing rods or through an increase of the boron concentration. On the other hand, the secondary circuit consists of the SGs, the Main Steam Lines (MSLs), the bypass system, the turbine, the condenser and the FW pumps.

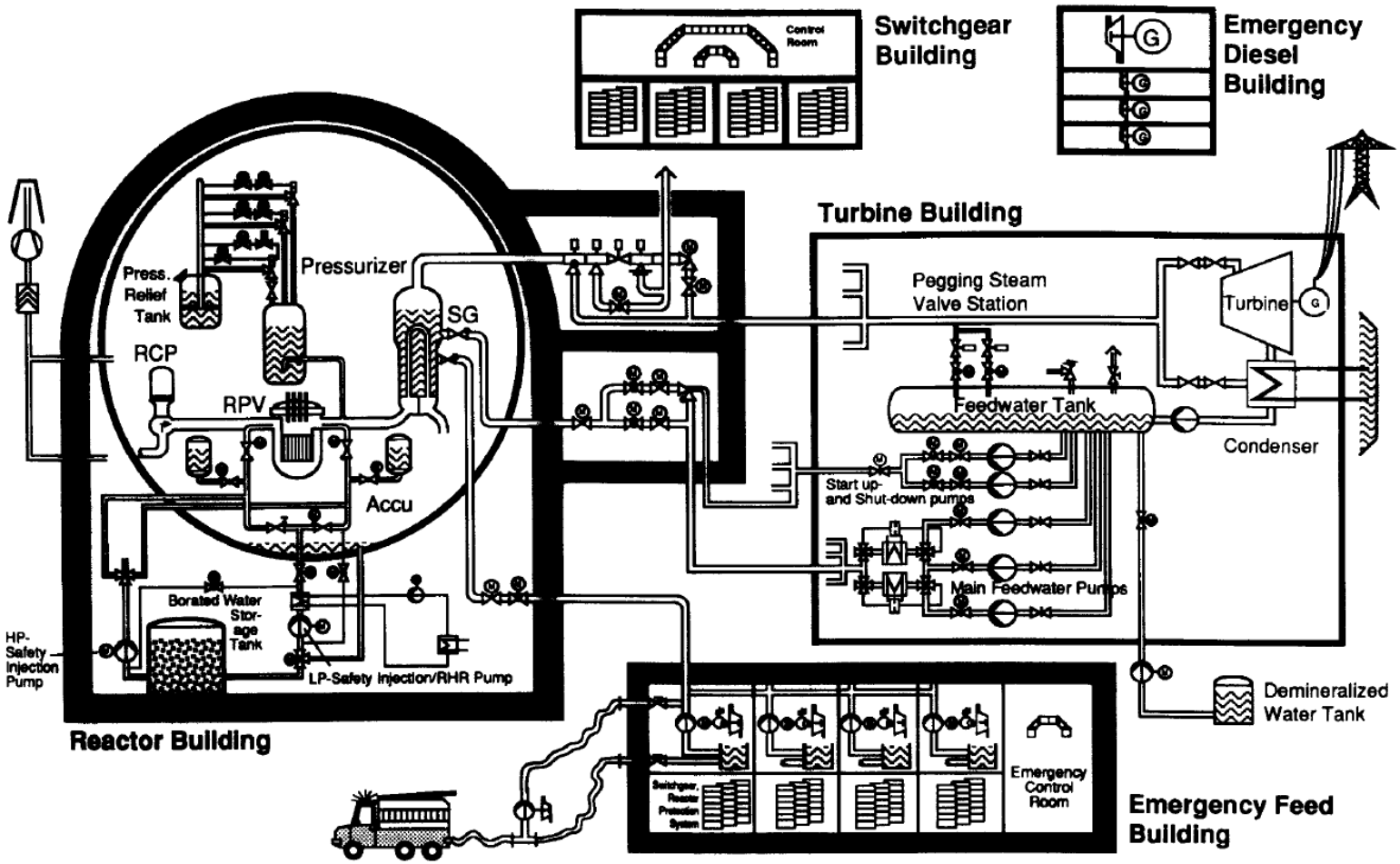

Figure A.1-1: Overview of operating systems of Konvoi PWR 1300 MWe [15].

A.2 Relevant safety systems

In order to prevent a hazardous release of radioactive material to the public, the Konvoi PWR introduces three physical barriers (fuel rod cladding, RCS and containment), which are protected by the five safety levels of the DiD (see **Table 3-1**). In particular, the plant has redundant and diverse safety systems that control the evolution of DBAs and even BDBAs-SAs (if required by AM procedures). The most important safety systems of the German Konvoi PWR are represented in **Figure A.1-1** and **Figure A.2-1** [27]. A brief summary of those is performed as follows:

- The reactor SCRAM system (see **1** in **Figure A.2-1**) allows a fast interruption of the nuclear chain reaction by the automatic insertion of control rod, the energy production being reduced to the decay heat within a few seconds.
- The CVCS compensates volume contractions and expansions of the reactor coolant inventory, and controls the boron concentration in the reactor coolant.
- The RCPS supervises all safety relevant variables and activates reactor protection signals, which trigger several actions, which are marked by yellow boxes in **Figure A.2-1** (e.g. SCRAM, activation of ECCS, activation of Emergency FW System)
- The electrical power supply is composed of the preferred power supply (for house load) and emergency power supply (see **7** and **8** in **Figure A.2-1**). The first feeds operational and safety system by means of the generator and the external grid, while the second feeds key components by means of DGs under the loss of the preferred power supply. Batteries supply electricity to key components (e.g. instrumentation and control systems) during the start-up of the DGs.
- The ECCS and the Residual Heat Removal System (RHRS) consist of four active HPIS trains (injecting in hot legs of the RCS), eight passive accumulators (injecting in hot and cold legs of the RCS) and four active LPI trains (injecting in cold and hot legs of the RCS). The three systems are represented in the zones **4**, **2** and **5** of **Figure A.2-1**. During LOCA sequences, the ECCS injects water into the RCS, the water coming either from the borated water storage tanks, the ACCUs or from the sump (see lower part lower part of the sphere in **Figure A.1-1**). During shutdown phases, the decay heat is removed by the RHRS via heat exchangers (see **6** in **Figure A.2-1**), the component cooling system and the service water system.
- The Emergency Feedwater System (see **9** in **Figure A.2-1**) feeds the SGs after the loss of the main FW and contributes to remove the decay heat of the primary side.
- The pressure resistant and technically gas-tight containment (design pressure 0.63 MPa absolute, design leakage < 0.25 vol. % / day) encloses the most important systems containing radioactive material. The containment function is supported by the valves of the containment isolation system. The containment is designed to withstand pressures and temperatures during a LOCA. In the containment sump, the water

draining from the primary circuit in the case of a LOCA is collected. The surrounding reinforced concrete shell protects the containment against external impacts. The annular room between containment and reinforced concrete shell can be kept under sub atmospheric pressure by a ventilation system. The air – ventilated from the annular room – is blown into the atmosphere via filters and the stack.

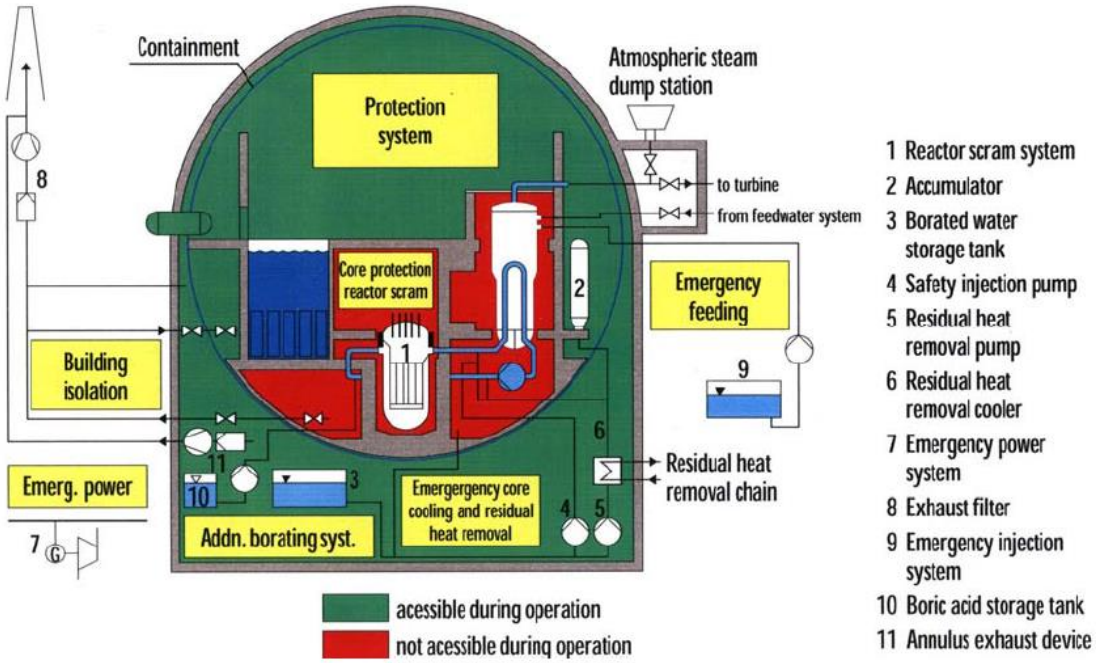

Figure A.2-1: Scheme of the principal safety installations of a German Konvoi PWR [27].

Appendix B Further results of the ASTECV2.0 Validation on the QUENCH-08 Experiment

The Chapter **5** was dedicated to the ASTECV2.0 validation based on the QUENCH-08 Experiment. Therein, the comparison between the ASTEC predictions and the Experimental data on key variables was performed. Within this Appendix, further results are shown with the purpose of supporting the conclusions drawn in Chapter **5**. The following types of graphs are shown:

- Temperature evolutions at several elevations during the experiment.
- Axial temperature and oxide profiles at several times.

B.1 Temperature evolutions at several locations during the experiment

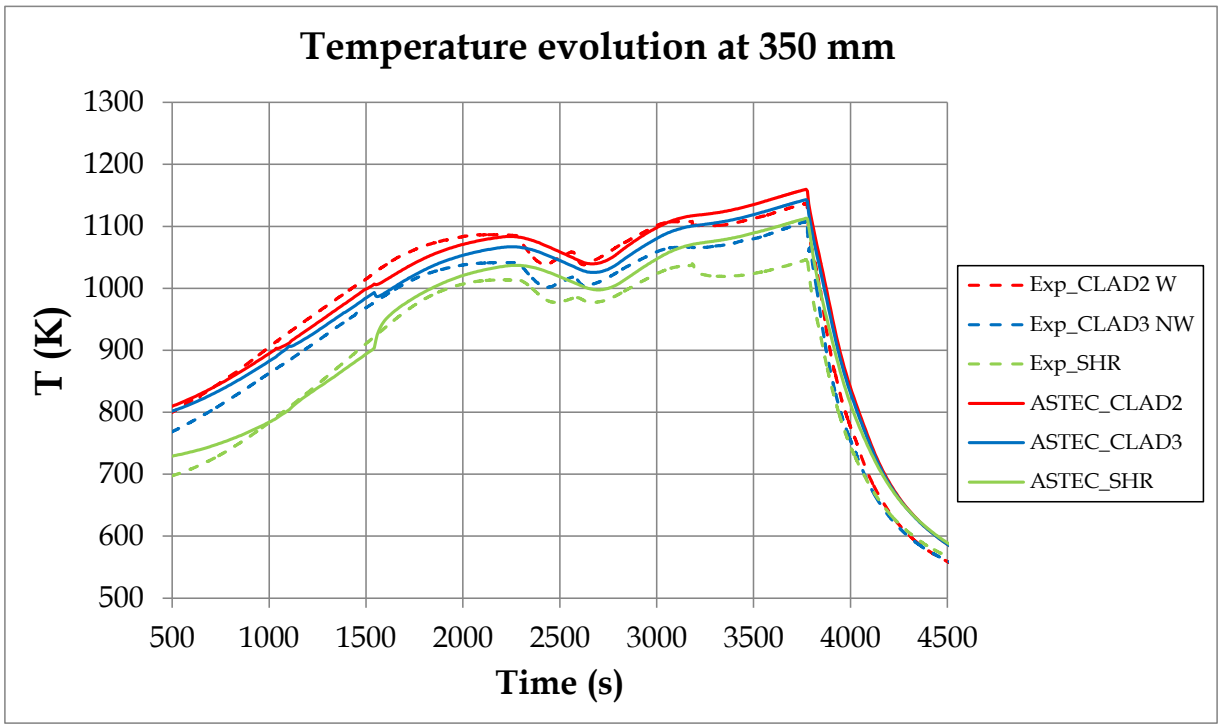

Figure B.1-1: Comparison of the temporal evolution of predicted (solid lines) and experimental (dashed lines) temperatures at an axial height of z = **350** mm at several radial positions (colour legend).

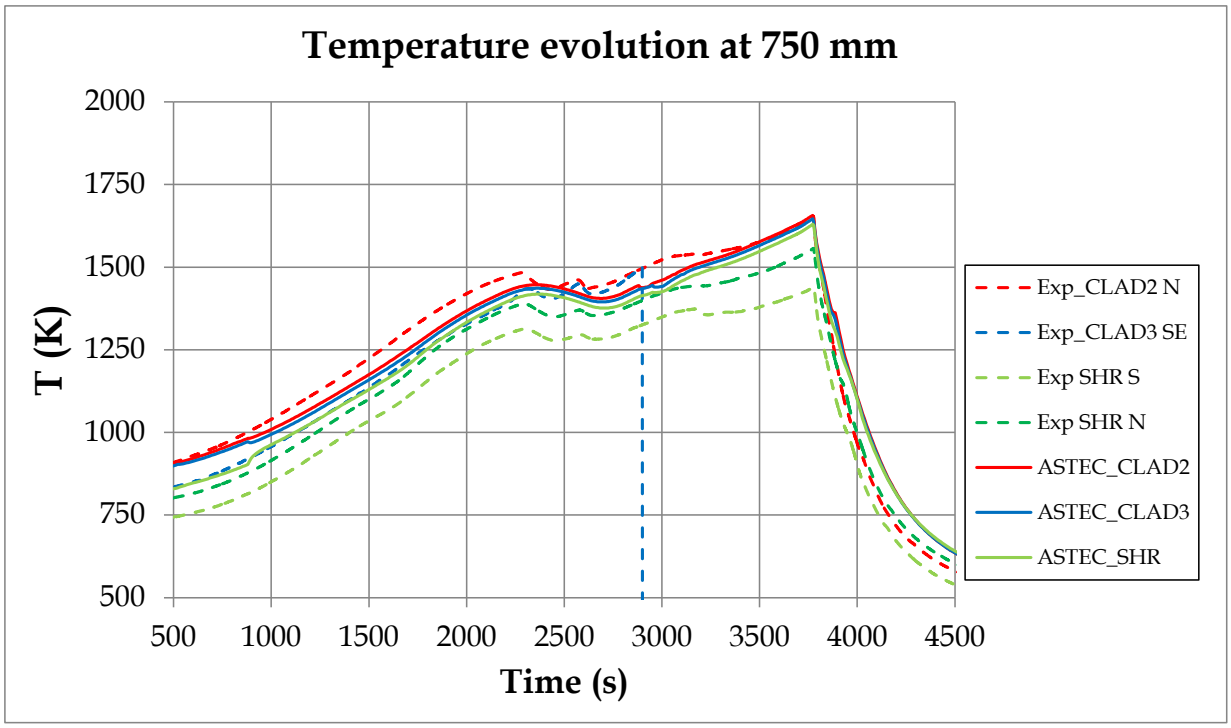

Figure B.1-2: Comparison of the temporal evolution of predicted (solid lines) and experimental (dashed lines) temperatures at an axial height of z = **750** mm at several radial positions (colour legend).

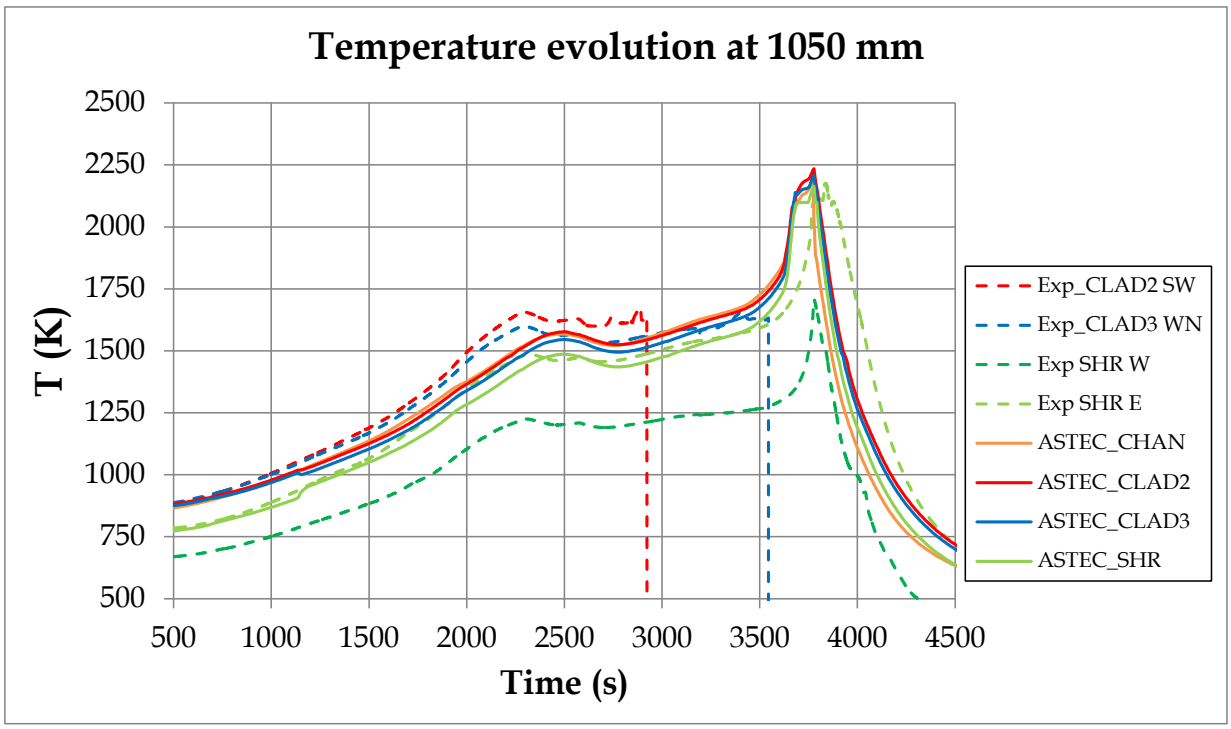

Figure B.1-3: Comparison of the temporal evolution of predicted (solid lines) and experimental (dashed lines) temperatures at an axial height of z = **1050** mm at several radial positions (colour legend).

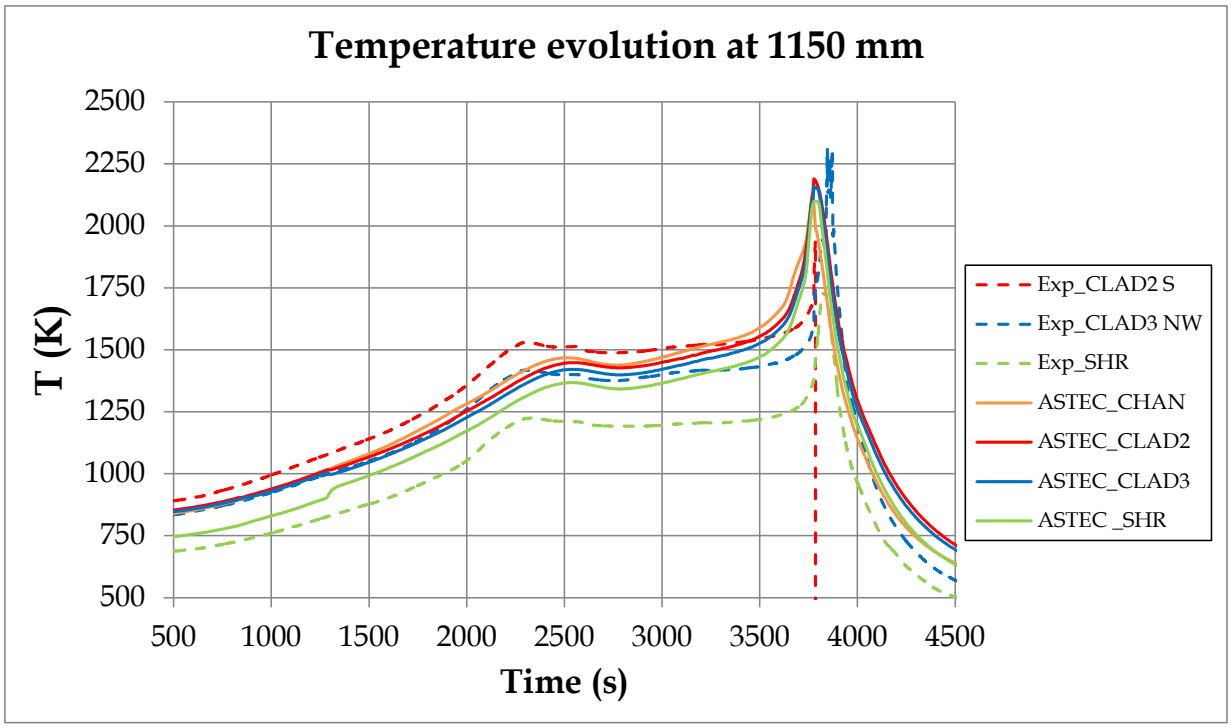

Figure B.1-4: Comparison of the temporal evolution of predicted (solid lines) and experimental (dashed lines) temperatures at an axial height of z = **1150** mm at several radial positions (colour legend).

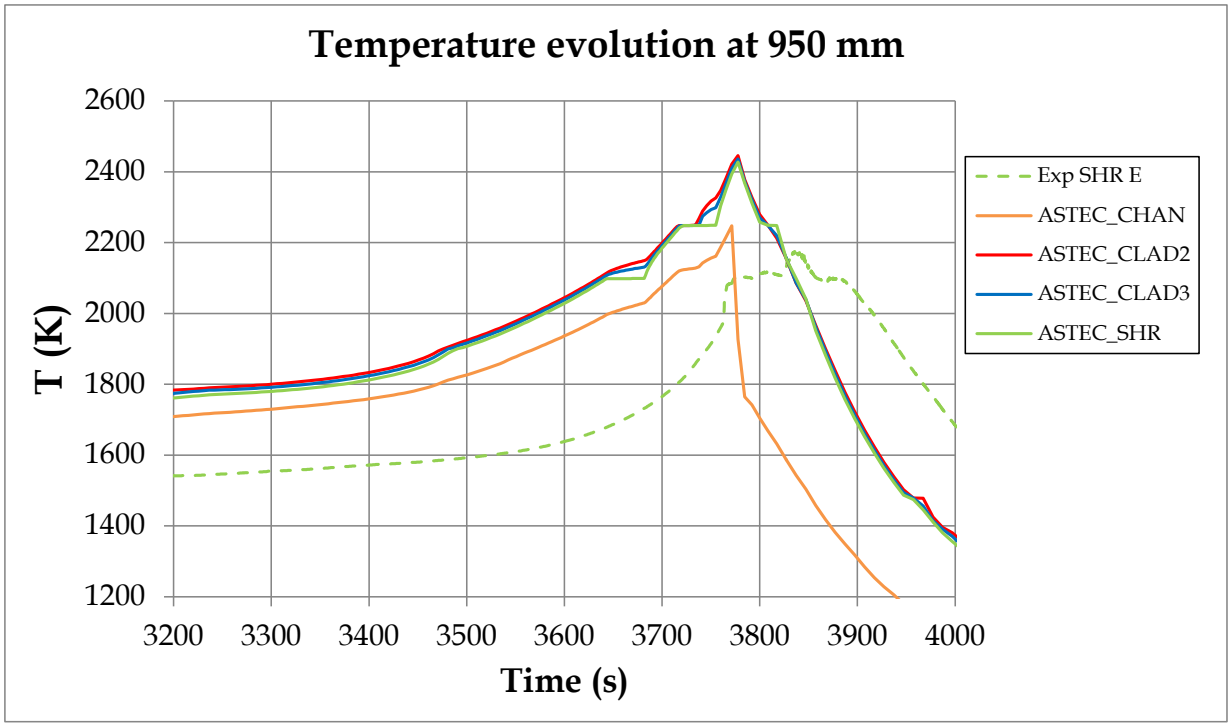

Figure B.1-5: Comparison of the temporal evolution of predicted (solid lines) and experimental (dashed lines) temperatures at an axial height of z = **950** mm at several radial positions (colour legend). Zoom for the second heat-up and reflooding phases.

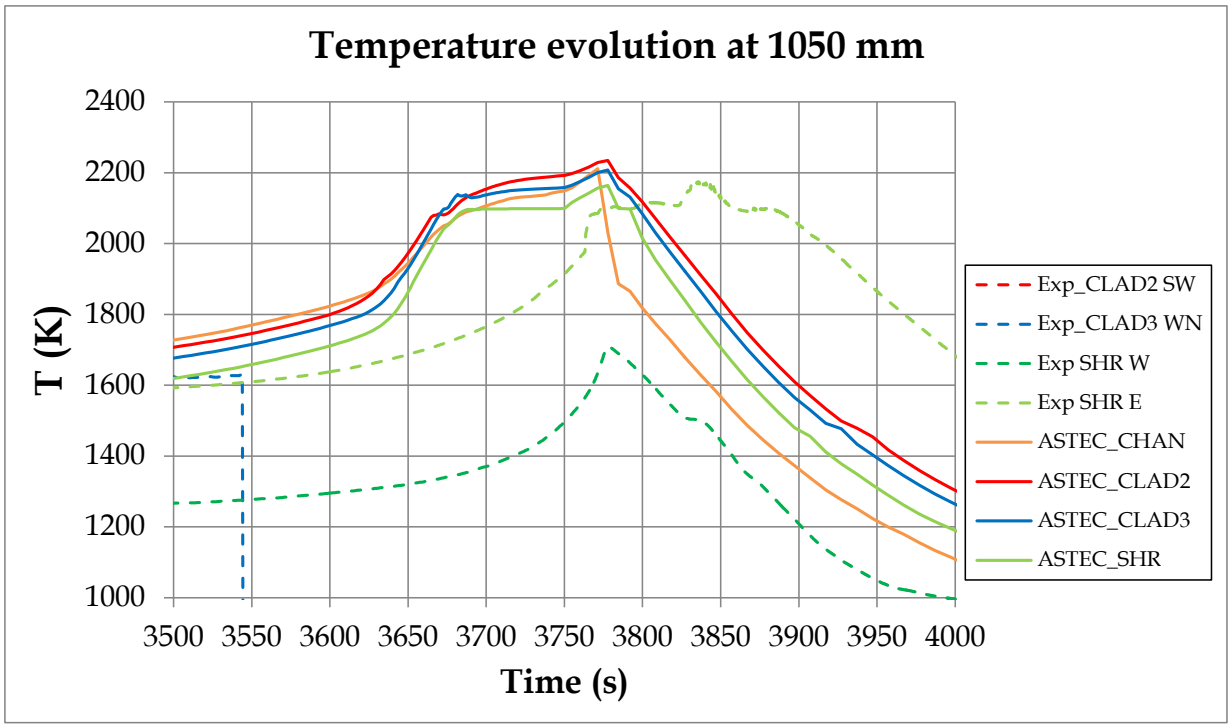

Figure B.1-6: Comparison of the temporal evolution of predicted (solid lines) and experimental (dashed lines) temperatures at an axial height of z = **1050** mm at several radial positions (colour legend). Zoom for the second heat-up and reflooding phases.

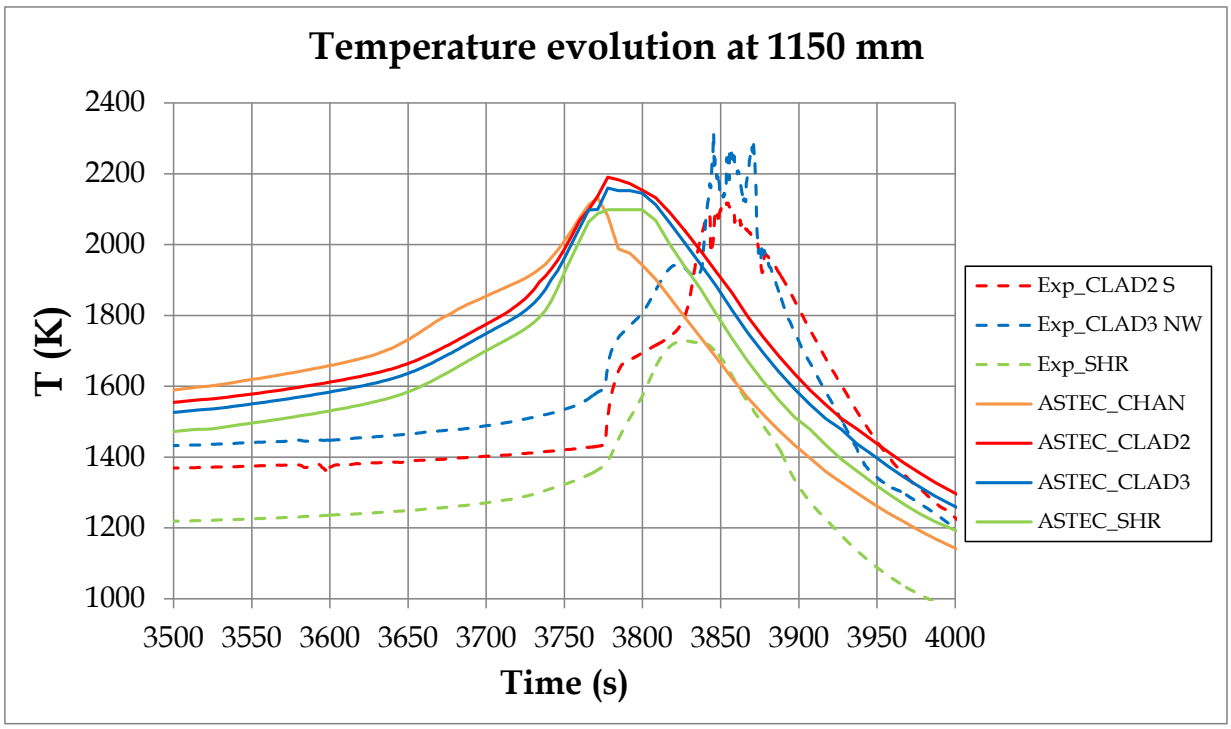

Figure B.1-7: Comparison of the temporal evolution of predicted (solid lines) and experimental (dashed lines) temperatures at an axial height of z = **1150** mm at several radial positions (colour legend). Zoom for the second heat-up and reflooding phases.

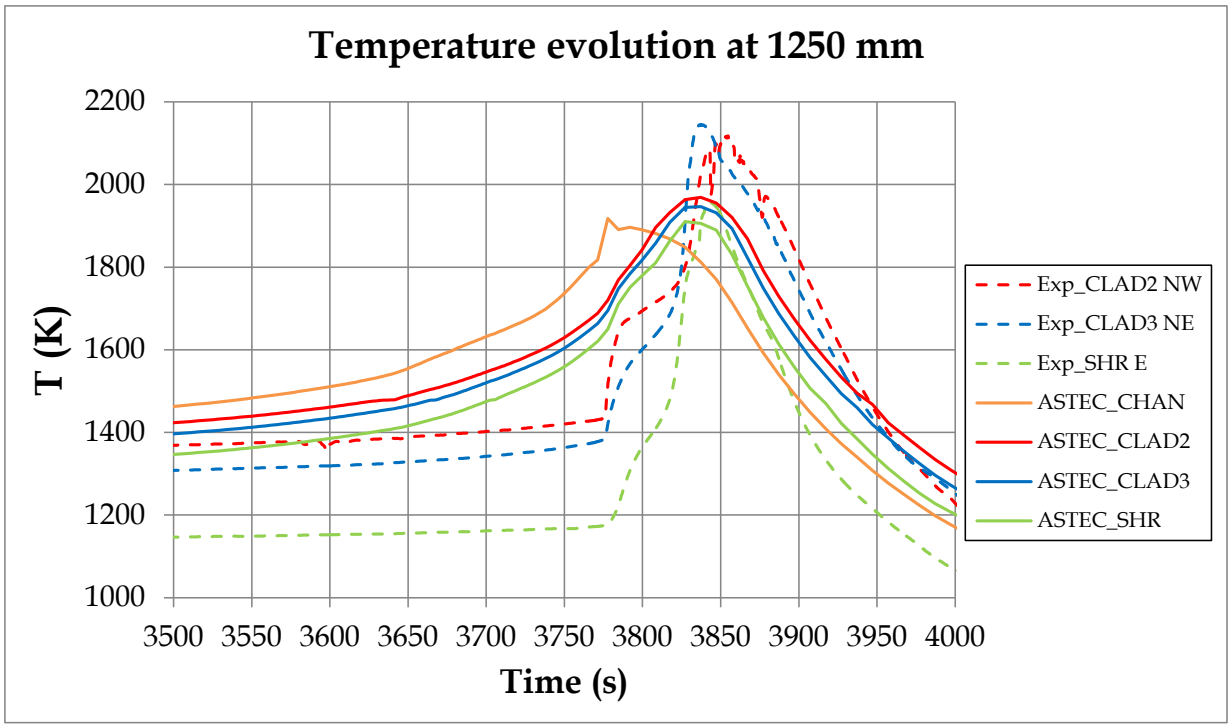

Figure B.1-8: Comparison of the temporal evolution of predicted (solid lines) and experimental (dashed lines) temperatures at an axial height of z = **1250** mm at several radial positions (colour legend). Zoom for the second heat-up and reflooding phases.

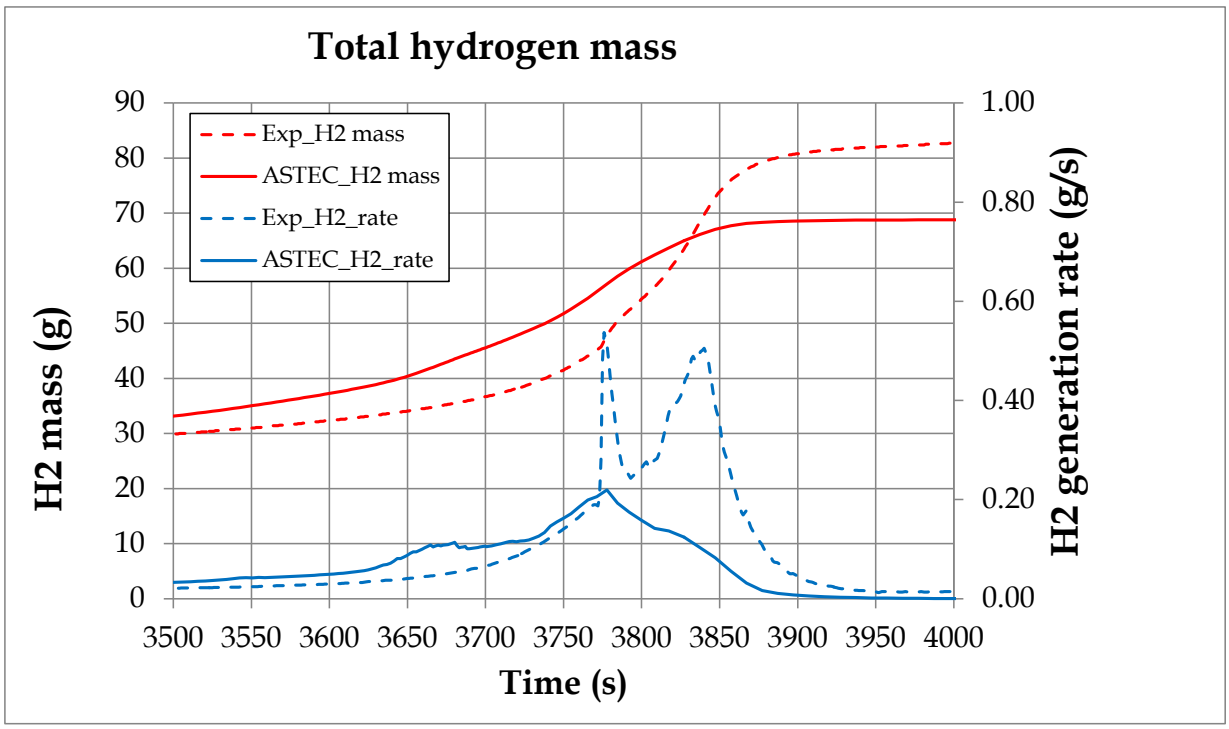

Figure B.1-9: Comparison of the temporal evolution of the predicted (solid lines) and experimental (dashed lines) hydrogen generation mass (red)/flow rate (blue). Zoom for the second heat-up and reflooding phases.

B.2 Axial temperature and oxide profiles at selected times

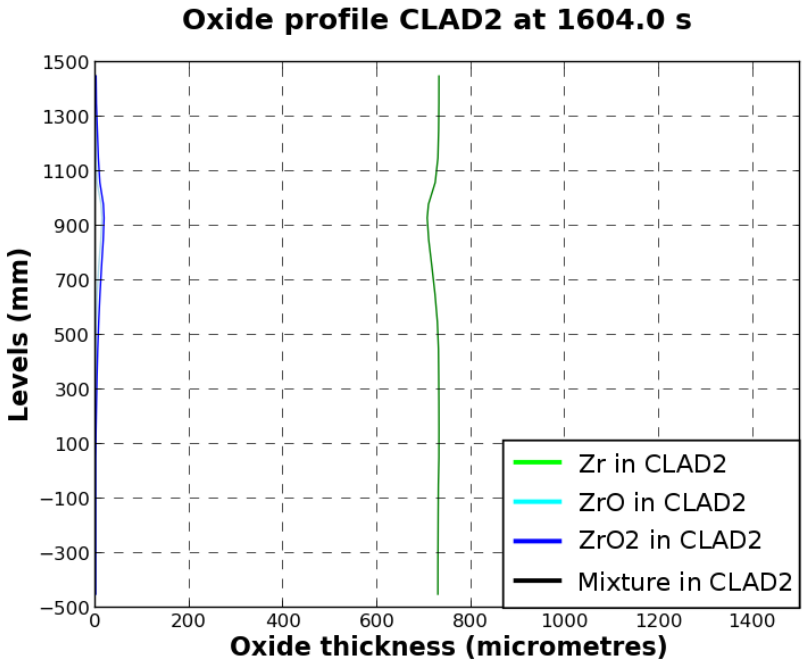

Figure B.2-1: Predicted oxidation profile on CLAD2 (representative cladding of the inner ring) at the end of the first heat-up phase.

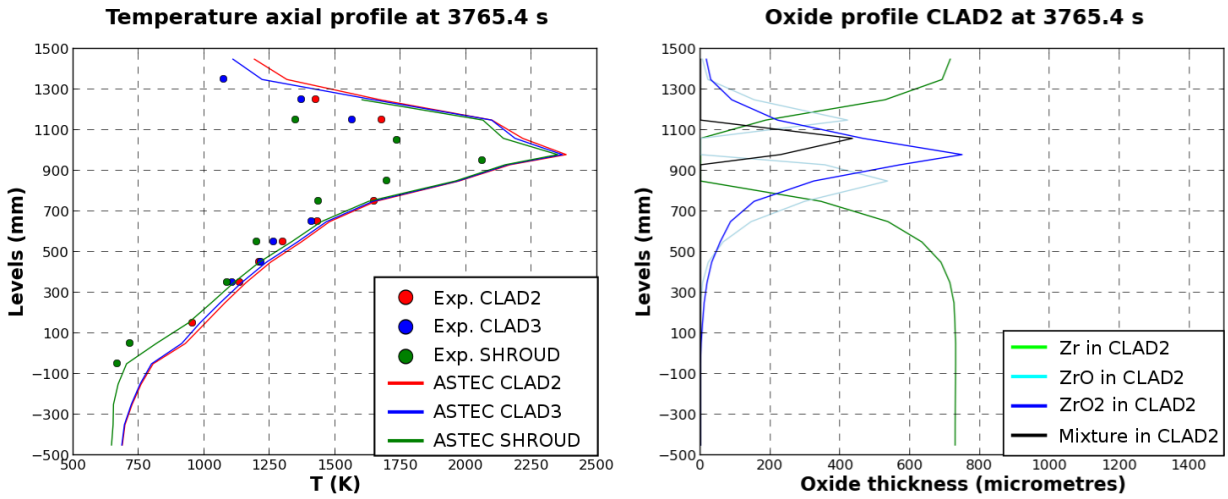

Figure B.2-2: Comparison of predicted (solid lines) and experimental (data points) axial temperature profiles at several radial positions (colour) 10 s before reflooding (**left**); Predicted oxidation profile on CLAD2 (representative cladding of the inner ring) at the same instant (**right**).

Appendix C Additional features of the generic ASTECV2.0 model of the German Konvoi PWR

The Chapter **6** was dedicated to the explanation of the ASTECV2.0 generic model of the German Konvoi PWR. However, due to spatial limitations, it was not possible to explain all the modelling details. The aim of this Appendix is to provide further information about the modelling of most relevant safety systems of the Konvoi PWR. The attention is focused on the pressure control in the pressurizer (section **C.1**), the ECCS (section **C.2**) and the External mobile pumps injecting into the RCS and the SG (section **C.3**).

C.1 Pressure control in the Pressurizer

The pressure in the RCS is controlled by the pressurizer through two main systems:

- Heaters, which provide a higher or lesser heating power depending on the deviation with the desired RCS pressure. If a higher pressure is required, then the heaters provide a higher power to increase the void fraction.
- Sprays, which provide a higher or lesser mass flow rate depending on the deviation with the desired RCS pressure. If a lower pressure is required, then the sprays provide a higher mass flow rate to condense part of the existing steam.

The control of the heating power and the spray flow rate as a function of the RCS pressure is represented in **Figure C.1-1**. Therein, three regimes of heating power can be differentiated: maximum and constant power for pressures below 155 bars; intermediate and constant power for pressures within 155-156 bars; proportional power input in order to finely control the RCS pressure around its reference value (i.e. 157 bars). On the other hand, the sprays provide their maximum flow rate for RCS pressures below 162 bars and decrease linearly this contribution until the system pressures fall to 158 bars.

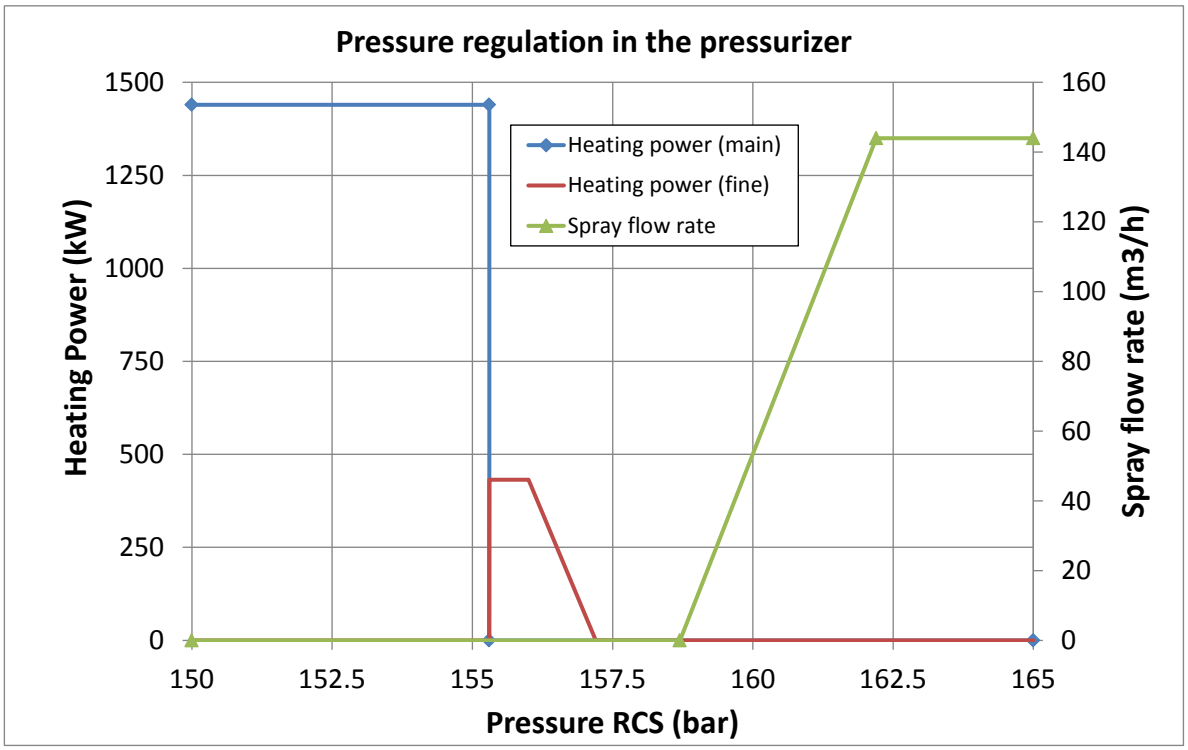

Figure C.1-1: Control of the heating power and spray flow rate in the generic ASTECV2.0 model of a German Konvoi PWR.

In addition, the pressurizer PORV limits the RCS pressure to avoid the intervention of the safety valves SV1 and SV2 while there is a change in the system power. Likewise, SV1 and SV2 protect the RCS from overpressures. Each valve has a pressure set-point to open and close according to a certain hysteresis as well as a delay when opening or closing. These are represented from **Figure C.1-2** to **Figure C.1-4**.

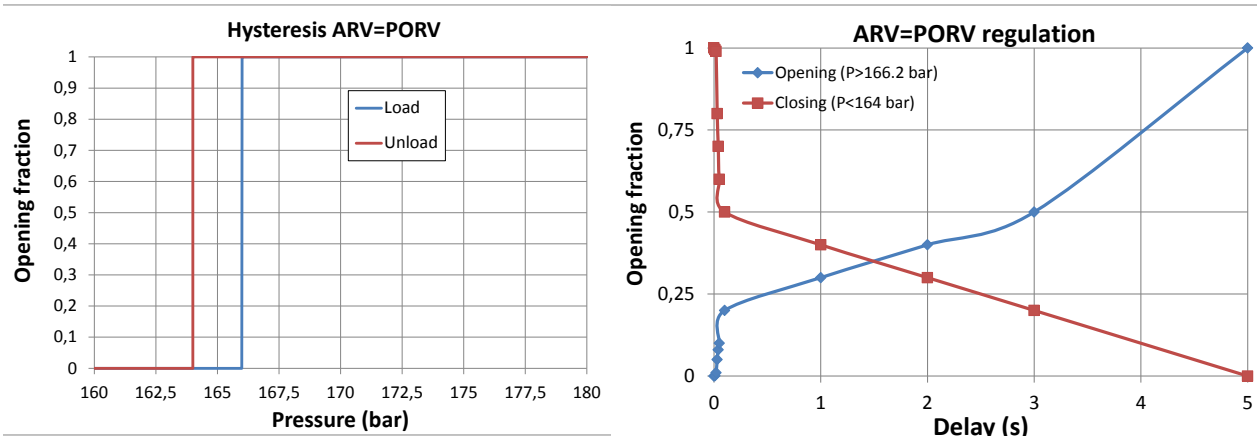

Figure C.1-2: Left: Opening fraction of the PORV as a function of the RCS pressure; Right: Evolution of PORV opening fraction in time (since criteria fulfilled).

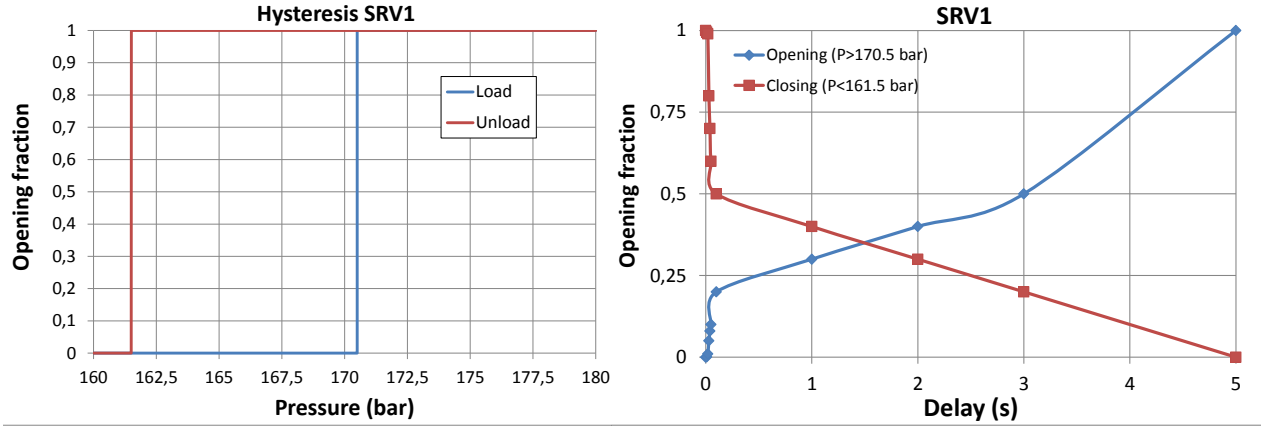

Figure C.1-3: Left: Opening fraction of the pressurizer SV1 as a function of the RCS pressure; Right: Evolution of SV1 opening fraction in time (since criteria fulfilled).

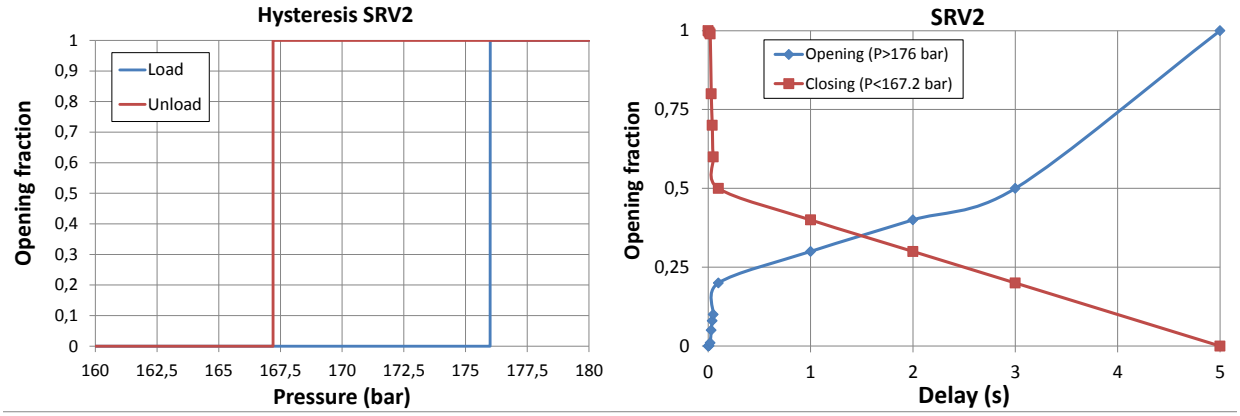

Figure C.1-4: Left: Opening fraction of the pressurizer SV2 as a function of the RCS pressure; Right: Evolution of SV2 opening fraction in time (since criteria fulfilled).

C.2 Active systems of the ECCS

The section **6.5** has introduced the pressure head and the maximum flow rates given by the pumps of the HPIS and the LPIS. However, for SAM purposes, it is also interesting to know the dependence of the supplied mass flow rate on the RCS pressure (see **Figure C.2-1**). Therein, it is shown that the HPIS provides less mass flow rate at a higher pressure head, whereas the LPIS provides a very high mass flow rate at a lower pressure head.

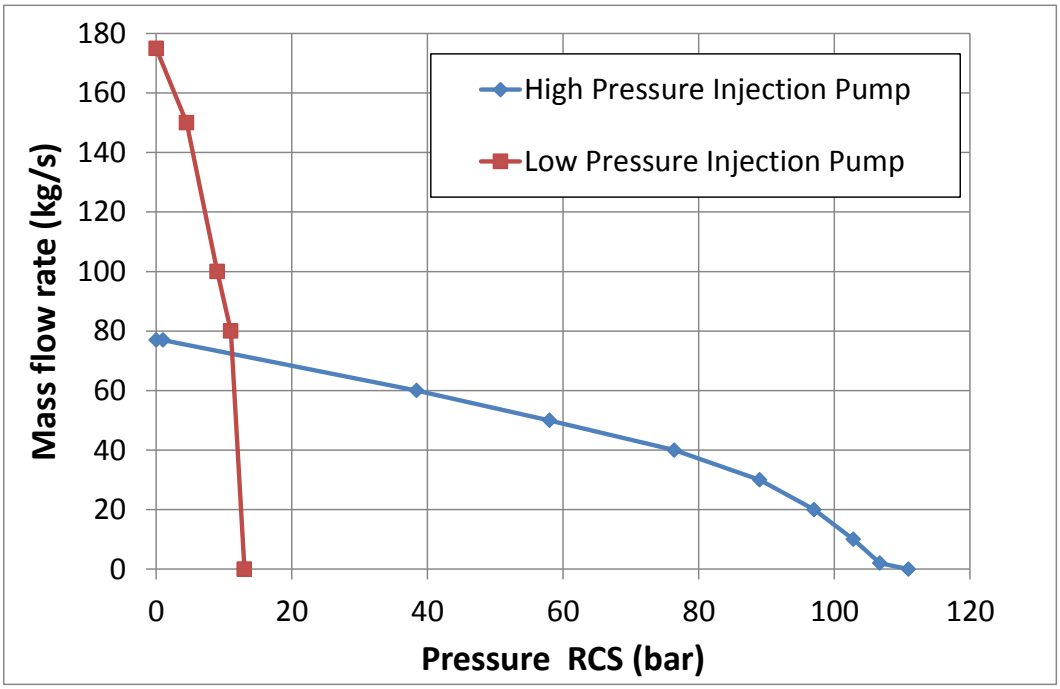

Figure C.2-1: Mass flow rate given by the HPIS and the LPIS pump as a function of the pressure in the RCS of a German Konvoi PWR.

C.3 External mobile pumps

Similarly to the LPI and HPI pumps, the section **6.5** has introduced the pressure head and the maximum mass flow rate given by each external pump. Within this section, more details about the ASTEC modelling of this characteristic curve are given. The pump XH100 has been taken as an example. The first step is to obtain the characteristic curve of the equipment from the technical specifications [140], represented in **Figure C.3-1**. Therein, the region with an optimum pump performance is provided by the manufacturer. In a second step, the optimum region is discretized in key values (see **Figure C.3-2**) and those are introduced in the ASTEC model of the German Konvoi PWR as a tabular function pressure-mass flow rate. The same procedure has been followed to discretize the optimum region of other external pumps.

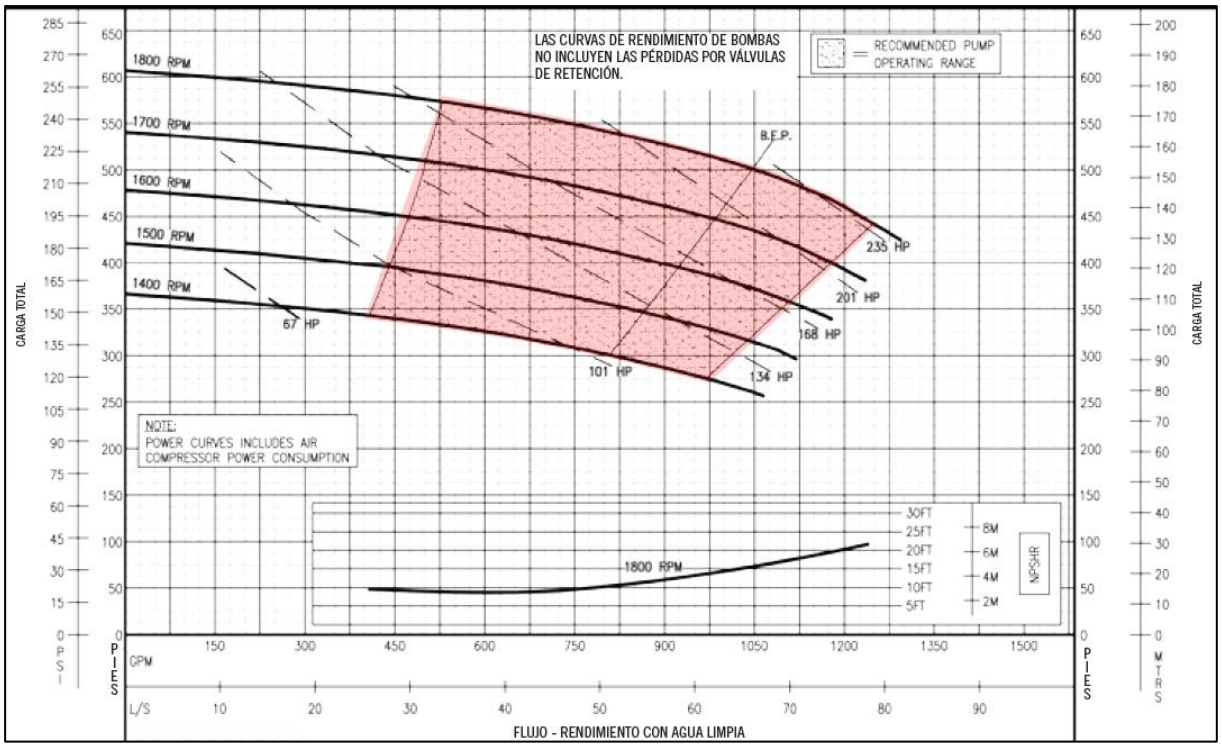

Figure C.3-1: Real characteristic curve of the pump XH100 [140]

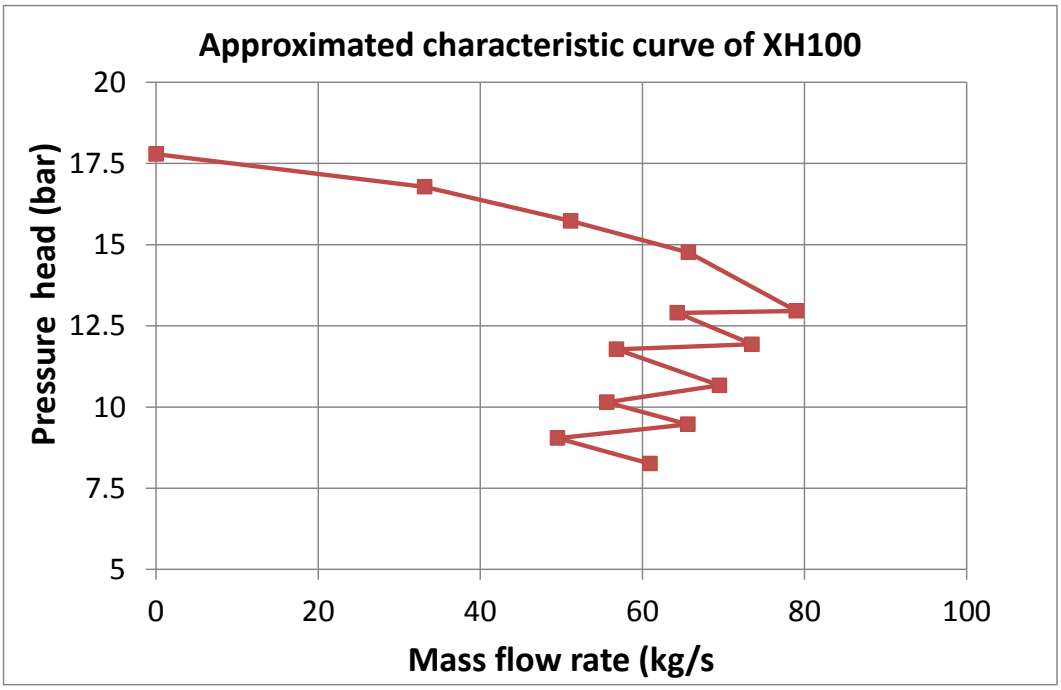

Figure C.3-2: Approximated characteristic curve of the pump XH100 in the generic ASTECV2.0 model of the German Konvoi PWR.

Appendix D Further Results of the performed sequences in a German Konvoi PWR using ASTECV2.0

A number of ASTECV2.0 simulations have been performed within Chapters **7** and **8**. Therein, the analyses were restricted to a few safety relevant parameters. Within this Appendix, the following information is shown:

- Timing and evolution of severe accident sequences without AM.
- Comparison between ASTECV2.0 predictions and those obtained with other SA codes by other institutions.
- Further results on the influence of selected SAM measures on the severe accident progression.

For that aim, the chapter is structured as follows, each section containing information about the different simulations that were performed in the aforementioned chapters.

- **D.1**: Medium Break LOCA (440 cm^2) in the cold leg of the pressurizer loop.
- **D.2**: Small break LOCA (10 cm^2) in the cold leg of the pressurizer loop.
- **D.3**: Station Blackout.

D.1 Medium Break LOCA (440 cm^2) in the cold leg of the pressurizer loop

Time (h)	Events
0.00	Break opening
0.00	SCRAM (Containment overpressure of 30 mbar): • Feed water loop A/B closed • Admission turbine A/B closed
0.00	ECCS signal (Pressurizer level below 2.30 m): • Activation Extra Borating System • Coast-down MCP loop A, B • Stop pressurizer regulations (heaters and sprays) • Activation LPI_AC1, LPI_AC2, LPI_AC3
0.08	ACCUs discharge into hot/cold legs
0.11	ACCUs hot/cold legs are empty
0.94	Initiate sump recirculation (volume tanks < $5m^3$)
1.00	Loss of AC current: • Stop Sump Recirculation • Stop Extra Borating System
1.67	Detection of CET 400 °C
1.68	Beginning of oxidation
1.80	Detection of CET 650 °C
1.84	First cladding creep rupture
2.00	First cladding dissolution by molten Zircaloy
2.27	First material slump into the lower plenum
2.38	20 tons of molten material in the lower plenum
3.37	Active zone of the core is uncovered
3.45	Lower head vessel failure

Table D.1-1: Summary of events for the sequence *MBLOCA-AC1h* relative to the break opening.

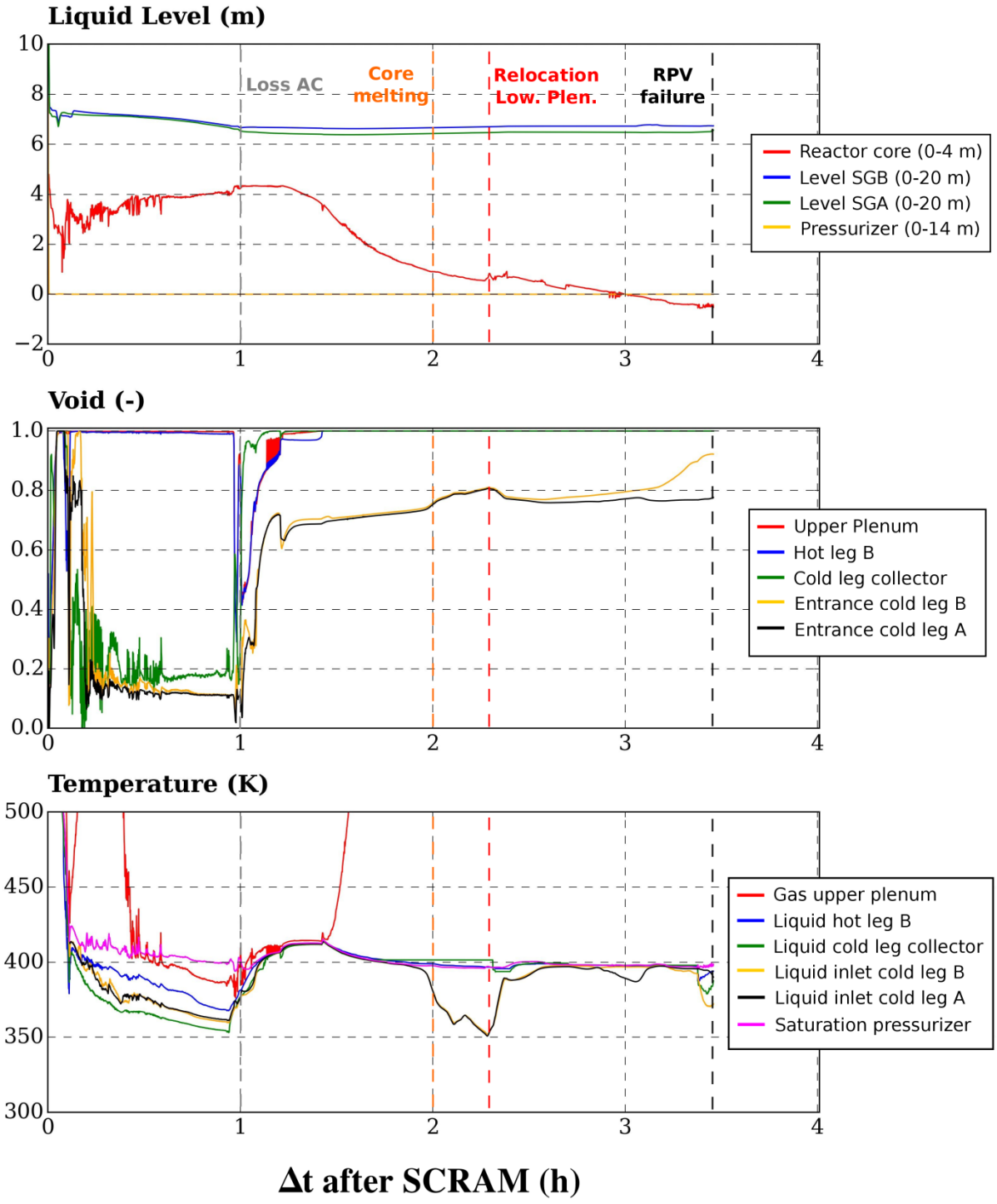

Figure D.1-1: Evolution of relative liquid levels (at relevant plant locations), void fractions and temperatures (at selected locations of the RCS) during *MBLOCA-AC1h* as a function of the Δt after SCRAM. Major events of the simulation are represented by dashed vertical lines.

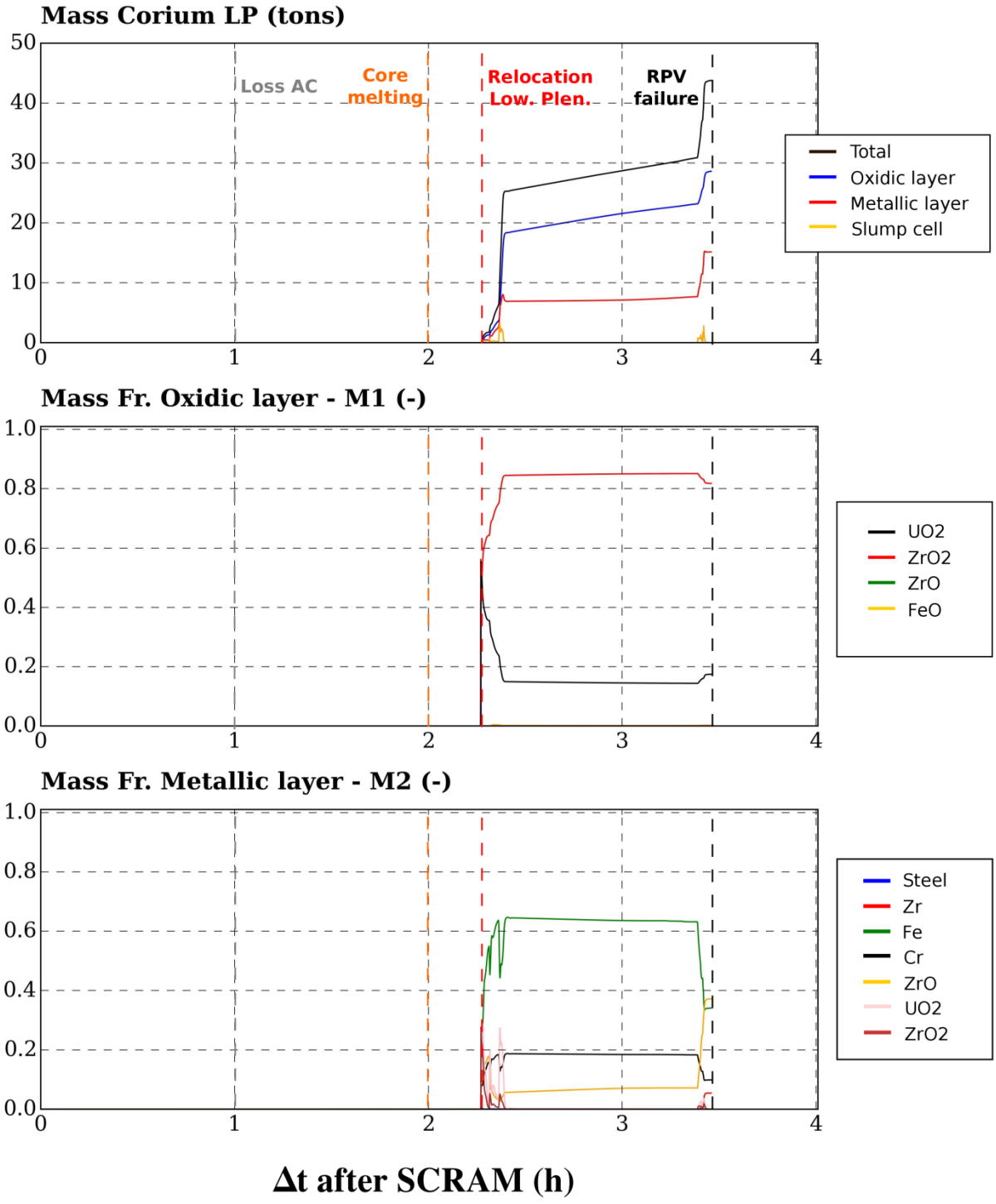

Figure D.1-2: Evolution of the mass of corium in the lower plenum and volumetric fractions of core materials in the metallic and the oxidic layer during *MBLOCA-AC1h* as a function of the Δt after SCRAM. Major events of the simulation are represented in dashed vertical lines.

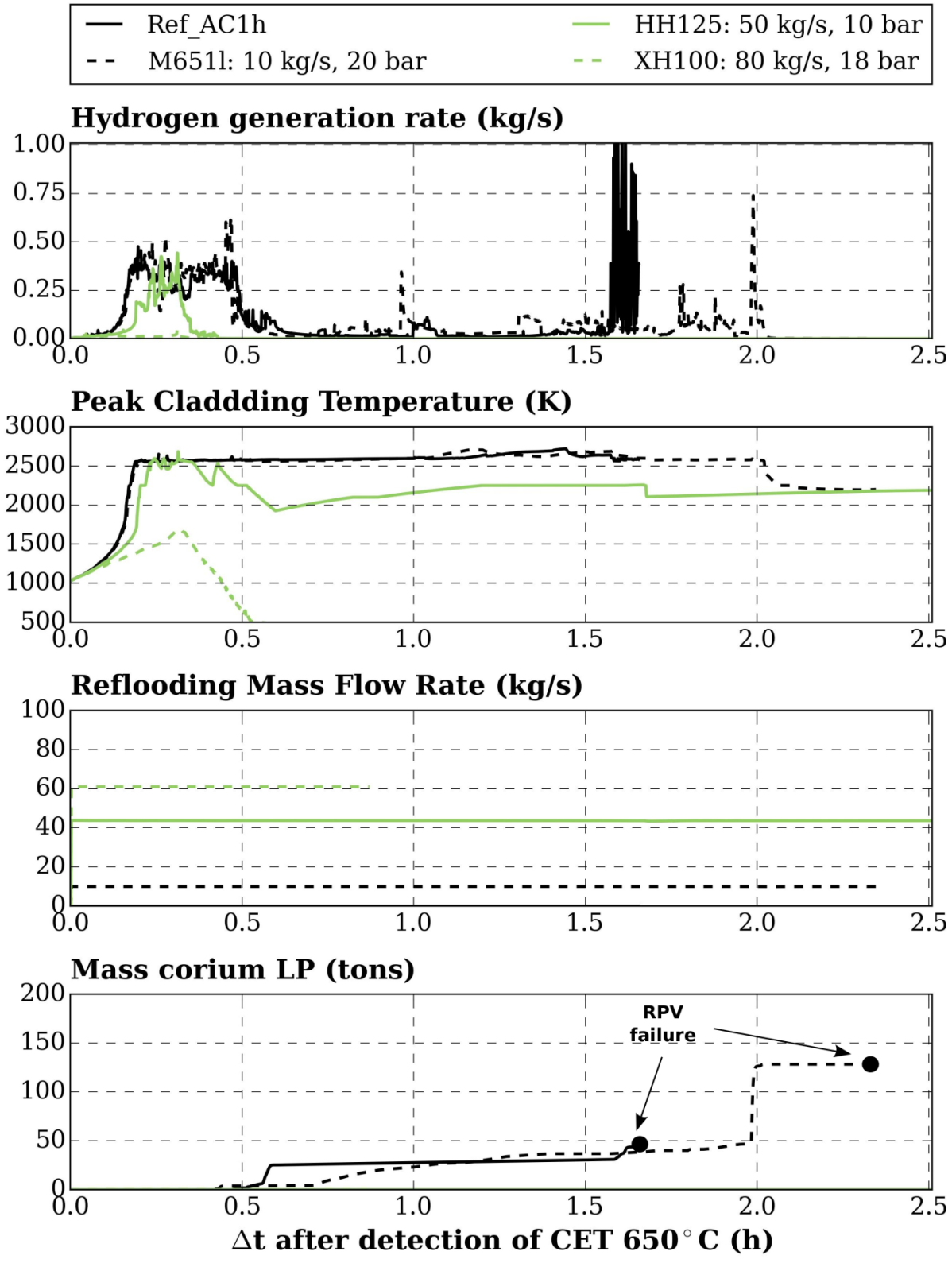

Figure D.1-3: Influence of mobile equipment during a 0-min delayed (after detection of CET=650 °C) core reflooding on the evolution of selected variables in comparison to the sequence *MBLOCA-AC1h* (MBLOCA with SBO **1 h** after SCRAM and without core reflooding). Black points mark RPV failure occurrences.

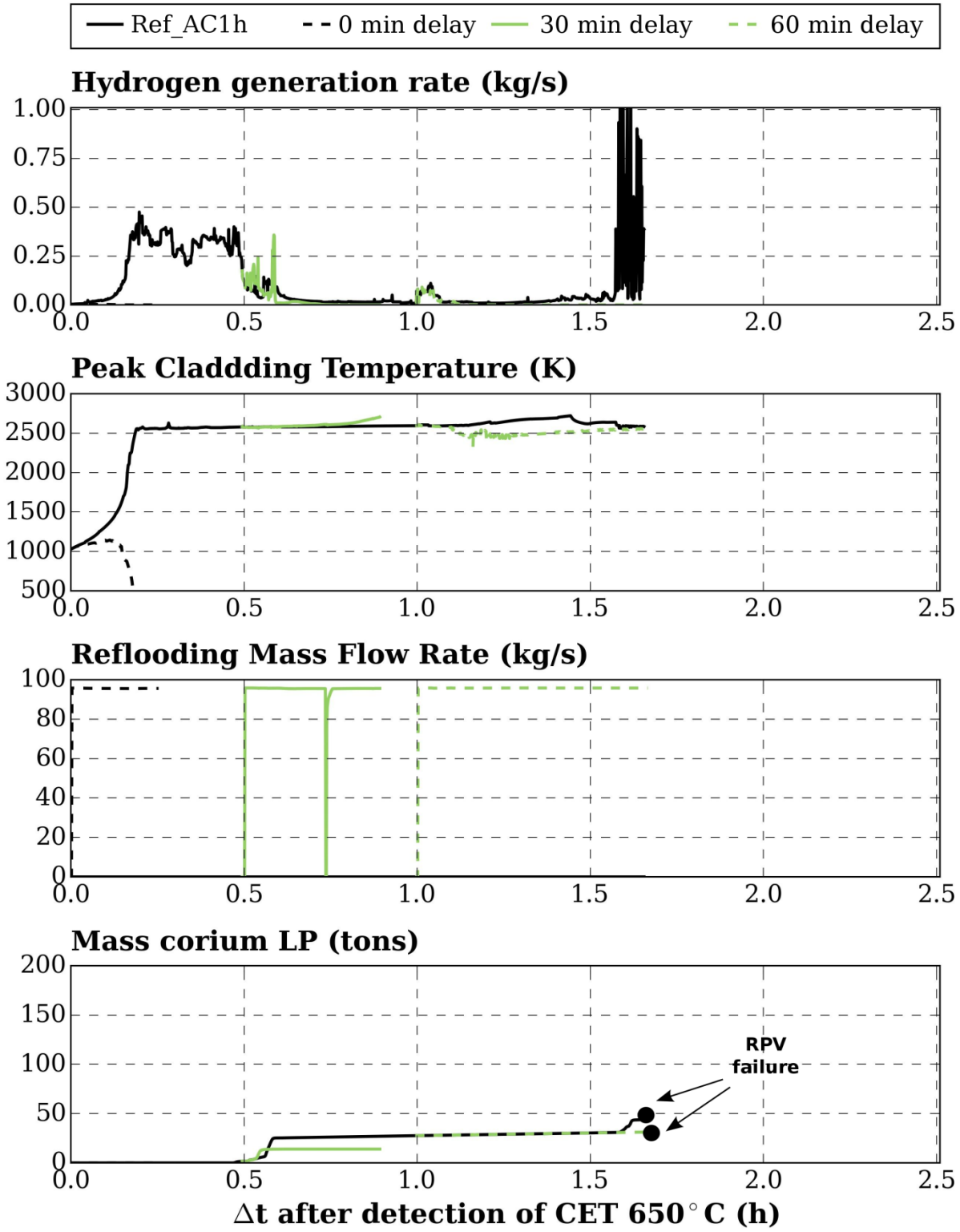

Figure D.1-4: Influence of a delayed (after detection of CET 650 °C) core reflooding by means of the mobile pump AE16Glp on the evolution of selected variables in comparison to the sequence *MBLOCA-AC1h* (MBLOCA with SBO **1 h** after SCRAM and without core reflooding). Black points indicate RPV failure occurrences.

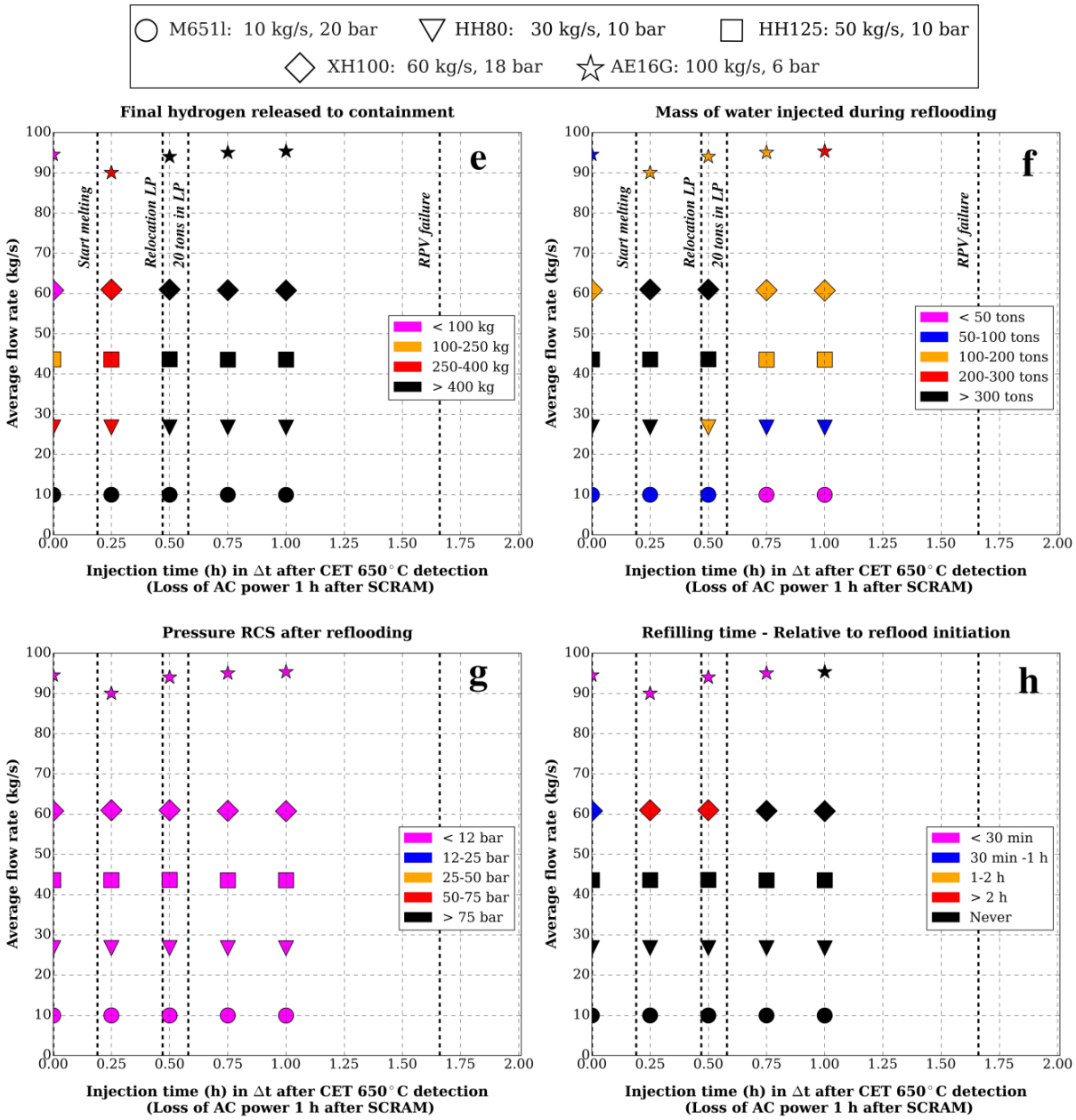

Figure D.1-5: Final value of selected FOMs as a function of the average RMFR and the injection time (relative to the detection of CET=650°C). Black dashed vertical lines represent occurrence times of major events in *MBLOC-AC1h* (MBLOCA with SBO at **1 h** after SCRAM and without core reflooding).

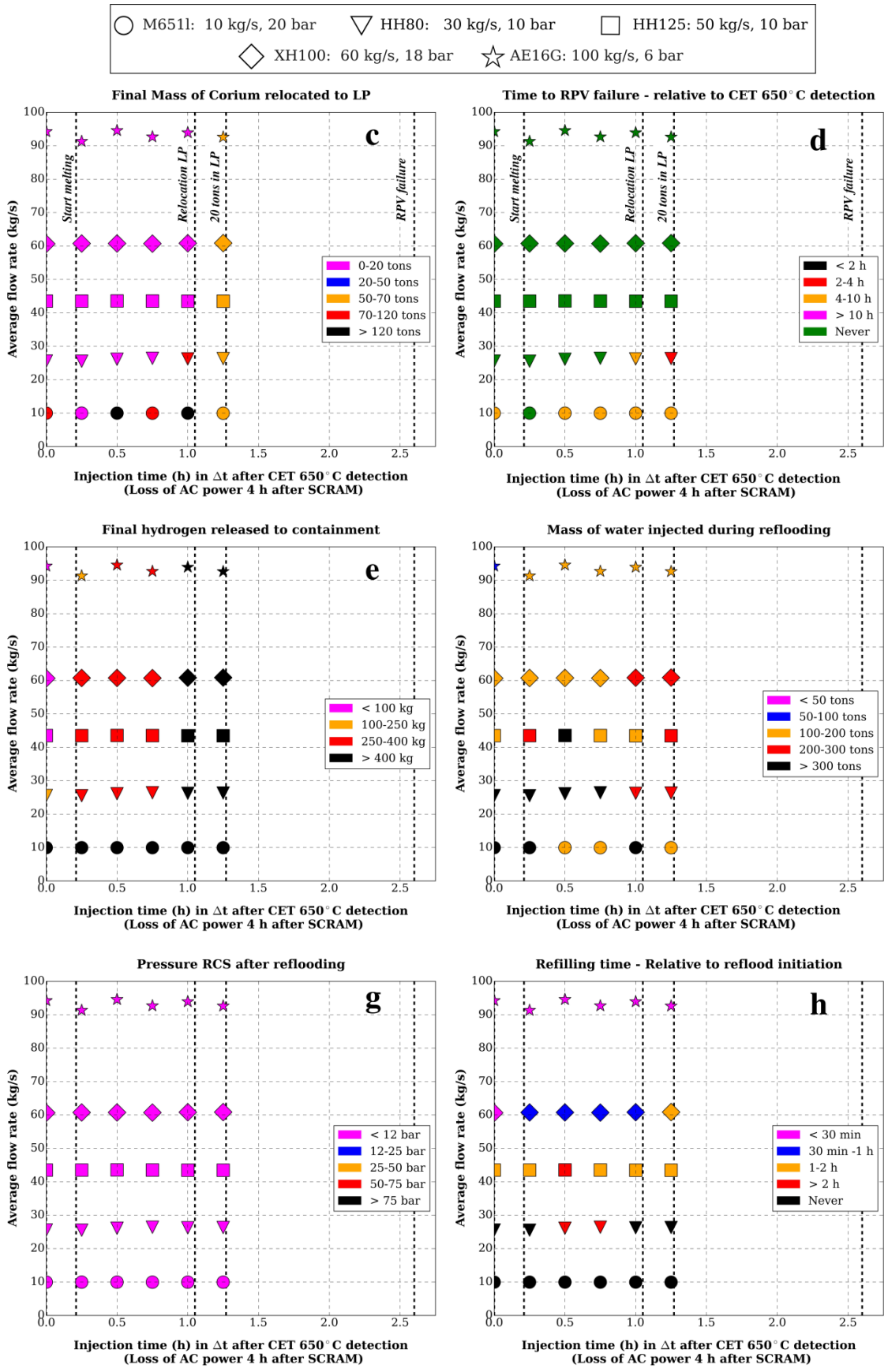

Figure D.1-6: Final value of selected FOMs as a function of the average RMFR and the injection time (relative to the detection of CET=650°C). Black dashed vertical lines represent occurrence times of major events in *AC4h* (MBLOCA with SBO at **4 h** after SCRAM and without core reflooding).

D.2 Small break LOCA (10 cm^2) in the cold leg of the pressurizer loop

Time (h)	Name of Event
0.00	Break opening
0.01	SCRAM (Containment overpressure of 30 mbars) • Feed water loop A/B closed • Admission turbine A/B closed
0.03	ECCS signal (Pressurizer level below 2.30 m): • Activation Extra Borating System • Coast-down MCP loop A, B • Stop pressurizer regulations (heaters and sprays) • Activation trains HPI_A1, HPI_A2, HPI_A3
2.26	Deactivation Extra Borating System (tanks empty)
2.51	EFWS injecting into SGB (Liquid level SGB < 4.5 m)
4.18	Deactivation of HPI_A1/2/3 (tanks empty)
4.20	Accumulator discharge into cold/hot legs
9.02	Beginning of oxidation
9.20	Detection of CET 400 °C
9.54	First cladding perforation by grid
9.62	Detection of CET 650 °C
9.67	First cladding dissolution by molten Zircaloy
9.98	First material slump into the lower plenum
10.30	20 corium tons in the lower plenum
10.70	Total core uncovery
11.50	Lower head vessel failure

Table D.2-1: Summary of events for the sequence SBLOCA with unlimited AC power supply (*Ref-SBLOCA*) relative to the break opening.

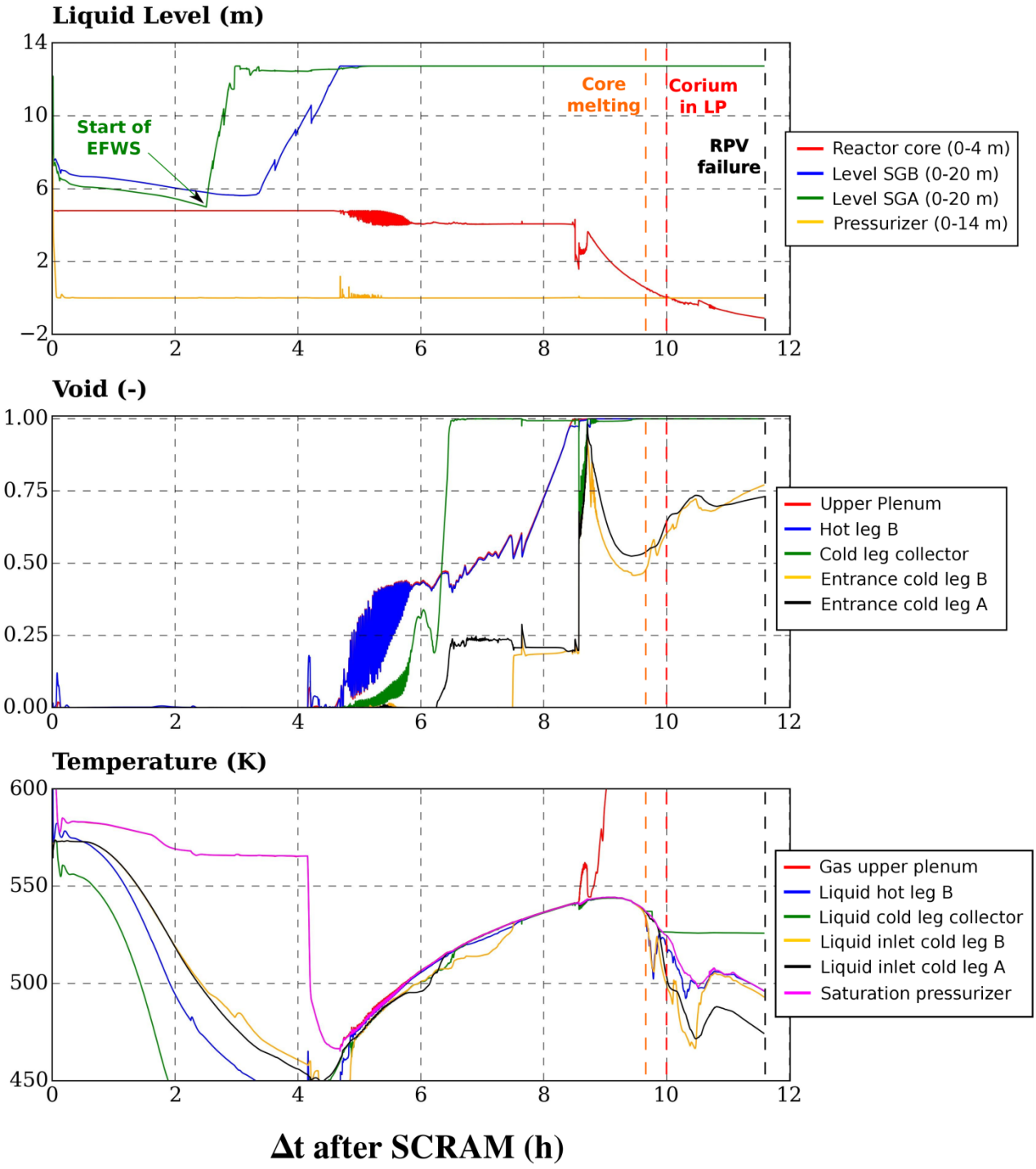

Figure D.2-1: Evolution of relative liquid levels (at relevant plant locations), void fractions and temperatures (at selected locations of the RCS) during *Ref-SBLOCA* as a function of the Δt after SCRAM. Major events of the simulation are represented by dashed vertical lines.

Time (h)	Name of Event
0.00	Break opening
0.01	SCRAM (Containment overpressure of 30 mbar) • Feed water loop A/B closed • Admission turbine A/B closed
0.03	ECCS signal (Pressurizer level below 2.30 m): • Activation Extra Borating System • Coast-down MCP loop A, B • Stop pressurizer regulations (heaters and sprays) • Activation trains HPI_A1, HPI_A2, HPI_A3
1.01	Loss of AC current: • Stop trains HPI_A1/2/3 • Stop Extra Borating System
3.39	Detection of CET 400 °C
3.65	Detection of CET 650 °C
3.69	First cladding perforation by grid
3.81	First cladding dissolution by molten Zircaloy
4.07	Start of FPs release from fuel pellets
4.07	First material slump into the lower plenum
4.18	20 corium tons relocated to LP
4.28	Total core uncovery
4.56	Lower head vessel failure

Table D.2-2: Summary of events for the sequence *SBLOCA-AC1h* relative to the break opening.

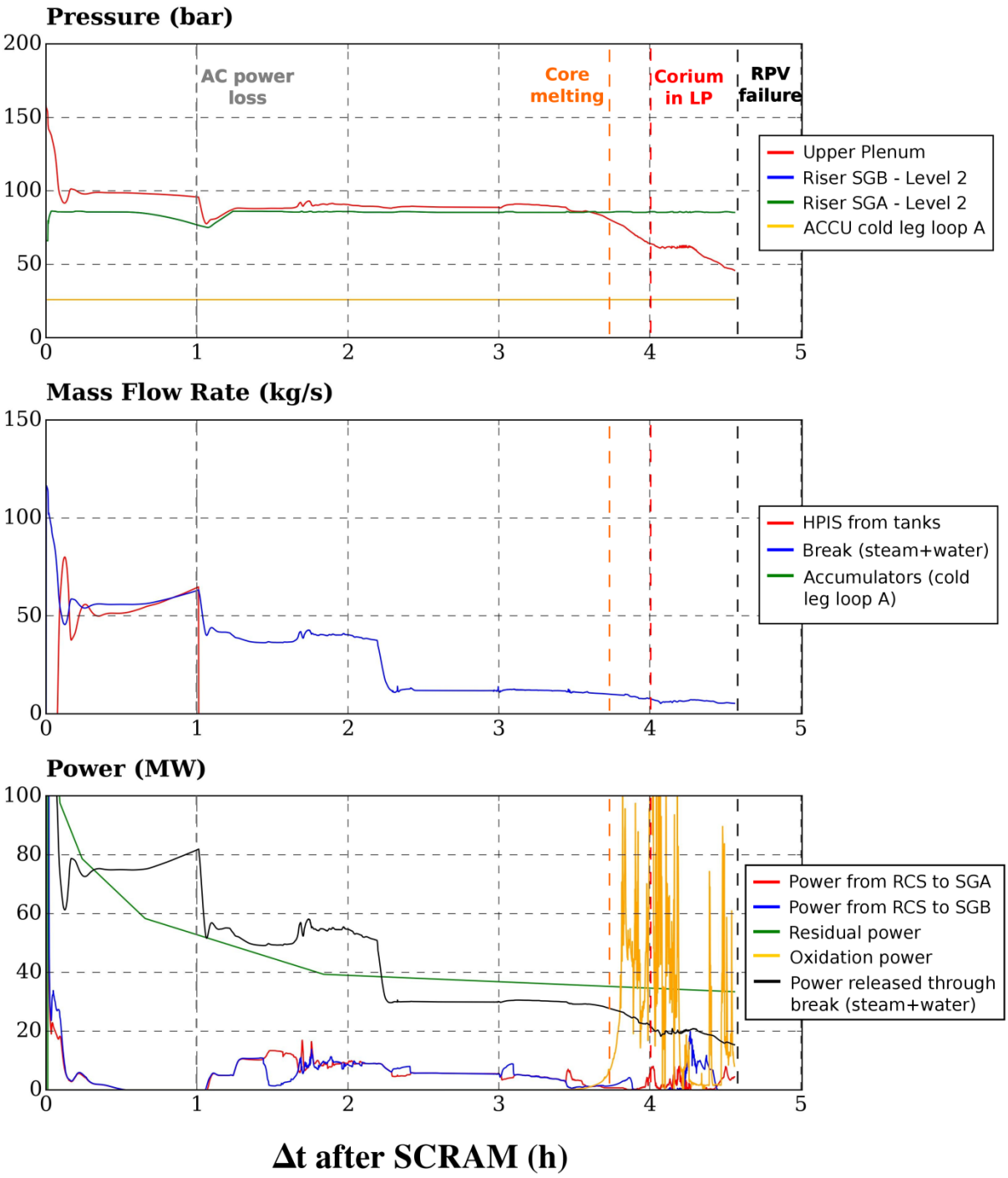

Figure D.2-2: Evolution of pressures (in selected control volumes), mass flow rates (given by relevant safety systems or exiting through the break) and relevant heat transfer rates during *SBLOCA-AC1h* as a function of the Δt after SCRAM. Major events of the simulation are represented by dashed vertical lines.

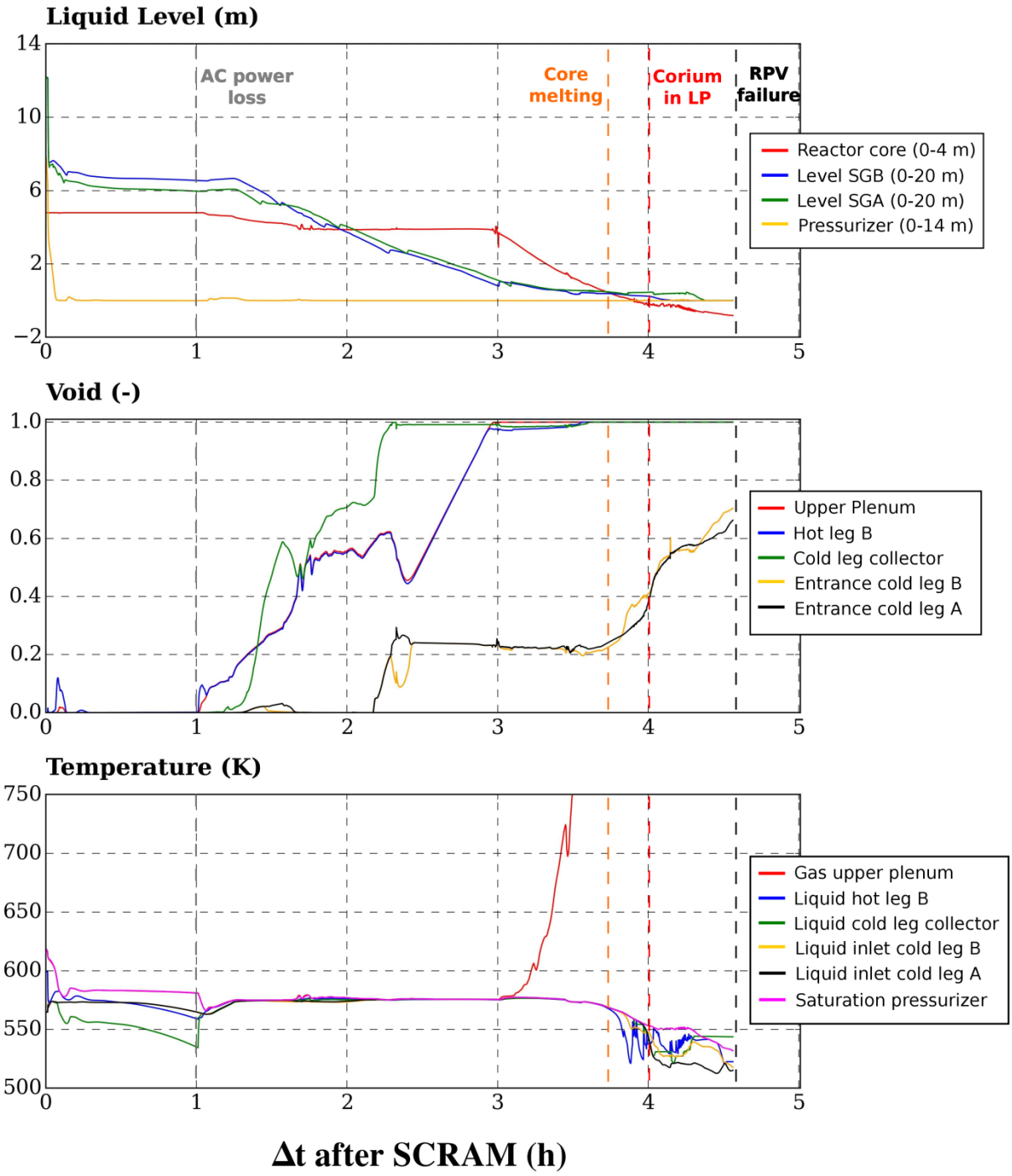

Figure D.2-3: Evolution of relative liquid levels (at relevant plant locations), void fractions and temperatures (at selected locations of the RCS) during *SBLOCA-AC1h* as a function of the Δt after SCRAM. Major events of the simulation are represented by dashed vertical lines.

Events	**ASTEC (h)**	**MELCOR (h)**
Injection from HPIS	0.04 – 4.05	0.04 – 5.10
Accumulator discharge	4.20 – 4.50	5.25 – 5.40
Start of FPs release from fuel pellets (s)	9.00	8.00
Core melting	9.67	8.25
Corium relocation to the lower plenum	10.25	9.38
Dry-out of lower plenum	10.80	9.40
Lower head vessel failure	11.50	9.75

Table D.2-3: Comparison between ASTECV2.0 (this work) and MELCOR 1.8.4 [144] on the scenario *Ref-SBLOCA.*

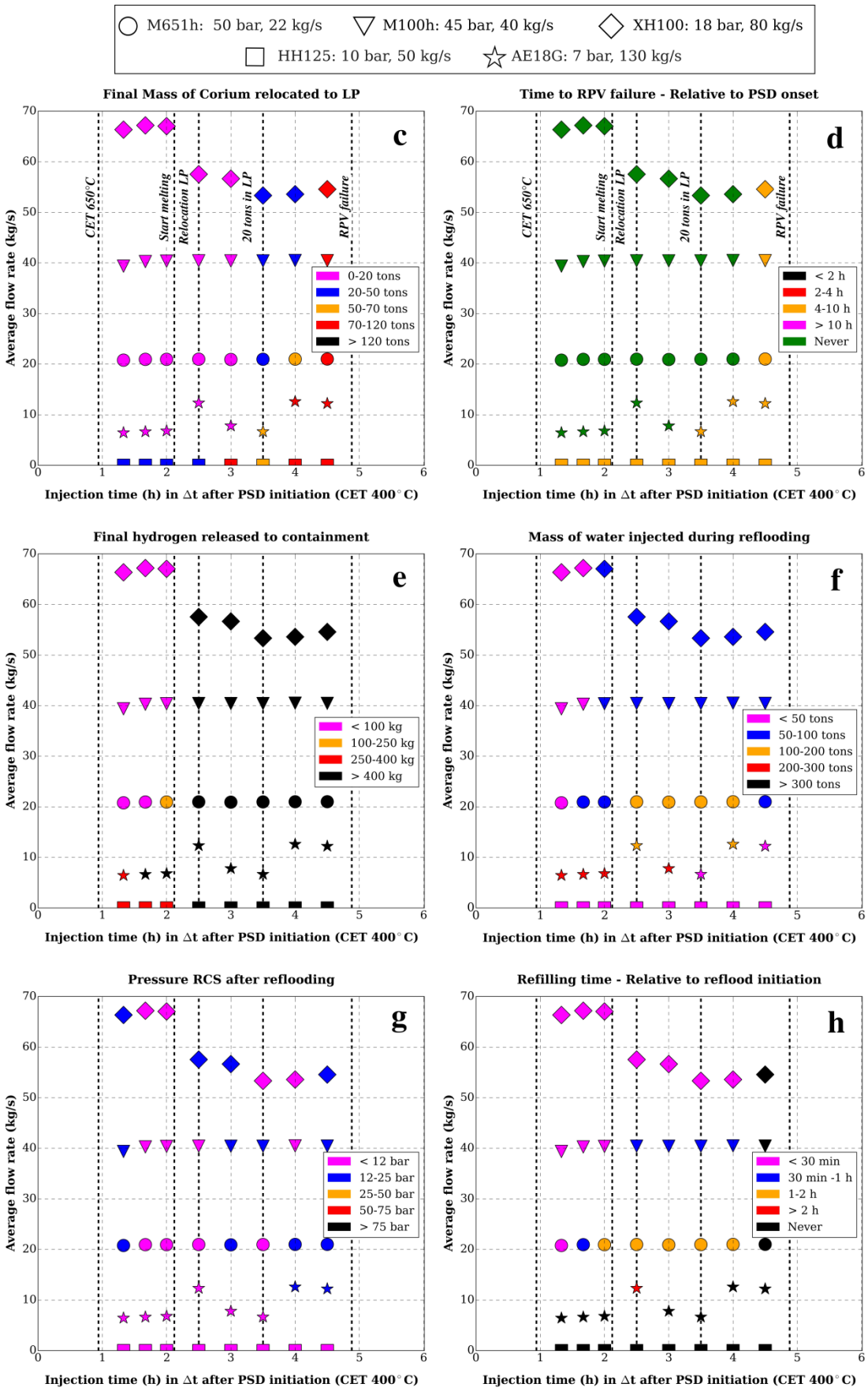

Figure D.2-4: Final value of selected FOMs as a function of the average RMFR and the injection time (relative to PSD initiation). Vertical lines represent occurrence times of major events in *AC1h*$_{PSDCET400}$ (SBLOCA with SBO at **1 h** after SCRAM with **PSD at CET 400 °C** and without core reflooding).

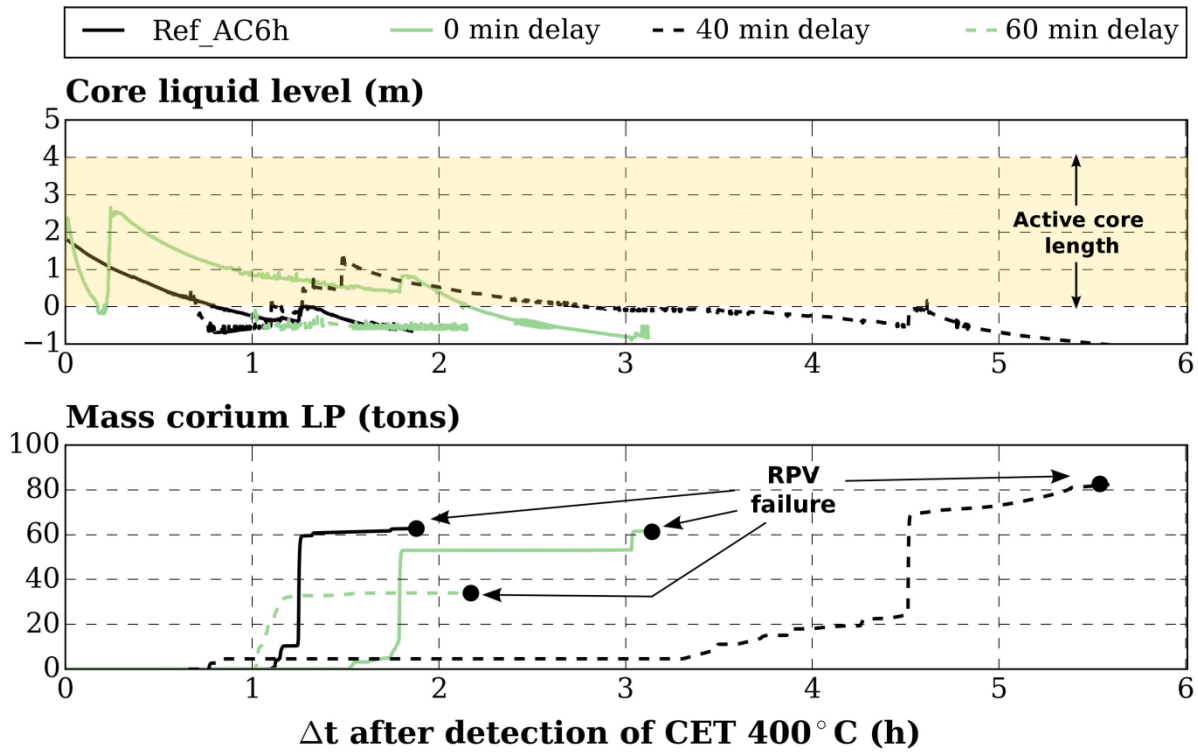

Figure D.2-5: Influence of a delayed (after the detection of CET 400 °C) PSD on the evolution of selected variables in comparison to the sequence *SBLOCA-AC6h* (SBLOCA with SBO at **6 h** after SCRAM without PSD). Red crosses mark PSD initiation; black points mark RPV failure occurrences.

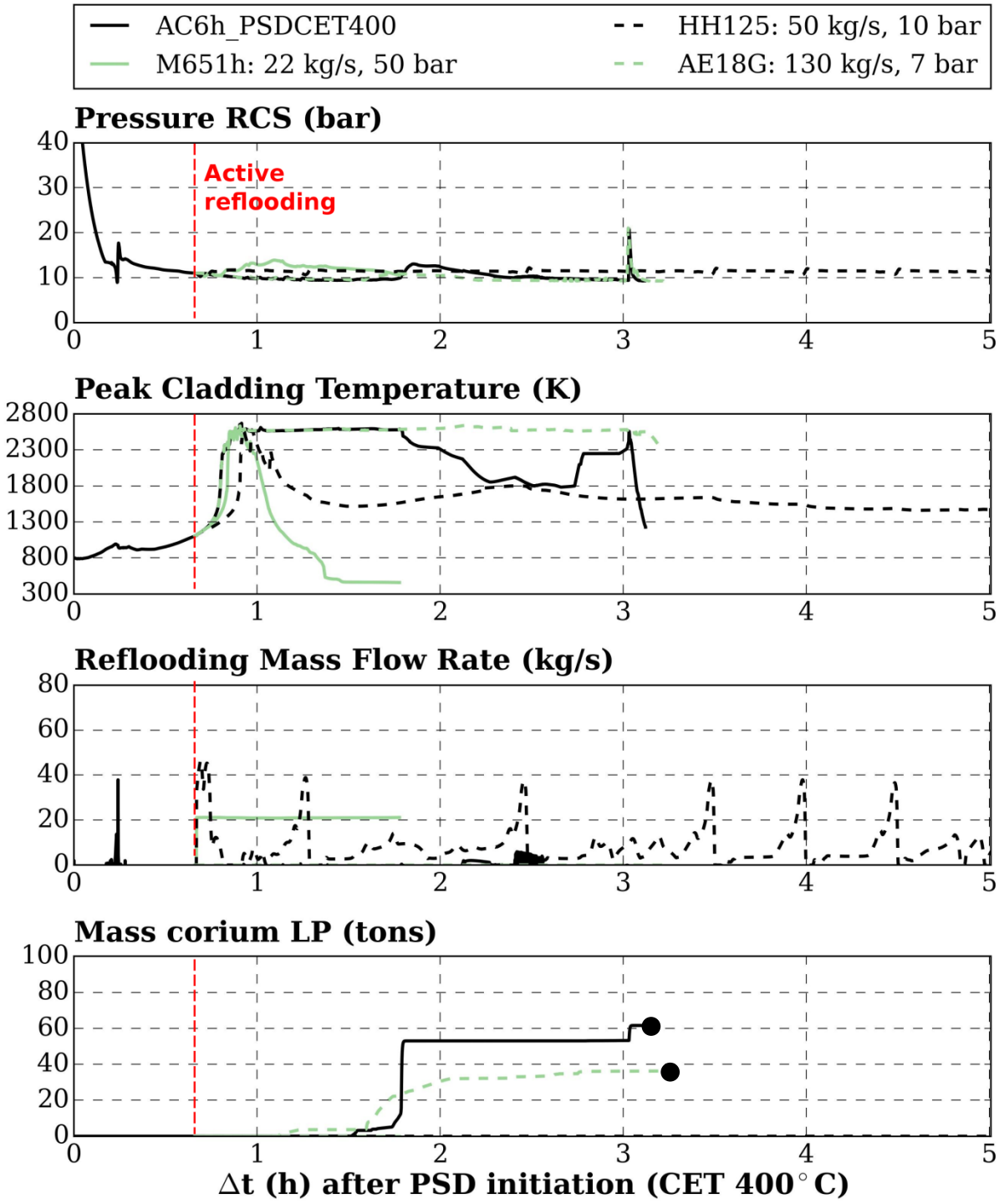

Figure D.2-6: Influence of mobile equipment during a 40-min delayed (after PSD initiation) core reflooding on the evolution of selected variables in comparison to the sequence *AC6h*$_{PSDCET400}$ (SBLOCA with SBO **6 h** after SCRAM, with **PSD at CET 400 °C** and without core reflooding). The red line marks reflooding initiation; black points mark RPV failure occurrences.

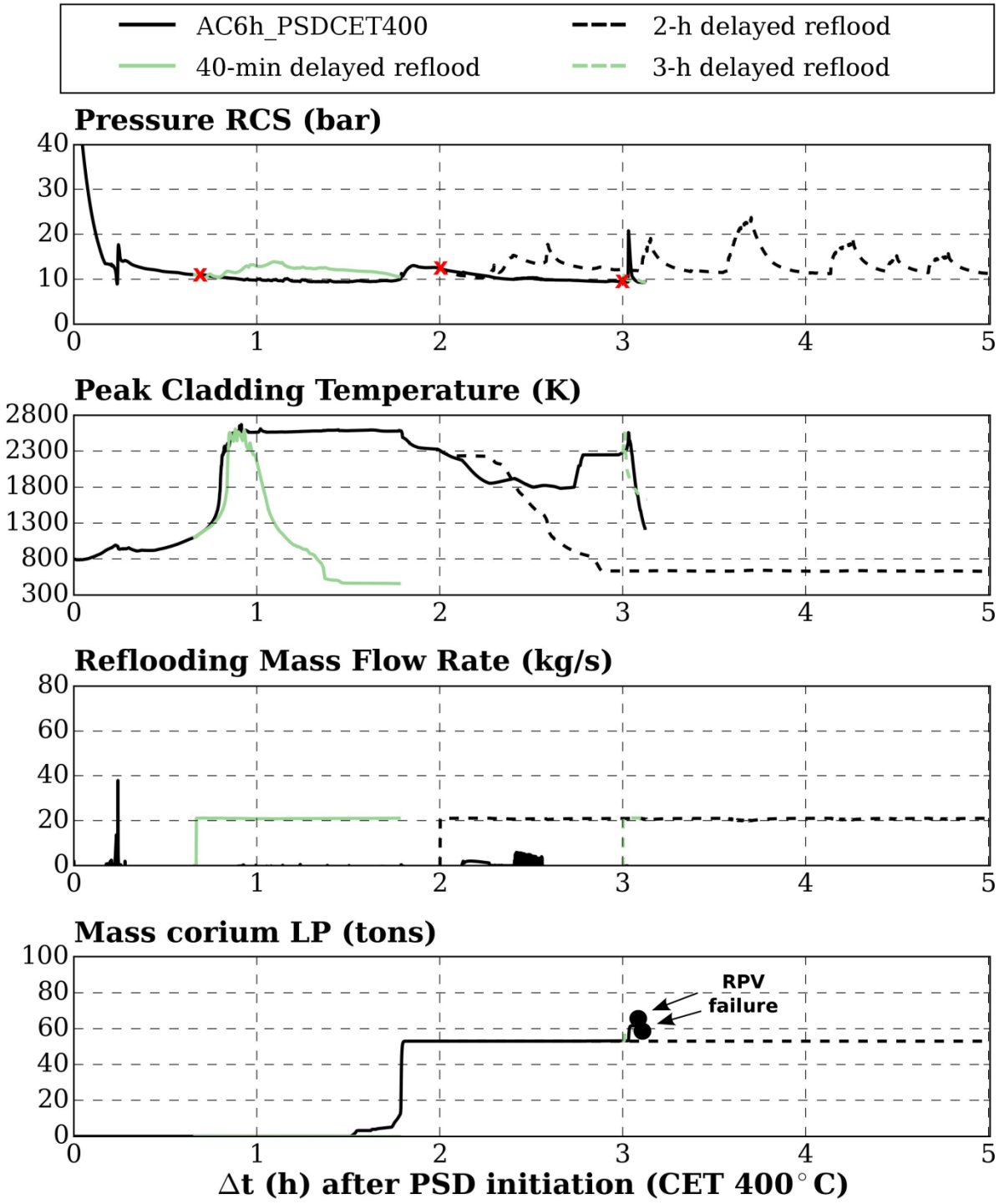

Figure D.2-7: Influence of a delayed (after PSD initiation) core reflooding by means of the equipment M651h on the evolution of selected variables in comparison to *AC6h*$_{PSDCET400}$ (SBLOCA with SBO **6 h** after SCRAM, with **PSD at CET 400 °C** and without core reflooding). Red crosses mark the initiation of core reflooding; black points mark RPV failure occurrences.

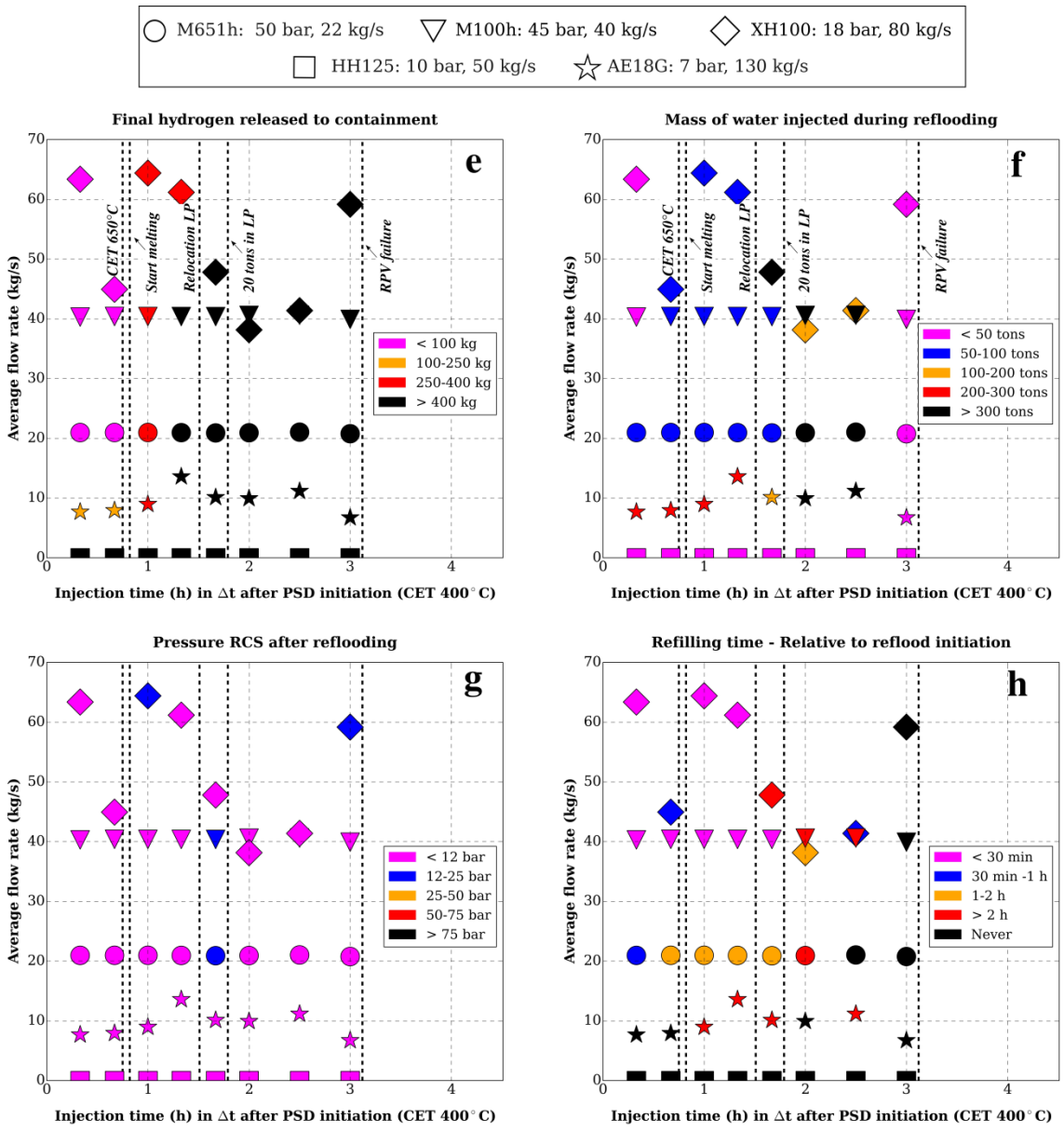

Figure D.2-8: Final value of selected FOMs as a function of the average RMFR and the injection time (relative to PSD initiation). Black dashed vertical lines represent occurrence times of major events in *AC6h*$_{PSDCET400}$ (SBLOCA with SBO at **6 h** after SCRAM, with **PSD at CET 400 °C** and without core reflooding).

D.3 Station Blackout

Time (h)	Events
0.00	Loss of AC power: • SCRAM • Coast-down of MCPA/B • Feed water to SGA/SGB off • No active safety systems available
0.00	Turbine trip (SCRAM): • Turbine valve A/B closed
0.33	Liquid level in SGA and SGB < 4 m.
1.20	Dry-out of SGA and SGB
1.61	Start of ICARE - automatic start
2.61	Beginning of oxidation
2.62	Detection of CET 400 °C
2.91	Detection of CET 650 °C
2.93	First cladding perforation by grid
3.40	First cladding dissolution by molten Zircaloy
3.76	ECCS criteria (Pressurizer level below 2.30 m and containment overpressure above 30 mbar)
3.84	First slump of corium in lower plenum
4.18	Total core uncovery
6.14	Lower head vessel failure

Table D.3-1: Summary of events for the sequence *Ref-SBO* relative to the loss of AC power supply.

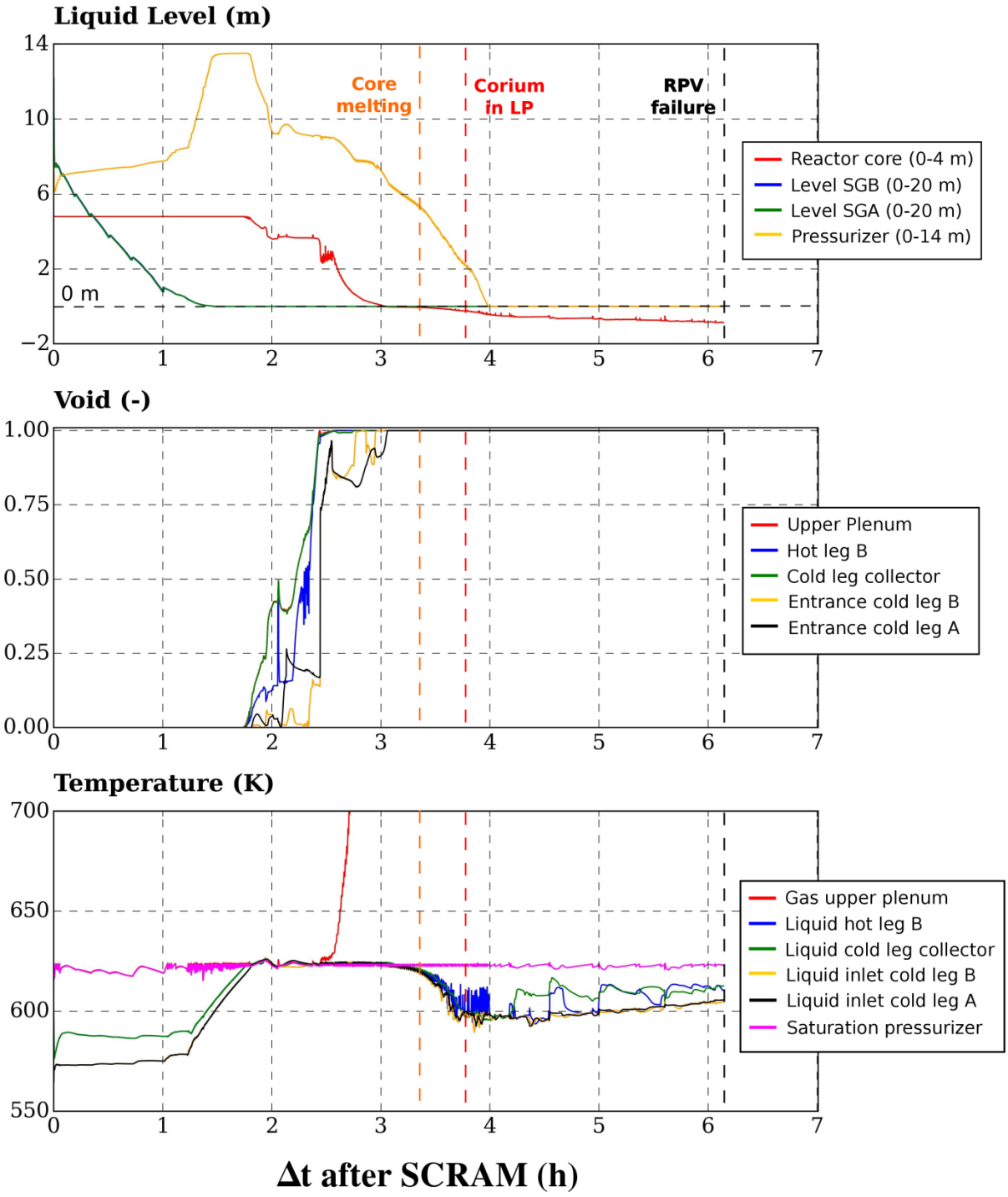

Figure D.3-1: Evolution of relative liquid levels (at relevant plant locations), void fractions and temperatures (at selected locations of the RCS) during the sequence *Ref-SBO* as a function of the Δt after SCRAM. Major events of the simulation are represented by dashed vertical lines.

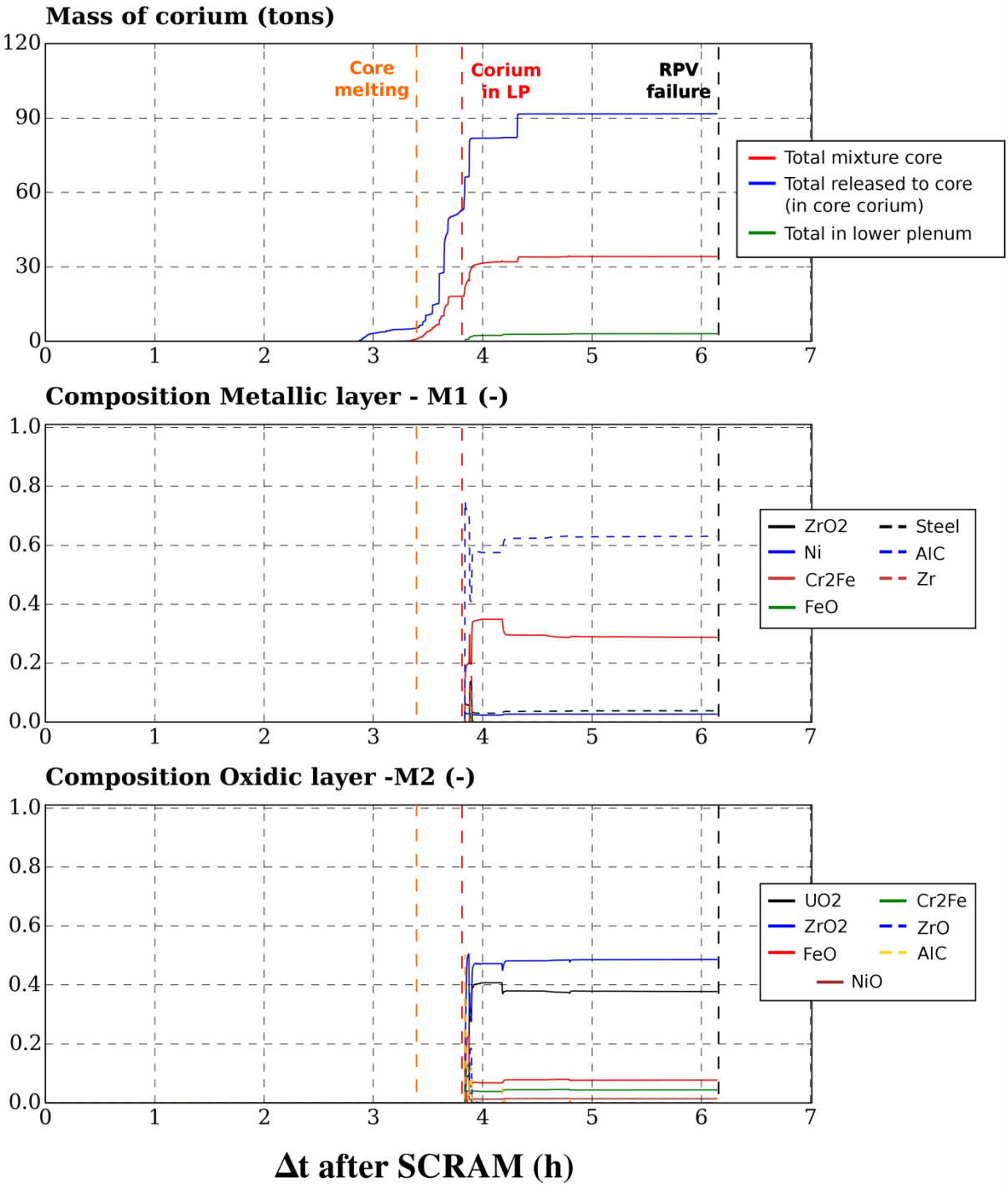

Figure D.3-2: Evolution of the mass of corium at selected locations of the RPV and volumetric fractions of core materials in the metallic and the oxidic layer during the sequence *Ref-SBO* as a function of the Δt after SCRAM. Major events of the simulation are represented in dashed vertical lines.

Events	**ASTEC (h)**	**ATHLET (h)**	**MELCOR (h)**
Station Blackout	0 s	0 s	0 s
Dry-out of SGs	1.20	0.78	0.57
Start of FPs release from fuel pellets (s)	3.28	2.45	2.22
Core melting	3.40	2.45	2.30
Corium relocation to the lower plenum	3.84	2.61	3.25
Dry-out of lower plenum	5.10	3.21	3.26
Lower head vessel failure	6.14	3.45	3.36

Table D.3-2: Comparison among ASTECV2.0 (this work), ATHLET-CD V3.0 [145] and MELCOR 1.8.4 [144] concerning (*SBO-) NOSAM*.

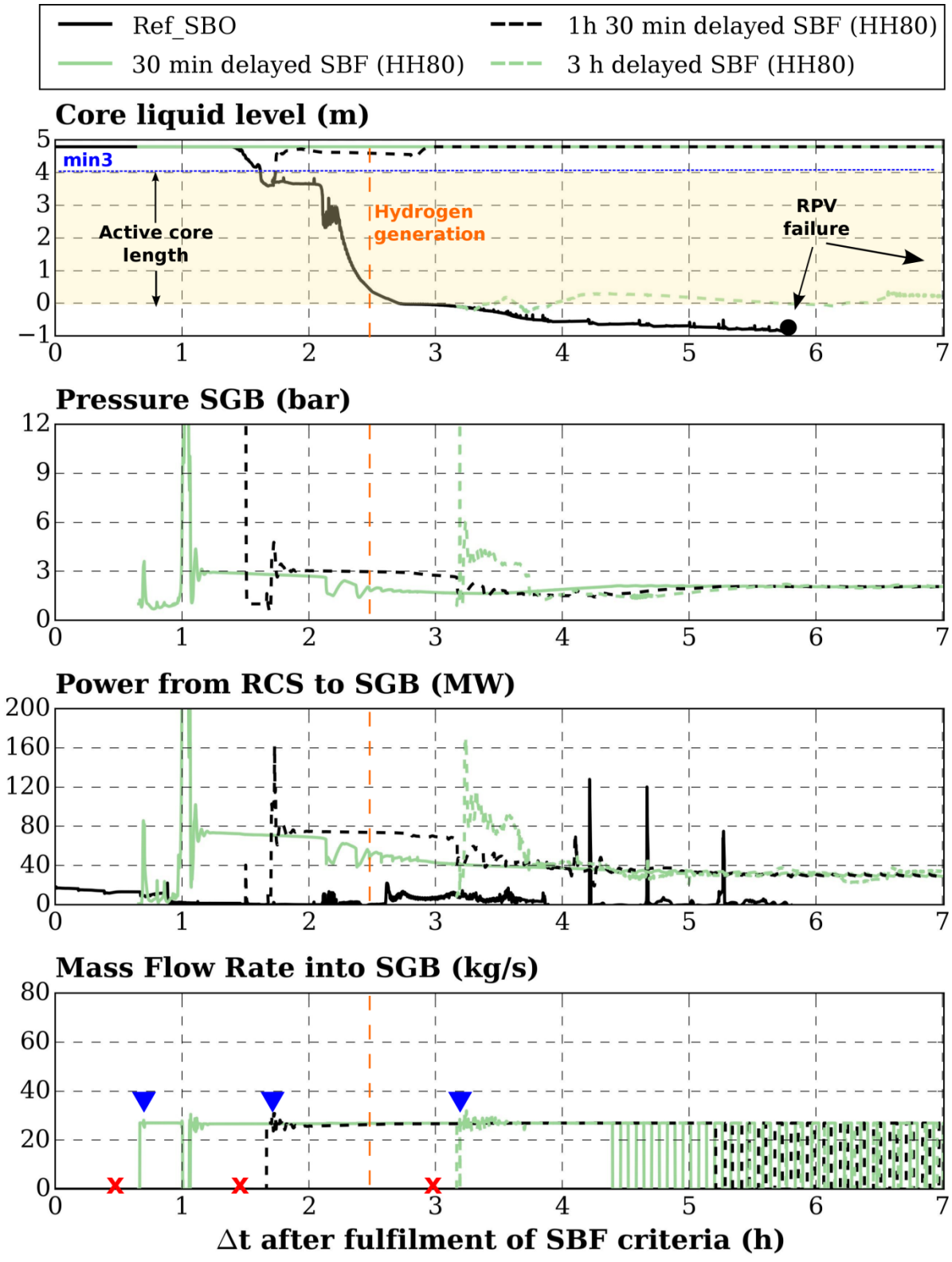

Figure D.3-3: Influence of a delayed SBF (after transgression of SBF criteria) of SGB by means of the pump HH80 on the evolution of selected variables compared to *Ref-SBO* (SBO at **0 h** without AM measures). The orange vertical line marks the hydrogen generation onset in *Ref-SBO*; crosses/triangles mark bleed/feed initiation (for sequences involving SBF); black dots mark RPV failure occurrences.

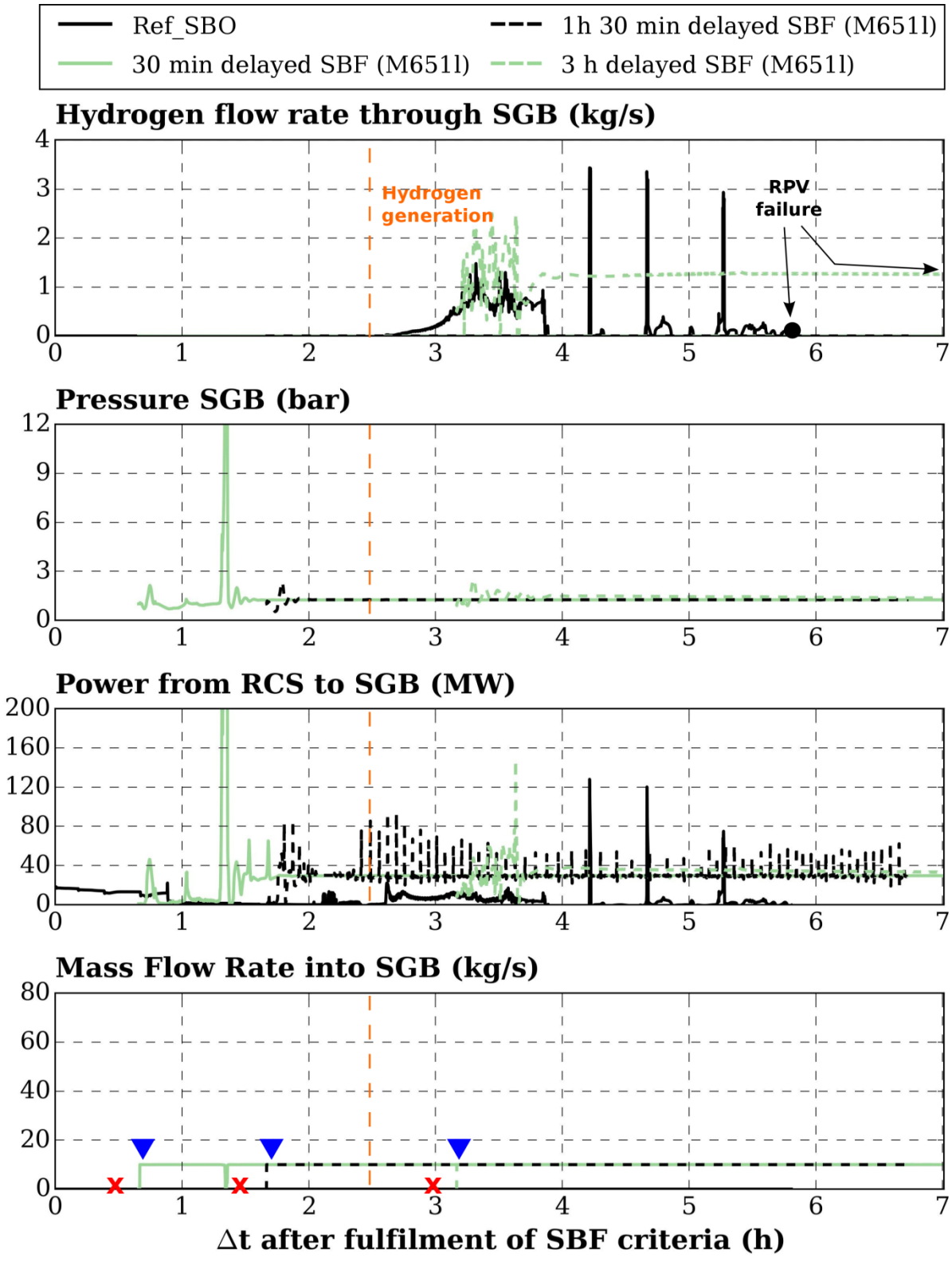

Figure D.3-4: Influence of a delayed SBF (after transgression of SBF criteria) of SGB by means of the pump M651h on the evolution of selected variables in comparison to *Ref-SBO* (SBO at **0 h** without AM measures). The orange vertical line marks the onset of hydrogen generation in *Ref-SBO*; crosses/triangles mark bleed/feed initiation (for the sequences involving SBF); black dots mark RPV failure occurrences.

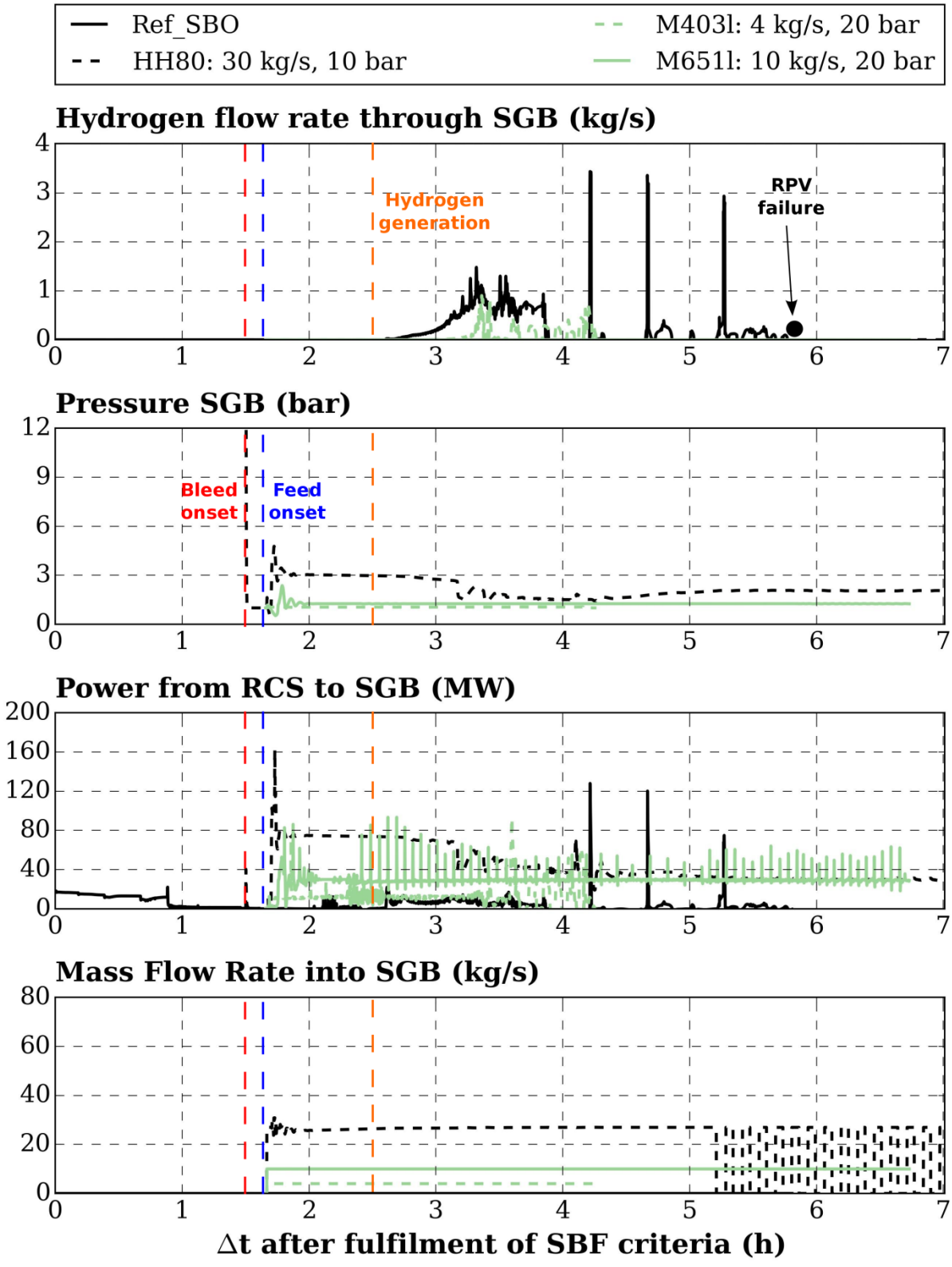

Figure D.3-5: Influence of mobile equipment during a 1.50 h-delayed SBF (after transgression of SBF criteria) of SGB on the evolution of selected variables compared to the *Ref-SBO* (SBO at **0 h** without AM measures). The orange vertical line marks the onset of hydrogen generation in *Ref-SBO*; red/blue lines mark the initiation of bleed/feed (for the sequences involving SBF); black points mark RPV failure occurrences.

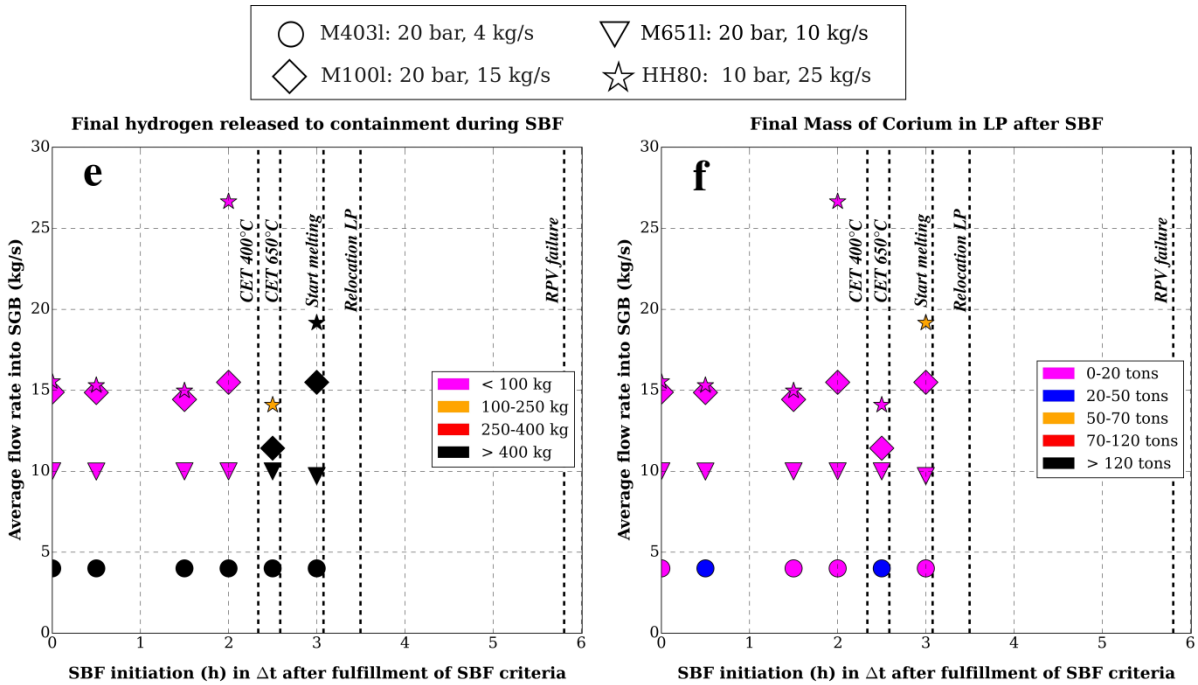

Figure D.3-6: Final (e) Hydrogen released to the containment and (f) Mass of corium in the lower plenum as a function as a function of the average injection rate into the SGB and the SBF initiation relative to the fulfilment of SBF criteria. Black dashed vertical lines represent occurrence times of major events in *Ref-SBO* (SBO at **0 h** without AM measures).

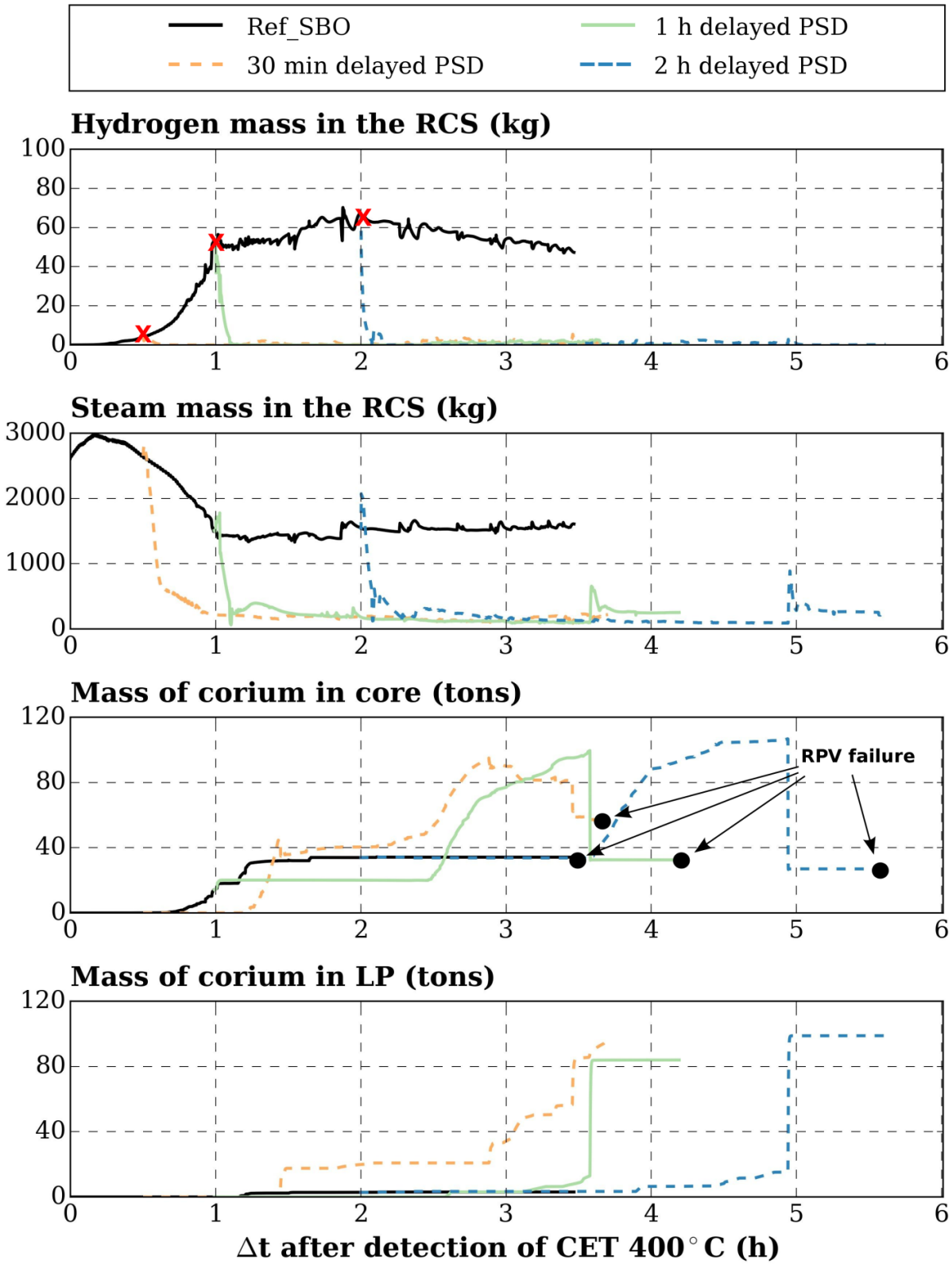

Figure D.3-7: Influence of a delayed (after the detection of CET=400 °C) PSD with all pressurizer valves on the evolution of a second set of variables in comparison to the sequence *Ref-SBO* (SBO at **0 h** after SCRAM without AM measures). Red crosses mark PSD initiation (for the cases involving PSD); black points mark RPV failure occurrences.

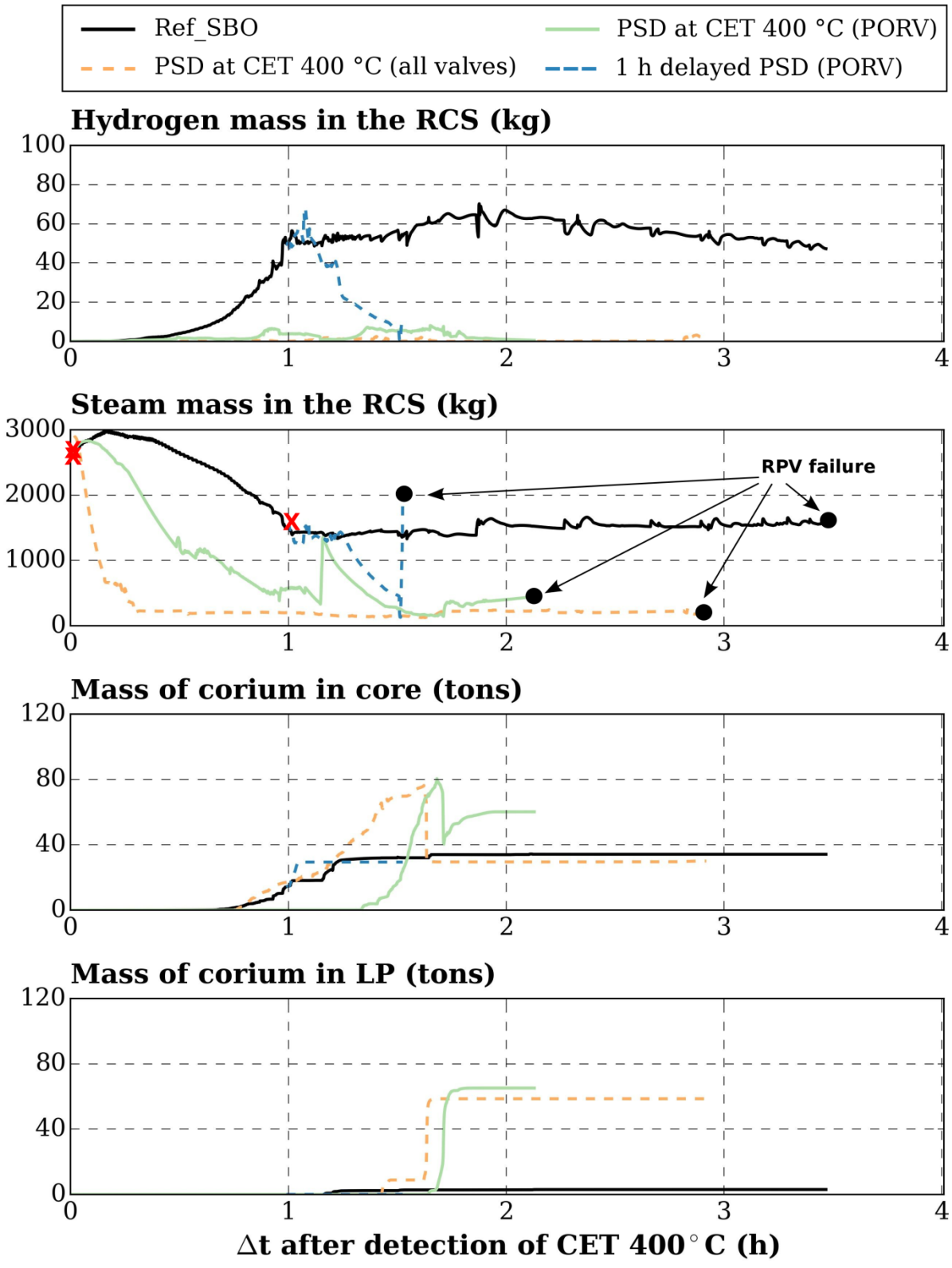

Figure D.3-8: Influence of delayed PSD by means of the pressurizer PORV on the evolution of a second set of variables in comparison to *Ref-SBO* (SBO at **0 h** after SCRAM without AM measures) and to the case where PSD is initiated at CET 400 °C by means of all pressurizer valves. Red crosses mark PSD initiation (for the cases involving PSD); black points mark RPV failure occurrences.

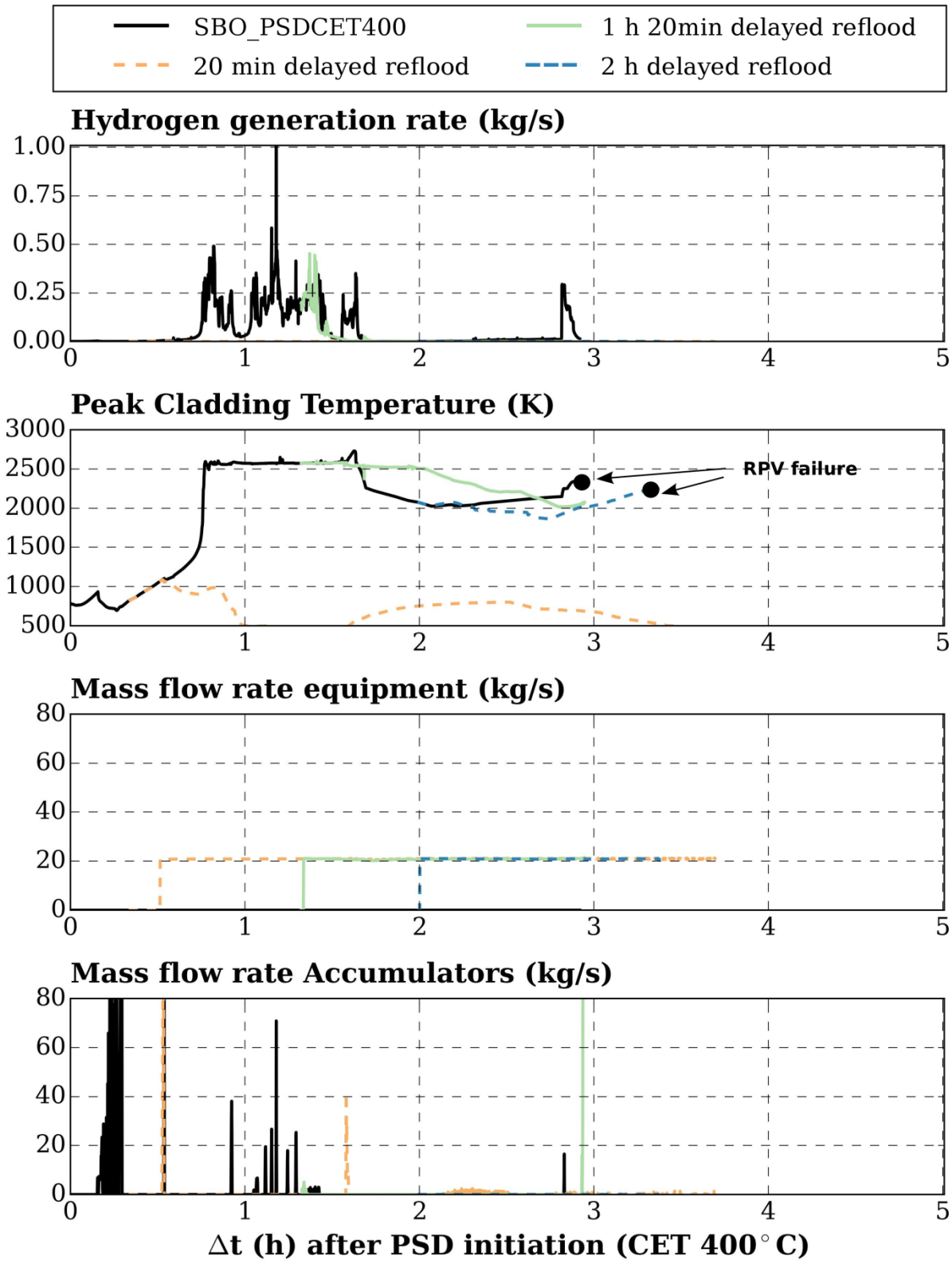

Figure D.3-9: Influence of a delayed reflooding (after PSD initiation i.e. CET 400 °C) by means of M651h on the evolution of a first set of variables in comparison to $SBO_{PSDCET400}$ (SBO at **0 h** after SCRAM, with **PSD at CET 400 °C** and without core reflooding). Black points mark RPV failure occurrences.

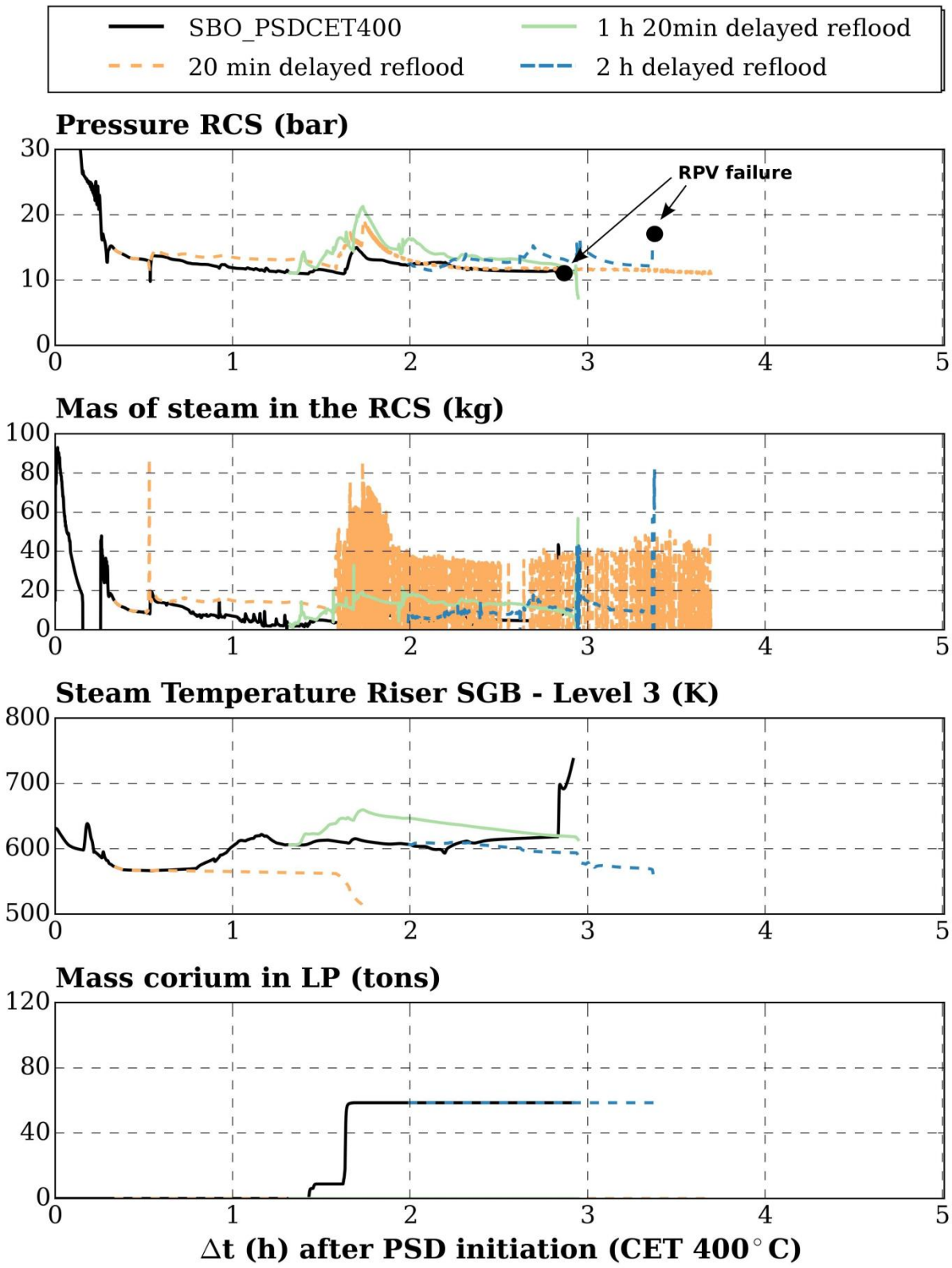

Figure D.3-10: Influence of a delayed reflooding (after PSD initiation i.e. CET 400 °C) by means of M651h on the evolution of a second set of variables in comparison to $SBO_{PSDCET400}$ (SBO at **0 h** after SCRAM, with **PSD at CET 400 °C** and without core reflooding). Black points mark RPV failure occurrences.

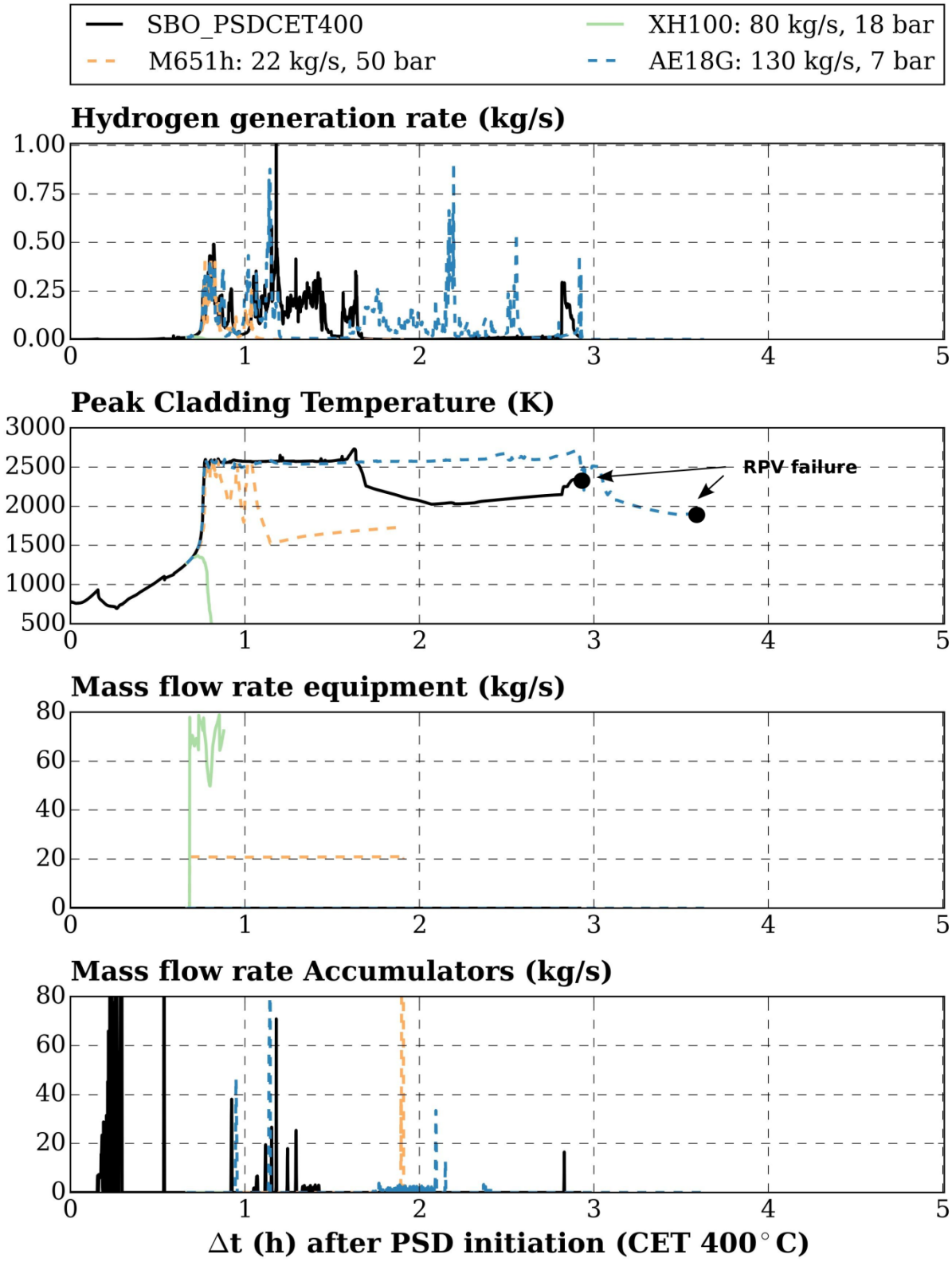

Figure D.3-11: Influence of mobile equipment for a 40-min delayed reflooding (after PSD initiation) on the evolution of a first set of variables compared to $SBO_{PSDCET400}$ (SBO at **0 h** after SCRAM, with **PSD at CET 400 °C** and without core reflooding). Black points mark RPV failure occurrences.

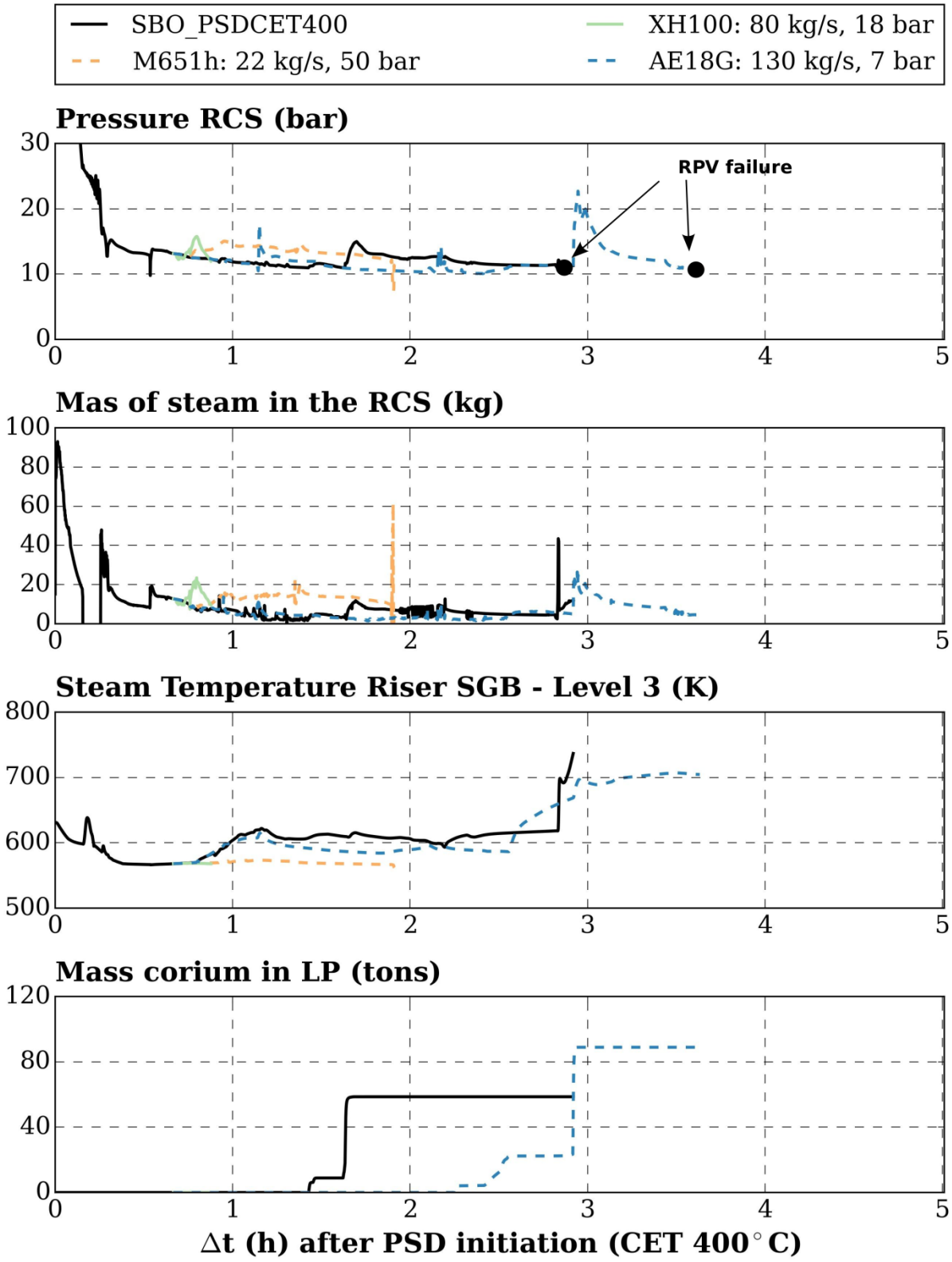

Figure D.3-12: Influence of mobile equipment for a 40-min delayed reflooding (after PSD initiation) on the evolution of a second set of variables compared to $SBO_{PSDCET400}$ (SBO at **0 h** after SCRAM, with **PSD at CET 400 °C** and without core reflooding). Black points mark RPV failure occurrences.

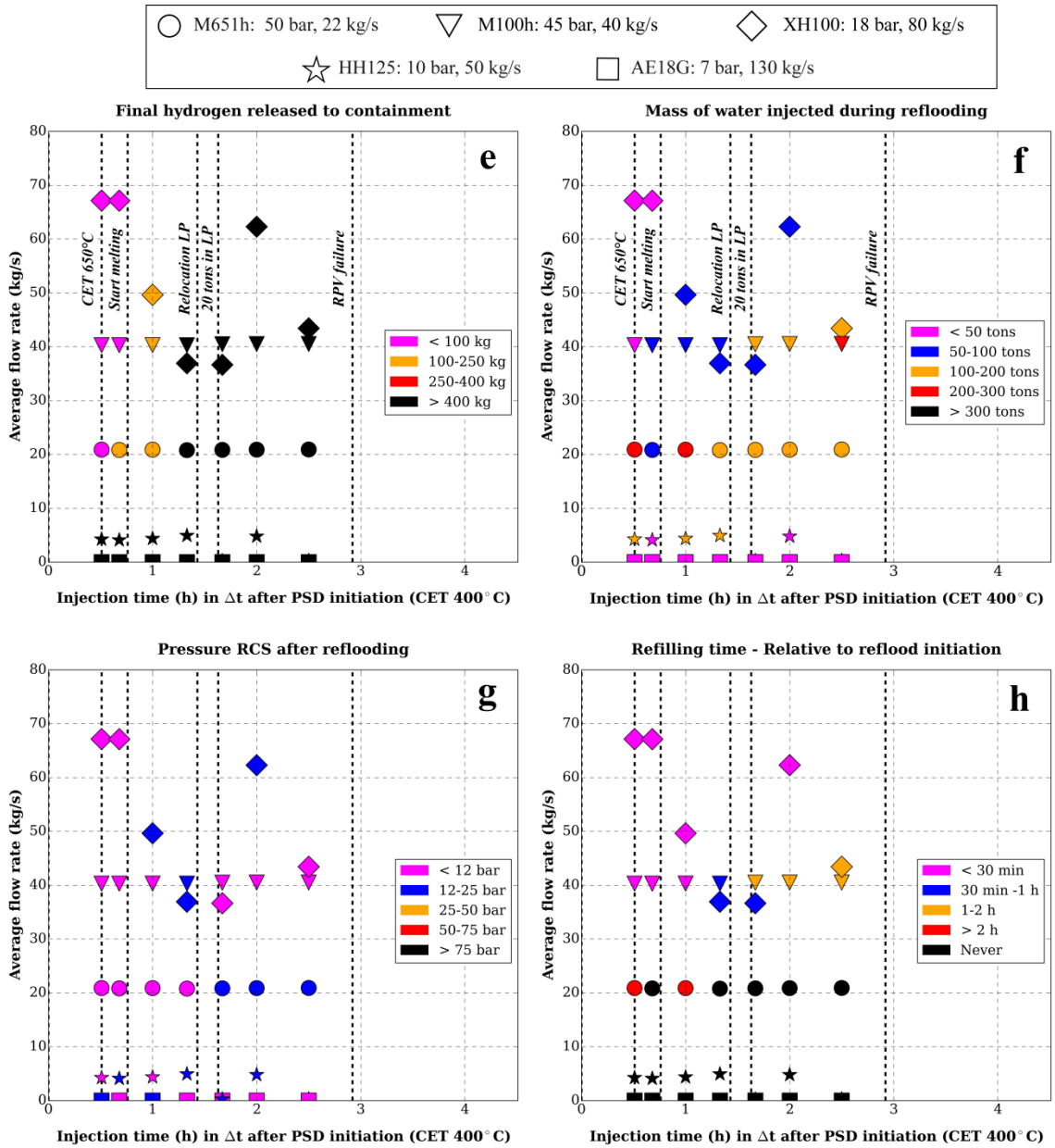

Figure D.3-13: Final value of selected FOMs as a function of the average RMFR and the injection time (relative to PSD initiation). Black dashed vertical lines represent occurrence times of major events in the sequence *Ref-SBO*$_{PSDCET400C}$ (SBO at **0 h** after SCRAM, with **PSD at CET 400 °C** and without core reflooding).

Bibliography

[1] IAEA. (1996) Defence in Depth in Nuclear Safety. INSAG-10. Vienna, Austria.

[2] IAEA. (2004) Implementation of Accident Management Programmes in Nuclear Power Plants - Safety Reports Series No. 32. Vienna, Austria.

[3] EPRI. (1993) Severe Accident Management Guidance Technical Basis Report, Volume 1: Candidate High-Level Actions and their Effects. TR-101869. Palo Alto, United States.

[4] EPRI. (1993) Severe Accident Management Guidance Technical Basis Report, Volume 2: The Physics of Accident Progression. TR-101869. Palo Alto, United States.

[5] EPRI. (2012) Severe Accident Management Guidance Technical Basis Report (Volumes 1 and 2). Report 1025295. Palo Alto, United States.

[6] NEA-OECD. (2013) The Fukushima Daiichi Nuclear Power Plant Accident: OECD/NEA Nuclear Safety Response and Lessons Learnt. NEA Report No. 7161. Paris, France.

[7] BMUB. (2011) EU Stress test National Report of Germany: Implementation of the EU Stress Tests in Germany.

[8] BMUB. (2012) German Action Plan for the implementation of measures after the Fukushima Dai-ichi reactor accident.

[9] BMUB. (2014) German Action Plan for the implementation of measures after the Fukushima Dai-ichi reactor accident.

[10] BMUB. (2016) Fortgeschriebener Aktionsplan zur Umsetzung von Maßnahmen nach dem Reaktorunfall in Fukushima.

[11] KTA. (2009) Requirements for the Emergency Manual (Anforderungen an das Notfallhandbuch), KTA 1203. Salzgitter, Germany.

[12] Braun, M., Löffler, M., Plank, H., Asse, D. and Dimmelmeier, H. (2014) Severe Accident Management – Optimized Guidelines and Strategies. *Proceedings of the 10th Conference on Nuclear Thermal Hydraulics, Operation and Safety (NUTHOS-10)*, 14th - 18th December, Okinawa, Japan.

[13] Loeffler, M., Braun, M. and Plank, H. (2012) SAMGs I : General Overview. *SARNET Course on Severe Accident Phenomenology and Management*, KIT, Karlsruhe, Germany.

[14] Loeffler, M., Braun, M. and Plank, H. (2012) SAMGs II : Plant Specific Application. *SARNET Course on Severe Accident Phenomenology and Management*, KIT, Karlsruhe, Germany.

[15] Roth-Seefrid, H., Feigel, A. and Moser, H.J. (1994) Implementation of bleed and feed procedures in Siemens PWRs. *Nuclear Engineering and Design*, **148**, 133–50. https://doi.org/10.1016/0029-5493(94)90105-8

[16] Steinbrück, M., Große, M., Sepold, L. and Stuckert, J. (2010) Synopsis and outcome of the QUENCH experimental program. *Nuclear Engineering and Design*, **240**, 1714–27. https://doi.org/10.1016/j.nucengdes.2010.03.021

[17] Sehgal, B.R. (2009) Light Water Reactor Safety : Past , Present and Future.

Proceedings of the 13th International Meeting on Nuclear Thermal-Hydraulics (NURETH-13), Kanazawa, Japan. p. 1–29.

[18] Broughton, J.M., Kuan, P., Petti, D. a and Tolman, E.L. (1989) A Scenario of the Three Mile Island Unit 2 Accident. *Nuclear Technology*, **87**, 34–53.

[19] Haste, T., Steinbrück, M., Barrachin, M., de Luze, O., Grosse, M. and Stuckert, J. (2015) A comparison of core degradation phenomena in the CORA, QUENCH, Phébus SFD and Phébus FP experiments. *Nuclear Engineering and Design*, Elsevier B.V. **283**, 8–20. https://doi.org/10.1016/j.nucengdes.2014.06.035

[20] Klein-Hessling, W., Sonnenkalb, M., Dorsselaere, J.-P. Van, Chatelard, P., Raimond, E., Clément, B. et al. (2012) Ranking of Severe Accident Research Priorities. *Proceedings of the 5th European Review Meeting on Severe Accident Research (ERMSAR-5)*, Köln, Germany.

[21] Bunt, R., Corradini, M., Ellison, P., Farmer, M.., Francis, M., Gabor, J. et al. (2015) Reactor Safety Gap Evaluation of Accident Tolerant Components and Severe Accident Analysis. *Proceedings of the 16th International Meeting on Nuclear Thermal-Hydraulics (NURETH-16)*, Chicago, USA. p. 4661–74.

[22] GRS. (2017) CESAM: Code for European Severe Accident Management. URL: http://www.cesam-fp7.eu/ [Internet].

[23] European Commission. (2017) FAST Nuclear Emergency Tools (FASTNET). [Internet].

[24] IRSN. (2016) The ASTEC software package. URL: ic-tools/Computer-codes/Pages/The-ASTEC-Software-Package-2949.aspx [Internet].

[25] Chatelard, P., Reinke, N., Arndt, S., Belon, S., Cantrel, L., Carenini, L. et al. (2014) ASTEC V2 severe accident integral code main features, current V2.0 modelling status, perspectives. *Nuclear Engineering and Design*, **272**, 119–35. https://doi.org/10.1016/j.nucengdes.2013.06.040

[26] Chatelard, P., Belon, S., Bosland, L., Carénini, L., Coindreau, O., Cousin, F. et al. (2016) Main modelling features of the ASTEC V2.1 major version. *Annals of Nuclear Energy*, Elsevier Ltd. **93**, 83–93. https://doi.org/10.1016/j.anucene.2015.12.026

[27] GRS. (2002) Assessment of the Accidental Risk of Advanced Pressurized Water Reactors in Germany. GRS-184. Germany.

[28] Sehgal, B.R. (2012) Nuclear Safety in Light Water Reactors: Severe Accident Phenomenology. ISBN 978-0-12-388446-6. Academic Press.

[29] Schanz, G., Hagen, S., Hofmann, P., Schumacher, G. and Sepold, L. (1992) Information on the evolution of severe LWR fuel element damage obtained in the CORA program. *Journal of Nuclear Materials*, **188**, 131–45. https://doi.org/10.1016/0022-3115(92)90462-T

[30] Clément, B. and Zeyen, R. (2013) The objectives of the Phébus FP experimental programme and main findings. *Annals of Nuclear Energy*, Elsevier Ltd. **61**, 4–10. https://doi.org/10.1016/j.anucene.2013.03.037

[31] Repetto, G., Garcin, T., Eymery, S. and Fichot, F. (2013) Experimental program on debris reflooding (PEARL) - Results on PRELUDE facility. *Nuclear Engineering and Design*, **264**, 176–86. https://doi.org/http://dx.doi.org/10.1016/j.nucengdes.2012.11.024

[32] Magallon, D. (2006) Characteristics of corium debris bed generated in large-scale fuel-

coolant interaction experiments. *Nuclear Engineering and Design*, **236**, 1998–2009. https://doi.org/10.1016/j.nucengdes.2006.03.038

[33] Asmolov, V. and Tsurikov, D. (2004) MASCA project: major activities and results. *CSNI Workshop, MASCA Seminar*, Aix-en-Provence, France.

[34] Gaus-Liu, X., Miassoedov, A., Cron, T. and Wenz, T. (2010) In-vessel melt pool coolibility test - Description and results of LIVE experiments. *Nuclear Engineering and Design*, **240**, 3898–903. https://doi.org/10.1016/j.nucengdes.2010.09.001

[35] Sehgal, B.R., Karbojian, a., Giri, a., Kymäläinen, O., Bonnet, J.M., Ikkonen, K. et al. (2005) Assessment of reactor vessel integrity (ARVI). *Nuclear Engineering and Design*, **235**, 213–32. https://doi.org/10.1016/j.nucengdes.2004.08.055

[36] Steinbrück, M. (2015) Experimental simulation of clad and absorber behavior during the early in-vessel phase of Severe Accidents. *Frédéric Joliot & Otto Hahn Summer School*, Karlsruhe.

[37] Steinbrück, M. (2012) Severe Accident Phenomenology I: Overview and Core Degradation. *SARNET Course on Severe Accidents Phenomenology and Management*, Karlsruhe, Germany.

[38] Abriata, J. and Garces, J.P. (1986) The O-Zr (Oxygen-Zirconium) System. *Bulletin of Alloy Phase Diagrams*, **7**, 116–24.

[39] Urbanic, V.F. and Heidrick, T.R. (1978) High-Temperature Oxidation of Zircaloy-2 and Zircaloy-4 in Steam. *Journal of Nuclear Materials*, **75**, 251–61.

[40] Prater, J.T. and Courtright, E.L. (1987) Oxidation of Zircaloy-4 in Steam at 1300 to 2400 ° C. *Zirconium in the Nuclear Industry: Seventh International Symposium*, Philadelphia, United States. p. 489–503.

[41] Leistikow, S. and Schanz, G. (1987) Oxidation kinetics and related phenomena of zircaloy-4 fuel cladding exposed to high temperature steam and hydrogen-steam mixtures under PWR accident conditions. *Nuclear Engineering and Design*, **103**, 65–84. https://doi.org/10.1016/0029-5493(87)90286-X

[42] Schanz, G., Adroguer, B. and Volchek, A. (2004) Advanced treatment of zircaloy cladding high-temperature oxidation in severe accident code calculations. Part I. Experimental database and modelling. *Nuclear Engineering and Design*, **232**, 75–84.

[43] Volchek, A., Zvonarev, Y. and Schanz, G. (2004) Advanced treatment of zircaloy cladding high-temperature oxidation in severe accident code calculations. Part II. Best-fitted parabolic correlations. *Nuclear Engineering and Design*, **232**, 85–96. https://doi.org/10.1016/j.nucengdes.2004.02.014

[44] Queral, C. (2016) Thermo-mechanical analyses with TRACE code. *Seminar Lecture*, KIT, Karlsruhe, Germany.

[45] Chung, H.M. (2005) Fuel Behavior under Loss-of-Coolant Accident Situations. *Nuclear Engineering and Technology*, **37**, 327–62.

[46] Hofmann, P. and Markiewicz, M. (1994) Chemical interactions between as-received and pre-oxidized Zircaloy-4 and Inconel-718 at High Temperatures. Report KfK-4729. [Internet]. Karlsruhe, Germany.

[47] Hofmann, P. and Markiewicz, M. (1990) Chemical Behavior of (Ag, In, Cd) Absorber Rods in Severe LWR Accidents. Report KfK-4670. [Internet]. Karlsruhe, Germany.

[48] Hofmann, P., Stuckert, J., Miassoedov, A., Veshchunov, M.S., Berdyshev, A.V. and Boldyrev, A.V. (1999) ZrO2 dissolution by molten zircaloy and cladding oxide shell failure. New experimental results and modelling. Report FZKA-6383. [Internet]. Karlsruhe, Germany.

[49] Sepold, L., Hering, W., Homann, C., Miassoedov, A., Schanz, G., Stegmaier, U. et al. (2004) Experimental and Computational Results of the QUENCH-06 Test (OECD ISP-45) [Internet]. Karlsruhe, Germany.

[50] Hofmann, P., Homann, C., Leiling, W., Miassoedov, A., Piel, D., Schanz, G. et al. (2002) Experimental and Calculational Results of the Experiments QUENCH-02 and QUENCH-03. Report FZKA-6295. [Internet]. Karlsruhe, Germany.

[51] Jacquemain, D., Vola, D., Meignen, R., Bonnet, J.M., Fichot, F., Raimond, E. et al. (2015) Past and Future R & D at IRSN on Corium Progression and Related Mitigation Strategies in a Severe Accident. *Proceedings of the 16th International Meeting on Nuclear Thermal-Hydraulics (NURETH-16)*, Chicago, United States. p. 7519–37.

[52] NEA-OECD. (1998) Molten Material Relocation into the Lower Plenum: a status report. NEA/CSNI/R(97)34. France.

[53] Rempe, J.L. and Knudson, D.L. (2013) TMI-2 – A Case Study for PWR Instrumentation Performance During a Severe Accident. INL/EXT-13-28043. Idaho, United States.

[54] Seiler, J.M. and Tourniaire, B. (2014) A phenomenological analysis of melt progression in the lower head of a pressurized water reactor. *Nuclear Engineering and Design*, Elsevier B.V. **268**, 87–95. https://doi.org/10.1016/j.nucengdes.2013.12.043

[55] Seiler, J.M., Tourniaire, B., Defoort, F. and Froment, K. (2007) Consequences of material effects on in-vessel retention. *Nuclear Engineering and Design*, **237**, 1752–8. https://doi.org/10.1016/j.nucengdes.2007.03.007

[56] Theofanous, T.G., Liu, C., Additon, S., Angelini, S., Kymäläinen, O. and Salmassi, T. (1997) In-vessel coolability and retention of a core melt. *Nuclear Engineering and Design*, **169**, 1–48. https://doi.org/10.1016/S0029-5493(97)00009-5

[57] Zhang, L., Zhou, Y., Zhang, Y., Tian, W., Qiu, S. and Su, G. (2015) Natural convection heat transfer in corium pools: A review work of experimental studies. *Progress in Nuclear Energy*, **79**, 167–81. https://doi.org/10.1016/j.pnucene.2014.11.021

[58] Willschütz, H.G., Altstadt, E., Sehgal, B.R. and Weiss, F.P. (2006) Recursively coupled thermal and mechanical FEM-analysis of lower plenum creep failure experiments. *Annals of Nuclear Energy*, **33**, 126–48. https://doi.org/10.1016/j.anucene.2005.08.006

[59] Bechta, S. V., Khabensky, V.B., Granovsky, V.S., Krushinov, E. V., Vitol, S.A., Gusarov, V. V. et al. (2006) Experimental study of interactions between suboxidized corium and reactor vessel steel. Paper 6054. *Proceedings of the Interntional Congress on Advances in Nuclear Power Plants (ICAPP-2006)*, Reno, United States.

[60] Altstadt, E. and Willschütz, H.G. (2007) Simulation of the Corium-RPV-Wall Interaction for an in-Vessel-Retention Scenario. *Proceedings of the 38th Kerntechnik Jahrestagung*, Karlsruhe, Germany. p. 87–92.

[61] Cronenberg, A.W. (1992) Hydrogen generation behaviour in the LOFT FP-2 and other

experiments: comparative assessment for migrated severe accident conditions. *Nuclear Technology*, **97**, 91–112.

[62] Hering, W. and Homann, C. (2007) Degraded core reflood: Present understanding and impact on LWRs. *Nuclear Engineering and Design*, **237**, 2315–21. https://doi.org/10.1016/j.nucengdes.2007.04.017

[63] Hering, W., Homann, C. and Stuckert, J. (2015) Integration of New Experiments into the Reflood Map. *Proceedings of the 15th International Congress on Advances in Nuclear Power Plants (ICAPP-15)*, 3rd - 6th May, Nice, France. p. 1420–8.

[64] Obot, N.T. and Ishii, M. (1989) Iwo-phase flow regime transition criteria in post dryout region based on flow visualization experiments, Int. *International Journal of Heat and Mass Transfer*, **31**, 2559–70.

[65] Chikhi, N. and Fichot, F. (2010) Reflooding model for quasi-intact rod configuration: quench front tracking and heat transfer closure laws. *Nuclear Engineering and Design*, **240**, 3387–96. https://doi.org/10.1016/j.nucengdes.2010.07.011

[66] Sehgal, B.R. (2006) Stabilization and termination of severe accidents in LWRs. *Nuclear Engineering and Design*, **236**, 1941–52. https://doi.org/10.1016/j.nucengdes.2006.03.040

[67] Chikhi, N. and Fichot, F. (2016) Experimental and theoretical study of large scale debris bed reflood in the PEARL facility. *Nuclear Engineering and Design*, **In Press**. https://doi.org/10.1016/j.nucengdes.2016.05.009

[68] Fischer, M., Herbst, O. and Schmidt, H. (2005) Demonstration of the heat removing capabilities of the EPR core catcher. *Nuclear Engineering and Design*, **235**, 1189–200. https://doi.org/10.1016/j.nucengdes.2005.02.022

[69] USNRC. (2002) Emergency Operating Procedures Ginna Nuclear Power Plant [Internet]. Washington D.C., United States.

[70] European Commission. (2000) Concerted Action on Severe Accident Management Implementation and Expertise in the European Union (SAMIME), Contract No. FI4S-CT98-0052.

[71] IAEA. (2009) Severe Accident Management Programmes for Nuclear Power Plants. Safety Guide No. NS-G-2.15. Vienna, Austria.

[72] WENRA. (2007) WENRA Safety Reference Levels for Existing Reactors.

[73] Hermsmeyer, S., Iglesias, R., Herranz, L.E., Reer, B., Sonnenkalb, M., Nowack, H. et al. (2014) Review of current Severe Accident Management (SAM) approaches for Nuclear Power Plants in Europe requirements. JRC93082. https://doi.org/10.2790/38824

[74] IAEA. (2015) The Fukushima Daiichi Accident: Report by the Director General. Report STI/PUB/1710. Vienna, Austria.

[75] Lutz, R.J. and Prior, R.P. (2016) Comparison of the Fukushima response in the United States and Europe. Paper No. 60101. *Proceedings of the24th International Conference on Nuclear Engineering (ICONE-24)*, Charlotte, United States.

[76] USNRC. (2011) Near Term Report and Recommendations for Agency Actions following the Events in Japan. SECY-11-0093. United States.

[77] NEI. (2012) Diverse and Flexible Coping Strategies (FLEX) Implementation Guide.

NEI 12-06. Washington D.C., United States.

[78] ENSREG. (2011) Annex 1 to the declaration of ENSREG: EU Stress Tests Specifications.

[79] WENRA. (2014) WENRA Safety Reference Levels for Existing Reactors Safety Reference Levels for Existing Reactors. Update in relation to the lessons learned from TEPCO Fukushima Daiichi Accident.

[80] RSK. (1986) Überprüfung der Sicherheit der Kernkraftwerke mit Leichtwasserreaktor in der Bundesrepublik Deutschland. Ergebnisprotokoll der 218. RSK-Sitzung.

[81] GRS. (1988) Deutsche Risikostudie Kernkraftwerke Phase B. TÜV Rheinland, Köln.

[82] RSK. (1988) Abschlussbericht über die Ergebnisse der Sicherheitsüberprüfung der Kernkraftwerke in der Bundesrepublik Deutschland durch die RSK. Ergebnisprotokoll der 238. RSK-Sitzung.

[83] RSK. (1992) Behandlung auslegungsüberschreitender Ereignisabläufe für die in der Bundesrepublik Deutschland betriebenen Kernkraftwerke mit Druckwasserreaktoren, Positionspapier der RSK zum anlageninternen Notfallschutz im Verhältnis zum anlagenexternen Katastrophen. Ergebnisprotokoll der 273. RSK-Sitzung.

[84] RSK. (1997) Maßnahmen zur Risikominderung bei Freisetzung von Wasserstoff in den Sicherheitsbehälter von bestehenden Kernkraftwerken mit Druckwasserreaktor nach auslegungsüberschreitenden Ereignissen. Ergebnisprotokoll der 314. RSK-Sitzung.

[85] Sonnenkalb, M. (2012) Severe Accident Mitigation in German NPP - Status and Future Activities. *EUROSAFE Forum 2012*, Brussels, Belgium.

[86] BMUB. (2012) Sicherheitsanforderungen an Deutsche Kernkraftwerke. Bonn, Germany.

[87] Prior, R. (2009) Criteria for the Transition to Severe Accident Management. *Proceedings of the OECD-NEA Workshop on Implementation of Severe Accident Management Measures (ISAAM)*, Böttstein, Switzerland.

[88] NEA-OECD. (2010) Core Exit Temperature (CET) Effectiveness in Accident Management of Nuclear Power Reactor. NEA/CSNI/R(2010)9.

[89] EPRI. (1993) Instrumentation performance under Severe Accidents. Ways to Acquire Information From Instrumentation Affected by an Accident. TR-102371. Palo Alto, United States.

[90] Rempe, J.L., Knudson, D.L. and Lutz, R.J. (2015) Scoping Study Investigating PWR Instrumentation during a Severe Accident Scenario. INL/EXT-15-35940. Idaho, United States.

[91] Queral, C. (2015) SBLOCA in PWR: Phenomenology. Course on Thermal-hydraulics and Probabilistic Safety Analysis. Universidad Politécnica de Madrid, Madrid, Spain.

[92] GRS. (1995) ATHLET-Analysen zur sekundärseitigen Druckentlastung und Bespeisung aus der Speisewasserleitung und dem Speisewasserbehälter am Beispiel einer KONVOI-Anlage. GRS-A-2296. Germany.

[93] GRS. (1995) ATHLET-Analysen für KONVOI Anlagen zur primärseitigen Bespeisung mit betrieblichen und Skherheitseinspeisesystemen. GRS-A-2306. Germany.

[94] USNRC. (1998) NUREG-1570. Risk Assessment of Severe Accident-Induced Steam Generator Tube Rupture.

[95] Van Dorsselaere, J.. P., Seropian, C., Chatelard, P., Jacq, F., Fleurot, J., Giordano, P. et al. (2009) The ASTEC integral code for Severe Accident simulation. *Nuclear Technology*, **165**, 293–307.

[96] Bandini, G., Buck, M., Hering, W., Godin-Jacqmin, L., Ratel, G., Matejovic, P. et al. (2010) Recent advances in ASTEC validation on circuit thermal-hydraulic and core degradation. *Progress in Nuclear Energy*, **52**, 148–57. https://doi.org/10.1016/j.pnucene.2009.09.008

[97] Van Dorsselaere, J.P. (2013) European view on severe accidents research. *Proceedings of the 44th Kerntechnik Jahrestagung*, Berlin, Germany.

[98] Klein-Heßling, W., Sonnenkalb, M., Jacquemain, D., Clément, B., Raimond, E., Dimmelmeier, H. et al. (2014) Conclusions on severe accident research priorities. *Annals of Nuclear Energy*, **74**, 4–11. https://doi.org/10.1016/j.anucene.2014.07.015

[99] Camous, F., Chatelard, P., Guillard, G. and Marchand, O. (2005) Safety Assessment, Code Validation and R&D Studies at the IRSN using the Best-estimate CATHARE 2 Code. *Proceedings of the 11th International Meeting on Nuclear Thermal-Hydraulics (NURETH-11)*, 2nd-6th October, Avignon, France. p. 1–20.

[100] Piar, L., Tregoures, N. and Moal, A. (2011) ASTEC V2 code: CESAR physical and numerical modelling. Saint-Paul-lez-Durance, France.

[101] Chatelard, P., Fleurot, J., Marchand, O. and Drai, P. (2006) Assessment of ICARE/CATHARE V1 Severe Accident Code. *Proceedings of 14th International Conference on Nuclear Engineering (ICONE-14)*, 17th - 20th July, Miami, United States. p. 145–54.

[102] Chatelard, P., Chikhi, N., Cloarec, L., Coindreau, O., Drai, P., Fichot, F. et al. (2009) ASTEC V2.0 code ICARE physical modelling. DPAM-SEMCA-2009-148. Saint-Paul-lez-Durance, France.

[103] Fichot, F., Adroguer, B., Volchek, A. and Zvonarev, Y. (2004) Advanced treatment of zircaloy cladding high-temperature oxidation in severe accident code calculations. Part III. Verification against representative transient tests. *Nuclear Engineering and Design*, **232**, 75–84. https://doi.org/10.1016/j.nucengdes.2004.02.013

[104] Fichot, F., Marchand, O., Drai, P., Chatelard, P., Zabiego, M. and Fleurot, J. (2006) Multi-Dimensional Approaches in Severe Accident Modelling and Analyses. *Nuclear Engineering and Technology*, **38**, 733–52.

[105] Chikhi, N. and Fleurot, J. (2012) Revisiting the QUENCH-11 integral reflood test with a new thermal-hydraulic model: existence of a minimum injection rate. *Annals of Nuclear Energy*, **49**, 12–22. https://doi.org/10.1016/j.anucene.2012.06.004

[106] Lefevre, B. (2006) UO2 Dissolution by magma. CS SI/311-1/AB03B221/NT/01 version 1.1 03/230. Saint-Paul-lez-Durance, France.

[107] Groneveld, D., Cheng, S. and Doan, T. (1986) Aecl-uo critical heat-flux look up table. *Heat Transfer Engineering*, **7**, 46–62. https://doi.org/10.1080/01457638608939644

[108] Chikhi, N., Nguyen, N.G. and Fleurot, J. (2012) Determination of the hydrogen source term during the reflooding of an overheated core: Calculation results of the integral reflood test QUENCH-03 with PWR-type bundle. *Nuclear Engineering and Design*, **250**, 351–63. https://doi.org/10.1016/j.nucengdes.2012.05.026

[109] Kruse, P., Brähler, T. and Koch, M.K. (2014) Validation of ASTEC core degradation

and containment models. *Nuclear Engineering and Design*, Elsevier B.V. **272**, 173–82. https://doi.org/10.1016/j.nucengdes.2014.01.012

[110] Gremme, F. and Koch, M.K. (2015) QUENCH-11 Simulations with the Severe Accident Analysis Code ASTEC V2.0 in CESAM. *Proceedings of the 46th Kerntechnik Jahrestagung*, Berlin, Germany.

[111] Bachrata, A., Fichot, F., Repetto, G., Quintard, M. and Fleurot, J. (2012) Code simulation of quenching of a high temperature debris bed: model improvement and validation with experimental results. *Proceedings of 20th International Conference on Nuclear Engineering (ICONE-20)*, Anaheim, United States. p. 1–9.

[112] Salay, M. and Fichot, F. (2005) Modelling of Metal-Oxide Corium Stratification in the Lower Plenum of a Reactor Vessel. *Proceedings of the 11th International Meeting on Nuclear Thermal-Hydraulics (NURETH-11)*, Avignon, France. p. 1–17.

[113] D'Alessandro, C., Buck, M. and Starflinger, J. (2014) Assessment of the integral code ASTEC with respect to the late in-vessel phase of core degradation. NUTHOS10-1194. *Proceedings of the 10th Conference on Nuclear Thermal Hydraulics, Operation and Safety (NUTHOS-10)*, Okinawa, Japan. p. 1–13.

[114] Carenini, L., Fleurot, J. and Fichot, F. (2014) Validation of ASTEC V2 models for the behaviour of corium in the vessel lower head. *Nuclear Engineering and Design*, **272**, 152–62. https://doi.org/10.1016/j.nucengdes.2013.06.041

[115] Koundy, V., Durin, M., Nicolas, L. and Combescure, A. (2005) Simplified modeling of a PWR reactor pressure vessel lower head failure in the case of a severe accident. *Nuclear Engineering and Design*, **235**, 835–43. https://doi.org/10.1016/j.nucengdes.2004.11.012

[116] Koundy, V., Fichot, F., Willschuetz, H.., Altstadt, E., Nicolas, L., Lamy, J.S. et al. (2008) Progress on PWR lower head failure predictive models. *Nuclear Engineering and Design*, **238**, 2420–9. https://doi.org/10.1016/j.nucengdes.2008.03.004

[117] Hagen, S., Hofmann, P., Noack, V., Schanz, G., Schumacher, G. and Sepold, L. (1993) Results of SFD Experiment CORA-13 (OECD International Standard Problem 31). Karlsruhe, Germany.

[118] Sepold, L., Hofmann, P., Leiling, W., Miassoedov, A., Piel, D., Schmidt, L. et al. (2001) Reflooding experiments with LWR-type fuel rod simulators in the QUENCH facility. *Nuclear Engineering and Design*, **204**, 205–20. https://doi.org/10.1016/S0029-5493(00)00308-3

[119] Miassoedov, A., Manara, D., Bottomley, D., Kiselova, M. and Gmbh, A. (2015) Severe Accident Facilities for European Safety Targets: The SAFEST Project. *Proceedings of the 16th International Meeting on Nuclear Thermal-Hydraulics (NURETH-16)*, Chicago, United States. p. 4604–16.

[120] Stuckert, J., Boldyrev, A.V., Miassoedov, A., Palagin, V., Schanz, G., Sepold, L. et al. (2005 August) Experimental and Computational Results of the QUENCH-08 experiment (reference for QUENCH-07). Report FZKA-6970. [Internet]. Karlsruhe, Germany.

[121] Erdmann, W. and Bals, C. (2004) Post-Test Calculation of QUENCH-07 and QUENCH-08 with ATHLET-CD. *10th QUENCH Workshop*, Karlsruhe, Germany.

[122] Spencer, J.H., Allison, C.M. and Hohorst, J.K. (2011) Assessment of new modeling in

RELAP/SCDAPSIM using experimental results from the QUENCH program. *Proceedings of the 11th International Congress on Advances in Nuclear Power Plants (ICAPP-11)*, 2nd - 5th May, Nice, France. p. 1418–24.

[123] Madokoro, H., Erkan, N. and Okamoto, K. (2015) Assessment of the models in RELAP/SCDAPSIM with QUENCH-06 analysis. *Journal of Nuclear Science and Technology*, 1–8. https://doi.org/10.1080/00223131.2015.1005717

[124] Steinbrück, M. (2004) Analysis of Hydrogen Production in QUENCH Bundle Tests. Report FZKA-6968. [Internet]. Karlsruhe, Germany.

[125] Seiler, N., Bertrand, F., Marchand, O., Repetto, G. and Ederli, S. (2008) Investigations on boron carbide oxidation for nuclear reactors safety-General modelling for ICARE/CATHARE code applications. *Nuclear Engineering and Design*, **238**, 820–36. https://doi.org/10.1016/j.nucengdes.2006.12.008

[126] Gómez-García-Toraño, I., Sánchez-Espinoza, V.-H., Stieglitz, R., Stuckert, J., Laborde, L. and Belon, S. (2017) Validation of ASTECV2.1 based on the QUENCH-08 experiment. *Nuclear Engineering and Design*, **314**. https://doi.org/10.1016/j.nucengdes.2016.12.039

[127] Siemens. (1991) Der Druckwasserreaktor: Aufbau und Wirkungsweise der Gesamtanlage.

[128] Ziegler, A. and Allelein, H.J. (2013) Reaktortechnik. Physikalisch-technische Grundlagen. Kapitel 10 - Moderne Leichtwasserreaktoren. Springer Vieweg. https://doi.org/10.1007/978-3-642-33846-5

[129] Ludwig, H. (2007) PWR Plant Design. *ENEN Safety Course PWR Plant Design PWR Plant Design*, Munich, Germany.

[130] Nowack, H., Erdmann, W. and Reinke, N. (2011) Application of ASTEC V2.0 to Severe Accident Analyses for German Konvoi Type Reactors. *Proceedings of the 14th International Meeting on Nuclear Thermal-Hydraulics (NURETH-14)*, Toronto, Canada.

[131] Reinke, N., Chan, H.-W. and Sonnenkalb, M. (2013) Comparative Analysis of LOCA for German PWR with ASTEC and ATHLET-CD. *Proceedings of the 44th Kerntechnik Jahrestagung*, Berlin.

[132] European Commission. (2015) D40 .42 – 1st set of reference NPP ASTEC input decks. CESAM FP7-GA-323264.

[133] Belloni, J., Goyeau, B., Quintard, M., Fichot, F. and Gobin, D. (2008) A chemical non-equilibrium two-phase model for the dissolution of ZrO in molten Zr. *Proceedings of the 5th European Conference on Thermal-Sciences*, 18th - 22nd May, Eindhoven, the Netherlands. p. 1–13.

[134] NEI. (2006) B.5.b Phase 2 & 3 Submittal Guideline. NEI 06-12. [Internet]. Walnut Creek, United States.

[135] de Blas Ortega, J. (2014) Fortalezas de diseño y nuevas estrategias de gestión de emergencias en Centrales Nucleares. *Proceedings of the 40th Annual Meeting of the Spanish Nuclear Society (SNE-40)*, Valencia, Spain.

[136] Rain for Rent. (2016) Technical specifications of High Head Pump HH80. URL: http://www.rainforrent.com/RainForRentProductDataFiles/HH80.pdf [Internet].

[137] Rain for Rent. (2016) Technical specifications of High Head Pump HH125. URL:

http://www.rainforrent.com/RainForRentProductDataFiles/HH125.pdf [Internet].

[138] Peerless Pump Company. (2016) Horizontal split case pumps, Single Stage Double Suction, Type AE. Hydraulic Performance Tolerance. Section 1240. URL: http://www.chamco.com/reference/peerlesscatalog/pdf/Horizontal_66_71.pdf [Internet].

[139] Lowara. (2016) Vogel Multistage Pumps. Designs MP, MPA, MPB, MPV. Sizes DN 40 - DN 125. URL: http://www.lowara.com/vogdata/doc/EN/mpmpampbmpv_07-ed-en.pdf [Internet].

[140] Power Prime Pumps. (2016) Technical specifications of pump XH100. URL: http://powerprime.com/Documents/pumps.cutsheets.pdf/XH100.fichatecnica.pdf [Internet].

[141] Strohm, A., Ehlkes, L., Schwarz, W., Khatib-Rahbar, M., Zavisca, M. and Rittig, D. (2010) An Approach to Classify the Risk of Operating Nuclear Power Plants - Case Study: Neckarwestheim Unit 1 and Unit 2. *Proceedings of PSAM10 Conference*, Seattle, United States.

[142] Sonnenkalb, M. (1998) Unfallanalysen für DWR mit dem Integralcode MELCOR 1.8.3. GRS-A-2579. Germany.

[143] Trometer, A., Pohlner, G., Buck, M., Tusheva, P., Schäfer, F., Kozmenkov, Y. et al. (2015) Intermediate results of accident analyses - M42. Stuttgart, Germany.

[144] Sonnenkalb, M. (2001) Unfallanalysen für DWR vom Typ Konvoi (GKN-2) mit dem Integralcode MELCOR 1.8.4. GRS-A-2954. Germany.

[145] Jobst, M., Wilhelm, P., Kozmenkov, Y., Kliem, S., Trometer, A., Buck, M. et al. (2016) Simulation postulierter schwerer Störfälle in deutschen DWR Simulation of hypothetical severe accidents in German PWRs - M35. Dresden, Germany.

[146] Queral, C., Mena-Rosell, L., Jimenez, G., Sanchez-Perea, M., Gomez-Magan, J. and Hortal, J. (2016) Verification of SAMGs in SBO sequences with Seal LOCA. Multiple damage domains. *Annals of Nuclear Energy*, **98**, 90–111. https://doi.org/10.1016/j.anucene.2016.07.021

[147] USNRC. (2012) NUREG/CR-7110, Vol. 2. State-of-the-Art Reactor Consequence Analyses Project. Volume 2: Surry Integrated Analysis.

List of Publications

Peer-Reviewed Magazine papers

2017 **I. Gómez-García-Toraño**, M.J. Rebollo Mena, V-H. Sánchez-Espinoza, C. Queral, R. Stieglitz. Assessment of primary and secondary bleed and feed strategies during a Station Blackout in a generic Konvoi PWR using ASTECV2.0. *Annals of Nuclear Energy* (*Accepted*).

2017 **I. Gómez-García-Toraño**, V-H. Sánchez-Espinoza, R. Stieglitz, C. Queral. Analysis of primary bleed and feed strategies during selected SBLOCA sequences along with SBO in a generic Konvoi PWR using ASTECV2.0. *Annals of Nuclear Energy*, **110**, 818–32. https://doi.org/10.1016/j.anucene.2017.08.003.

2017 **I. Gómez-García-Toraño**, V-H. Sánchez-Espinoza, R. Stieglitz. Investigation of SAM measures during selected MBLOCA sequences along with Station Blackout in a generic Konvoi PWR using ASTECV2.0. *Annals of Nuclear Energy*, **105**, 226–39. https://doi.org/http://dx.doi.org/10.1016/j.anucene.2017.02.030.

2017 **I. Gómez-García-Toraño**, V-H. Sánchez-Espinoza, R. Stieglitz, J. Stuckert, L. Laborde, S. Belon. Validation of ASTECV2.1 based on the QUENCH-08 experiment. *Nuclear Engineering and Design*, **314**, 29–43. https://doi.org/http://dx.doi.org/10.1016/j.nucengdes.2016.12.039.

Peer-Reviewed Conference papers

2017 **I. Gómez-García-Toraño**, V-H. Sánchez-Espinoza, M.J. Rebollo. ASTEC Investigation of Accident Management measures for a Station Blackout scenario in a German Konvoi PWR. *Proceedings of the 7th European Review Meeting on Severe Accident Research (ERMSAR-8)*, Warsaw, Poland, 16-18th May.

2016 **I. Gómez-García-Toraño**, V-H. Sánchez-Espinoza, R. Stieglitz. Investigation of primary bleed and feed procedures during a SBLOCA combined with a loss of AC power in a German Konvoi PWR using ASTECV2.0. *42nd Annual Meeting of the Spanish Nuclear Society*, Santander, Spain, 28-30th September.

2016 **I. Gómez-García-Toraño**, V-H. Sánchez-Espinoza, R. Stieglitz. Simulation of Severe Accident Management Measures for a generic PWR Konvoi with the ASTEC code. *Proceedings of the International Congress on Advances in Nuclear Power Plants (ICAPP-2016)*, San Francisco, United States, 17-20th April.

2015 **I. Gómez-García-Toraño**, V-H. Sánchez-Espinoza, R. Stieglitz. Simulation of a Large Break LOCA in a German Konvoi PWR with the Severe Accident code ASTEC. *46th Annual Meeting on Nuclear Technology*, Berlin, Germany, 5-7th May.

2014 **I. Gómez-García-Toraño**, V-H. Sánchez-Espinoza, R. Stieglitz. Validation of ASTEC on the QUENCH-08 Experiment. *International Youth Nuclear Congress (IYNC'14)*, Burgos, Spain, 6-12th July.

2014 **I. Gómez-García-Toraño**, V-H. Sánchez-Espinoza, R. Stieglitz. ASTEC validation on the KIT reflooding Experiment QUENCH-08. *45th Annual Meeting on Nuclear Technology*, Frankfurt am Main, Germany, 6-8th May.

Other Conference articles

2017 **I. Gómez García-Toraño**, V-H. Sánchez-Espinoza. Analysis of PWR Severe Accident sequences including mitigative measures to prevent or delay the failure of the safety barriers with the severe accident code ASTEC. *International Conference on Topical Issues in Nuclear Installation Safety Demonstration of Advanced Water Cooled Nuclear Power Plants*. Vienna, Austria, 6-9th June.

2015 **I. Gómez García-Toraño**, V. Sánchez. Validation of ASTECV2.1 based on the QUENCH-08 Experiment. *21st QUENCH Workshop*, Karlsruhe, Germany, 27-29th October.